TESE DE DOUTORAMENTO

INTERPLAY BETWEEN ELECTRONIC, MAGNETIC AND STRUCTURAL DEGREES OF FREEDOM IN CRYSTALLINE TRANSITION METAL COMPOUNDS

Adolfo Otero Fumega

ESCOLA DE DOUTORAMENTO INTERNACIONAL DA UNIVERSIDADE DE SANTIAGO DE COMPOSTELA

PROGRAMA DE DOUTORAMENTO EN CIENCIA DE MATERIAIS

SANTIAGO DE COMPOSTELA

2021

USC
UNIVERSIDADE
DE SANTIAGO
DE COMPOSTELA

DECLARACIÓN DO AUTOR/A DA TESE

Interplay between Electronic, Magnetic and Structural Degrees of Freedom in Crystalline Transition Metal Compounds

D./Dna. Adolfo Otero Fumega

Presento a miña tese, seguindo o procedemento axeitado ao Regulamento, e declaro que:

1) A tese abarca os resultados da elaboración do meu traballo.
2) De selo caso, na tese faise referencia ás colaboracións que tivo este traballo.
3) A tese é a versión definitiva presentada para a súa defensa e coincide coa versión enviada en formato electrónico.
4) Confirmo que a tese non incorre en ningún tipo de plaxio doutros autores nin de traballos presentados por min para a obtención doutros títulos.

En Santiago de Compostela, 13 de Maio de 2021

Asdo.....

USC
UNIVERSIDADE
DE SANTIAGO
DE COMPOSTELA

AUTORIZACIÓN DOS DIRECTORES / TITOR DA TESE

Interplay between Electronic, Magnetic and Structural Degrees of Freedom in Crystalline Transition Metal Compounds

D./Dna. Víctor Pardo Castro

D./Dna. José Francisco Rivadulla Fernández

INFORMA/N:

Que a presente tese, correspóndese co traballo realizado por D/Dna. Adolfo Otero Fumega, baixo a nosa dirección, e autorizamos a súa presentación, considerando que reúne os requisitos esixidos no Regulamento de Estudos de Doutoramento da USC, e que como directores desta non incorre nas causas de abstención establecidas na Lei 40/2015.

De acordo co indicado no Regulamento de Estudos de Doutoramento, declaramos tamén que a presente tese de doutoramento é idónea para ser defendida en base á modalidade Monográfica con reproducción de publicaciones, nos que a participación do/a doutorando/a foi decisiva para a súa elaboración e as publicacións se axustan ao Plan de Investigación.

En Santiago de Compostela, 13 de Maio de 2021

USC
UNIVERSIDADE
DE SANTIAGO
DE COMPOSTELA

Abstract

Interplay between Electronic, Magnetic and Structural Degrees of Freedom in Crystalline Transition Metal Compounds

---

Adolfo Otero Fumega

USC UNIVERSIDADE DE SANTIAGO DE COMPOSTELA

Adolfo Otero Fumega

Crystalline Transition Metal Compounds (TMC) show a diverse amount of physical properties. They can be good metals, semiconductors or insulators, and they can develop intriguing ordered phases such as ferromagnetism or superconductivity. The partially filled d electrons provided by the transition metal atom play a fundamental role to determine these. It is the subtle interplay between their electronic, magnetic and structural degrees of freedom that leads to different ground state properties and phase transitions. This heterogeneous physical behaviour makes TMC highly interesting from a technological point of view, but also from a more fundamental perspective. Therefore, this kind of compounds represent an ideal platform to study emergent phenomena in Condensed Matter Physics. In this thesis we have studied from a theoretical point of view the interplay between the electronic, magnetic and structural degrees of freedom in TMC. The first three chapters are devoted to explain the theoretical aspects and methods required to perform the different studies in the subsequent chapters. In what follows, we will summarize the content and results of the chapters presented in this thesis.

In Chapter 1 we provide the theoretical aspects to describe materials at the nanoscale. Nuclei and electrons are the fundamentals particles that determine the properties of materials. An unsolvable many-body interacting Hamiltonian is presented as the corner stone to describe a real material. Therefore, different approximations are required to make the problem tractable. We start with the Born-Oppenheimer and adiabatic approximations that allow to separate the analysis for nuclei and electrons. The multielectronic problems is discussed in the framework of the Density Functional Theory (DFT). This theory is developed upon the Hohenberg-Kohn theorems, where the electronic density is demonstrated to uniquely determine the properties of a material. DFT is made practical through the Kohn-Sham approach. An independent electron system is used to mimic the interacting one. However, in this formulation the electron correlation, introduced via the so-called exchange-correlation term, remains elusive. Hence, approximations to this term are required. We provide definitions of different exchange-correlation functionals. After that, we present the methods used to solve the Kohn-Sham equations, from full-electron localized-orbital approaches to pseudopotential plane-wave methods. Moreover, simplified models, like spin or tight-binding Hamiltonians, are introduced at this step. Regarding the nuclear motion, a classical lattice dynamic approach is introduced. We describe first the harmonic approximation to obtain the phonon spectrum of a crystal. After that, we see how to compute anharmonic effects. This will be essential to correctly describe the lattice heat transport. Different methods to compute the lattice dynamics are exposed. Therefore, in this first chapter we pave the way to study from a theoretical point of view any material.

In Chapter 2, the fundamental concept of symmetry is analyzed. We start providing a definition of symmetry group. After that we describe the different symmetry groups that are encountered in a crystal, and in particular when dealing with TMC. A detailed exposition of different point groups and their effect on d electrons is given. Translational symmetry is presented as a fundamental symmetry in crystals. The notion of (electronic and phonon) energy bands is shown to be determined by this symmetry. Here, we provide

a bird's eye on the different band features that we may encounter in a crystal. Following that, time-reversal symmetry is defined and its connection to different magnetic orders is shown. Finally, a brief introduction to the novel topic of topological invariants is provided.

In Chapter 3 the connection between the nanoscale and the macroscale of a material is provided through Statistical Mechanics and transport properties. We start defining some special quantities in thermal equilibrium. The density of states and the projected density of states are introduced. After that, the Bose-Einstein distribution function for phonons and the Fermi-Dirac distribution function for electrons are defined. They provide the number of occupied states per unit volume at a given energy for a system in thermal equilibrium. A discussion is introduced on how to interpret the density of states and the distribution function in terms of the properties and stability of a system. Subsequently, we leave the system from equilibrium in order to compute its transport properties. This is performed in the framework of the Boltzmann transport equation. External fields modify the distribution functions that tend to restore the equilibrium in a relaxation time. This time takes into account different scattering processes that restore an equilibrium in the system. The constant relaxation time approximation is considered for electrons, while for the case of phonons it is directly computed through the introduction of anharmonic effects. All this allows to define different transport coefficients: electrical conductivity, electronic thermal conductivity, Seebeck coefficient and lattice thermal conductivity. Apart from that, we discuss how these transport coefficients interplay and determine the goodness of a thermoelectric material.

After the first three chapters in which we expose the theory and methods to solve the many-body problem, we begin the different studies on TMC. In particular, special attention is given to complex oxides and layered van der Waals materials. These classes of compounds present a huge variety of physical properties. Importantly, they can be easily synthesized and engineered in different nanostructures. Specifically, complex oxides are remarkably stable in normal conditions and layered van der Waals materials permit reaching the two dimensional limit. Therefore, these compounds are promising candidates to study novel emergent phenomena at room temperature. Apart from these materials, other kind of compounds are analyzed to demonstrate the important role that d electrons may play.

We start studying the transport properties of $SrTiO_3$ in Chapter 4. $SrTiO_3$ is a prototypical example of complex oxide where different phenomena can be studied. Notably, doped $SrTiO_3$ has been highlighted as a good thermoelectric material. This kind of compounds are able to efficiently convert a thermal gradient into an electrical potential difference and vice versa. Transport properties play a fundamental role to determine how good a thermoelectric material is. In particular, the thermopower or Seebeck coefficient needs to be maximized in order to optimize the potential difference at a given thermal gradient; and the lattice thermal conductivity needs to be minimized in order to maintain the thermal gradient. As we report in Chapter 3, these macroscopic properties are determined by the electronic and crystal structure. Therefore, in this chapter we analyze, from an *ab initio* perspective, what are the main features that determine these transport

coefficients and how they can be tuned via structural distortions. The first part is devoted to the study of thermopower. We analyze the effect of the orbital degeneracy on the Seebeck coefficient as a function of strain and the doping level. In order to do so, we build a simplified model for the thermopower. This is based on the Mott and Heikes formulas. A strain-dependent degeneracy factor that models the effect on the thermopower of the orbital degeneracy of the t_{2g} electrons is introduced. The degeneracy factor can be computed using DFT. This allows to decouple the effect of strain and doping coming either from entropy-related electronic degeneracies or from modifications to the band structure. An analysis of the electronic degeneracies and effective masses as a function of strain is provided. These two quantities are found to determine the thermopower. The generated model is applied to the particular case of $SrTiO_3$. Two different doping regimes are encountered. At low doping any kind of strain reduces the thermopower due to the dominance of the entropy-related term that reduces the degeneracy factor when applying strain. At high doping, the useful limit for thermoelectric applications, the energy transport term is dominant. Thus, tensile strain enhances the thermopower, since it increases the volume of the unit cell. This increase of the unit cell leads to a favourable modification of the bandwidth and hence to the effective mass. In the second part we analyze the lattice thermal conductivity of $SrTiO_3$. A detailed examination of the main sources of thermal transport is presented. We study in both structural phases of $SrTiO_3$, the high temperature cubic phase and the low temperature tetragonal one, how different structural distortions affect the lattice thermal conductivity. In the cubic phase, the computation of the phonon lineshape allows to determine that the acoustic bands and the low-energy triply degenerate polar mode are the main heat carriers. Reducing the unit cell increases the dispersion of the acoustic bands and shifts to higher energies the polar modes. This increases the group velocity and reduces the phonon scattering rate leading to an enhancement of the lattice thermal conductivity. The opposite behavior is found when the unit cell volume is increased. If a tetragonal distortion is applied to the cubic phase the degeneracy of the polar modes is broken. A softening of the c-axis polar mode occurs and the dispersion of the acoustic bands is modified. All this leads to a decrease in the thermal conductivity. In the low temperature phase, octahedral rotations appear bringing a new degree of freedom to consider when analyzing the lattice thermal conductivity. As in the high-temperature phase, the acoustic bands and the polar modes are found to be responsible for the heat transport. The effect of the unit cell volume, the c/a ratio and the octahedral rotation angle are independently investigated. Again, an increase of the unit cell volume decreases the acoustic bands' dispersion and lowers the polar modes frequency, thus increasing the thermal conductivity. The enlargement of the c/a ratio decreases the acoustic bands' dispersion and hence the thermal conductivity. Finally, the octahedral rotation angle is found to be strongly coupled to the phonon-active polar modes. An increase of this angle raises the energy of the polar modes, decreasing the scattering rate and increasing the thermal conductivity. Taking into account the analyses of both transport coefficients, the thermoelectric response of $SrTiO_3$ can be optimized by reducing the thermopower and decreasing the lattice thermal conductivity. This can

be achieved by increasing the volume of the unit cell and decreasing octahedral rotations in the system via nanostructural engineering. These studies provide a guide to find better thermoelectric materials. Moreover, they produce fundamental understanding on the transport properties of similar perovskite-based oxides.

In Chapter 5 we analyze the ferromagnetic and insulating behaviour that emerges on $LaCoO_3$ when grown on top of $SrTiO_3$ in the (001) direction. *Ab initio* calculations provide a description of the thermodynamic stability of different stoichiometries in which oxygen vacancies are introduced mimicking the results encountered in experiments. They allow to determine the ground state configuration of $LaCoO_3$ when subject to tensile strain when grown on top of $SrTiO_3$. Moreover, DFT calculations allow to analyze the electronic structure and magnetic properties of $LaCoO_3$. We found that the most stable configuration is given by an off-stoichiometry of the form $LaCoO_{2.83}$ produced by about 6% oxygen vacancies. Those oxygen vacancies form chains perpendicular to the (001) direction. Moreover, the distance between La layers and the lattice parameter in the (001) direction is in agreement with experimental findings. From an electronic structure perspective, we found that the Co atoms set in the plane of oxygen vacancies are a mixture of Co^{2+} low-spin and Co^{2+} high-spin with ferromagnetic exchange couplings. The remaining Co^{3+} cations in an octahedral environment are non magnetic. This configuration leads to a total magnetic moment that agrees with experiments and explains the ferromagnetic behaviour. Regarding the insulating character, we found a natural gap opening due to the crystal field splitting induced by the oxygen vacancies and the addition of a reasonable U value. Therefore, we explain the ferromagnetic insulating phase from a simple ionic picture. This result provides better understanding of ferromagnetic insulators and provides guidance to find this unusual phase in similar oxides in which oxygen vacancies might play a fundamental role.

In Chapter 6 we analyze the effect of Sr-doping in the electronic structure and magnetic properties of infinite-layer nickelates $RNiO_2$ (R= La, Nd). This family of compounds had been theoretically proposed to be analogous to high-temperature-superconducting cuprates. However, it was just a few years ago when those predictions were confirmed by experiments. Superconducting cuprate and nickelate parent compounds, i.e., their undoped states, show a radically different electronic and magnetic behaviour. While cuprates are antiferromagnetic insulators, nickelates show a non-magnetic metallic behaviour. However, upon hole doping (doping with Sr atoms) superconductivity emerges in both families. In order to address the nature of the hole doping, in this study we perform DFT calculations on the infinite-layer nickelates $RNiO_2$ as a function of the cation R (R= La, Nd) and Sr-doping (11% or 25%). The *ab initio* analyses are carried out with two different double counting schemes in the framework of LDA+U calculations. The results show critical changes in the electronic structure of these nickelates upon Sr-doping. Sr reduces the so-called self-doping effect by shifting above the Fermi level the rare-earth d bands leading to a single-band picture in which the Ni $d_{x^2-y^2}$ band dominates. Moreover, the charge transfer energy between the Ni and the O atom is reduced. Regarding the magnetic properties, our calculations show that the low-spin Ni^{2+} state is lower in energy.

Therefore, all these results demonstrate that Sr-doping induces a cuprate-like character in the electronic and magnetic properties of infinite-layer nickelates. Thus, they suggest a cuprate-like description for the superconducting state.

Chapter 7 is devoted to study the electronic structure of Cs_2CuCl_4, a compound that has been discussed in the framework of geometrically frustrated quantum spin liquids. A combination of experimental techniques, Resonant Inelastic X-ray Scattering (RIXS) and X-ray Absorption Spectroscopy (XAS), and *ab initio* calculations allow to determine its spectrum. The analysis shows that the electronic structure is mainly determined by the crystal field splitting that Cu^{2+} d electrons experience when placed in the strongly distorted tetrahedral environment created by the Cl^{1-} ions. The different crystal field splittings in the RIXS spectrum are correctly addressed by the DFT calculations. Apart from that, a charge transfer gap between the $[CuCl_4]^{2-}$ cluster and the Cs^{1+} s states is identified. This study shows the potential to combine experiment and theory. The spectroscopy results that we obtain pave the way to further examination of the exotic behaviour of this compound at low temperatures.

In the subsequent chapters we enter into the field of layered van der Waals crystals. This kind of compounds provide an excellent platform to study low-dimensional properties. In particular, magnetism in the two-dimensional limit has attracted a great deal of attention due to their numerous applications. In Chapter 8, a comparative study between the electronic structure and magnetic properties of two Cr-based van der Waals ferromagnets is presented. We study the effect of dimensionality on $CrBr_3$ and $Cr_2Ge_2Te_6$ from a theoretical and a experimental point of view. Instead of going to the two dimensional limit we go to a more three dimensional one by applying pressure on these systems. A Mott-Hubbard like insulator character with a d-d energy gap is found for $CrBr_3$. Moreover, that insulating behaviour remains under pressure. Differently, the energy gap of $Cr_2Ge_2Te_6$ is found to have p-d character, leading to a charge transfer insulating description. Our calculations predict an insulator to metal transition at around 6 GPa, which could be related to the structural transition that we observe in the high pressure X-ray experiments. The different insulating character of each compound and its evolution with pressure lead to a distinct evolution of the magnetic properties with pressure. Our experiments show a reduction of the Curie temperature of each compound when pressure is applied. However, a different trend is identified. The theoretical analysis concludes that the different pressure dependence of the in- and out-of-plane magnetic exchange couplings is responsible for that dissimilar tendency. Therefore, this work highlights the role of the electronic structure in the spin-spin interactions that cause the ferromagnetic order in these compounds. In particular, the effect of pressure, and consequently dimensionality, on the electronic structure and magnetic properties is remarked for Cr-based van der Waals materials.

In Chapter 9 we continue studying promising van der Waals candidates to hold long-range ferromagnetic order in the single-layer limit. In particular we focus our analysis on two transition metal dichalcogenides (TMDs), $CrTe_2$ and VSe_2. Many of these TMDs develop a charge density wave (CDW) phase at low temperatures that interacts with the

so-pursued ferromagnetic order. Therefore, the aim of this chapter is to study the interplay between ferromagnetic and CDW orders in TMDs. In the first part we focus on $CrTe_2$. In bulk it is a room-temperature ferromagnet with magnetic moments pointing in-plane. We perform an *ab initio* study in which we show how to drive the moments out-of-plane. Then, we study in detail the monolayer limit. We demonstrate that a CDW phase emerges at low temperatures. We provide a symmetry analysis of this structural phase and show guidance to experimentally detect it. The phonon mode responsible of the transition is identified, thus highlighting a way to switch between the two structural phases. In the CDW phase pseudogaps are opened around the Fermi level and the d orbitals get more localized. This brings the moments to point out-of-plane, overwhelming the constraints imposed by the Mermin-Wagner theorem and leading to long-range ferromagnetic order in the monolayer. Tensile strain is found to cause a similar effect, localizing the d orbitals and driving the moments out-of-plane. The second part of this chapter is devoted to the study of VSe_2. Experiments on bulk VSe_2 show that a CDW phase emerges below 110 K and a non-magnetic behaviour is reported. We perform a cautious *ab initio* study that shows that the CDW phase quenches magnetism in bulk VSe_2. Our results reconcile the disagreement between experiments and previous DFT calculations in which the effect of the CDW had not been taken into account, thus, predicting a wrong ferromagnetic behaviour for this compound. Apart from that, the CDW structure that we obtain is able to explain the kink in the thermopower observed in experiments at the transition temperature. The study of the monolayer is still an active are of research. However, we show that the presence of a CDW phase also affects in a detrimental way the ferromagnetic order. This chapter highlights the crucial role of the low-temperature or CDW structure when determining the magnetic properties of TMDs.

Finally, in Chapter 10 a theoretical analysis on $BaSn_2$ is performed. This layered compound is a topological nodal-line semimetal when spin-orbit coupling is neglected. Topological materials have attracted a great deal of attention due to their robust surfaces states that could prompt to emergent phenomena and promising applications. We use $BaSn_2$ as a theoretical playground to analyze pressure-driven topological transitions. A combined set of DFT calculations and a model tight-binding Hamiltonian are used in this chapter. We found that uniaxial pressure leads to a topological-to-topological phase transition at around 4 GPa. In the high-pressure phase the number of topological nodal lines increases. We found that Ba d electrons play a fundamental role to explain the transition. The hopping energies between Ba d_{xz} and d_{yz} with Sn p_z orbitals increases with pressure. Thus, we provide the microscopic mechanism behind this kind of novel transitions. Moreover, we present a way to experimentally detect them by means of magnetotransport measurements.

The theoretical aspects and methods presented in this thesis together with the studies on TMC provide a reliable source of fundamental understanding in the contemporary area of Condensed Matter Physics.

Resumo

Interacción entre os Graos de Liberdade Electrónicos, Estruturais e Magnéticos en Compostos Cristalinos con Metais de Transición

Adolfo Otero Fumega

USC UNIVERSIDADE DE SANTIAGO DE COMPOSTELA

USC
UNIVERSIDADE
DE SANTIAGO
DE COMPOSTELA

Os compostos cristalinos con metais de transición, TMC das súas siglas en inglés, amosan propiedades físicas moi diversas. Son dende bos metais ata semicondutores ou aillantes, e moitos de eles desenvolven fases ordenadas como o ferromagnetismo ou a superconductividade. Os metais de transición achegan electróns d parcialmente ocupados, serán estes os que xoguen un papel fundamental á hora de determinar as propiedades destes materiais. A sutil interacción entre os graos de liberdade electrónicos, estruturais e magnéticos é a responsable de establecer diferentes estados fundamentais e de ocasionar transicións entre fases ordenadas. Este comportamento tan heteroxéneo fai que os TMC sexan altamente interesantes dende un punto de vista tecnolóxico, pero tamén dende unha perspectiva puramente teórica. Estes compostos representan unha excelente plataforma para estudar fenómenos emerxentes en Física da Materia Condensada. Nesta tese estudamos dende un punto de vista teórico a interacción entre os graos de liberdade electrónicos, estruturais e magnéticos nos TMC. Os primeiros tres capítulos están adicados a explicar os fundamentos e métodos teóricos necesarios para levar a cabo os estudos da segunda parte. No que segue resumiremos o contido e os resultados de cada un dos capítulos.

No capítulo 1 amosamos como se describen os materiais na nanoescala. Electróns e núcleos son as partículas fundamentais que determinan as propiedades dos materiais a través das súas interaccións. Estás veñen descritas por un Hamiltoniano irresoluble de moitos corpos. Polo tanto, será preciso realizar numerosas aproximación para facer o problema tratable. Comezamos introducindo as aproximacións de Born-Oppenheimer e a adiabática. Estas permiten separar a análise para electróns e núcleos. O problema multielectrónico discutirémolo no marco da teoría do funcional da densidade, DFT do inglés. Está teoría baséase nos teoremas de Hohenberg e Kohn que demostran que a densidade electrónica determina de xeito unívoco as propiedades do material. O xeito de facer práctica esta teoría é por medio da aproximación de Kohn e Sham, que considera que o problema de electróns interaccionantes se pode mapear nun de electróns independentes. Non obstante, nesta formulación a correlación entre os electróns, incluída a través do termo de correlación e intercambio, é descoñecida e polo tanto serán precisas aproximacións a este termo. Amosaremos diferentes aproximacións ao funcional de correlación e intercambio. Despois presentaremos os métodos empregados para resolver as ecuación de Kohn-Sham, dende aproximacións con orbitais localizados e tódolos electróns ata ondas planas e pseudopotenciais. Ademáis, introduciremos neste punto un par de modelos simplificados: Hamiltonianos de espín e modelos tipo *tight-binding*. Con respecto á dinámica nuclear esta será aproximada dun xeito clásico. Describiremos primeiro a aproximación harmónica que permite obter o espectro de fonóns do cristal. Despois veremos como introducir efectos anharmónicos. Estes serán esenciais para describir axeitadamente o transporte de calor por fonóns. Amosaremos diferentes métodos para calcular a dinámica nuclear. Polo tanto, este primeiro capítulo sentará as bases teóricas no estudo de materiais.

No capítulo 2 analizamos o concepto fundamental de simetría. Comezaremos dando unha definición de grupo de simetría para despois describir os diferentes grupos de simetría que se atopan nun cristal e, máis en particular, nos TMC. Proporcionaremos unha exposición detallada do efecto causado nos electróns d por diferentes grupos puntuais de

simetría. Presentaremos logo o simetría traslacional como unha das simetrías máis fundamentais dun cristal. Veremos que a noción de bandas de enerxía (electrónicas e fonónicas) emerxe desta simetría. Amosaremos a vista de páxaro diferentes características que podemos atopar nas bandas dun cristal. Seguidamente, definimos a simetría de inversión temporal conectándoa con diferentes ordes magnéticos. Por último, presentaremos unha breve introdución ao renovado tema de invariantes topolóxicas en materia condensada.

No capítulo 3 estableceremos a conexión entre a nanoescala e a macro escala dun material por medio da mecánica estatística e as propiedades de transporte. Comezaremos definindo cantidades especias no equilibrio térmico como a densidade de estados ou a densidade de estados proxectada. As distribucións de Bose-Einstein e Fermi-Dirac para fonóns i electróns respectivamente serán definidas. Estas dan o número de estados ocupados por unidade de volume a unha enerxía dada para un sistema en equilibrio. A estabilidade dun sistema será discutida en termos da densidade de estados e as funcións de distribución. De seguido levaremos o sistema fóra do equilibrio para estudar as súas propiedades de transporte. Esto farémolo no marco da ecuación de transporte de Boltzmann, onde campos externos modificarán as funcións de distribución tratando de restrablecer o equilibrio nun tempo de relaxación. Este tempo relacionase cos diferentes procesos de collisións entre as partículas que tratan de restaurar o equilibrio. Para transporte electrónico aproximaremos o tempo de relaxación a unha constante, mentres que no caso de fonóns o tempo de relaxación será calculado por medio de termos anharmónicos. Todo isto permitiranos definir os seguintes coeficientes de transporte: condutividade eléctrica, condutividade térmica electrónica, coeficiente Seebeck e condutividade térmica fonónica. Tamén discutiremos a interacción que existe entre estes coeficientes para determinar como de bo termoeléctrico é un material.

Despois destes tres capítulos nos que expoñemos a teoría e os métodos para resolver o problema de moitos corpos xa estamos en disposición de comezar os nosos estudos en TMC. En particular, centrarémonos en óxidos complexos e materias laminares de van der Waals. Estas clases de compostos presenta unha gran variedade de propiedades físicas e poden ser sintetizados en multitude de estruturas de forma sinxela. No caso dos óxidos complexos é salientable a súa gran estabilidade en condicións normais de presión e temperatura. No tocante aos materiais laminares de van der Waals, o feito de estar formados por capas permite exfolialos ata chegar ao limite en dúas dimensións. Polo tanto, estas familias de compostos presentanse como prometedores á hora de estudar novos fenómenos emerxentes a temperatura ambiente. Aparte de estes materiais, outro tipo de compostos serán analizados para mostrar o importante rol dos electróns d.

Comezaremos no capítulo 4 estudando as propiedades de transporte no $SrTiO_3$. Este composto representa un prototipo para o estudo de diferentes fenómenos físicos. Dexeito remarcable, o $SrTiO_3$ dopado atópase dentro dos mellores materiais termoeléctricos. Este tipo de materiais son capaces de converter de forma eficiente un gradiente térmico nunha diferenza de potencial e viceversa, polo que son moi interesantes dende o punto de vista da innovación. Neste tipo de materiais é importante que o coeficiente Seebeck sexa maximizado coa finalidade de optimizar a diferenza de potencial xerada por un gradiente

térmico dado. A maiores, tamén é importante que a condutividade térmica fonónica sexa a mínima posible para que así se manteña o gradiente de temperatura. Como recollemos no capítulo 3, estas propiedades de transporte veñen determinadas pola estrutura electrónica e cristalina. Polo tanto, o obxectivo deste capítulo será estudar dende unha perspectiva *ab initio* cales son as características fundamentais destes coeficientes de transporte e como poden ser alteradas por medio de distorsións estruturais. A primeira parte deste estudo estará adicada ao coeficiente Seebeck. Analizaremos o efecto da dexeneración orbital no coeficiente Seebeck como función de distorsión (compresión e tensión) da celda unidade e do nivel de dopaxe. Para facer isto construiremos un modelo simplificado para o coeficiente Seebeck fundamentado nas ecuacións de Mott e Heikes. Introduciremos un factor dependente da tensión que modelizará o efecto causado pola dexeneración dos orbitais t_{2g} no coeficiente Seebeck. Poderemos calcular dende DFT este factor de dexeneración, desacoplando deste modo o efecto da tensión e a dopaxe debidas á entropía da dexeneración electrónica ou debidas a modificacións da estrutura de bandas. Atoparemos que as masas electrónicas efectivas e a dexeneración electrónica son os actores principais que determinan o coeficiente Seebeck como función da distorsión. Aplicando o modelo ao caso do $SrTiO_3$ atopamos dous réximes de dopaxe. A baixas dopaxes calquer tipo de distorsión diminúe o valor do coeficiente Seebeck debido a que o termo dominante é o das dexeneracións, polo que calquera distorsión reduce o factor de dexeneración. A altas dopaxes, o réxime interesante en aplicacións, o termo enerxético domina e atopamos que aplicar unha tensión aumenta o coeficiente Seebeck. Isto é debido a que a tensión produce un aumento do volume da celda unidade que modifica de xeito favorable o ancho de banda e polo tanto a masa efectiva. Na segunda parte deste capítulo analizaremos a condutividade termica fonónica do $SrTiO_3$. Faremos un escrutinio das principais causas do transporte térmico nas dúas fases estruturais do $SrTiO_3$ e como modificalas aplicado distorsións na estrutura. A altas temperaturas teremos unha fase cúbica e a baixas unha tetragonal con rotacións dos octaedros. Na fase cúbica, determinamos que as bandas acústicas e o modo polar triplemente dexenerado son os principais responsables do transporte de calor. Unha redución do volume da celda unidade aumenta a dispersión dos fonóns acústicos e a enerxía dos modos polares. Deste xeito incrementase a velocidade de grupo e redúcense as colisións fonónicas aumentando a condutividade térmica. O comportamento oposto ocorre se aumentamos o volume da celda unidade. No caso de aplicar unha distosión tetragonal a dexeneración dos modos polares rómpese baixando en enerxía o modo na dirección c e modificando a dispersión das bandas acústicas. Todo isto causa unha diminución do transporte térmico. Na fase a baixa temperatura a aparición de rotacións octaédricas proporciona novos graos de liberdade a considerar cando analizamos a condutividade térmica. Do mesmo xeito que ocorre na fase cúbica, os fonóns acústicos e polares son os responsables do transporte. Analizando de xeito independente o efecto do volume da celda unidade, o ratio c/a e o ángulo das rotacións octaédricas observamos que: i) un incremento do volume causa unha diminución da dispersión das bandas acústicas e baixa a enerxía dos modos polares, diminuindo a condutiviade térmica; ii) incrementar o ratio c/a reduce a dispersión das bandas acústicas e con elo a condutividade térmica; iii) atopamos que o ángulo das

rotación octaédricas está fortemente acoplado cos modos polares, un aumento do ángulo aumenta a enerxía dos modos polares diminuíndo as interaccións fonónicas e aumentando a condutividade térmica. Se consideramos conxuntamente as dúas análises para os coeficientes de transporte, a resposta termoeléctrica pode optimizarse incrementando o volume da celda unidade con tensión e reducindo as rotacións octaédricas. Os resultados deste capítulo proporcionan un coñecemento fundamental das propiedades de transporte de óxidos similares e guían a procura de mellores materiais termoeléctricos.

No capítulo 5 analizeremos a fase ferromagnética e aillante que emerxe no $LaCoO_3$ cando se medra sobre $SrTiO_3$ na dirección (001). Os cálculos *ab initio* que realizaremos pertimirán estudar a estabilidade termodinámica de estruturas con distintas estequiometrías nas que introduciremos vacantes de oxíxeno de acordo coas observacións experimentais. Seremos capaces de determinar o estado fundamental e a estrutura electrónica e propiedades magnéticas do $LaCoO_3$ medrado sobre $SrTiO_3$. Atopamos que a estequiometría máis estable é $LaCoO_{2,83}$; é dicir, un 6 % de vacantes de oxíxeno. Así mesmo, determinamos que as vacantes forman cadeas perpendiculares á dirección (001); e que o parámetro de rede c e as distancias entre as capas de átomos de La están en consonancia coas medidas experimentais. Dende o punto de vista electrónico, veremos que os átomos de Co que se encontran no plano das vacantes son unha mistura de Co^{2+} con alto espín e Co^{2+} con baixo espín con acoplamentos ferromagnéticos. Os restantes cobaltos manteñense como Co^{3+} non magnéticos no entorno octaédrico. A configuración que atopamos da lugar a un momento magnético que concorda co experimental, así como a un orde ferromagnético. Con respecto ao comportamento aillante, observamos que un *gap* enerxético emerxe como consecuencia do desdobramento do campo cristalino inducido polas vancante de oxíxeno a un valor razoable de U. Polo tanto, neste traballo explicamos a fase ferromagnética e aillante dende unha perspectiva iónica moi sinxela. Estes resultados ofrecen unha maior comprensión da natureza dos aillantes ferromagnéticos e guían a procura de novos óxidos con esta inusual fase nos que as vancantes de oxíxeno puidesen xogar un papel relevante.

No capítulo 6 analizaremos o efecto da dopaxe con átomos de Sr na estrutura electrónica e propiedades magnéticas dos niquelatos de capa infinita $RNiO_2$ (R= La, Nd). Esta familia de compostos levaba anos proposta de xeito teórico como análogo natural dos cupratos superconductores a alta temperatura. Non obstante, a confirmación experimental deste feito non ocorreu ata vai un par de anos. Os chamados compostos pais; é dicir, sen dopar, dos cupratos e niquelatos amosan un comportamento electrónico e magnético radicalmente diferente. Mentres que os cupratos son aillantes antiferromagnéticos, os niquelatos son metais e non magnéticos. Sen embargo, ao introducir dopaxe de ocos (dopaxe con átomos de Sr) a supercondutividade emerxe nas dúas familias. Polo que a natureza dos ocos preséntase como un estudo a realizar. Neste traballo realizaremos cálculos DFT en $RNiO_2$ como función do catión R (R=La, Nd) e da dopaxe con Sr (11 % e 25 %). Empregaremos dous esquemas diferentes de contaxe dobre nos cálculos LDA+U. Os resultados amosarán cambios moi substanciais na estrutura electrónica destes niquelatos ao seren dopados con Sr. Por unha parte, o Sr reduce o efecto da chamada autodopaxe desprazando as bandas *d* da terra rara por riba do nivel de Fermi. Esto da lugar a unha descripción

cunha sóa banda onde o orbital $d_{x^2-y^2}$ do átomo de Ni é dominante. Ademáis, redúcese a enerxía transferencia de carga entre os átomos de Ni e O. Con respecto ás propiedades magnéticas, observamos que o estado de baixo espín para o Ni^{2+} é favorable. Polo tanto, todos estes resultados demostrans que dopando con átomos de Sr os niquelatos adquiren un comportamento semellante ao dos cupratos, suxerindo que a supercondutividade dos niquelatos presentará unha descripción como a dos cupratos.

No capítulo 7 estudaremos a estrutura electrónica do Cs_2CuCl_4, un composto que se ten discutido no marco dos líquidos de espín xeometricamente frustrados. Empregaremos de xeito combinado técnicas experimentais, como a dispersión inelástica por resonancia de raios X (RIXS do inglés) e a espectroscopía por absorción de raios X (XAS do inglés), e cálculos para determinar o espectro deste comoposto. A análise mostra que a estrutura electrónica está deteminada na súa maioría polo desdobramento dos electróns d do Cu^{2+} a causa do campo cristalino tetraédrico fortemente distorsionado xerado polos ións de Cl^{1-}. Os cálculos DFT permiten determinar os diferentes desdobramentos enerxéticos observados por RIXS. A maiores tamén identificamos o *gap* de transferencia de carga entre o cluster de $[CuCl_4]^{2-}$ e os estados s do Cs^{1+}. Este traballo amosa o potencial de combinar experimento e teoría e os resultados sentan as bases para un escrutinio máis detallado das exóticas propiedades deste composto a baixas temperaturas.

Nos seguintes capítulos achegarémonos ao estudo de materiais laminares de van der Waals. Este tipo de compostos representa unha plataforma excelente para estudar propiedades en materials con baixa dimensionalidade. En particular, o magnetismo neste límite de baixa dimensionalidade resulta moi interesante polas prometedoras aplicacións que podería ter. No capítulo 8 presentaremos un estudo comparativo entre a estrutura electrónica e as propiedades magnéticas de dous compostos de van der Waals ferromagnéticos. Estudaremos o efecto da dimensionalidade en $CrBr_3$ e $Cr_2Ge_2Te_6$ dende un punto de vista experimental e teórico. Para esto, no canto de ir ao límite puramente bidimensional estudaremos a evolución aplicando presión; isto é, índonos a un límite máis tridimensional. Atoparemos que o composto de $CrBr_3$ amosa un comportamento de tipo Mott cun *gap* $d-d$ e se mantén aillante ao aplicar presión. De modo diferente, o $Cr_2Ge_2Te_6$ presenta un *gap* enerxético tipo $p-d$ e polo tanto unha descripción de aillante por transferencia de carga. Os nosos cálculos predín unha transición aillante-metal arredor de 6 GPa, que podería estar relacionada coa transición structural observada nos experimentos de raios X a alta presión. O diferente carácter da estrutura electrónica e conseguinte evolución coa presión destes compostos implica unha evolución diferente das súas propiedades magnéticas coa presión. Os nosos experimentos amosas unha redución da temperatura de Curie nos dous compostos ao aplicar presión, non obstante a súa tendencia é diferente. A nosa análise teórica complúe que a diferente evolución dos acoplamentos magnéticos dentro e fóra do plano para cada composto determina a diferente tendencia das temperaturas de Curie. Polo que este traballo resalta o importante rol da estrutura electrónica para explicar as interaccións entre espíns que causan a orde ferromagnética. En particular, salientamos o efecto da presión, e por tanto da dimensionalidade, na estrutura electrónica e nas propiedades magnéticas en materias de van der Waals baseados en Cr.

No capítulo 9 seguiremos a estudar materiais de van der Waals que se presentan como prometedores candidatos para atopar orde ferromagnético de largo alcance no límite bidimensional. En concreto centrarémonos na análise de dous dicalcoxenuros d metais de transición (TMDs do inglés), $CrTe_2$ e VSe_2. Moitos destes compostos desenvolven unha fase de densidade de carga ondulatoria, ou fase *charge density wave* (CDW) en inglés, a baixas temperaturas que interacciona co procurado orde ferromagnético. Polo tanto o obxectivo principal deste capítulo será estudar a interacción entre os ordes ferromagneticos e CDW nos TMDs. Na primeira parte centrarémonos no $CrTe_2$ con infinitas capas, un ferromagnético a temperatura ambiente cos momentos apuntando dentro dos planos de van der Waals. Despois, pasamos ao estudo do límite monocapa, é dicir bidimensional, e atopamos que unha fase CDW emerxe a baixas temperaturas. Proporcionamos unha análise detalla da nova simetría cristalina e como recoñecela experimentalmente. O fonón responsable desta transición é identificado o que abre a posibilidade para saltar dunha fase á outra activando o devandito modo. Na fase CDW ábrense *pseudogaps* enerxéticos arredor do nivel de Fermi e os orbitais d localízanse máis. Isto fai que os momentos magnéticos apunten fóra do plano, superando as restricións impostas polo teorema de Mermin e Wagner e dando lugar a orde ferromagnético de largo alcance na monocapa. Tamén atopamos que unha distorsión tensionante da monocapa causa un efecto similar, localizando os electróns d e levando os momentos a apuntar fóra do plano. Na segunda parte deste capítulo centrámonos no estudo do VSe_2. Experimentalmente demóstrase que a forma multicapa deste composto desenvolve unha fase CDW por debaixo de 110 K e non se reporta ningún tipo de comportamento magnético. O noso estudo *ab initio* amosará que a fase CDW destrúe o magnetismo no VSe_2 multicapa. Esta minuciosa análise permite reconciliar o desacordo entre os experimentos e cálculos DFT anteriores nos que o efecto da CDW non se estaba a considerar; e que polo tanto predicían de xeito erróneo un comportamento ferromagnético neste material. A maiores, a estrutura CDW que obtivemos é capaz de explicar o salto atopado experimentalmente no coeficiente Seebeck á temperatura de transición. O estudo da monocapa continúa a ser un campo de investigación moi activo; sen embargo, neste traballo amosamos que a presenza dunha fase CDW afecta de xeito negativo ao ferromagnetismo. Polo tanto, neste capítulo salientamos o papel fundamental que xoga a estrutura CDW para determinar as propiedades magnéticas nos TMDs.

Por último, no capítulo 10 presentamos un estudo teórico no $BaSn_2$. Este composto laminar é un semimetal cunha liña nodal topolóxica cando se despreza o acoplamento espín orbital. Os materiais topolóxicos están a atraer moito interese debido a que presentan estados superficiais robustos que poderían dar lugar a fenómenos emerxentes e a prometedoras aplicacións. Neste estudo empregaremos ao $BaSn_2$ como prototipo para investigar transicións topolóxicas inducidas pola presión. Para elo, utilizaremos unha combinación de cálculos DFT e un modelo *tight-binding*. Atopamos que a presión uniaxial produce unha transitión de fase entre topoloxías non-triviais arredor de 4 GPa. Na fase a alta presión o número de liñas nodais topolóxicas aumenta. Nesta transición os electróns *d* xogan un papel fundamental, xa que é o aumento coa presión das enerxías de *hopping*

entre os orbitais d_{xz} e d_{yz} do Ba cos p_z do Sn o que fai emerxer as novas liñas nodais. Ademáis, amosamos a forma de detectar experimentalmente este tipo de transicións mediante medidas de magnetotransporte.

Os aspectos e métodos teóricos presentados nesta tese, xunto cos estudos nos distintos TMC, proporcionan unha mostra representativa do coñecemento fundamental que se está a levar a cabo na área de Física da Materia Condensada.

USC UNIVERSIDADE DE SANTIAGO DE COMPOSTELA

USC
UNIVERSIDADE
DE SANTIAGO
DE COMPOSTELA

Contents

Introduction and Objectives **xxiii**

I Theory and Methods 1

1 The Physical System 3

1.1 A Many-Body Quantum System . . . 3
1.2 Nuclei are heavier than Electrons . . . 6
1.3 Interacting Electrons . . . 9
1.3.1 Density Functional Theory . . . 10
1.3.2 What about Electron Independence? . . . 13
1.3.3 Spin and Relativistic Effects . . . 18
1.3.4 Electronic Structure Methods . . . 19
1.3.5 Simplified Models . . . 24
1.4 Nuclei and Vibrations . . . 26
1.4.1 Harmonic Approach . . . 27
1.4.2 Anharmonic Effects . . . 29
1.4.3 Nuclear Dynamics Methods . . . 30

2 Symmetry 35

2.1 Definition of a Symmetry Group . . . 35
2.2 Point Group Symmetry . . . 36
2.3 Translational Symmetry . . . 39
2.4 Time-Reversal Symmetry . . . 44
2.5 Topological Invariants . . . 46

3 Statistics and Transport 49

3.1 Thermal Equilibrium . . . 49
3.2 Transport Properties . . . 52

USC UNIVERSIDADE DE SANTIAGO DE COMPOSTELA

II Studies on Crystalline Transition Metal Compounds 57

4 Transport Properties of $SrTiO_3$ 59
4.1 Introduction . . . 59
4.2 Thermopower of $SrTiO_3$ . . . 60
4.2.1 Computational Methods . . . 61
4.2.2 Thermopower Modeling . . . 61
4.2.3 Results of the Model on $SrTiO_3$ . . . 66
4.3 Lattice Thermal Conductivity of $SrTiO_3$ . . . 76
4.3.1 Computational Methods . . . 77
4.3.2 Results and Discussion . . . 77
4.4 Conclusions . . . 89

5 Ferromagnetic and Insulating Behavior of $LaCoO_3$ 91
5.1 Introduction . . . 91
5.2 Computational Methods . . . 92
5.3 Results and Discussion . . . 93
5.3.1 Structural Characterization . . . 94
5.3.2 Electronic Structure and Magnetic behavior . . . 98
5.4 Conclusions . . . 104

6 Sr-doping on Infinite-layer Nickelates 105
6.1 Introduction . . . 105
6.2 Computational Methods . . . 107
6.3 Electronic Structure and Magnetism . . . 107
6.4 Conclusions . . . 113

7 Spectroscopy of Cs_2CuCl_4 115
7.1 Introduction . . . 115
7.2 Experimental and Computational Methods . . . 117
7.3 Results and Discussion . . . 118
7.4 Conclusions . . . 123

8 Cr-based van der Waals Ferromagnets 125
8.1 Introduction . . . 125
8.2 Experimental and Computational Methods . . . 127
8.3 Electronic Structure . . . 128
8.4 Magnetic Properties . . . 131
8.5 Conclusions . . . 135

9 Ferromagnetism and Charge Density Waves in TMDs 137
9.1 Introduction . . . 137
9.2 Computational Methods . . . 139

USC UNIVERSIDADE DE SANTIAGO DE COMPOSTELA

9.3 The case of $CrTe_2$ . . . 139
9.3.1 The Bulk . . . 140
9.3.2 The Monolayer . . . 142
9.4 The case of VSe_2 . . . 149
9.4.1 The Bulk . . . 151
9.4.2 The Monolayer . . . 155
9.5 Conclusions . . . 158

10 Topological Transitions in $BaSn_2$ **159**
10.1 Introduction . . . 159
10.2 Computational Methods . . . 161
10.3 Results and Discussion . . . 161
10.3.1 DFT Calculations . . . 161
10.3.2 Tight-binding Model . . . 164
10.4 Conclusions . . . 172

Final Remarks and Outlook **173**

Acknowledgements **175**

List of Publications **177**

Bibliography **201**

USC UNIVERSIDADE DE SANTIAGO DE COMPOSTELA

USC
UNIVERSIDADE
DE SANTIAGO
DE COMPOSTELA

Introduction and Objectives

> "With great power comes great responsibility."
>
> — Uncle Ben, The amazing Spiderman

This thesis has been written in the framework of a Material Science PhD program and it has been founded by the Spanish government through an FPU grant. Then, I would like to start reflecting on the impact that materials have in the world we live in, and why we should foster scientific research in this area.

From a historical point of view, it is not a coincidence that prehistoric Ages were termed with the name of the materials people used at that time: Stone, Bronze and Iron. Primitive societies and the interactions between different cultures were shaped by the use of such materials. Refinement of technologies based on metals and the widespread use of them led to the appearance of great empires in the Ancient and Middle Ages in which silver and gold became the standard good for trade. With the advent of the Modern Age the whole world became interconnected for the first time. New scientific developments were boosted in the Renaissance and were improved during that Era. They were essential to build the global world where we live. In the Contemporary Age the pursuit of the so-called welfare state has been the leitmotiv. Industrial Revolutions have brought new devices and appliances powered by electricity and fossil fuels that have made our lives easier. Advanced medical therapies and diagnose techniques have been promoted thanks to new developments in the area of Nanoscience. Interconnection between people all over the world has been possible due to the great progress in Condensed Matter Physics and Material Engineering. These advances have changed our world in such a drastic way that many people state that we have already entered into a new Era. Due to the silicon chips in which modern computers rely on, that new Era has been called the Silicon Age.

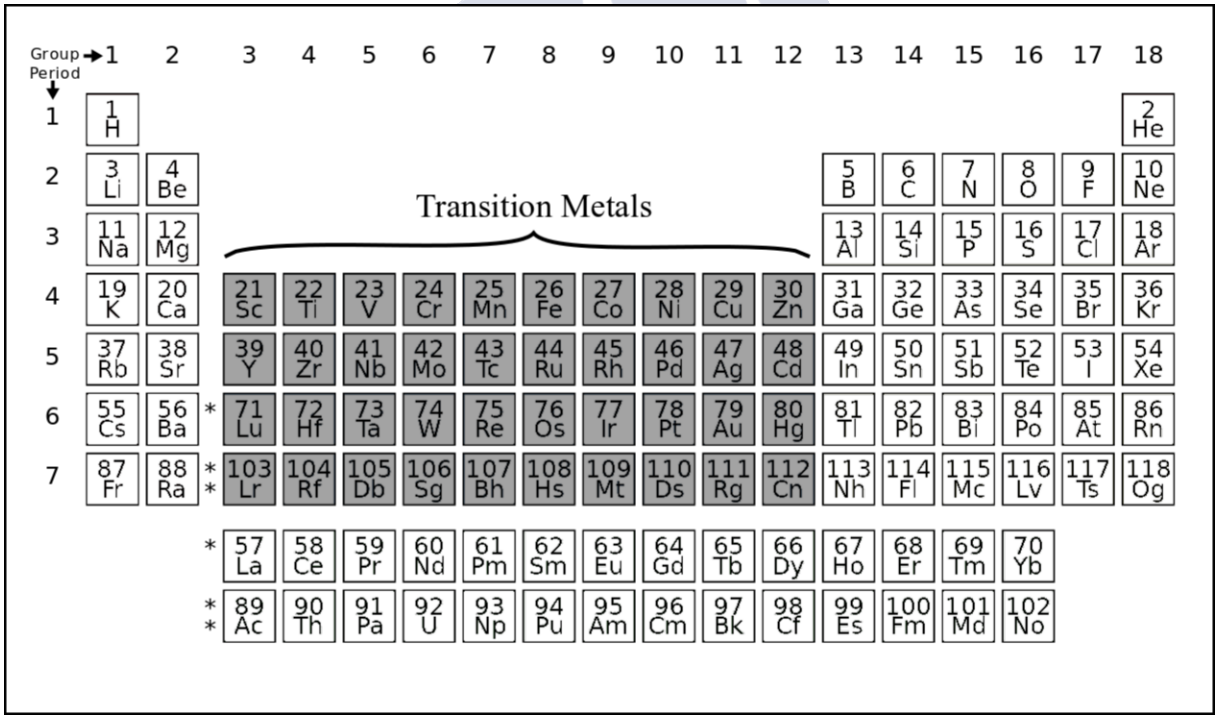
Nevertheless, that welfare state that we have been claiming might not be that real as we believe. The other side of the coin is always present, and we should think on the consequences that those technologies and developments have carried along them. The pursuit of the welfare state has created an increasing demand and dependence on energy and new materials. Most of the resources used to satisfy that demand are limited. This

has given rise to wars between nations of different cultures with the pretext of controlling more territories and make use of their natural resources. That apparent prosperity enjoyed in the richest nations has been possible due to the outsourcing of a much less demanding lifestyle to faraway regions. That global world shaped by conquests is nowadays becoming smaller due to the recent developments in telecommunications, human mobility infrastructures and engines. Year after year, the number of people looking for better life conditions grows. Migrations from the so-called less-developed countries to the rich areas occur. Materials and energy resources are managed by the wealthier regions in a way that makes impossible to satisfy the demand for everyone in the world. Even more, not only human inequalities are being generated, but also a destructive environmental impact is being caused. In this social context of increasingly interconnected globalization and energy demand, the word unsustainable has been evoked. A dramatic situation is expected to happen if the welfare state is not rethought. Material Science offers the opportunity to obtain new renewable energetic resources and provide an efficient management of them. Therefore, technologies based on materials that allow to create a more sustainable and fair world for everyone must be the goal to chase.

The aim of this thesis is to provide a fundamental understanding of materials. This entails the theoretical resolution of one of the most exciting physical problems of all time. From a purely humanistic point of view this could be enough for many of us. However, as we have stated, knowing the principles in which materials are based on will help to fulfill the global issues that we face. Moreover, the many-body physical models used to describe materials at the nanoscale could provide understanding of other natural and social systems that are nowadays more relevant than ever in the highly interconnected world that we live.

The main body of this thesis is divided in two parts. In Part I we will summarize the theory and methods used to analyze the materials presented in Part II. This theoretical introduction will not be new in content since many excellent books cover this topic in much more detail than what we will do here [1–5]. However, I will try to adapt the form of that content in order to introduce the reader into the studies of the second part. In Chapter 1 we will see how to describe materials at the nanoscale. We will show different approximations that we will use to simplify the many-body problem. Moreover, the *ab initio* methods required to solve systems of electrons and nuclei will be presented here. Richard M. Martin's book [1] will be the main reference followed in this chapter to present those theoretical aspects. Chapter 2 will be devoted to the fundamental concept of symmetry. We will make special emphasis on the symmetry transformations that are usually encountered in crystalline transition metal compounds. Mildred Dresselhaus's book on symmetry [3] has guided the confection of this part. Chapter 3 will be the last chapter of this part. A brief introduction to statistical mechanics and transport is presented here. Ziman's [4] and Terry M. Tritt's books [6] were the main references for this chapter. As we have said, this first part is devoted to present the required theory that paves the way to the studies of the second part. Therefore, the advanced reader in the field can feel confident to skip it.

In Part II we will focus on the study of Crystalline Transition Metal Compounds from a theoretical point of view. This class of compounds are made by one or more transition metal atoms forming a crystalline solid structure. The family of transition metal compounds presents one of the most heterogeneous physical phenomena. They can be good metals, but also good semiconductors and insulators. They can hold many different orders, such as ferromagnetism or antiferromagnetism, but also charge, orbital or spin-state ordering. They can show piezoelectricity, ferroelectricity or even a multiferroic behaviour. Colossal magnetoresistance has been discovered in these compounds. They are among the best thermoelectric materials and some of them even show high temperature superconductivity. All these diverse physical properties make crystalline transition metal compounds not only highly interesting from a fundamental point of view, but also from a technological one. The origin of such miscellaneous phenomena lies in the partially filled d electrons of the transition metal atoms. d electrons are extremely flexible particles, appearing either as localized or itinerant, and the interplay between the electronic, magnetic and structural degrees of freedom will be responsible of the different behaviour in these materials.



Transition metal compounds are usually formed not only by transition metal atoms, but also by other elements of the periodic table. In particular, in this thesis, we will pay special attention to the family of complex oxides and layered van der Waals materials. A huge variety of physical phenomena can be encountered in both species. On the one hand, oxide compounds contain at least one oxygen atom. This makes them pretty interesting from a experimental point of view. They are easily grown, synthesized and engineered

in different structures. Importantly, this kind of compounds tend to be extremely stable in normal conditions due to the oxidized atmosphere where we live. In fact, many of the most intriguing oxides occur naturally. On the other hand, layered van der Waals materials are formed by layers that are bonded via van der Waals interactions. This weak bonding allows to grow and manipulate this kind of compounds in the few-layer limit. Even more, layers can be exfoliated to obtain a monolayer. This dimensionality control prompts to emergent phenomena. Considering all that, the main body of this thesis will be devoted to the study of this kind of materials. However, other classes of compounds will also be invited to exemplify the important role that d electrons play in nature.

Part II will start with studies on oxides. Chapter 4 will be devoted to the analysis of the thermoelectric properties of $SrTiO_3$, in particular we will see how the thermopower and the lattice thermal conductivity can be tuned by structural modifications. In Chapter 5 we will see how $LaCoO_3$ becomes an insulating ferromagnet when grown on top of $SrTiO_3$. The effect of doping in infinite-layer nickelates will be analyzed in Chapter 6. Recently, this class of compounds has been found to be high-temperature-superconducting-cuprate analogs. In Chapter 7 we make a break before entering in the study of layered van der Waals materials. We show how the experimental spectrum of Cs_2CuCl_4, a compound discussed in the framework of spin liquids, can be explained in combination with the methodology presented in this thesis. A comparative study between the electronic and magnetic properties of two similar Cr-based van der Waals ferromagnets, $CrBr_3$ and $Cr_2Ge_2Te_6$, is provided in Chapter 8. In Chapter 9 the interplay between ferromagnetic and charge density wave phases is discussed. Two different transition metal dichalcogenides are studied, $CrTe_2$ and VSe_2. Finally, in Chapter 10 we analyzed how d electrons can play a role in topological phase transitions by studying $BaSn_2$ under pressure. The articles where these works have been published are referred in the List of Publications section, at the end of the thesis.

All the theoretical aspects and methods presented in Part I, as well as the works described in Part II, will provide many of the basics to understand the state-of-the-art research in Solid State Physics. This thesis will delve into the fundamentals of Materials Science, and hopefully will serve to achieve some of the global goals that we have discussed in this introduction.

Part I

Theory and Methods

USC UNIVERSIDADE DE SANTIAGO DE COMPOSTELA

USC
UNIVERSIDADE
DE SANTIAGO
DE COMPOSTELA

1 The Physical System

> "The more we simplify our material needs the more we are free to think of other things."
>
> —Eleanor Roosevelt

In this chapter we will describe from a fundamental point of view the physical system that describes a material. We will show that different approximations are needed to deal with that system. Moreover, we will present the methods that we will use in the analysis of the second part.

1.1 A Many-Body Quantum System

In the Introduction we have been talking about the prominent role materials have for our modern societies. However, we have not provided yet a formal definition of what a material is. In terms of its constituents a material is formed by atoms, which were first postulated by Democritus in Ancient Greece and finally discovered by the fathers of modern Chemistry Antoine Lavoisier and John Dalton. Thus, the building blocks of any material are the atoms of the different elements collected in the Periodic table. The way in which these elements are grouped leads to a plethora of materials with completely different properties that can be used for technological applications.

It was at the beginning of the 20^{th} century when it was discovered that atoms are formed by nuclei and electrons. This defines a length scale of nanometers to describe the structure of materials, the nanoscale. Electrons have negative electric charge and surround the nucleus, and this, in turn, is formed by neutral neutrons and positive protons. The number of protons in the nucleus, called the atomic number, determines the particular element of an atom. Many models were proposed to explain the atomic structure, i.e., how electrons and nuclei are arranged together. The Quantum Theory was developed with that purpose since electrons are a kind of object that cannot be interpreted in terms of the Classical theory. It was Schrödinger's equation that first treated the electrons in a satisfactory way in terms of a wavefunction [7]. Then, Dirac provided a more natural description of spin by writing a relativistic equation [8]. Thus, materials at the nanoscale

must be described quantum mechanically.

We have established that nuclei and electrons are the fundamental particles that constitute materials.[1] In a quantum mechanical system like this, physical states for n electrons and N nuclei are codified by a vector of a complex Hilbert space, usually called wavefunction $\Psi(\mathbf{r}_1, \mathbf{r}_2, ..., \mathbf{r}_n, \mathbf{R}_1, \mathbf{R}_2, ..., \mathbf{R}_N)$. This wavefunction depends on the coordinates $\mathbf{r}_i$ and $\mathbf{R}_I$ (including position and spin) of each electron and nucleus respectively, and can be expressed as a sum of a complete set of s states $\Psi_s(\mathbf{r}_1, \mathbf{r}_2, ..., \mathbf{r}_n, \mathbf{R}_1, \mathbf{R}_2, ..., \mathbf{R}_N)$ weighted by a probability in that Hilbert space. The measurable quantities will be given by Hermitian operators. The results of a measurement and their probability to occur can be computed from the wavefunction and the eigenvectors of such operator. An essential case to consider is the Hamiltonian $\hat{H}$, which corresponds to the total energy operator of a system. The eigenvalues and eigenvectors of the Hamiltonian provide the possible values for the energy E_s and the states $|\Psi_s\rangle$ that the system can take:

$$\hat{H}\,|\Psi_s\rangle = E_s\,|\Psi_s\rangle \tag{1.1}$$

The Hamiltonian is given by the sum of the kinetic and potential energies of all the particles. Therefore, in general, we can write the Hamiltonian of any material with n electrons and N nuclei as

$$\begin{aligned}\hat{H} = &-\sum_{I=1}^{N}\frac{\hbar^2}{2M_I}\nabla_I^2 + \frac{1}{2}\sum_{I=1}^{N}\sum_{I\neq J}^{N}\frac{Z_I Z_J e^2}{|\mathbf{R}_I - \mathbf{R}_J|} \\ &-\frac{\hbar^2}{2m_e}\sum_{i=1}^{n}\nabla_i^2 + \frac{1}{2}\sum_{i=1}^{n}\sum_{i\neq j}^{n}\frac{e^2}{|\mathbf{r}_i - \mathbf{r}_j|} - \sum_{i=1}^{n}\sum_{I=1}^{N}\frac{Z_I e^2}{|\mathbf{r}_i - \mathbf{R}_I|},\end{aligned} \tag{1.2}$$

where we encounter 5 terms well differentiated. The first is the kinetic energy of the nuclei of mass M_I, the second is the Coulomb interaction between the different nuclei of charge Z_I, the third one is the kinetic energy of electrons with mass m_e, the fourth term is the Coulomb interaction between electrons and the final term is the Coulomb interaction between electrons and nuclei.

Note that spin terms have been avoided in the many-body Hamiltonian written in eq. (1.2). These terms will be of capital importance for the correct description of many systems such as magnetic and topological ones. We will come back to them in the following sections. The important idea that we want to highlight at this point is that materials are described by many-body Hamiltonians, i.e., Hamiltonians that contain interactions between many different particles (electrons and nuclei). Since the wavefunction Ψ_s depends on the set of coordinates $\{\mathbf{r}\}$ and $\{\mathbf{R}\}$ of n electrons and N nuclei respectively, we have an enormous amount of degrees of freedom coupled by the different terms in

[1] Note that the word “fundamental" is usually referred to the elementary particles described by the Standard model in High Energy Physics. However, the energy scale needed to describe materials is much lower, and hence it is fine to consider nuclei and electrons as the fundamental particles of our theory.

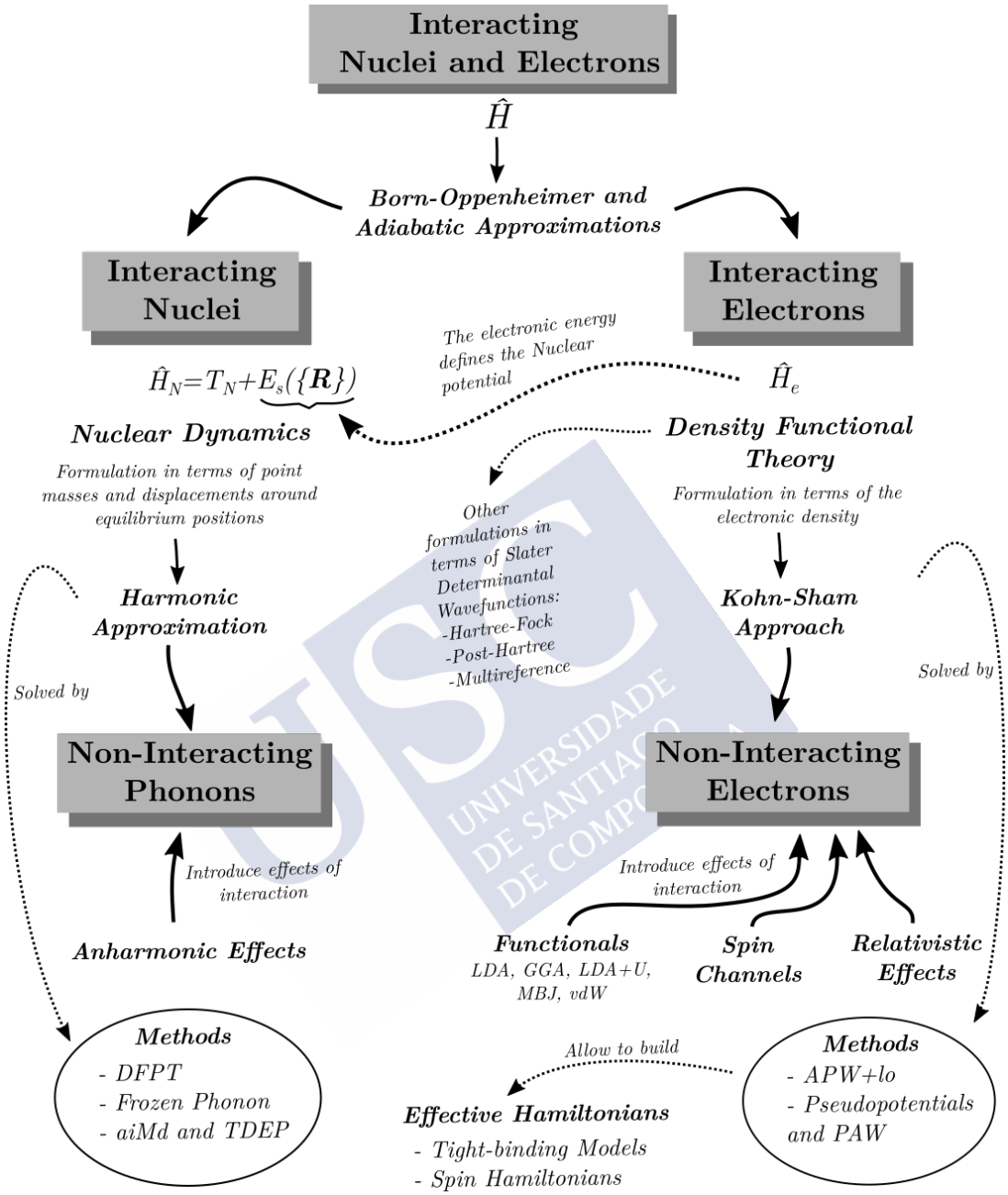


Figure 1.1: Scheme with the theoretical approach to the many-body problem. The different parts will be explained in the main text.

the many body-Hamiltonian of eq. (1.2). This represents a highly difficult problem to solve as soon as we have a system with more than two particles (like the hydrogen atom). A real material is a macroscopic system formed by a number of atoms of the order of Avogadro's number ($N_{Av} \simeq 10^{23}$). This makes the problem impossible to solve. Hence,

we will need to find ways to simplify the many-body Hamiltonian. This will be the task of the following sections. In order to have at a glance all the approximations that we are going to performed, we have summarized them in the sketch of Fig. 1.1.

1.2 Nuclei are heavier than Electrons

The first approximation that we will perform on the many-body Hamiltonian of eq. (1.2) is the so-called Born-Oppenheimer approximation [9]. Taking a close look to that Hamiltonian, we can observe that the nuclear kinetic energy terms are very small compared to the others, as long as the masses M_I of the nuclei are much heavier than the electron mass m_e. This allows to treat the nuclear kinetic energy terms as a perturbation upon the Hamiltonian of eq. (1.2). The result leads to the decoupling of the electronic ($\{\mathbf{r}\}$) and nuclear ($\{\mathbf{R}\}$) degrees of freedom in the many-body wavefunction

$$\Psi_s(\{\mathbf{r}\},\{\mathbf{R}\}) = \sum_{s'} \chi_{ss'}(\{\mathbf{R}\})\psi_{s'}(\{\mathbf{r}\};\{\mathbf{R}\}), \tag{1.3}$$

where we have expressed the coupled states in terms of a complete set of s' electronic states $\psi_{s'}(\{\mathbf{r}\};\{\mathbf{R}\})$ for each nuclear configuration in the set $\{\mathbf{R}\}$. The $\chi_{ss'}(\{\mathbf{R}\})$ are functions of the nuclear coordinates and the coefficients of the electronic states $\psi_{s'}(\{\mathbf{r}\};\{\mathbf{R}\})$. Therefore, we can reduce the many-body (nuclear and electronic) Hamiltonian of eq. (1.2) to a purely electronic Hamiltonian $\hat{H}_e$. We have to neglect the kinetic energy of the nuclei and consider the nuclear coordinates as parameters instead of variables. Then, the Hamiltonian reduces to

$$\hat{H}_e = \hat{T}_e + \hat{V}_{ext} + \hat{V}_{int} + E_{Nuc} \tag{1.4}$$

where $\hat{T}_e$ is the kinetic energy operator for electrons

$$\hat{T}_e = -\frac{\hbar^2}{2m_e}\sum_{i=1}^{n}\nabla_i^2, \tag{1.5}$$

$\hat{V}_{ext}$ is the potential that acts on electrons due to the nuclei, in which positions are treated now as parameters

$$\hat{V}_{ext} = -\sum_{i=1}^{n}\sum_{I=1}^{N}\frac{Z_I e^2}{|\mathbf{r}_i - \mathbf{R}_I|}, \tag{1.6}$$

$\hat{V}_{int}$ is the Coulomb interaction between electrons

$$\hat{V}_{int} = \frac{1}{2}\sum_{i=1}^{n}\sum_{i\neq j}^{n}\frac{e^2}{|\mathbf{r}_i - \mathbf{r}_j|}, \tag{1.7}$$

and finally E_{Nuc} is the Coulomb interaction between nuclei. It contributes to the total energy but is not relevant to describe the electronic states.

$$E_{Nuc} = \frac{1}{2}\sum_{I=1}^{N}\sum_{I\neq J}^{N}\frac{Z_I Z_J e^2}{|\mathbf{R}_I - \mathbf{R}_J|} \tag{1.8}$$

Diagonalizing the electronic Hamiltonian of eq. (1.4) we can obtain the energy $E_{s'}(\{\mathbf{R}\})$ and the electronic states $\psi_{s'}(\{\mathbf{r}\};\{\mathbf{R}\})$.

The coefficients $\chi_{ss'}(\{\mathbf{R}\})$ that couple the nuclear-electron system can be thought as the nuclear wavefunctions. They can be obtained inserting the expression (1.3) into eq. (1.1) and integrating over the electron variables $\{\mathbf{r}\}$ leading to the following equations

$$\left[\hat{T}_{Nuc} + E_{s'}(\{\mathbf{R}\}) - E_s\right]|\chi_{ss'}(\{\mathbf{R}\})\rangle = -\sum_{i'} C_{si'}\,|\chi_{si'}(\{\mathbf{R}\})\rangle \tag{1.9}$$

where $\hat{T}_{Nuc}$ is the nuclear kinetic energy and the matrix elements $C_{si'}$ are given by

$$\begin{aligned} C_{si'} = &\sum_{J=1}^{N}\left[\frac{m_e}{M_J}\,\langle\psi_s(\{\mathbf{r}\};\{\mathbf{R}\})|\,\nabla_J\,|\psi_{i'}(\{\mathbf{r}\};\{\mathbf{R}\})\rangle\,\nabla_J\right] \\ &\sum_{J=1}^{N}\left[\frac{m_e}{2M_J}\,\langle\psi_s(\{\mathbf{r}\};\{\mathbf{R}\})|\,\nabla_J^2\,|\psi_{i'}(\{\mathbf{r}\};\{\mathbf{R}\})\rangle\right] \end{aligned} \tag{1.10}$$

we can apply now the adiabatic approximation by ignoring the off-diagonal terms of $C_{si'}$ matrix elements.[2,3] Thus, the electrons are considered to remain in their state s' as the nuclei move. In spite of the change in the energy $E_{s'}(\{\mathbf{R}\})$ and the wavefunction $\psi_{s'}(\{\mathbf{r}\};\{\mathbf{R}\})$, the s' state does not change and the nuclear motion does not cause any electronic excitation. Therefore, in the adiabatic approximation, the nuclear dynamics are described by a purely electronic potential and the full set of states s is a product of nuclear and electronic states. If all the $C_{si'}$ elements are ignored,[4] the equation for the nuclear motion simplifies to

$$\left[\hat{T}_{Nuc} + E_{s'}(\{\mathbf{R}\})\right]|\chi_{n's'}(\{\mathbf{R}\})\rangle = E_{n's'}\,|\chi_{n's'}(\{\mathbf{R}\})\rangle \tag{1.11}$$

where n' here labels nuclear states. The nuclear potential energy, that we have seen that corresponds to the electronic energy $E_{s'}(\{\mathbf{R}\})$, is usually termed as the Born-Oppenheimer energy surface. A sketch of a potential energy surface is shown in Fig. 1.2. We can see there several minima, they correspond to different structural phases in the

[2] In most books the Born-Oppenheimer and adiabatic approximations are referred as the same approach even though we have seen they are not strictly the same.

[3] Off-diagonal terms are responsible of the electron-phonon coupling.

[4] Diagonal terms are neglected for the calculation of phonon energies in the adiabatic approximation in the frozen-phonon and perturbation methods that we will see below.

set of possible nuclear configurations $\{\mathbf{R}\}$. In principle, the ground state of the system will be the configuration $\{\mathbf{R}_0\}$ that corresponds to the absolute minimum of the potential energy surface. Phase transitions between different structural phases can be driven by external fields such as pressure, electromagnetic fields or temperature.

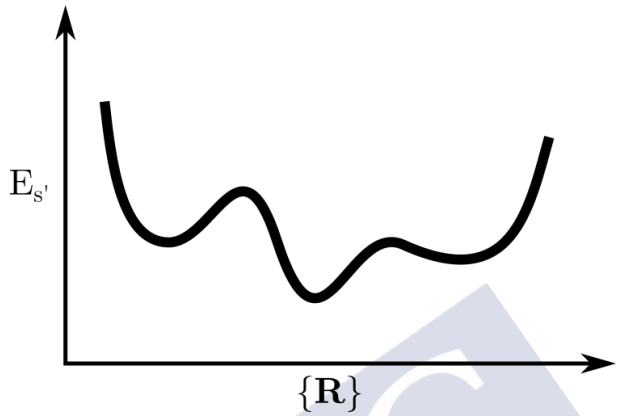


Figure 1.2: Sketch of a Born-Oppenheimer energy surface $E_{s'}(\{\mathbf{R}\})$. Different minima have been drawn, they correspond to different structural phases in the set of possible nuclear configurations $\{\mathbf{R}\}$. Phase transitions between these phases can be driven by external fields such as pressure, electromagnetic fields or temperature.

The ground state configuration $\{\mathbf{R}_0\}$, i.e., where the nuclei are located in the ground state, can be computed using the force or Hellmann-Feynman theorem [10]. It allows to compute the nuclear forces as

$$\mathbf{F}_I = -\frac{\partial E_{s'}}{\partial \mathbf{R}_I} = -\left\langle \psi_{s'} \right| \frac{\partial \hat{H}_e}{\partial \mathbf{R}_I} \left| \psi_{s'} \right\rangle , \tag{1.12}$$

where $\mathbf{R}_I$ is the position of nucleus I and $\mathbf{F}_I$ is the force on it. In the ground state configuration the forces on all atoms must be zero, since the $\{\mathbf{R}_0\}$ configuration is a minimum of the potential energy surface.

The force theorem can be generalized to any parameter λ of the Hamiltonian as

$$\frac{\partial E_{s'}}{\partial \lambda} = \left\langle \psi_\lambda \right| \frac{\partial \hat{H}_e}{\partial \lambda} \left| \psi_\lambda \right\rangle , \tag{1.13}$$

and a finite energy difference between two different λ states, considered to be ground states for each λ value, can be obtained as an integral over a continuous variation of the Hamiltonian from one state to the other. This is called the adiabatic connection [11].

Finally, note that the adiabatic approximation that we have considered in this section is well justified as long as the gap in the electronic excitation spectrum is larger than the energies involved in the nuclear dynamics. In metals or systems where the electronic states are degenerate the approximation might fail.

In this section we have split the many-body problem into two: on one side electrons and on the other nuclei. We will see in the following two sections how to deal with each of them separately.

1.3 Interacting Electrons

The Born-Oppenheimer and adiabatic approximations left us with an electronic problem to solve. The interacting electron Hamiltonian that describes this system is given by eq. (1.4). The total energy E of the electronic system is the expectation value of that Hamiltonian $\hat{H}_e$

$$E = \frac{\langle \Psi | \hat{H}_e | \Psi \rangle}{\langle \Psi | \Psi \rangle}, \tag{1.14}$$

where Ψ is the many-body electronic wavefunction $\Psi(\{\mathbf{r}\};\{\mathbf{R}\})$. At this point, we stop using explicit notation for the dependence on the nuclear coordinates $\{\mathbf{R}\}$ since they are just parameters in the electronic problem.

If we consider Ψ as a variable trial function, the eigenstates of the Hamiltonian correspond to the stationary points of the energy E. As we have seen in the first section of this chapter, the eigenvalues and eigenstates of the Hamiltonian can be obtained by solving the time-independent Schrödinger's equation (eq. (1.1)). The ground state wavefunction Ψ_0 will be the state with the lowest energy. We can obtain it by minimizing the total energy with respect to all variables $\{\mathbf{r}\}$ in Ψ. All the ground state properties will be determined by the ground state wavefunction Ψ_0. Therefore, in order to characterize the electronic structure of a material, at least its intrinsic electronic properties, we need to obtain the ground state wavefunction.[5]

A widely known method to obtain the ground state wavefunction Ψ_0 is the Hartree-Fock method [12]. This approach assumes that the many-electron wavefunction $\Psi(\{\mathbf{r}\})$ can be expressed as an antisymmetrized determinantal wavefunction for a fixed number n of electrons. The requirement to be antisymmetric comes from the fact that electrons are fermions. In case that no spin-orbit interaction is included in the electronic Hamiltonian $\hat{H}_e$, the wavefunction takes the form of a Slater determinant [13]

$$\Psi(\{\mathbf{r}\}) = \frac{1}{(n!)^{1/2}} \begin{vmatrix} \phi_1(\mathbf{r}_1) & \phi_1(\mathbf{r}_2) & \dots & \phi_1(\mathbf{r}_n) \\ \phi_2(\mathbf{r}_1) & \phi_2(\mathbf{r}_2) & \dots & \phi_2(\mathbf{r}_n) \\ \vdots & \vdots & \ddots & \vdots \\ \phi_n(\mathbf{r}_1) & \phi_n(\mathbf{r}_2) & \dots & \phi_n(\mathbf{r}_n) \end{vmatrix} \tag{1.15}$$

[5]The other stationary points in the energy with respect to Ψ correspond to excited states. In this thesis we will focus on the ground state and small perturbations to it, such as the ones produced by small nuclei displacements.

where $\phi_i(\mathbf{r}_j)$ corresponds to a single-electron spin-orbital wavefunction. The term spin-orbital is used because each single particle wavefunction ϕ_i depends on spatial coordinates and spin, both included in $\mathbf{r}_j$. In case of no spin-orbit interaction, ϕ_i can be expressed as a product of a function of the position and a function of spin. This last assumption is termed as spin-restricted Hartree-Fock approximation.[6]

The Hartree-Fock method is an approximation by definition since it assumes the shape for the many-electron wavefunction in terms of single-electron wavefunctions and finds the determinant that minimizes the energy of eq. (1.14). Therefore, only the electron correlation due to the Pauli exclusion principle that electrons must fulfill is captured by this approach. This is usually referred as the exchange energy, leaving the term correlation energy to the rest of the correlation that is not included by the Hartree-Fock approximation.[7] The correlation energy always lowers the total energy of the ground state. This correlation energy is much more complicated to compute than the exchange energy, since correlation affects both kinetic and potential energies. Post-Hartree-Fock methods, such as perturbation or configuration-interaction methods, can include effects of correlation by introducing more degrees of freedom in the approach performed to the many-electron wavefunction $\Psi(\{\mathbf{r}\})$. In some cases a single determinant does not provide a good approach to the many-electron wavefunction. Multi-Configuration methods expand $\Psi(\{\mathbf{r}\})$ as a linear combination of Slater determinants. Similar Post-Hartree-Fock techniques are adapted to this Multi-reference methods in order to include correlation effects.

All these methods that try to approach the correct shape of the wavefunction are widely used in Quantum Chemistry. They provide a very accurate description of molecules and their excited states, which are essential to find the correct description of chemical processes. However, for systems with a large number of atoms these methods become very expensive, in terms of computation. We will see in the following subsection a different perspective to tackle the problem. Instead of trying to obtain an accurate approach to the many-electron wavefunction, the electron density will be used to calculate the ground state properties. This approach is called Density Function Theory and hugely simplifies the electronic problem. All the studies that we will perform in this thesis will be based on this theory.

1.3.1 Density Functional Theory

The first attempt to work with the electron density $\rho(\mathbf{r})$ instead of the many-electron wavefunction $\Psi(\{\mathbf{r}\})$ was made by Thomas [14] and Fermi [15] in 1927. In the Thomas-Fermi method a density functional is proposed for the kinetic energy. They approached the system to a homogeneous gas of non-interacting electrons with a density equal to the local density at any point. They both neglected exchange and correlation in their

[6] In the case of a closed-shell system the spin-restricted approximation is exact.

[7] Therefore, the correlation energy is defined regarding a reference state. This leads to a different definition of this term in the Hartree-Fock approximation and in Density Functional Theory as we will see below.

approximation. It was Dirac in 1930 the one that included a local approximation for exchange [16].

The advantage of working with the density instead of the wavefunction is clear. While Schrödinger's equation implies dealing with $3n$ degrees of freedom for n electrons, an equation for the electron density involves only 3, since the density is a scalar field. However, the approach provided by the Thomas-Fermi method is too rough, and consequently shows major flaws in the description of the electronic structure of real materials. It does not predict the shell structure of atoms or the binding of molecules. For these reasons, a theory based on the density was dismissed for more than 30 years till Hohenberg and Kohn formulated their celebrated theorems.

In 1964 Hohenberg and Kohn formulated an exact many-body Density Functional Theory (DFT) [17]. This theory is valid for any system of interacting particles in an external potential. Therefore, it will apply to the many-electron Hamiltonian $\hat{H}_e$ of eq. (1.4). DFT is based on two theorems that we will enunciate and prove here for completeness:

- **Theorem I**: for any system of interacting particles in an external potential $V_{ext}(\mathbf{r})$, this potential is determined uniquely, except for a constant, by the ground state particle density $\rho_0(\mathbf{r})$. Therefore, the Hamiltonian and all the properties of the system are fully determined by the ground state density.

  Proof: Let us suppose that there are two different external potentials $V_{ext_1}(\mathbf{r})$ and $V_{ext_2}(\mathbf{r})$ differing by more than a constant and leading to the same ground state density $\rho_0(\mathbf{r})$. Therefore, each external potential leads to a different Hamiltonian $\hat{H}_1$ and $\hat{H}_2$, and hence to two different ground state wavefunctions $\Psi_1(\{\mathbf{r}\})$ and $\Psi_2(\{\mathbf{r}\})$ respectively. Considering that $\Psi_2(\{\mathbf{r}\})$ is not the ground state of $\hat{H}_1$, we will have

  $$E_1 = \langle\Psi_1|\,\hat{H}_1\,|\Psi_1\rangle < \langle\Psi_2|\,\hat{H}_1\,|\Psi_2\rangle \tag{1.16}$$

  the last term can be written as

  $$\begin{aligned}\langle\Psi_2|\,\hat{H}_1\,|\Psi_2\rangle =& \langle\Psi_2|\,\hat{H}_2\,|\Psi_2\rangle + \langle\Psi_2|\,\hat{H}_1 - \hat{H}_2\,|\Psi_2\rangle \\ =& E_2 + \int d\mathbf{r}\,[V_{ext_1}(\mathbf{r}) - V_{ext_2}(\mathbf{r})]\,\rho_0(\mathbf{r})\end{aligned} \tag{1.17}$$

  which introduced above leads to

  $$E_1 < E_2 + \int d\mathbf{r}\,[V_{ext_1}(\mathbf{r}) - V_{ext_2}(\mathbf{r})]\,\rho_0(\mathbf{r}). \tag{1.18}$$

  We can obtain an analogous expression for E_2 performing again the derivation:

  $$E_2 < E_1 + \int d\mathbf{r}\,[V_{ext_2}(\mathbf{r}) - V_{ext_1}(\mathbf{r})]\,\rho_0(\mathbf{r}). \tag{1.19}$$

  Adding together the last two equations leads to the contradiction $E_1+E_2 < E_1+E_2$, which demonstrates that the density uniquely determines the external potential to within a constant.

- **Theorem II**: A universal functional of the energy $E[\rho]$ in terms of the density $\rho(\mathbf{r})$ can be defined for any external potential $V_{ext}(\mathbf{r})$. For a given $V_{ext}(\mathbf{r})$, the ground state of the system is the global minimum of that functional, and the density $\rho(\mathbf{r})$ that minimizes that functional is the ground state density $\rho_0(\mathbf{r})$. The Hohenberg-Kohn functional $E_{HK}[\rho]$ takes the form of

$$E_{HK}[\rho] = T[\rho] + E_{int}[\rho] + \int d\mathbf{r} V_{ext}(\mathbf{r})\rho(\mathbf{r}) + E_{II}, \tag{1.20}$$

  where the last term corresponds to the interaction energy of the nuclei, and the first two terms are the kinetic and potential energy of the interacting system. They both must be universal for a given system of interacting particles, since they are only functionals of the density.

  Proof: Suppose a system with a ground state density $\rho_1(\mathbf{r})$ that corresponds to a external potential $V_{ext_1}(\mathbf{r})$. The Hohenberg-Kohn functional for the energy evaluated at this density must be the expectation value of the Hamiltonian in the ground state that has a wavefunction Ψ_1

$$E_1 = E_{HK}[\rho_1] = \langle \Psi_1 | \hat{H}_1 | \Psi_1 \rangle . \tag{1.21}$$

  If we consider now a different density $\rho_2(\mathbf{r})$ corresponding to a different wavefunction Ψ_2, the energy E_2 that corresponds to this state must be greater than E_1

$$E_1 = \langle \Psi_1 | \hat{H}_1 | \Psi_1 \rangle < \langle \Psi_2 | \hat{H}_1 | \Psi_2 \rangle = E_2. \tag{1.22}$$

  Therefore, this proves that the energy given by the Hohenberg-Kohn functional evaluated at the ground state density $\rho_0(\mathbf{r})$ is lower than any other energy evaluated at a different density $\rho(\mathbf{r})$.

The definition of DFT can be extended to other ensembles at finite temperature and fluctuating number of particles. It is also possible to generalized DFT to a time-dependent DFT. The Hohenberg-Kohn DFT applies only to time-reversal invariant systems. If there are terms in the Hamiltonian that break this symmetry (an external magnetic field or a time-dependent electric field) the properties will not only be determined by the density, but also by a current density.

We have seen that the Hohenberg-Kohn theorems provide a different formulation in terms of a functional of the density. The knowledge of this functional is enough to determine all the properties of the system. However, the theorems do not give any clue to obtain such a universal functional for a given system of interacting particles. Therefore, a practical implementation of DFT requires approximations to the exact unknown functional.

1.3.2 What about Electron Independence?

In 1965, just a year after the formulation of DFT, Kohn and Sham provided a formulation to DFT known as the Kohn-Sham approach [18]. Their idea was to replace the many-electron system by an auxiliary non-interacting electron system. The connection between both systems is that the auxiliary system is defined to have the same ground state electronic density $\rho_0(\mathbf{r})$ the interacting one has. Consequently, the Kohn-Sham Hamiltonian $\hat{H}_{KS}$ that acts on each single-electron orbital $\phi_i(\mathbf{r})$ is given by

$$\hat{H}_{KS} = -\frac{\hbar^2}{2m_e}\nabla^2 + V_{eff}(\mathbf{r}), \tag{1.23}$$

where the first term is the kinetic energy operator. Thus, we can compute the total kinetic energy T_{KS} for the independent-electron system as

$$T_{KS} = -\frac{\hbar^2}{2m_e}\sum_{i=1}^{n}\langle\phi_i|\,\nabla^2\,|\phi_i\rangle, \tag{1.24}$$

and $V_{eff}(\mathbf{r})$ in eq. (1.23) is an effective potential that acts on the single-electron wavefunctions $\phi_i(\mathbf{r})$. This potential is supposed to take into account all the interactions between the particles of the real system. Therefore, we see that the Kohn-Sham approach is nothing but a mean-field theory in which the kinetic energy term is expressed as contributions of independent particles, and the effective potential will be treated as a functional of the density. The electron density of the Kohn-Sham system is equal to the sum of the densities of the independent orbitals:

$$\rho(\mathbf{r}) = \sum_{i=1}^{n}|\phi_i(\mathbf{r})|^2 \tag{1.25}$$

recall that the Kohn-Sham condition implies that the ground state density $\rho_0(\mathbf{r})$ of the Kohn-Sham system is equal to the ground state density of the real system.

In order to write the energy associated to the effective potential in a more elucidating way, we can define at this point the Hartree energy $E_{Hartree}[\rho]$ as

$$E_{Hartree}[\rho] = \frac{e^2}{2}\int d\mathbf{r}d\mathbf{r}'\frac{\rho(\mathbf{r})\rho'(\mathbf{r})}{|\mathbf{r}-\mathbf{r}'|}, \tag{1.26}$$

which corresponds to the classical Coulomb interaction energy of the electron density with itself. Considering this term, the Kohn-Sham energy functional $E_{KS}[\rho]$ can be written as

$$E_{KS}[\rho] = T_{KS} + E_{Hartree}[\rho] + \int d\mathbf{r}V_{ext}(\mathbf{r})\rho(\mathbf{r}) + E_{II} + E_{xc}[\rho], \tag{1.27}$$

so, within this definition, all the many-electron effects of exchange and correlation are included in the last term $E_{xc}[\rho]$, known as the exchange-correlation energy or functional.

If we consider the Hohenberg-Kohn energy functional $E_{HK}[\rho]$ for the interacting electron system given in eq. (1.20) and the Kohn-Sham energy functional of eq. (1.27), we can solve $E_{xc}[\rho]$ as

$$E_{xc}[\rho] = (T[\rho] + E_{int}[\rho]) - (T_s + E_{Hartree}[\rho]), \tag{1.28}$$

from this last equation we see that the exchange correlation functional is the difference of the kinetic and interaction energies of the real many-electron system and those from the Kohn-Sham system of independent particles, in which the electronic interactions have been replaced by the Hartree energy of eq. (1.26).

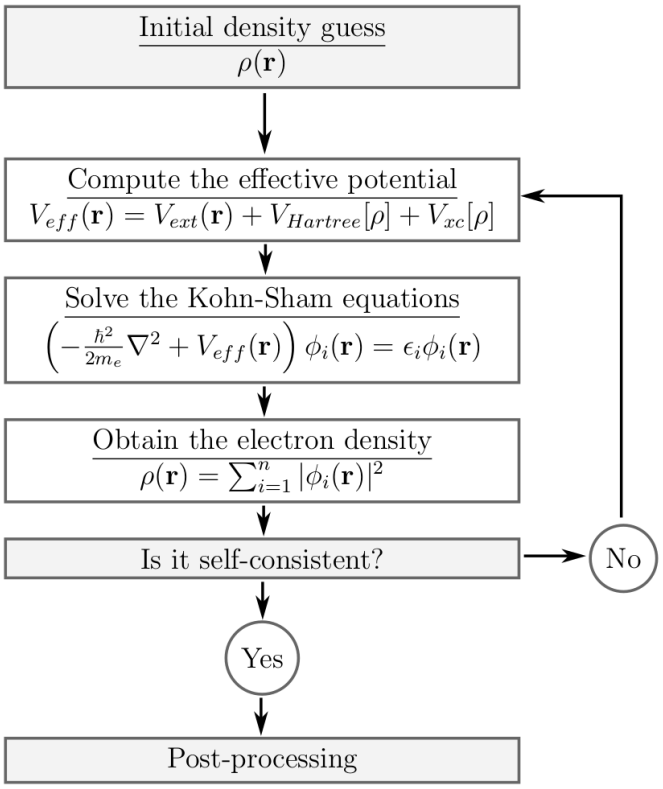


Figure 1.3: Representation of the self-consistent cycle to solve the Kohn-Sham equations. Once the density is self-consistent, it can be used to compute other quantities.

The solution to the Kohn-Sham approach can be view as a variational problem, where the electron density produced by the single-electron orbitals (Kohn-Sham orbitals) $\rho[\mathbf{r}]$ is varied to obtain the energy minimum of $E_{KS}[\rho]$. This leads to Schrödinger-like Kohn-Sham equations for the single-electron wavefunctions with the form

$$\left(\hat{H}_{KS} - \epsilon_i\right)\phi_i(\mathbf{r}) = 0, \tag{1.29}$$

where ϵ_i are the Kohn-Sham eigenvalues. The total energy of the Kohn-Sham system is equal to the sum of all the eigenvalues:

$$E_{KS} = \sum_{i=1}^{n} \epsilon_i \tag{1.30}$$

It is important to note that Kohn-Sham eigenvalues have no physical meaning, i.e., they cannot be interpreted as the energies of adding or subtracting electrons from the interacting system. The only exception is the highest eigenvalue in a finite system, which is equivalent to the minus ionization energy. Therefore, regarding an insulator where there is an energy gap, i.e., a finite energy difference between the highest occupied state and the lowest unoccupied one, the ground state Kohn-Sham potential should not produce the correct gap value. Nevertheless, we will see that the exchange-correlation functionals can be optimized to treat gaps accurately.

The Kohn-Sham equations can be solved self-consistently as shown in Fig. 1.3. An initial guess of the density is required, this is usually built as a sum of the atomic densities of the atoms that form the material. An iterative process is then implemented till a self-consistent density is obtained. Once this happens, we can use it to compute other electronic properties. This final step is usually called post-processing. The self-consistent cycle shown in Fig. 1.3 is the one implemented in the *ab initio* codes that we will use in the studies of the second part.

At this point we have seen that the Kohn-Sham approach provides a simplified way to solve the many-electron problem. However, we have not talked yet about the shape of the exchange-correlation term that appears in this formulation. If the universal exchange-correlation functional $E_{xc}[\rho]$ were known, we could obtain the exact ground state energy and density of the interacting electron system. However, this is not the case, and the Kohn-Sham formulation requires the use of approximations to the exchange-correlation functional. Some of these approximations have provided a great success explaining the electronic structure of a broad range of physical systems. The Local Density Approximation (LDA) and the Generalized Gradient Approximation (GGA) are the basic standard in computation. Modifications to these functionals are required to explain other kind of systems where electron correlations or non-local interactions need to be taken into account. We will briefly summarize in the next paragraphs the main characteristics of the exchange-correlation functionals that we will use in this thesis.

Exchange-Correlation Functionals

- Local Density Approximation (**LDA**): this was the first approximation, already pointed out by Kohn and Sham in their original paper [18]. It assumes that the exchange-correlation energy density ε_{xc} at each point is the one of a homogeneous electron gas ε_{xc}^{hom} with that density. Therefore the total exchange-correlation energy is given by the integral over all space:

$$E_{xc}^{LDA}[\rho] = \int d^3r \rho(\mathbf{r}) \varepsilon_{xc}^{hom}(\rho(\mathbf{r})). \tag{1.31}$$

The exchange energy of a homogeneous electron gas as a function of the density can be computed analytically. On the other hand, the correlation term has been computed with great accuracy with quantum Monte Carlo methods. The LDA exchange-correlation functional provides in general a good approximation for solids. It gives bond-lengths with an accuracy around the 1% error. Thus, it is capable of making highly accurate structural predictions. However, the energy gaps tend to be underestimated within this approach.

- Semilocal Generalized Gradient Approximation (**GGA**): this approach is the next natural step to the LDA. The gradient of the density $\nabla\rho(\mathbf{r})$ is introduced in the exchange-correlation energy as

$$E_{xc}^{GGA}[\rho] = \int d^3r \rho(\mathbf{r}) \varepsilon_{xc}^{hom}(\rho(\mathbf{r}), |\nabla\rho(\mathbf{r})|). \tag{1.32}$$

There is some freedom in the way that the gradient is incorporated, so different GGA approaches can be defined. We will use the one given by Perdew, Burke and Enzerhof (PBE) [19]. This approach has been used in a huge number of systems for benchmarking most of the codes that we will use. It improves LDA for many structural predictions. However, as happens with LDA, band gaps are also underestimated, and sometimes a metallic behaviour (no energy gap) is predicted for correlated insulators. This behaviour has been termed the *band gap problem* of LDA and GGA.

- Localized-orbital approximation (**LDA+U**): localized orbital approaches have been developed to overcome the *band gap problem* in systems where electrons tend to show a localized behaviour, like transition metal oxides and rare-earth elements [20]. These systems have partially filled d and f states in which electron-electron interactions become strong, and so does the correlation energy. One of such localized-orbital approximations is the LDA+U, which is based on the LDA and includes the correlation term U given by a Hubbard model.[8] The method divides the system in two kinds of electrons:

  - Delocalized electrons that are treated with the usual LDA approach.

[8]The Hubbard model is a widely used model Hamiltonian in the field of highly-correlated electron systems. It leads to useful results for Mott insulators, in which correlations play a fundamental role to explain the insulating behaviour. It has also been used as the building block to treat more exotic systems like high-temperature superconductors or spin-liquids.

– Localized electrons that include an on-site Coulomb interaction with the form $\frac{1}{2}U\sum_{i\neq j} n_i n_j$, where n_i and n_j represent orbital filling. The orbital energies ϵ_i of these localized electrons can be computed leading to

$$\epsilon_i = \epsilon_i^{LDA} + U\left(\frac{1}{2} - n_i\right) \tag{1.33}$$

where ϵ_i^{LDA} is the LDA contribution to the energy and the last term take into account the Coulomb interactions. Thus, we have that for occupied orbitals $n_i = 1$, and hence the energy of those orbitals is

$$\epsilon_i = \epsilon_i^{LDA} - \frac{1}{2}U$$

and for unoccupied $n_i = 0$

$$\epsilon_i = \epsilon_i^{LDA} + \frac{1}{2}U.$$

We can observe that the effect of the U is to produce an energy shift between the occupied and the empty states. Thus, leading to an energy gap due to electron-electron interactions in Mott-Hubbard systems.

The U term can be calculated by means of many-body methods that are far beyond the scope of the present thesis. The important point for us is that LDA+U improves substantially (quantitative and qualitative) LDA and GGA approaches for systems in which electron localization happens. Since this thesis is devoted to the study of transition metal systems, we will find in the LDA+U approach a good description for many of such systems. It will upgrade band gaps, magnetic moments or exchange coupling constants.

- Modified Becke-Johnson potential (**MBJ**): this method is able to provide Kohn-Sham gaps close to experimental values. The potential is built upon the Becke-Johnson potential (BJ) [21], whose goal is to reproduce the uniform gas limit and describe shell structures which are characteristic of exact exchange potentials. The kinetic energy density is introduced to treat correctly hydrogenic systems. The BJ potential was then modified by Tran and Blaha [22], and is the one that we will use in this thesis.

  The MBJ potential is a semilocal potential, what makes MBJ computationally cheaper than non-local hybrid functionals. However, it must be noted that it is a potential and not a functional, so it cannot be used to minimize the total energy. It is employed along another functional such as LDA or GGA used to solve the Kohn-Sham problem. The density and eigenfunctions are then used to build the MBJ potential and to compute the desired band gaps with high accuracy.

- Van der Waals (**vdW**): these non-local functionals are designed to treat dispersive forces that are originated from the long-range interactions of quantum fluctuating electric dipoles. The local and semilocal LDA and GGA are not able to describe any interaction of such characteristics. In our studies on transition metal compounds we will deal with layered compounds, whose layers are slightly bonded via van der Waals interactions. Therefore, we will need to use such a kind of non-local functionals to correctly predict their structural properties. An alternative is to include van der Waals interactions in a semiempirical way. This is done by adding a dispersion energy term E_{disp} to the total energy:

$$E_{disp} = -\frac{1}{2}\sum_{I=1}^{N}\sum_{I\neq J}^{N}\frac{C_{6IJ}}{|\mathbf{R}_I - \mathbf{R}_J|^6} f_d(|\mathbf{R}_I - \mathbf{R}_J|) \tag{1.34}$$

  where the summations range over the number of atoms N, C_{6IJ} is the dispersion coefficient for the atom pair IJ, and $f_d(|\mathbf{R}_I - \mathbf{R}_J|)$ is a damping function that avoids divergences at near distances. It varies smoothly from 0 at close distances to 1 at large ones.

Finally, some general remarks about exchange and correlation are: i) the exchange energy dominates over correlation, since the main effect of exchange is to remove the spurious self-interaction introduced by the Hartree energy, and ii) the inclusion of exchange and correlation always lowers the ground state energy of the system. They introduce what has been termed as the exchange-correlation hole, which is a decrease in the probability of finding electrons near each other due to the exclusion principle and the repulsive Coulomb interactions.

1.3.3 Spin and Relativistic Effects

So far we have not directly talked about spin. As we know, electrons are Dirac fermions of spin 1/2. Spin arises naturally in the covariant Dirac formulation of quantum mechanics. The Dirac equation is linear in time and momenta in order to be Lorentz invariant. Solutions to this equation involve commutation requirements fulfilled by certain matrices[9] and a four-component wavefunction, called spinor. We see that this new formulation entails more complexity to the many-electron problem that we have been simplifying. As a result, the approach that is taken is to continue working with the Schrödinger's equation that we have been using thus far, and include the relativistic effects that come from the Dirac equation on it. The electronic wavefunction is then expressed in terms of a two component wave function:

$$\Psi(\mathbf{r}) = \begin{bmatrix}\Psi_\uparrow(\mathbf{r})\\ \Psi_\downarrow(\mathbf{r})\end{bmatrix} \tag{1.35}$$

[9]The way in which these matrices are chosen leads to describe Dirac or Majorana fermions.

where $\Psi_\uparrow(\mathbf{r})$ and $\Psi_\downarrow(\mathbf{r})$ represent each spin wavefunction along a chosen axis.[10] New terms due to the magnetic nature of spin and relativistic effects are included in Schrödinger's equation:[11]

$$i\hbar\frac{\partial\Psi(\mathbf{r})}{\partial t} = \hat{H}_e = \left[\frac{\pi^2}{2m_e} + V + \hat{H}_Z + \hat{H}_{SO}\right]\Psi(\mathbf{r}) \tag{1.36}$$

where the effects of a magnetic field $\mathbf{B}$ introduce the vector potential $\mathbf{A}$ in the momentum operator $\mathbf{p}$ as $\boldsymbol{\pi} = \mathbf{p} - (e/c)\mathbf{A}$. Also a Zeeman term $\hat{H}_Z = \mu_B\boldsymbol{\sigma}\mathbf{B}$, where $\mu_B = e\hbar/2m_ec$ is the Bohr magneton. Finally, the spin-orbit interaction $\hat{H}_{SO}$, which can be viewed as the interaction of the electron with momentum $\mathbf{p}$ and spin σ moving in an electric field, or equivalently as a magnetic field in the rest frame of the electron. This term is the only one that mixes spin $\uparrow$ and $\downarrow$ components as

$$\hat{H}_{SO} = \begin{bmatrix}\hat{H}_{SO}(\uparrow\uparrow) & \hat{H}_{SO}(\downarrow\uparrow)\\ \hat{H}_{SO}(\uparrow\downarrow) & \hat{H}_{SO}(\downarrow\downarrow)\end{bmatrix} \tag{1.37}$$

Equation (1.36) provides a way to introduce spin-orbit and magnetic effects in the non-interacting electron Hamiltonian. Therefore, they can be included in the Kohn-Sham DFT leading to a spin-DFT. The inclusion of a magnetic field in DFT is not trivial, it would require going to a density-current functional theory to treat correctly the first term in eq. (1.36). This term will be responsible for the effect of the magnetic field in the orbital motion.[12] However, the Zeeman term can be easily included, since it affects only the spin, leading to an energy shift between both spin channels. Thus the effective potential that appears in the Kohn-Sham equation will have from now on a spin σ dependency V^σ_{eff}. Therefore, we will have two different spin channels for the electron density $\rho(\mathbf{r}) = \rho_\uparrow(\mathbf{r}) + \rho_\downarrow(\mathbf{r})$.

In the absence of an external Zeeman field, it may occur that the lowest-energy solution is spin polarized, and hence $\rho_\uparrow(\mathbf{r}) \neq \rho_\downarrow(\mathbf{r})$, thus, breaking the spin degeneracy and leading to a magnetic system.

In our calculations, the spin-orbit interaction will be introduced in a second-variational manner using the scalar relativistic approach. This approximation is derived when spin-orbit is treated as a perturbative effect [23].

1.3.4 Electronic Structure Methods

In this part we will see different implementations to solve the Kohn-Sham equations that we have been describing above. All the methods that we will see agree when used

[10] In the calculations presented in this thesis we will consider that spin is quantized along a given axis. This simplifies enormously the treatment of spin effects. However, it must be noted that for the study of certain systems, like the ones that present spin textures, a noncollinear treatment of spin is required.

[11] Spin-independent scalar terms (Darwin and mass-velocity) are not included.

[12] In general, we will not deal with the inclusion of magnetic fields in this thesis. The only study in which we have included a magnetic field is the one in Chapter 10. The effect on the orbital motion is included there through a Peierls substitution in a tight-binding Hamiltonian.

with enough care and convergence [24]. However, each of them has its advantages and intricacies that must be considered when tackling a particular problem. The methods can be divided by the choice of basis set used to expand the Kohn-Sham orbitals and also by the number of electrons and potential considered.

A natural basis set to expand the Kohn-Sham orbitals in crystals is the plane-wave basis set. Crystals are the kind of system that we will study in this thesis and, as we will see in the next Chapter, have a spatial periodicity that can be exploited by the use of plane waves. Plane waves are eigenfunctions of the Schrödinger equation with constant potential, so they are an excellent choice for systems in a nearly-free-electron regime. However, near the nuclei electrons tend to be localized, so their wavefunctions vary rapidly. They are usually called core electrons. The use of plane waves to describe these wavefunctions becomes inappropriate, since an enormous amount of plane waves would be required to expand such localized core wavefunctions. Thus, the methods that we present below correspond to the ones implemented in the codes that we will use. They basically show different ways to deal with core electrons.

The APW+lo method

The augmented plane wave plus local orbitals (APW+lo) is one of the most accurate and efficient methods to solve the Kohn-Sham equations [25, 26]. The method is based on the original augmented plane wave method APW by Slater in 1937 [27]. The idea is to divide the space in two regions as shown in Fig. 1.4. We will have the muffin-tin spheres centered on the atoms[13] and an interstitial region between them. Different basis functions are used in each region:

$$\varphi(\mathbf{r}) = \begin{cases} \sum_n c_n e^{i\mathbf{k}_n\mathbf{r}} & \text{if } \mathbf{r} \in \text{Interstitial region} \\ \sum_{lm} A_{lm} u_l(r, E_l) Y_{lm} & \text{if } \mathbf{r} \in \text{Muffin-tin sphere} \end{cases} \tag{1.38}$$

So we see that the interstitial region is expanded by plane waves, while within the muffin-tin spheres a combination of radial functions $u_l(\mathbf{r}, E_l)$ times spherical harmonics Y_{lm} is used, since they are solutions to the radial Schrödinger equations. The coefficients of the expansion are c_n and A_{lm}. These must fulfill certain requirements in terms of crystal periodicity and boundary matching of the muffin-tin and interstitial regions.

In the original APW method the radial basis set was energy dependent $u_l(\mathbf{r}, E_l)$, which induces undesired non-linearities in the Kohn-Sham problem. Different schemes were proposed to solve this issue like the linearized augmented plane wave method (LAPW) [28, 29]. In the APW+lo, the energy E_l of the radial functions $u_l(\mathbf{r}, E_l)$ is fixed in order to keep linear the problem. This reduces the variational flexibility of the radial basis set. In order to recover it, local orbitals $\varphi^{lo}(\mathbf{r})$ are included within the muffin-tin region:

$$\varphi^{lo}(\mathbf{r}) = \left[a_{lm} u_l(r, E_{1l}) + b_{lm} \dot{u}_l(r, E_{1l})\right] Y_{lm} \tag{1.39}$$

[13] The name muffin-tin spheres comes from their similar shape to kitchen molds for muffins.

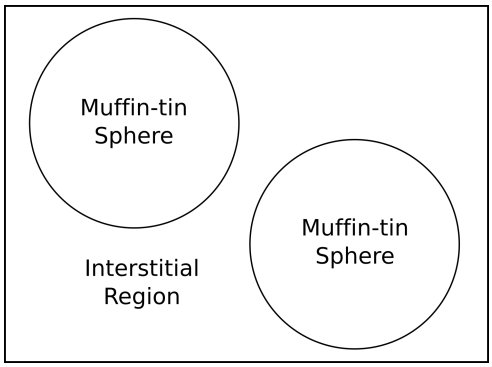


Figure 1.4: Schematic representation of the space division in terms of muffin-tin spheres around the atoms and the interstitial region between them.

where a_{lm} and b_{lm} are coefficients of the expansion and E_{1l} are the linearization energies where the solutions of the radial Schrödinger equation are evaluated. These local orbitals are required to be zero at the sphere boundary as well as normalized.

The potential is expanded in the APW+lo method as

$$V(\mathbf{r}) = \begin{cases} \sum_{\mathbf{k}} V_{\mathbf{k}} e^{i\mathbf{kr}} & \text{if } \mathbf{r} \in \text{Interstitial region} \\ \sum_{lm} V_{lm}(r) Y_{lm} & \text{if } \mathbf{r} \in \text{Muffin-tin sphere} \end{cases} \tag{1.40}$$

and the charge density in an analogous way. So, no approximations are made to its shape, which is the reason why this method is a full-potential all-electron method. Thus, compared to other methods is by far the most efficient and accurate.

The convergence of the APW+lo basis set is controlled by the parameter $R_{mt}K_{max}$, where R_{mt} is the smallest atomic sphere radius and K_{max} is the value of the largest $\mathbf{k}_n$ vector in the expansion given by eq. (1.38). Values of $R_{mt}K_{max} \sim 7$ provide a good convergence for the transition metals that we have studied in this thesis.

The APW+lo method is implemented in the WIEN2K code [30] that we will use in most of the studies presented in the second part.

Pseudopotentials and the PAW method

As we have mentioned, our aim is to use plane waves as the basis set. However, the basis set becomes too large for localized electrons near the nuclei, i.e., for the core electrons. Thus, making plane waves impractical.

The idea of pseudopotentials was first proposed by Hans Hellman in 1934 [31]. This approach is based on the fact that in a material, the electrons that are going to play a role in its properties are the valence electrons, while the core electrons of a specific atom remain practically unaffected by the other atoms. The bonding between atoms will be determined by the valence electrons, and hence they will be the important electrons to describe.

The pseudopotential approach proposes to build an effective potential and replace with it the atomic all-electron full-potential eliminating the core electrons. Valence electrons are then described by pseudowavefunctions $\varphi_{i,ps}$ that oscillate much less, i.e., they have less nodes, and hence it is possible to describe them with a reasonable plane-wave basis set. A schematic of the pseudopotential idea is shown in Fig. 1.5. Note the smoothness of the pseudowavefunction which allows to describe it with fewer plane waves.

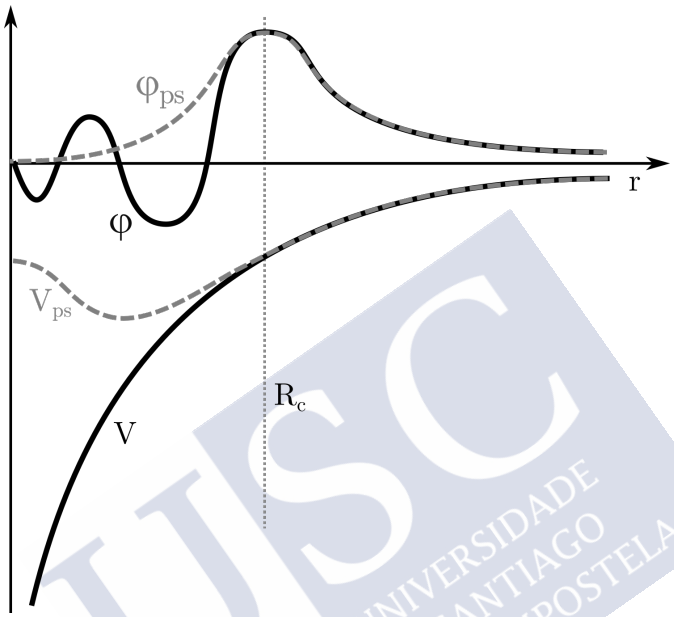


Figure 1.5: Schematic of a pseudopotential and pseudowavefunction. A smaller plane-wave basis set is required to describe the pseudowavefunctions due to their less oscillating behaviour. The pseudowavefunctions and pseudopotential match the real ones outside the cut-off radius.

Pseudopotentials are usually constructed from *ab intio* atomic calculations. An atomic reference state is considered by defining a cut-off radius R_c for the core. Outside R_c, the pseudowavefunctions and the real wavefunctions for the valence electrons are required to have the same energies and amplitude (density). Soft pseudopotentials are those that have a large cut-off radius. This helps to reduce the size of the plane wave basis set needed to describe the pseudowavefunctions. However, these pseudopotentials are less transferable, i.e., accuracy is lost depending on the chemical environment. Thus, pseudopotentials deal with a compromise between transferability and basis-set size. The so-called small core approximation is taken by assuming that there is no overlap between core and valence states. Problems might arise when dealing with semicore electrons.

The most common forms of pseudopotentials are the norm-conserving and ultrasoft pseudopotentials [32, 33]. In the case of norm-conserving pseudopotentials, the norm of the pseudowavefuntions and the real Kohn-Sham wavefuntion are required to be the same inside R_c. Ultrasoft pseudopotentials relax this constraint, which reduces the size of the

required basis set. In return, a generalized eigenvalue problem is introduced. If we define the non-zero norm difference $\tilde{\mathrm{n}}_{ij}$ inside R_c as:

$$\tilde{\mathrm{n}}_{ij} = \langle\varphi_i|\varphi_j\rangle - \langle\varphi_{i,ps}|\varphi_{j,ps}\rangle\,, \tag{1.41}$$

so now the normalized state of the pseudo Hamiltonian $\hat{H}_{ps}$ obeys the equation:

$$\hat{H}_{ps}\varphi_i = \epsilon_i \hat{T}_{ups}\varphi_{i,ps}, \tag{1.42}$$

with the operator $\hat{T}_{ups}$ being a transformation

$$\hat{T}_{ups} = \mathbf{1} + \sum_{r<R_c,ij} |p_i\rangle\, \tilde{\mathrm{n}}_{ij}\, \langle p_j|, \tag{1.43}$$

where p_i are projectors that form a basis with the pseudo reference state inside R_c.

We have seen that the idea of pseudopotentials entails neglecting the core electrons. However, based on the projectors introduced for ultrasoft pseudopotentials and the notion of augmentation explained for the APW method, core states can be somehow recovered within the Projector Augmented Wave (PAW) method [34]. The idea is to introduce a transformation $\hat{T}_{PAW}$ similar to the one in eq. (1.43) for ultrasoft pseudopotentials. However, in this new transfomation, the full-electron Kohn-Sham wavefunctions φ_i calculated in the atomic reference system are still involved:

$$\hat{T}_{PAW} = \mathbf{1} + \sum_i \left[|\varphi_i\rangle - |\varphi_{i,ps}\rangle\right] \langle p_i|. \tag{1.44}$$

The PAW method is usually combined with the frozen core approximation, where core wavefunctions are considered to be unaffected by the environment. Therefore, they are not modified through the calculation.

Pseudopotentials and the PAW method are implemented in the QUANTUM ESPRESSO [35] and VASP [36] codes. We will make use of them in the studies shown in the second part.

A clear advantage of the pseudopotentials and PAW method is that they are much faster than the APW+lo method and therefore materials with more atoms can be treated more easily. Forces are also implemented in an easier way. This is the reason why we will use many times pseudopotentials for structural relaxations and related properties. In contrast, the APW+lo method is the most accurate method for solving the Kohn-Sham equations. Analysis of the electronic structure and magnetic properties of transition metal compounds requires a good description of the d electrons. These electrons might be considered as semicore states when they appear localized at low enough energies. The pseudopotential method could be scarce in this case, meanwhile the APW+lo method ensures a fair treatment of the d electrons.

1.3.5 Simplified Models

In this final subsection we will see that it is possible to work with simple models that describe the essentials of a particular electronic structure. These models can be built from theoretical assumptions or can be distilled from *ab initio* calculations.

We will discuss two simple models: the so-called tight-binding and Heisenberg models. They are probably the easiest models that we can find. However, they allow to gain insight into the physical problem and to compute certain properties that otherwise could not be calculated.

Tight-Binding Model

The first tight-binding (TB) model was introduced by Bloch in 1928 [37]. He considered a simple s-symmetry function as the basis for it. In 1934 Jones, Mott and Skinner 1934, extended the model to a basis of different atomic orbitals [38].

The idea of the TB model is to represent the electronic wavefunctions as localized orbitals $a_i(\boldsymbol{r} - \boldsymbol{R}_I)$, each associated with an atom at position $\boldsymbol{R}_I$, where i labels all the states in the basis. Hence the matrix elements of the Hamiltonian H_{ij} for a pair of states i and j centered at $\boldsymbol{R}_I$ and $\boldsymbol{R}_J$ respectively, are:

$$H_{ij} = \int d\boldsymbol{r} a_i(\boldsymbol{r} - \boldsymbol{R}_I)\hat{H}a_j(\boldsymbol{r} - \boldsymbol{R}_J), \tag{1.45}$$

and the overlap between the states S_{ij} is:

$$S_{ij} = \int d\boldsymbol{r} a_i(\boldsymbol{r} - \boldsymbol{R}_I)a_j(\boldsymbol{r} - \boldsymbol{R}_J). \tag{1.46}$$

Thus, the problem is represented in a matrix form, where the basis set does not need to be explicitly specified. Only the matrix elements of the overlap and the Hamiltonian are required to solve the electronic structure problem. Nothing but a matrix diagonalization is needed to obtain the eigenvalues of the energy and the eigenfunctions as linear combinations of atomic orbitals.

Atomic orbitals are usually taken as the localized basis, since the different bonding types between them are well known.[14] In Fig. 1.6 σ and π bondings between s and p orbitals are depicted. In 1954 Slater and Koster set the fundamentals of the TB method, where they included the celebrated Slater-Koster tables for the interatomic matrix elements [39]. Orbital and translational symmetries are considered to derive the matrix elements that appear on those tables.

The real space approach provided by a TB Hamiltonian enables to compute things like surface states of non-trivial topological materials, or to include the effect of a magnetic field in the orbitals. Scalability is another advantage for this kind of models, thus, allowing to treat systems with a huge number of atoms.

[14] Other basis sets like the ones obtained from a Wannierization are commonly used.

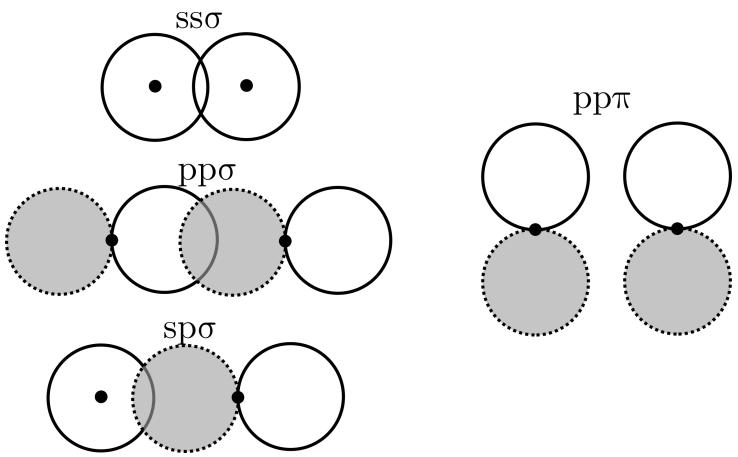


Figure 1.6: Schematic representation of the different σ and π bondings between s and p atomic orbitals used to built a tight-binding model.

The TB Hamiltonian can be formulated in the frame of second quantization leading to a summation of kinetic and potential energy terms:

$$\hat{H} = \sum_i E_i a_i^\dagger a_i + \sum_{i \neq j} t_{ij} \left[a_i^\dagger a_j + a_j^\dagger a_i \right], \tag{1.47}$$

where E_i is the so-called onsite energy for a given orbital, i.e., the sum of the kinetic and potential energies of orbital i, and the t_{ij} is the so-called hopping term between the orbital i and j. It represents the kinetic energy an electron needs to hop from one orbital to the other. More complex terms could be included in the simple TB Hamiltonian given by eq. (1.47). Those new terms would lead to very different models like the Hubbard model that can be used to explain metal-insulator transitions, or many others to explain more exotic phenomena like superconductivity or topological insulators.

We will work with TB Hamiltonians on the second part. The `PythTB` [40] and `Pybinding` [41] packages will be used to build TB Hamiltonians and to compute different properties.

Heisenberg Model

Finally, we present the Heisenberg model. This is the most representative example of a spin Hamiltonian. In systems that show a magnetic insulator behaviour it is possible to get rid of the charge degrees of freedom and build an effective spin Hamiltonian. The insulator behaviour could also be relaxed when the spin Hamiltonian is built for localized states, like the d electrons found in the transition metal compounds that we analyze in the second part. Thus, the system is simplified to a spin model, where spins lay localized at a given site i and interact between them. A schematic of the model is depicted in Fig. 1.7. In the case of the Heisenberg model, continuous rotations of spins are allowed. The Hamiltonian is given by:

$$\hat{H} = -\sum_{i<j} J_{ij} \boldsymbol{S}_i \cdot \boldsymbol{S}_j, \tag{1.48}$$

where J_{ij} is the interaction between spin $\boldsymbol{S}_i$ and $\boldsymbol{S}_j$, usually called the exchange interaction. A ferromagnetic exchange between spin $\boldsymbol{S}_i$ and $\boldsymbol{S}_j$ occurs for $J_{ij} > 0$, i.e., the spins tend to a parallel alignment. In case of $J_{ij} < 0$, the exchange is antiferromagnetic, spins tend to an antiparallel alignment. The exchange values J_{ij} of a particular system can be derived from *ab initio* calculations building different magnetic configurations and comparing their total energies. Goodenough-Kanamori rules [42] can be used to understand the exchange paths that appear in a real system and see the competition between them. Crystal symmetries and the atomic bonding type will be fundamental to determine those exchange paths. Moreover, many more terms can be added to the Hamiltonian. These can include for example anisotropic or relativistic effects.

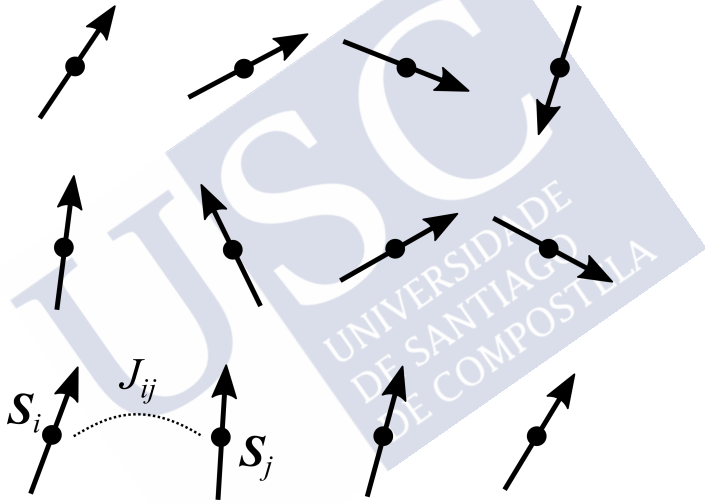


Figure 1.7: Schematic representation of the Heisenberg model. Note the exchange interaction J_{ij} between spin $\boldsymbol{S}_i$ and $\boldsymbol{S}_j$.

Monte Carlo simulations based on the Metropolis algorithm [43] can be used to solve the Heisenberg Hamiltonian of eq. (1.48) to determine the magnetic order at a finite temperature, thus, calculating the critical temperature or Curie temperature of a ferromagnet. We will code in *Fortran90* one of these simulations in the work presented in Chapter 8.

1.4 Nuclei and Vibrations

In section 1.2 the Born-Oppenheimer and adiabatic approximations allowed us to separate electrons and nuclei. We focused first on the multi-electronic problem. It is time to deal with the other piece of the puzzle, the nuclei.

Let us recall that the electronic energy $E_s(\{\boldsymbol{R}\})$ for a set of nuclear coordinates $\{\boldsymbol{R}\}$ defines the potential (or Born-Oppenheimer) energy surface in the nuclear problem. In Fig. 1.2 we showed a sketch of it. Thus, the nuclear Hamiltonian $\hat{H}_{Nuc}$ is expressed as a sum of the kinetic energy terms and the potential energy surface given by the electronic problem:

$$\hat{H}_{Nuc} = -\sum_{I=1}^{N} \frac{\hbar^2}{2M_I} \nabla_I^2 + E_s(\{\boldsymbol{R}\}) \tag{1.49}$$

This Hamiltonian determines the nuclear motion. However, we introduce at this step a key assumption. We will treat the nuclei in a classical way, i.e., we will consider that nuclei have a well defined position in space and their motion is determined by Newtonian dynamics. Thus, the kinetic energy operator is substituted by the classical kinetic terms and each nuclei is represented as a point mass M_I with velocity $\boldsymbol{v}_I$. This crude approximation might break at temperatures near the absolute zero, high pressures or for light elements such as hydrogen, where quantum effects play an important role. None of these will be the case in this thesis.

Therefore, we are left with a many-body classical problem to solve. We will see in the following subsections how to deal with it.

1.4.1 Harmonic Approach

We have already mentioned that we can minimize $E_s(\{\boldsymbol{R}\})$ with respect to the nuclear coordinates $\{\boldsymbol{R}\}$ and obtain the equilibrium geometry $\{\boldsymbol{R}_0\}$ for a particular material. We used the force theorem to obtain the forces, minimize them and obtain the minimum, see eq. (1.12). The next crucial assumption is to consider that nuclear displacements are much smaller than internuclear distances. This assumption is well justified for the case of solids well below their melting temperature. Our studies will be in the safe regime to apply it. Due to this small displacement of the nuclei, a Taylor expansion can be performed on the potential energy surface around the equilibrium positions $\{\boldsymbol{R}_0\}$. Thus, we define the displacement $\boldsymbol{u}_I$ of a nucleus I from its equilibrium position $\boldsymbol{R}_{I0}$ as:

$$\boldsymbol{u}_I = \boldsymbol{R}_I - \boldsymbol{R}_{I0} \tag{1.50}$$

The first approach to deal with the nuclear motion problem is the so-called harmonic approximation. The Taylor expansion of the potential energy surface E_s is truncated at second order, which is the lowest order expansion that can be performed. The first order terms are zero, since this expansion is around a minimum. Therefore, we have the following expansion:

$$E_s(\{\boldsymbol{R}\}) \approx E_s^{Har}(\{\boldsymbol{R}\}) = E_s(\{\boldsymbol{R}_0\}) + \sum_{I\alpha} \sum_{I'\alpha'} u_{I\alpha} D^{I\alpha,I'\alpha'} u_{I'\alpha'} \tag{1.51}$$

where we have introduced the interatomic force constants $D^{I\alpha,I'\alpha'}$ defined as:

$$D^{I\alpha,I'\alpha'} = \left.\frac{\partial^2 E_s}{\partial u_{I\alpha}\partial u_{I'\alpha'}}\right|_{\{\boldsymbol{R}_0\}}. \tag{1.52}$$

which are nothing but the second derivatives with respect to the displacements of each atom. The α index runs over the spacial coordinates x, y, z. Therefore, the interatomic force constants form the Hessian of the potential energy surface, usually addressed as the dynamical matrix D. The dynamical matrix is real and symmetric, and presents the so called sum rule, i.e., all the forces vanish when the displacements are equal:

$$\sum_{I'\alpha'} D^{I\alpha,I'\alpha'} = 0. \tag{1.53}$$

More constraints to the dynamical matrix appear in the presence of point group and translational symmetries.

Once we have approached the nuclear Hamiltonian to a harmonic one, we are driven to the following Newtonian equations:

$$M_I \ddot{u}_{I\alpha} = \frac{\partial E_s^{Har}}{\partial u_{I\alpha}} = \sum_{I'\alpha'} D^{I\alpha,I'\alpha'} u_{I'\alpha'}, \tag{1.54}$$

which can be solved with the following *ansatz*:

$$u_{I\alpha}(t) = a_{I\alpha} e^{-i\omega t}, \tag{1.55}$$

which introduced in eq. (1.54) leads to the following secular equation

$$\omega^2 a_{I\alpha} = \sum_{I'\alpha'} \frac{D^{I\alpha,I'\alpha'}}{\sqrt{M_I M_{I'}}} a_{I'\alpha'}, \tag{1.56}$$

that can be solved by diagonalizing the dynamical matrix. The solutions ω are the eigenvalues that correspond to the vibrational frequencies. The eigenvectors $\boldsymbol{a}_I$ are called the polarization vectors, and correspond to the vibrational modes, i.e., a set of independent harmonic oscillations. This classical view can be complemented with a quantum analysis of the harmonic Hamiltonian, that can be written as:

$$\hat{H}^{Har} = E_s(\{\boldsymbol{R}_0\}) + \sum_{j=1}^{3N} \omega_j \left(\hat{b}_j^\dagger \hat{b}_j + \frac{1}{2}\right), \tag{1.57}$$

where $\hat{b}_j^\dagger$ and $\hat{b}_j$ are the creation and annhilation bosonic operators. These bosons are the quasiparticles called phonons, the energy quanta of vibrations. Hence, $\hat{n}_j = \hat{b}_j^\dagger \hat{b}_j \in \mathbb{Z}^{0+}$ counts the number of phonons in the state j. The summation runs over the $3N$ modes, i.e., the $3N$ independent harmonic oscillators of frequency ω_j, that have an individual contribution to the total energy:

$$E_j = \left(\hat{n}_j + \frac{1}{2}\right)\omega_j, \tag{1.58}$$

and the total energy can be expressed as:

$$E_s^{Har} = E_s(\{\boldsymbol{R}_0\}) + \sum_{j=1}^{3N}\left(\hat{n}_j + \frac{1}{2}\right)\omega_j, \tag{1.59}$$

In Chapter 2 we will see how to exploit the translational symmetry of a crystal. A $\boldsymbol{q}$-dependent harmonic spectrum will be obtained and analyzed. This analysis will be crucial to determine structural phase transitions that might be present in our material. For example, the presence of imaginary frequencies when solving eq. (1.56) by diagonalizing the dynamical matrix points out to a structural phase transition. This kind of phononic studies will be essential for the analysis that we will perform in the second part.

1.4.2 Anharmonic Effects

The harmonic phonon spectra that we have described in the previous section provides useful understanding of many physical properties of a material. However, it fails dramatically when trying to explain many others. The harmonic phonons are well-defined quasiparticles in energy that do not interact with each other., i.e., they have infinite lifetimes. Therefore any harmonic phonon carrying a thermal current does not decay on time, which entails that a crystal composed by purely harmonic interactions has an infinite thermal conductivity. Moreover, the harmonic theory is not able to explain the temperature dependence of the phonons.

In order to overcome the unreal predictions given by the harmonic theory, anharmonic terms are introduced in the Taylor expansion of the potential energy surface. Thus, we can define the third-order force constants as:

$$D^{I\alpha,I'\alpha',I''\alpha''} = \left.\frac{\partial^3 E_s}{\partial u_{I\alpha}\partial u_{I'\alpha'}\partial u_{I'''\alpha'''}}\right|_{\{\boldsymbol{R}_0\}}. \tag{1.60}$$

As happened to the second-order force constants, third-order force constants are subjected by symmetry constraints. Given these third-order force constants we can compute the scattering strength of processes involving three phonons $D^{j,j',j''}$, where the j index labels a phonon mode:

$$D^{j,j',j''} = \sum_{I\alpha,I'\alpha',I''\alpha''} D^{I\alpha,I'\alpha',I''\alpha''}\frac{a^j_{I\alpha}a^{j'}_{I'\alpha'}a^{j''}_{I''\alpha''}}{\sqrt{M_I M_{I'} M_{I''}}\sqrt{\omega_j\omega_{j'}\omega_{j''}}} \tag{1.61}$$

where the different $a^j_{I\alpha}$ represent the α component of the eigenvector of the mode j and atom I.

Non-interacting quasiparticles (the harmonic phonons) are well defined in energy and have an infinite lifetime, thus they are represented by Dirac-δ functions in the spectrum. When interactions are included, the Dirac-δ functions are replaced by distributions with a finite width. Thus, interactions renormalize the quasiparticle by *dressing* it with the so-called self energy, which is a complex function of the energy or frequency Ω:[15]

$$\Sigma(\Omega) = \Delta(\Omega) + i\Gamma(\Omega) \tag{1.62}$$

The imaginary part $\Gamma(\Omega)$ is related to the lifetime of the quasiparticle, i.e., its broadening in the spectrum. The imaginary part of the self-energy of a phonon mode j is given by the sum of all-possible (conserving energy and momentum) three scattering processes weighted by the occupation of the modes involved in those process and their scattering strength:

$$\begin{aligned}\Gamma_j(\Omega) = \frac{\hbar\pi}{16}\sum_{j',j''}|D^{j,j',j''}|^2[&(n_{j'}+n_{j''}+1)\delta(\Omega-\omega_{j'}-\omega_{j''}) \\ &+(n_{j'}-n_{j''})(\delta(\Omega-\omega_{j'}+\omega_{j''})-\delta(\Omega+\omega_{j'}-\omega_{j''}))],\end{aligned} \tag{1.63}$$

where the first term in the summation corresponds to emission processes and the second to absorption, and n'_j, n''_j are the occupation numbers of the modes involved in the process.

The real part of the self-energy $\Delta(\Omega)$ is usually computed making use of the Kramers-Kronig relationships for complex analytical functions. This real part introduces a shift in the energy of the phonon mode.

Finally, once we know how to compute the self-energy of the phonon modes, we will define the lineshape σ_j. The lineshape is the one-phonon neutron cross section, and it can be measured in inelastic neutron scattering experiments. It is found that:

$$\sigma_j \propto \frac{2\omega_j\Gamma_j(\Omega)}{[\Omega_j^2-\omega_j^2-2\omega_j\Delta_j(\Omega)]+[2\omega_j\Gamma_j(\Omega)]^2}. \tag{1.64}$$

1.4.3 Nuclear Dynamics Methods

In this subsection we will see different methods to compute, in the framework of DFT calculations, the harmonic spectrum and the anharmonic interactions. Moreover, we will see a method to compute phonon spectra at high temperature structural phases.

Density Functional Perturbation Theory

We have seen that the force theorem allows to easily compute the forces acting on a given nucleus. We can obtain the second-order dynamical matrix by differentiating the

[15] We have denoted the energy or frequency in which the self-energy depends on as Ω to avoid confusion with the harmonic frequency ω

forces with respect to the nuclear coordinates. Since we are interested in implementing this approach in a DFT calculation, for the case of the Kohn-Sham energy functional (eq. 1.27) we have:[16]

$$D^{I\alpha,I'\alpha'} = \frac{\partial^2 E_{II'}}{\partial u_{I\alpha}\partial u_{I'\alpha'}} + \int d\boldsymbol{r}\frac{\partial^2 V_{ext}(\boldsymbol{r})}{\partial u_{I\alpha}\partial u_{I'\alpha'}}\rho(\boldsymbol{r}) + \int d\boldsymbol{r}\frac{\partial \rho(\boldsymbol{r})}{\partial u_{I\alpha}}\frac{\partial V_{ext}(\boldsymbol{r})}{\partial u_{I'\alpha'}}, \tag{1.65}$$

where we can see that the calculation of $D^{I\alpha,I'\alpha'}$ requires the computation of the ground-state electron charge density $\rho(\boldsymbol{r})$ and its linear response to a distortion of the nuclear geometry $\partial\rho(\boldsymbol{r})/\partial u_{I\alpha}$ [45]. The way to obtain this linear response from DFT is known as Density Functional Perturbation Theory (DFPT)[46]. The idea is to linearize the Kohn-Sham equations, the density and the functional (eqs. (1.30), (1.25) and (1.27)) with respect to wavefunction, density and potential variations. Such linearization leads to the following expressions:

$$\begin{aligned}
\left(\hat{H}_{KS} - \varepsilon_i\right)|\Delta\phi_i(\mathbf{r})\rangle =& -\left(\Delta V_{eff}(\mathbf{r}) - \Delta\varepsilon_i\right)|\phi_i(\mathbf{r})\rangle \\
\Delta\rho(\boldsymbol{r}) =& 2\,\mathrm{Re}\left(\sum_{i=1}^{n}\phi_i^*(\boldsymbol{r})\Delta\phi_i(\boldsymbol{r})\right) \\
\Delta V_{eff}(\mathbf{r}) =& \Delta V_{ext}(\mathbf{r}) + \frac{e^2}{2}\int\frac{\Delta\rho(\mathbf{r}')}{|\mathbf{r}-\mathbf{r}'|}d\mathbf{r}' + \left.\frac{dV_{xc}}{d\rho}\right|_{\rho=\rho(\boldsymbol{r})}\Delta\rho(\boldsymbol{r}),
\end{aligned} \tag{1.66}$$

where Δ denotes the finite-difference operator,[17] which for the case of a nuclear displacement takes the form:

$$\Delta_I = \sum_{\alpha}\Delta u_{I\alpha}\frac{\partial}{\partial u_{I\alpha}}. \tag{1.67}$$

We have also introduced in eqs. (1.66) the first-order corrections to the Kohn-Sham eigenvalues $\Delta\varepsilon_i$ and eigenfunctions $\Delta\phi_i(\mathbf{r})$ given by:

$$\begin{aligned}
\Delta\varepsilon_i =& \langle\phi_i(\mathbf{r})|\,\Delta V_{eff}(\mathbf{r})\,|\phi_i(\mathbf{r})\rangle \\
\Delta\phi_i(\mathbf{r}) =& \sum_{j\neq i}\phi_j(\mathbf{r})\frac{\langle\phi_j(\mathbf{r})|\,\Delta V_{eff}(\mathbf{r})\,|\phi_i(\mathbf{r})\rangle}{\varepsilon_i - \varepsilon_j}.
\end{aligned} \tag{1.68}$$

Thus, the linearized eqs. (1.66) can be solved iteratively in a similar way as the one introduced to solve the Kohn Sham equations (See Fig. 1.3). Only the knowledge of the occupied Kohn-Sham states is needed. So the computational cost of determining the

[16] The following discussion can be found in the review by Stefano Baroni et al. [44].

[17] Do not confuse it with the real part of the self-energy operator given in the previous section

linear response to a single perturbation is of the same order as the one for the unperturbed density.

One particular advantage of DFPT to compute the harmonic phonon spectra compared to other methods is that the response to perturbations of different wavelengths is decoupled. In return it must be noted that it is a perturbative method, which entails that the approximation breaks for high-energy anharmonic corrections to the phonons or when dealing with unstable structures.

DFTP is implemented in the quantum espresso and VASP codes. We will make used of it in the studies of the second part to compute harmonic properties.

Frozen Phonon method

A different approach to obtain the coefficients of the Taylor expansion of the potential energy surface is the so-called frozen-phonon method or finite-displacement approach [47]. The idea of this method is very simple, a set of structures is generated where different atomic displacements $\Delta u_{I\alpha}$ are performed. The interatomic force constants $D^{I\alpha,I'\alpha'}$ are then approximated as:

$$D^{I\alpha,I'\alpha'} \approx -\frac{F_{I'\alpha'+\Delta u_{I\alpha}} - F_{I'\alpha'}}{\Delta u_{I\alpha}} \tag{1.69}$$

Thus, for the set of structures with the displacements we will have to compute the atomic forces $F_{I'\alpha'+\Delta u_{I\alpha}}$ with respect to the undistorted structure. Usually $F_{I'\alpha'} = 0$ since the undistorted structure is the one where the atomic positions are in equilibrium.

The interatomic force constants can be obtained from eq. (1.69); the Parlinski-Li-Kawazoe method [48], which is just a numerical fitting approach to obtain the force constants from a set of forces and displacements.

Therefore, only the computation of the forces from a set of structures with different displacements is required. The size of the set can be cleverly limited by introducing the symmetries of the structure. An analogous procedure can be developed to obtain the third-order force constants.

One advantage of this method is that it allows to include anharmonic effects that would be difficult to study through DFPT. Moreover, it can be implemented in any standard DFT code able to compute total energies and forces. However, the frozen-phonon approach is much more computationally demanding, in the case of crystals it might require unaffordable supercells to compute the phonon spectra at a desired wavelength vector.

The frozen-phonon approach to compute the second and third-order force constants is implemented in the **Phonopy** [49] and **Phono3py** [50] packages. We will use them in the studies of Part II.

Ab initio Molecular Dynamics and the Temperature Dependence Effective Potential method

Finally, we will briefly present how to include the effect of finite temperature in a phonon calculation via the temperature effective potential (TDEP) method [51].

Until now, we have been working with the potential energy surface or Born-Oppenheimer energy surface. The energy minimum of such surface gives the equilibrium positions of the nuclei. This is appropriate when the effect of temperature can be neglected, i.e., if there are no temperature-dependent dynamical instabilities or strong anharmonic effects that lead to structural transitions. In such cases, where finite temperature or pressure is introduced, the potential energy surface is not suitable, and the Gibbs free energy becomes the proper thermodynamic quantity to minimize.

We will be interested in the situation where a structural phase transition occurs at a transition temperature T_s, i.e., equilibrium positions $\{\boldsymbol{R}_0\}$ will be different in each phase. Thus, we will have two different regimes. On one hand, the low temperature one that can be analyzed by the methods that we have been describing for the potential energy surface. On the other hand, the high temperature phase that requires a different treatment.

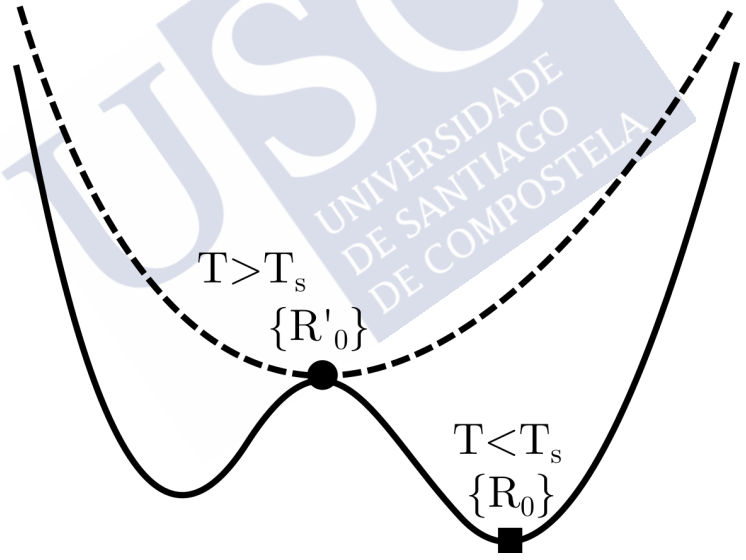


Figure 1.8: Schematic representation of the free energy surface as a function of temperature. Equilibrium positions $\{\boldsymbol{R}_0\}$ ($\{\boldsymbol{R}'_0\}$) are represented in the low (high) temperature phase $T < T_s$ ($T > T_s$) as the minimum of the solid (dashed) line.

The TDEP is based on the idea of generating a set of thermalized structures at a finite temperature and extracting the force constants for a model Hamiltonian that matches the configurations. The way to explore the phase space at a given temperature is by means of an *ab initio* molecular dynamics (aiMD) simulation in the canonical ensemble. At a certain number of time steps the system will be equilibrated at the chosen temperature. Then, the interatomic force constants at a given order can be extracted by minimizing

the difference in the forces obtained in the aiMD and those from the model Hamiltonian introduced by the TDEP method.[18]

We end this chapter in which we have described how to tackle the many-body problem of nuclei and electrons. The Born-Oppenheimer and adiabatic approximations allowed to split the analysis in nuclei and electrons. Density functional theory was described for the treatment of electrons and lattice dynamics for nuclei. Their practical implementation was presented along with methods to solve them. All the approximations and the methods that we have been describing so far are summarized in Fig. 1.1.

USC UNIVERSIDADE DE SANTIAGO DE COMPOSTELA

[18]In an aiMD atomic positions are *moved* through a period of time. A small time step is defined, a DFT calculation is performed at each of these steps to determine the forces and produce the atomic displacements that lead from one step to the next one. Thus, producing the dynamics. In the canonical ensemble the set of possible configurations is restricted by the given temperature. The way to introduce it in the calculations is by means of a heat bath that enters the Hamiltonian constraining the phase space. Different thermostats can be found.

2 Symmetry

> "Beauty is rather a light that plays over the symmetry of things than that symmetry itself."
>
> — Plotinus

In this chapter we will talk about the concept of symmetry and how it is applied to the many-body problem. Symmetry is probably the most fundamental idea in Physics. According to Emmy Noether's theorem, every conservation law is a consequence of the presence of a particular symmetry in the system [52]. For instance, translational symmetry of space entails linear momentum conservation, or angular momentum is related to rotational invariance. In a quantum system, the eigenvalues' degeneracy or the eigenfunctions' properties are determined by symmetry, and their transformation due to phase transitions can be understood as changes in the symmetry. More than that, many of the methods that we have already been describing in Chapter 1, are based on symmetry considerations, such us the basis sets needed to describe core and valence electrons. Therefore, such a fundamental concept deserves a closer look.

The aim of this chapter will be to provide the basics to analyze a system of nuclei and electrons through the eyes of symmetry groups. We will see in the second part how symmetry guides all the analysis that we perform.

2.1 Definition of a Symmetry Group

The way in which symmetry enters in the mathematical description of a system is through transformations. If a transformation U is performed to the wavefunction Ψ that codifies the state of a quantum system as

$$U\Psi = \Psi, \tag{2.1}$$

and we obtain that the transformation keeps the system in the same state Ψ, we say that the system is invariant under such transformation U.

A set of transformations $\{U\}$ forms a group if all its elements fulfill the following four requirements:

- The product of any two elements of the group is itself an element of the group.
- The associative law applies.
- The unit (or identity) element E is present in any group and its product with any element of the group leaves the element unaltered.
- For every element of the group there is an inverse element such that the product of the element and its inverse leads to the identity element.

The group will be a symmetry group if its elements leave the system invariant as given by eq. (2.1). Moreover, the group will be called Abelian if all the elements of the group commute. In general, this case does not happen. Non-Abelian groups are an active area of research due to their promising applications.

We have stated in the previous chapter that the Hamiltonian of a system describes all the interactions between nuclei and electrons. The ground state of the system is obtained as the lowest energy eigenstate of the Hamiltonian. For this reason, the symmetry analysis is usually performed on the Hamiltonian. If a system is invariant under a transformation of a given symmetry group, the Hamiltonian must commute with the elements of that group. For instance, for the case of eigenstates with the same energy (degenerate), we can obtain one of the eigenfunctions and then obtain the others by applying to it the symmetry operations that leave the Hamiltonian invariant.

Since this thesis is focused on the analysis of crystalline transition metal compounds, in the following sections we will analyze the kind of transformations that are encountered in those systems. Such transformations define the different symmetry groups that characterize the properties of the crystal.

2.2 Point Group Symmetry

Rotations, inversions, reflections and their different combinations that leave a system invariant are called point symmetries. The operation of a point transformation R_p on a function $f(\boldsymbol{r})$ (such as the density of a system) is:

$$R_p f(\boldsymbol{r}) = f(R_p \boldsymbol{r}). \tag{2.2}$$

If a system has inversion symmetry, it means that it is invariant under the change of sign of all the coordinates, for instance $f(x, y, z) = f(-x, -y, -z)$. In the case of mirror symmetry (or reflection), the system is invariant under sign inversion with respect to the mirror plane. For example, if the mirror plane is the xy plane, the system is invariant as $f(x, y, z) = f(x, y, -z)$.

Let us focus now on the case of rotations. For a free atom, all rotations about any axis are symmetry operations, i.e., they commute with the Hamiltonian. Thus, the free atom has full rotation symmetry. The basis functions for the full rotation group are the

spherical harmonics Y_{lm}. This is the reason why the atomic orbitals s, p, d and so on, are expressed as a product of a radial function R_{nl} and a linear combination of spherical harmonics. Thus, for the s orbitals we have

$$s = R_{n0}Y_{00}, \tag{2.3}$$

for the p orbitals

$$\begin{aligned} p_z &= R_{n1}Y_{10} \\ p_x &= \frac{R_{n1}}{\sqrt{2}}\left(Y_{11} + Y_{1-1}\right) \\ p_y &= \frac{R_{n1}}{i\sqrt{2}}\left(Y_{11} - Y_{1-1}\right), \end{aligned} \tag{2.4}$$

and for the d orbitals

$$\begin{aligned} d_{z^2} &= R_{n2}Y_{20} \\ d_{x^2-y^2} &= \frac{R_{n2}}{\sqrt{2}}\left(Y_{22} + Y_{2-2}\right) \\ d_{xy} &= \frac{R_{n2}}{i\sqrt{2}}\left(Y_{22} - Y_{2-2}\right) \\ d_{xz} &= \frac{R_{n2}}{\sqrt{2}}\left(Y_{21} - Y_{2-1}\right) \\ d_{xy} &= \frac{R_{n2}}{i\sqrt{2}}\left(Y_{21} + Y_{2-1}\right), \end{aligned} \tag{2.5}$$

where the subscript n here denotes the principal quantum number.

We see that these orbitals expand the electronic states of a free atom. More than that, core electrons hardly feel the presence of neighbouring atoms in a material, i.e., the interactions of core electrons with the electrons of neighbouring atoms are tiny. For this reason, atomic-like orbitals are a good basis to describe them. This is the idea behind the APW method explained in the previous chapter, where core electrons inside the muffin-tin sphere are expanded as a product of radial functions and spherical harmonics (eq. (1.38)).

In the free atom (or nearly free atom, like the core states that we mention), the energy levels of a given n and l quantum numbers are degenerate. For instance, the five $3d$ orbitals are degenerate in energy.[1] This situation changes when breaking the full rotational symmetry by placing the free atom within a crystal. The environment created by the neighbouring atoms breaks the full rotational symmetry, thus, driving the infinite symmetry group to a finite one, in which only rotations of a certain angle leave the system invariant.

[1] At this point we are not considering spin degeneracy explicitly. However, note that for the $3d$ orbital we have 10 degenerate energy levels if we count spin.

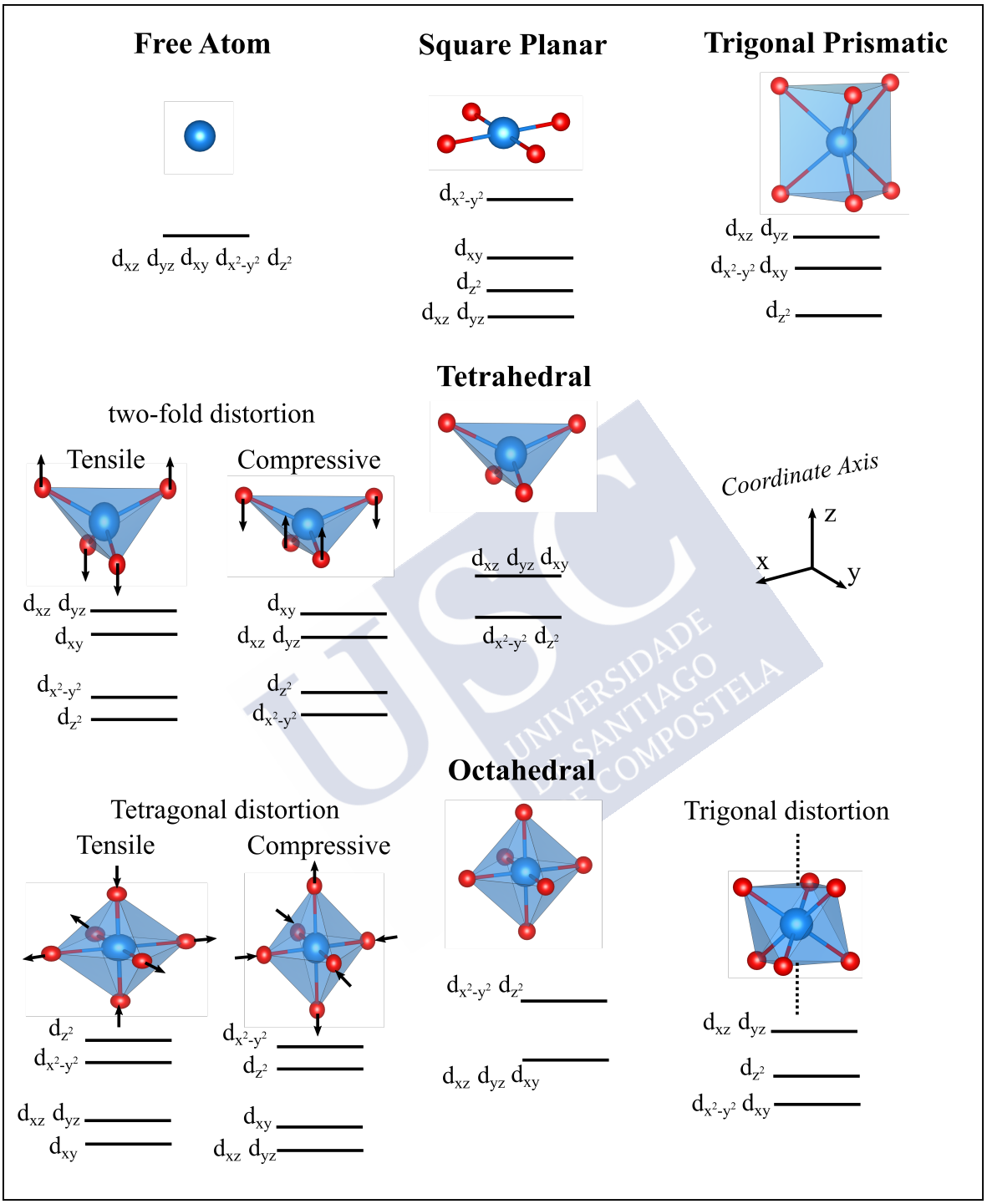


Figure 2.1: Crystal-field splittings of the *d*-orbital energy levels in different environments. The central atom is depicted in blue and ligands in red.

The finite rotation groups that appear by the placement of nuclei in a crystal break the degeneracy according to their symmetry operations. This effect is what is usually known as crystal-field splitting of the orbitals. Since our aim is to study crystalline transition metal compounds, in Fig. 2.1 we summarize the crystal-field splitting on d orbitals for different kinds of environments (ligand atoms surrounding a central atom). Octahedral, square planar, tetrahedral environments and different distortions to them are analyzed there. We show how the energy levels corresponding to the d orbitals of the central atom are split.

Of course, in the case of s orbitals there is no crystal-field splitting, since the s orbital is non-degenerate. The p orbitals, which are triply degenerate in the free atom, might be split by a crystal field. These splittings can be explained in terms of spatial anisotropies. If there is no anysotropy, the three p orbitals remain degenerate. If there is anisotropy along one axis, the orbital that corresponds to that axis gets split from the other two. Finally, if the three axes are inequivalent, all p orbitals become non-degenerate.

We have been analyzing point group symmetry in terms of the electronic wavefunctions. However, point group symmetry affects or, better to say, constrains the energy levels of the phonon modes too. The polarization vectors of the modes can be analyzed in an analogous way to the electronic states by point group symmetry. Even more, anisotropies in macroscopic properties such as conductivity are also related to the point group symmetries of the nanostructure.

2.3 Translational Symmetry

In this thesis we are concerned with the study of crystals, in which translational symmetry plays a fundamental role. Crystals are an ordered state of matter in which the equilibrium positions of the nuclei are repeated periodically in space. Therefore, all the properties of a crystal can be specified regarding a unit cell (the spatial periodicity) and the atoms that it contains. In Fig. 2.2 a crystal lattice formed by a two-atom unit cell is illustrated.

A unit cell is characterized by the set of lattice vectors $\boldsymbol{a}_\alpha$ and by the position of the atoms inside the unit cell given by their vectors $\boldsymbol{\tau}_I$, usually known as the basis of the unit cell. Therefore, any translation $\boldsymbol{T}_n$ produced by a linear combination of integer multiples n_α of the lattice vectors

$$\boldsymbol{T}_n = n_1\boldsymbol{a}_1 + n_2\boldsymbol{a}_2 + n_3\boldsymbol{a}_3 \tag{2.6}$$

will leave the system invariant, i.e., any function of the system $f(\boldsymbol{r})$ (such as the equilibrium positions of the nuclei or the electron density) is invariant under such translations as

$$f(\boldsymbol{r}) = f(\boldsymbol{r} + \boldsymbol{T}_n). \tag{2.7}$$

This periodicity encountered in crystals allows the representation of those periodic functions in terms of Fourier components at wavevectors $\boldsymbol{k}$, which are defined in the Fourier transform of the real space, know as the reciprocal space.

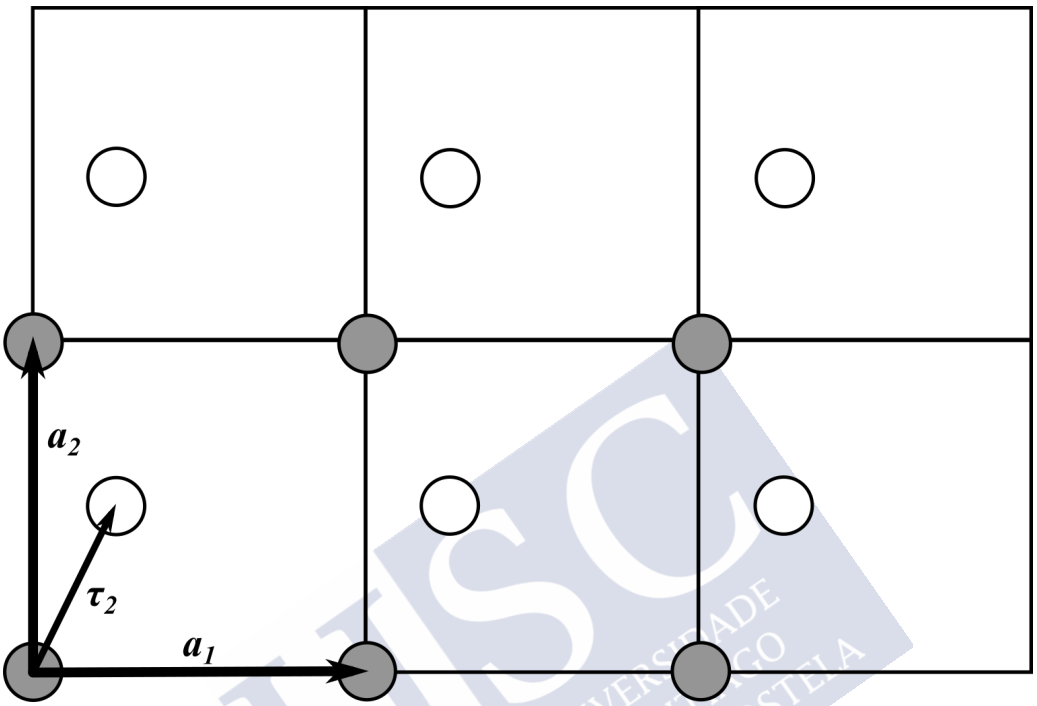


Figure 2.2: Schematic of a crystal lattice with two atoms (grey and white) per unit cell. Six unit cells are depicted, the lattice vectors $\boldsymbol{a}_1$ and $\boldsymbol{a}_2$, and the atomic basis vector $\boldsymbol{\tau}_2$ for the white atom.

If we consider a crystal formed by a large number of unit cells $N_c = N_{c1} \times N_{c2} \times N_{c3}$, where $N_{c\alpha}$ denotes the number of cells in each spatial direction α, we can simplify the problem by restricting to a discrete set of Fourier components periodic in that crystal volume. This implies that each Fourier component must fulfill a set of periodic boundary conditions that, in the limit of large crystal volume, restrict the wavevectors to:

$$\boldsymbol{k}\boldsymbol{a}_\alpha = 2\pi \times integer \tag{2.8}$$

where the set of wavevectors that fulfill this condition form the reciprocal lattice. Thus, we can define the set of reciprocal lattice vectors $\boldsymbol{b}_\beta$ as:

$$\boldsymbol{b}_\beta \cdot \boldsymbol{a}_\alpha = 2\pi\delta_{\beta\alpha}. \tag{2.9}$$

The reciprocal lattice vectors $\boldsymbol{b}_\beta$ determine a volume Ω_{1BZ} in the reciprocal space known as the first Brillouin zone.

The Hamiltonian that describes the many-body system is invariant under lattice translations. Considering the previous chapter, we can consider the Kohn-Sham Hamil-

tonian for electrons and the harmonic Hamiltonian for phonons. They both commute with the translation operator $\hat{T}_{\boldsymbol{n}}$, thus eigenstates of the Hamiltonian can be chosen to be eigenstates of the translation operators and *vice versa*. Therefore, the eigenstates of the translation operator can be used to block diagonalize the Hamiltonian. This result is known as the Bloch theorem [37]

$$\hat{T}_{\boldsymbol{n}}\phi(\boldsymbol{r}) = \phi(\boldsymbol{r} + \boldsymbol{T}_n) = e^{i\boldsymbol{k}\boldsymbol{T}_n}\phi(\boldsymbol{r}). \tag{2.10}$$

where $\boldsymbol{k}$ is a wavevector in reciprocal space:

$$\boldsymbol{k} = \sum_{\beta} \frac{n_\beta}{N_\beta}\boldsymbol{b}_\beta, \tag{2.11}$$

whose range can be restricted to the first Brillouin zone by taking $n_\beta < N_\beta$. Therefore, the eigenstates of the Hamiltonian can be chosen with definite value of k within the first Brillouin zone:

$$\phi_{\boldsymbol{k}}(\boldsymbol{r}) = e^{i\boldsymbol{k}\boldsymbol{r}}u_{\boldsymbol{k}}(\boldsymbol{r}). \tag{2.12}$$

These $\phi_{\boldsymbol{k}}(\boldsymbol{r})$ are termed Bloch functions and we can see that they are built as the product of a plane wave $e^{i\boldsymbol{k}\boldsymbol{r}}$ and a periodic function $u_{\boldsymbol{k}}(\boldsymbol{r})$. The Bloch theorem is the reason why the methods that we have been describing for solving the Kohn-Sham and the lattice dynamics equations are based on plane waves. Therefore, the Hamiltonians that lead to these equations are block-diagonal in $\boldsymbol{k}$, and consequently Kohn-Sham equations for independent electrons (eq. (1.30)) and the secular equation for the harmonic phonon spectrum (eq. (1.56)) become independent for each wavevector $\boldsymbol{k}$ in the first Brillouin zone. Then, we can compute the eigenvectors independently for each $\boldsymbol{k}$ and obtain a set of eigenvalues labeled by $\varepsilon_{i,\boldsymbol{k}}$.

In the macroscopic limit of the crystal the spacing between $\boldsymbol{k}$ points, given by eq. (2.12), tends to zero and hence we can take a continuum limit for $\boldsymbol{k}$. This results in the concept of continuum energy bands $\varepsilon_i(\boldsymbol{k})$.

Figure 2.3 shows a schematic of electronic energy bands for a metal and for a band insulator. In general, we can determine the occupied levels as those that lay below the Fermi energy. The energy bands that lay well below the Fermi energy correspond to core electrons. We can notice that the energy dispersion in $\boldsymbol{k}$ of these bands is practically zero. This means that core levels are well localized that barely suffer the effect of neighbour atoms, being that the reason that justifies the use of pseudopotentials and atomic-like functions to describe them. Near the Fermi level, we found the valence bands below the Fermi level and the conduction bands above. If there is a gap between the highest energy valence band and the lowest energy conduction band the system is an insulator. A band insulator requires the complete filling of the band, with degenerate spin states. A different kind of insulating behaviour, e.g., the Mott insulator, will need a symmetry breaking driven by electronic interactions. A metallic behaviour arises for the gapless case. The energy dispersion of these bands is in general different. However, localized

bands can also appear near the Fermi level. For instance, it is quite common that d-electrons in transition metal compounds show a localized behaviour near the Fermi level. This leads to many of the intriguing properties associated to these systems. We will see in the studies of the second part that different effects, like electron-electron interactions or structural transitions, can cause an electron localization and the opening of gaps at certain $\boldsymbol{k}$ points of the energy bands.

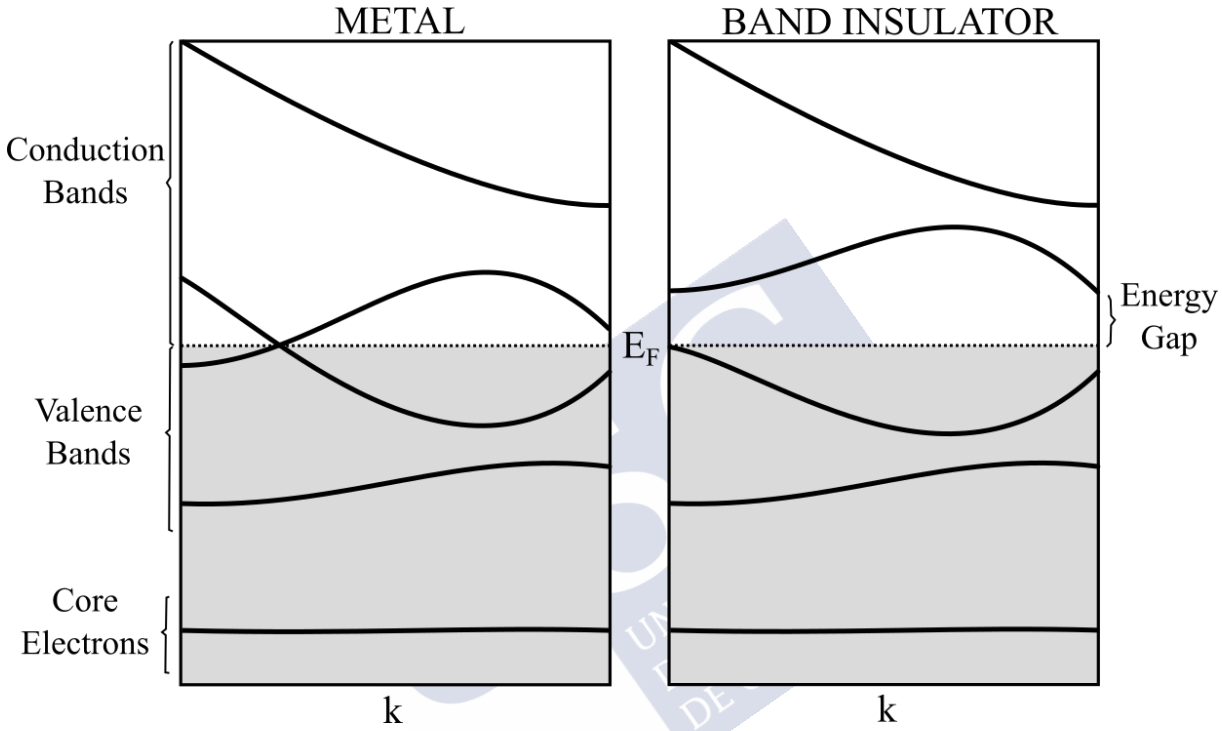


Figure 2.3: Schematic of electronic band structures for a metal and a band insulator. Occupied bands correspond to those in the shaded area, below the Fermi level E_F.

Figure 2.4 shows a schematic of phonon band structures for a structurally stable phase and a structurally unstable phase. The stability of a structural phase is governed by the absence of imaginary modes (usually shown as negative frequencies in band structure plots) in the phonon spectrum. Different distortions to the unit cell or the coupling to external fields can induce a softening of a phonon mode, and the mode becomes imaginary leading to a structural transition. In the studies of the second part, we will analyze how instabilities can be associated to particular structural transitions.

A classification of the phonon modes can be performed in terms of the long wavelength limit ($\boldsymbol{k} \rightarrow 0$). Considering the energy dispersion of the phonon modes in this limit, a group velocity is defined for each of them. Then, we can divide in acoustic and optical modes:

- In the acoustic branches the atoms in the unit cell vibrate in phase and with the same amplitude. There are 3 acoustic modes in the unit cell, one per lattice dimension.

We can think about them as the vibrations of the unit cell. The group velocity of these modes is usually known as the sound velocity. These modes are usually the main responsible for the heat transport in insulators, since their group velocity is greater compared to the other modes. In general, the larger the sound velocity (large bandwidth of the acoustic modes), the higher the thermal conductivity.

- In the optical branches the atoms in the unit cell vibrate with different phases and amplitudes, but keeping the center of mass of the unit cell fixed. We can think of these modes as the internal vibrations of the atom basis, similar to the frequencies of a free molecule. Optical modes owe their name to the fact that they can couple strongly with an electromagnetic field (of the appropriate frequency). Modes that involve oscillating electric dipoles are called optically active since they can couple directly to photons. These couplings lead to the creation of new quasiparticles called polaritons. Moreover, the softening of a polar mode might be related to a structural transition to a ferroelectric phase. The frequencies associated to the optical modes are in the infrared (THz). As we have said, these modes are practically the ones of a free molecule, but with a small effect of the surrounding lattice. This explains that they are characterized by narrow bandwidths. Therefore, the group velocities of these branches will be small and in general they would not make a significant contribution to heat transport in insulators, unless they have a very low energy.

We end this section by mentioning that a crystal is characterized by a space group. A space group is the summation of the translation group and the point group. In a three-dimensional space there are 230 different space groups, each of them characterized by different symmetry operations.

The symmetries encountered in real space are also contained in the reciprocal one. Therefore, the Brillouin zone for a crystal will be determined by its space group and high symmetry points will be defined on it. Usually these points are the most representative ones for band structure analysis. This is the reason why band plots show the energy levels along $\boldsymbol{k}$-paths that connect high symmetry points in the Brillouin zone.[2]

Finally, note that according to Landau theory of phase transitions, whenever a structural phase transition occurs there would be a symmetry breaking associated to a change in the space group [53]. Structural transitions are possible between a space group and its corresponding subgroups.[3] The order parameter predicted by Landau theory corresponds to the phonon mode that drives the transition. We will perform this kind of analyses in the second part.

[2]Standard notation is used to denote the high symmetry points. For instance, the Γ point corresponds to $\boldsymbol{k} = (0, 0, 0)$

[3]A subgroup is a group contained inside a group. Moreover, a group is also a subgroup of itself. Therefore, structural transitions where the space group remains the same are possible.

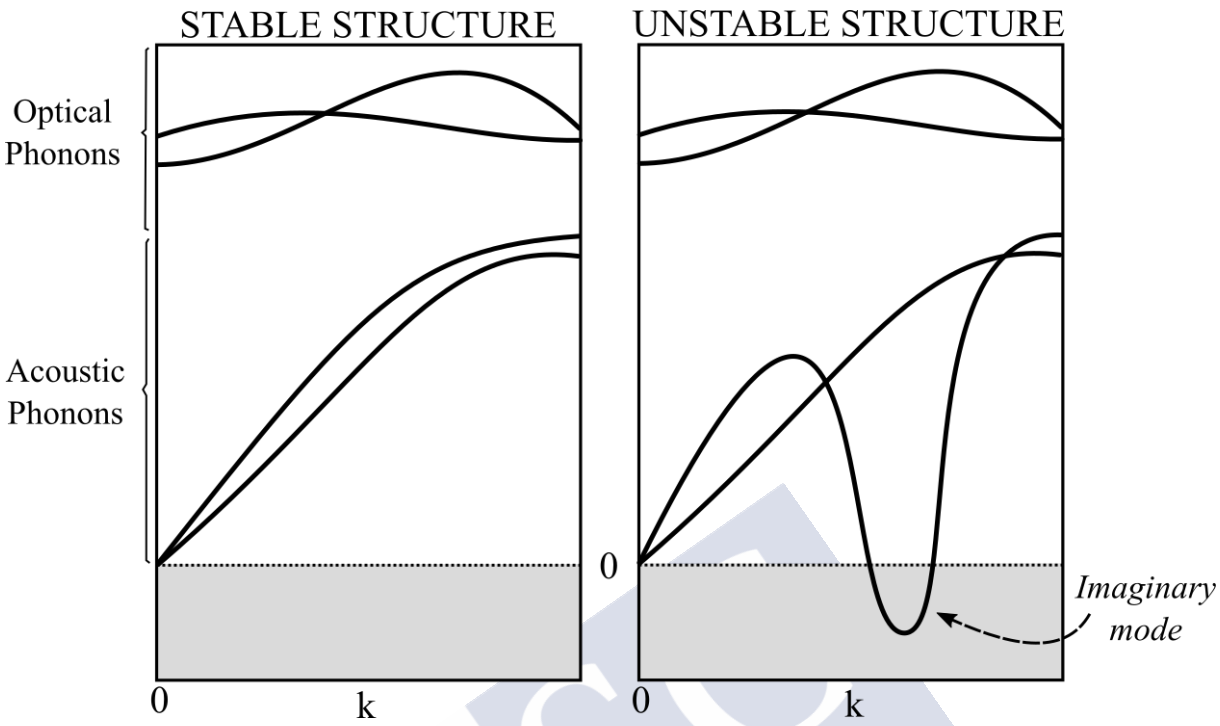


Figure 2.4: Schematic of phonon band structures for a structurally stable phase and a structurally unstable phase. Imaginary phonon frequencies correspond to those in the shaded area, usually depicted as negative frequencies.

2.4 Time-Reversal Symmetry

Time-reversal symmetry is another kind of symmetry that we can encounter in an electronic system. This symmetry is present in the absence of external magnetic fields or if the system is non-magnetic. In those cases, the Hamiltonian is time-reversal invariant, i.e., we can make the transformation $t \rightarrow -t$ and the system will remain unchanged. Therefore, the Hamiltonian can be chosen to be real. This entails that for the Kohn-Sham system of independent electrons, if ϕ is an eigenvector with real eigenvalue ε, then ϕ^* is also an eigenvector with the same energy. If we are dealing with a crystal that satisfies the Bloch theorem, then this last result leads to:

$$\phi^*_{i,\boldsymbol{k}}(\boldsymbol{r}) = \phi_{i,-\boldsymbol{k}}(\boldsymbol{r}) \tag{2.13}$$

and the eigenvalues of $\boldsymbol{k}$ and $-\boldsymbol{k}$ are equal $\varepsilon_{i,\boldsymbol{k}} = \varepsilon_{i,-\boldsymbol{k}}$. This result simplifies the resolution of the Kohn-Sham equations.

An important point to consider is the effect of time reversal symmetry on spin. Up to now the kind of symmetries that we have been analyzing have not been applied to spin. However, time reversal leads not only to reversal of momentum $\boldsymbol{k}$, but spin σ too. Consequently we are left with degenerate states as:

$$\phi_{i,\boldsymbol{k}}(\sigma, \boldsymbol{r}) = \phi^*_{i,-\boldsymbol{k}}(\sigma, \boldsymbol{r}), \tag{2.14}$$

which corresponds to the celebrated Kramers theorem [54]. This theorem combined with spatial symmetries guarantees that states are doubly degenerate in energy at certain $\boldsymbol{k}$ points in the Brillouin zone of the system. Importantly, neither spin-orbit interaction nor crystal field splitting break time reversal symmetry.

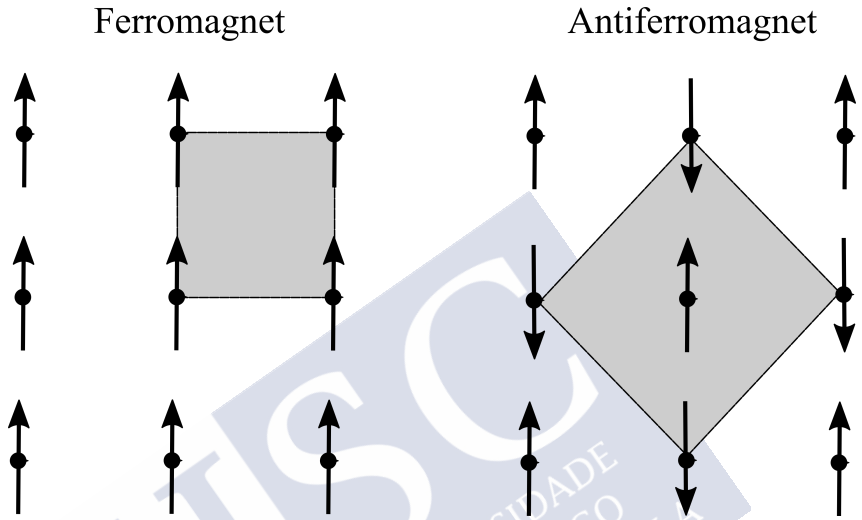


Figure 2.5: Schematic of a ferromagnet and an antiferromagnet. The unit cell of each system is depicted as the grey area.

The application of an external magnetic field breaks time-reversal invariance leading to interesting effects. However, it is also possible to encounter a spontaneous breaking of time-reversal symmetry. This is the case of magnetic systems like those in Fig. 2.5.

In a ferromagnet spins get ordered in a parallel configuration, thus generating the same effect in the material as if an external magnetic field were applied. However, this spin alignment is caused by electronic interactions. This results in the breaking of spin degeneracy. From a DFT point of view, one of the spin channels is more populated than the other.

A different situation occurs in an antiferromagnet. A long-range antiparallel spin order is produced and a combination of translational and time-reversal symmetries is involved. As shown in Fig. 2.5, the symmetry breaking associated to an antiferromagnet leads to a bigger unit cell that allows to describe the system as time-reversal invariant. In Part II we will analyze antiferromagnets that are Mott insulators. Apart from that, antiferromagnetic order can be frustrated. This happens in systems where their spatial group forbids an antiparallel alignment with all the neighbours of a given site. This frustation may lead to exotic spin liquid behaviour.

Finally, notice that the introduction of magnetic order increases the number of groups that a crystal can have. There are 1651 different magnetic space groups.

2.5 Topological Invariants

In this section we will briefly touch the concept of topology in condensed matter. The main studies of this thesis do not deal with topology. However, in Chapter 10 we will see how d electrons can also play a role in topological transitions. Therefore, we will introduce some basics on topology to understand the problem, probably oversimplifying the discussion. We will focus on some definitions that can help us to determine the topological character of a system.

A topological property is a global property of a system. It is usually illustrated as the possibility to connect two different objects by a continuous deformation. For instance, a sphere and a potato can be connected by a continuous deformation. As a result, from a topological point of view, a potato and a sphere represent the same object. Such an object will be characterized by what is called a topological invariant.

Regarding electronic structure, topology is referred to the change eigenfunctions may undergo as a function of $\boldsymbol{k}$ in reciprocal space. The theory is built upon the periodic part of the Bloch functions $u_{\boldsymbol{k}}(\boldsymbol{r})$. Thus, in a two dimensional reciprocal space like the one shown in Fig. 2.6, we can define the two component Berry connection $\mathcal{A}(\boldsymbol{k}) = (\mathcal{A}_x(\boldsymbol{k}), \mathcal{A}_y(\boldsymbol{k}))$ where:

$$\begin{aligned} \mathcal{A}_x(\boldsymbol{k}) &= -Im\,\langle u_{\boldsymbol{k}} | \partial_{k_x} u_{\boldsymbol{k}} \rangle \\ \mathcal{A}_y(\boldsymbol{k}) &= -Im\,\langle u_{\boldsymbol{k}} | \partial_{k_y} u_{\boldsymbol{k}} \rangle \,. \end{aligned} \tag{2.15}$$

We can define with it the Berry phase φ for any closed loop in reciprocal space as:

$$\varphi = \oint \mathcal{A}(\boldsymbol{k}) \cdot d\boldsymbol{k} \tag{2.16}$$

which provides the relative phase change of $u_{\boldsymbol{k}}$ in the loop. The Berry phase is gauge invariant. However, the Berry connection is not. The topological character of a material is determined by the so-called Berry curvature $\Omega(\boldsymbol{k})$, which is the curvature of the surface described by the Berry connection, and is equivalent to the Berry phase for a small patch in the limit of a small loop (see Fig. 2.6), therefore it is gauge invariant:

$$\Omega(\boldsymbol{k}) = \partial_{k_x}\mathcal{A}_y(\boldsymbol{k}) - \partial_{k_y}\mathcal{A}_x(\boldsymbol{k}) = -2Im\,\langle \partial_{k_x} u_{\boldsymbol{k}} | \partial_{k_y} u_{\boldsymbol{k}} \rangle \,. \tag{2.17}$$

The integral of the Berry curvature over the whole surface is called the Berry flux Φ:

$$\Phi = \oint \Omega(\boldsymbol{k}) \cdot d\boldsymbol{S}, \tag{2.18}$$

which allows to define the Chern C number as $C = \Phi/2\pi$. The Chern number is a topological invariant that can take any integer value, and characterizes the topology of a system. If the Berry flux is zero $C = 0$, this determines a trivial topology. A non-trivial

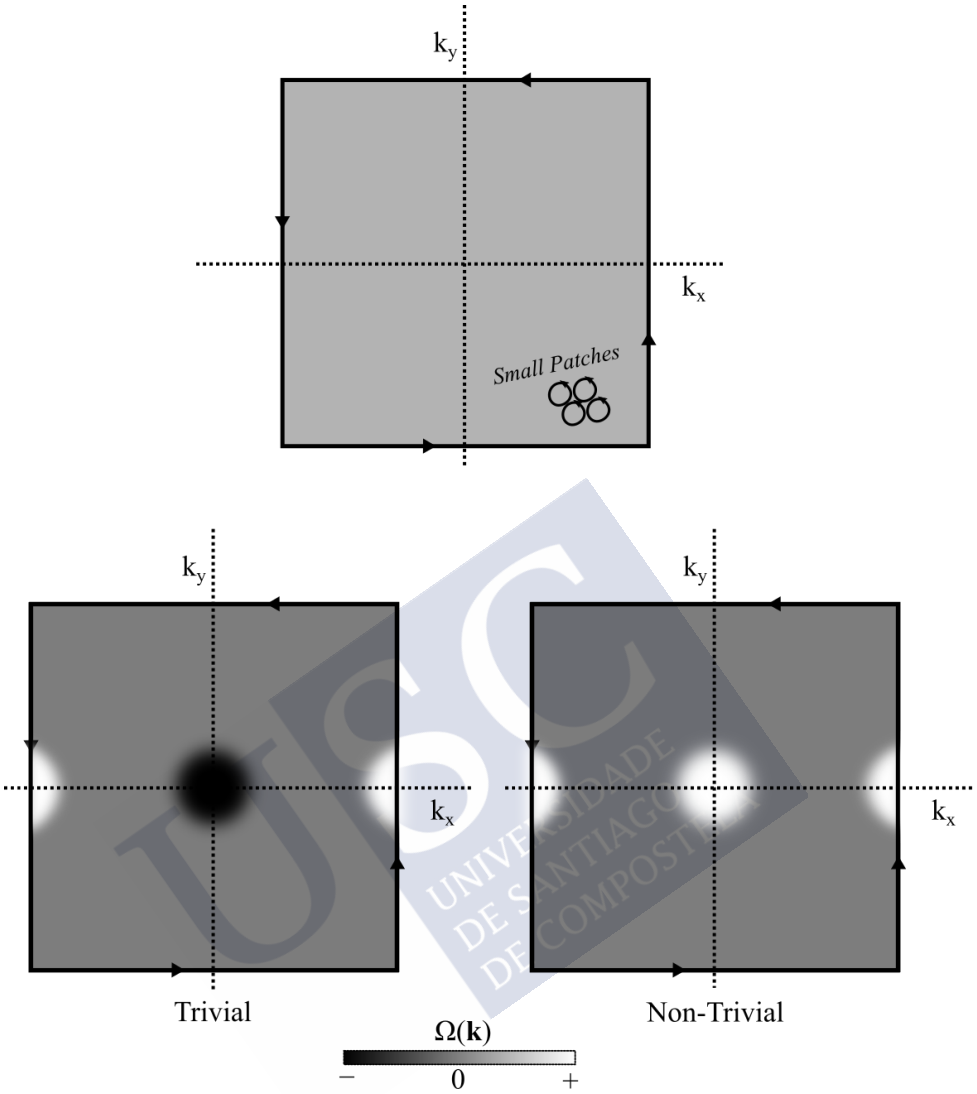


Figure 2.6: Top panel: schematic of a loop in the Brillouin zone, small patches are depicted to guide the derivation of the Berry curvature. Low panels: representation of the Berry curvature in the first Brillouin zone for trivial (left) and non-trivial (right) topological phases.

topology emerges when the Berry flux is non-zero, and then $C \neq 0$. This is illustrated in the low panels of Fig. 2.6, where the sign of the curvature is plotted as a function of $\boldsymbol{k}$.

In order to determine the topological character of a material the Berry curvature of the occupied states is analyzed. A non-trivial topology is associated with band inversions between occupied and unoccupied bands. The most famous physical consequence of such a non-trivial character is the emergence of surface states.

Different kind of topological materials can be encountered: topological insulators, nodal-line semimetals, etc. Here we have shown the simplest case of a Chern systems in

order to grasp the idea of topology. Thus, different signatures to detect the topological character of materials are defined other than the Chern number. Crystal symmetries, like time reversal or inversion play a key role in the Berry Curvature of a system.

In this chapter we have analyzed the fundamental concept of symmetry in the frame of condensed matter physics. A definition of symmetry group has been provided. Point groups, translations and time-reversal symmetry groups were described. Finally, a brief introduction to topological invariants was also given.

USC UNIVERSIDADE DE SANTIAGO DE COMPOSTELA

3 Statistics and Transport

> "Why do they called it rush hour
> when nothing moves?"
>
> — Robin Williams

In this small chapter we will present some important quantities that help to reveal the physical behaviour of a system. We will provide a definition for the density of states per unit energy and the distribution functions for electrons and phonons in thermal equilibrium. Amongst other things, the analysis of the density of states allows to determine the stability of a system as well as to compute different equilibrium properties. Moreover, we will define transport coefficients through the Boltzmann transport equation. We will see how to compute them from first principles calculations. Thus, connecting the nanoscale description and the macroscopic properties of a material.

3.1 Thermal Equilibrium

One of the most important quantities that we can obtain when solving the many-body problem is the density of states per unit energy $DOS(E)$:

$$DOS(E) = \sum_i \frac{1}{\Omega_{1BZ}} \int_{1BZ} d\boldsymbol{k} \delta(\varepsilon_{i,\boldsymbol{k}} - E) \tag{3.1}$$

where $\varepsilon_{i,\boldsymbol{k}}$ can represent the energy of an electron or phonon. For independent particle approximations, like the Kohn-Sham for electrons or the harmonic one for phonons, eq. (3.1) corresponds to the number of states per unit energy. The dimensions of a system, its symmetries and particle interactions play a fundamental role determining the shape of the DOS a given configuration might present.

The number of occupied states per unit volume at a given energy for a system in thermal equilibrium at a temperature T is given by the product of the density of states and a probability distribution function $f(E)$. Since phonons are bosons, a Bose-Einstein distribution function $f_{BE}(E)$ is applied:

$$f_{BE}(E) = \frac{1}{e^{\frac{E-\mu}{k_B T}} - 1}, \tag{3.2}$$

where k_B is the Boltzmann constant and μ is the chemical potential. In a different way, electrons are fermions and hence they will be ruled by a Fermi-Dirac distribution function $f_{FD}(E)$:

$$f_{FD}(E) = \frac{1}{e^{\frac{E-\mu}{k_B T}} + 1}, \tag{3.3}$$

where the chemical potential μ is called the Fermi level E_F when $T = 0$.

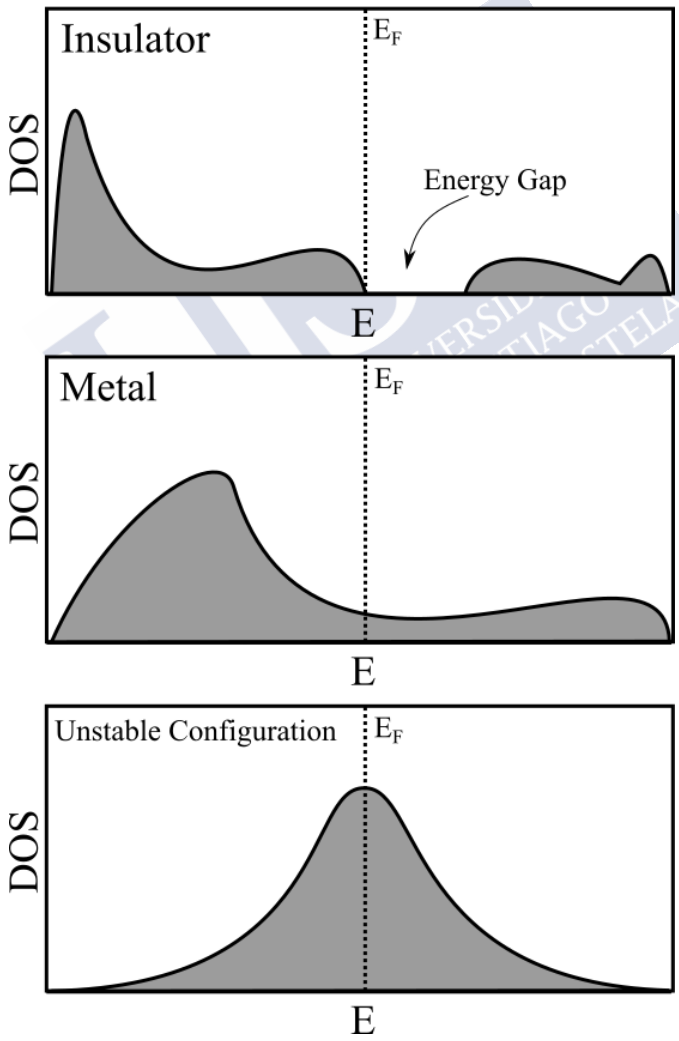


Figure 3.1: Schematic for different electronic DOS cases. The Fermi level is depicted as a dashed line.

Figure 3.1 shows a schematic of different DOS situations. A semiconductor or insulator is shown in the top panel. Note the presence of an energy gap above the Fermi level. In the middle panel a metallic case is exemplified. In the lowest panel an unstable configuration is depicted. When a high density of states occurs at the Fermi level for a given configuration, the system might be unstable. This high DOS at the Fermi level can be seen as a hint that prompts to a phase transition to a lower energy ground state of the system. A small perturbation will lead the system to a different ground state. In the framework of a mean field theory, it can be shown that the system gets stable by breaking a symmetry. An order parameter is associated to that transition. Note that a peak in the Fermi level could occur, but in such cases electron correlations or topological features would be required.

As we have stated in Chapter 1, we are dealing with a many-body problem in which different degrees of freedom compete. Therefore, the path the system takes to get stabilized depends on energy considerations. For instance, the system might break time-reversal symmetry and become a ferromagnet. In the Kohn-Sham description the spin degeneracy is broken and one of the spin channels gets more occupied than the other.[1] This is the case of a Stoner ferromagnet [55]. Alternatively, the system might undergo a structural transition by breaking spatial symmetry. Jahn-Teller distortions [56] and charge density waves [57] are examples of structural transitions. Electronic interactions might also play a fundamental role driving the system to an insulating scenario. This is known as Mott insulator behaviour [58]. In all these phenomena, and in many others, a symmetry is spontaneously broken lowering the DOS at the Fermi level, and thus lowering the energy of the system. The emergence of gaps or pseudogaps[2] around the Fermi level is associated to that transitions. Apart from that, note that temperature is introduced through the Fermi-Dirac distribution function (eq. (3.3)), and it will play a major role in the stability of a given configuration. The *DOS* can be used to compute different physical quantities like the internal energy or the specific heat.

Finally, let us define the so called projected density of states ($PDOS_j(E)$). It provides the contribution of a particular atom or orbital j to the total DOS. In the case of phonons the projection is performed along the polarization vector of one of the modes and atoms. Meanwhile, in the the case of electrons the projection can be performed on a set of orthonormal states φ_j that can represent an atomic orbital or a localized state of a given atom.

$$PDOS_j(E) = \sum_i \frac{|\langle \varphi_j | \phi_i \rangle|^2}{\Omega_{1BZ}} \int_{1BZ} d\boldsymbol{k} \delta(\varepsilon_{i,\boldsymbol{k}} - E), \tag{3.4}$$

where ϕ_i can be seen as the Kohn-Sham states determined in the electronic problem. Thus, the total DOS is given by adding all the contributions of the projected $PDOS_j(E)$. Analysis of the DOS and PDOS will be crucial in the studies presented in the second part.

[1] The DOS of each spin channel is usually represented with different sign. Positive for majority spin and negative for the minority channel.

[2] Pseudogaps are energy gaps that occur at certain $\boldsymbol{k}$ points of the Brillouin zone.

3.2 Transport Properties

In the previous section we have introduced the concept of density of states and the distribution functions for phonons and electrons. As we have seen, these functions provide the number of occupied states for a system in thermal equilibrium. In this part we will analyze the situation when an electric field $\boldsymbol{E}$ or thermal gradient ∇T is present in the crystalline solid. In such cases, a steady-state flow of charge or heat is established as a consequence of the external fields and the internal scattering processes trying to restore equilibrium. This phenomenon is known as transport, and therefore a non-equilibrium statistical theory is required to study it. We will make use of the Boltzmann transport equation to fulfill this task.

In the presence of external fields, the Boltzmann formulation considers that the system undergoes a small deviation from the equilibrium distribution. Hence, a linear expansion on time t can be performed on the distribution function f that describes the steady-state that is established. This leads to the following equation:

$$\frac{df}{dt} = \left.\frac{\partial f}{\partial t}\right|_{force} + \left.\frac{\partial f}{\partial t}\right|_{diff} + \left.\frac{\partial f}{\partial t}\right|_{scatt} = 0, \tag{3.5}$$

where we can see that a steady flow is achieved by the competition between the deviations from the equilibrium distribution caused by the external fields (first term), the diffusion of the particles (second term) and the scattering processes trying to restore the equilibrium (third term). We will analyze separately electronic and phonon transport. Different approximations, and hence different levels of theory, will be used for each kind of particles. In order to underline that crystals are the kind of systems that we are going to study, from now on we will explicitly include the $\boldsymbol{k}$-dependence in the development of those transport approximations.

The relaxation time approximation is a widely used approach to solve the Boltzmann transport equation for electrons. It is based on the idea that the scattering processes can be related to a relaxation time $\tau(\boldsymbol{k})$:

$$\left.\frac{\partial f}{\partial t}\right|_{scatt} = -\frac{f(\boldsymbol{k}) - f_0(\boldsymbol{k})}{\tau(\boldsymbol{k})}, \tag{3.6}$$

where the numerator describes the deviation of the distribution $f(\boldsymbol{k})$ from the equilibrium $f_0(\boldsymbol{k})$, and the relaxation time $\tau(\boldsymbol{k})$ provides how the system returns to equilibrium. Introducing this last equation on eq. (3.5), and linearizing it by considering that the external fields are weak and hence the deviation of the distribution from equilibrium is small, we arrive to the following equation for the perturbed distribution function $f(\boldsymbol{k})$:

$$\begin{aligned} f(\boldsymbol{k}) =& f_0(\boldsymbol{k}) - \tau(\boldsymbol{k})\boldsymbol{v}(\boldsymbol{k}) \left(\frac{\partial f_0(\boldsymbol{k})}{\partial T} \nabla T + \frac{\partial f_0(\boldsymbol{k})}{\partial E(\boldsymbol{k})} e\boldsymbol{E} \right) \\ =& f_0(\boldsymbol{k}) - \tau(\boldsymbol{k})\boldsymbol{v}(\boldsymbol{k}) \frac{f_0^2(\boldsymbol{k})}{k_B T} e^{\frac{E(\boldsymbol{k})-\mu}{k_B T}} \left(\frac{(E(\boldsymbol{k})-\mu)}{T} + e\boldsymbol{E} \right), \end{aligned} \tag{3.7}$$

where $E(\boldsymbol{k})$ is the electronic energy and $\boldsymbol{v}(\boldsymbol{k})$ is the electronic group velocity:

$$\boldsymbol{v}(\boldsymbol{k}) = \frac{2\pi}{\hbar} \frac{\partial E(\boldsymbol{k})}{\partial \boldsymbol{k}}. \tag{3.8}$$

Therefore, eq. (3.7) provides the electron population perturbed by a weak electric field and a small temperature gradient. Note that in an independent electron theory like the Kohn-Sham, the distribution is generalized for each electronic state with energy $\varepsilon_i(\boldsymbol{k})$.

Now that we know the perturbed population of electrons produced by the external fields, we can analyze the currents that emerge leading the system to the steady state. The electron current density $\boldsymbol{J}_e$ and the heat current density $\boldsymbol{J}_Q$ can be defined as:

$$\begin{aligned} \boldsymbol{J}_e &= \frac{2e}{8\pi^3} \int \boldsymbol{v}(\boldsymbol{k}) f(\boldsymbol{k}) d\boldsymbol{k} \\ \boldsymbol{J}_Q &= \frac{2}{8\pi^3} \int (E(\boldsymbol{k}) - \mu) \boldsymbol{v}(\boldsymbol{k}) f(\boldsymbol{k}) d\boldsymbol{k}, \end{aligned} \tag{3.9}$$

and introducing eq. (3.7) we arrive at the following relationships:

$$\begin{aligned} \boldsymbol{J}_e &= e^2 K_0 \boldsymbol{E} - \frac{eK_1}{T} \nabla T \\ \boldsymbol{J}_Q &= eK_1 \boldsymbol{E} - \frac{K_2}{T} \nabla T, \end{aligned} \tag{3.10}$$

where the K_n terms are integrals defined as:

$$K_n = \frac{1}{4\pi^3 \hbar} \iint \tau(\boldsymbol{k}) (E(\boldsymbol{k}) - \mu)^n \frac{\boldsymbol{v}(\boldsymbol{k})\boldsymbol{v}(\boldsymbol{k})}{|\boldsymbol{v}(\boldsymbol{k})|} \left(-\frac{\partial f_0(\boldsymbol{k})}{\partial E(\boldsymbol{k})} \right) dS dE, \tag{3.11}$$

where the integral over volume in $\boldsymbol{k}$ has been converted into an integral over surfaces of constant energy. This is quite convenient since only states near the Fermi level (or chemical potential) contribute to the transport. Moreover, the relaxation time is usually approximated as a constant τ. This is known as the constant relaxation time approximation. Apart from that, in *ab initio* calculations, the so-called rigid-band approximation is commonly introduced. It assumes that the electronic band structure is independent to changes in temperature or chemical potential.

Note that eq. (3.10) shows that either an electric field or thermal gradient can generate both an electron or heat current. Such relationship allows us to define the usual transport

coefficients (electrical conductivity, electronic thermal conductivity, Seebeck coefficient, etc.) that can be measured in experiments.[3] Thus, they provide a clear connection between macroscopic properties of materials and their nanoscale description.

The isothermal electrical conductivity σ provides the relation $\boldsymbol{J}_e = \sigma \boldsymbol{E}$ between the applied electric field and the current generated in the material. It is given by:

$$\sigma_{ij} = \frac{e^2\tau}{4\pi\hbar} \int_{E=\mu} \frac{\boldsymbol{v}_i(\boldsymbol{k})\boldsymbol{v}_j(\boldsymbol{k})}{|\boldsymbol{v}(\boldsymbol{k})|} dS_E. \tag{3.12}$$

For metals the electronic thermal conductivity κ_e can be well approximated by the Wiedemann-Franz law through the electrical conductivity as:

$$\kappa_e = \frac{(\pi k_B)^2}{3e^2} T\sigma, \tag{3.13}$$

where the ratio κ_e/σ is known as the Lorenz number. For semiconductors and insulators there is no substantial charge flow, hence heat transport is governed by phonons. We will analyze it below.

The relationship between the electric field generated in a material by a thermal gradient $\boldsymbol{E} = S_s \nabla T$ is ruled by the Seebeck coefficient S_s. It is given by:

$$S_s = \frac{(\pi k_B)^2 eT}{3\sigma} \left(\frac{\partial K_0}{\partial E} \right) \Bigg|_{E=\mu}. \tag{3.14}$$

Note that the Seebeck coefficient, also known as the thermopower, is independent of the scattering rate in the constant relaxation time approximation. Thus, it will be one of the most accurate coefficients that we can compute in that approach. The thermopower will play a fundamental role for thermoelectric applications.

In Part II we will make use of the *BoltzTrap2* code [59] to solve the Boltzmann transport equations in the constant relaxation time approximation and obtain the electronic transport coefficients.

In the study of phonon transport properties only thermal gradients will be considered as the external fields. Therefore, in this case, the linearized Boltzmann transport equations lead to a perturbed distribution function

$$f(\boldsymbol{k}) = f_0(\boldsymbol{k}) - \tau(\boldsymbol{k})\boldsymbol{v}(\boldsymbol{k}) \frac{\partial f_0(\boldsymbol{k})}{\partial T} \nabla T, \tag{3.15}$$

where now the equilibrium distribution function $f_0(\boldsymbol{k})$ corresponds to the Bose-Einstein distribution given by eq. (3.2). In the harmonic approximation for phonons the perturbed distribution of eq. (3.15) is applied for each phonon mode.

Differently from the electronic case where the relaxation time $\tau(\boldsymbol{k})$ was considered a given constant, for the case of phonons we can compute the relaxation time using the

[3] Note that these coefficients are second rank tensors that provide the relationship between the external fields and the current that they generate in the material.

anharmonic approximation described in Chapter 1. It can be computed as the inverse of the imaginary part of the self-energy (eq. (1.63)).

The lattice thermal conductivity κ_l provides the relationship $\boldsymbol{J}_Q = -\kappa_l \nabla T$ between a thermal gradient and a heat flow. It can be computed as:

$$\kappa_l^{ij} = \frac{1}{k_B T^2} \int E(\boldsymbol{k}) \tau(\boldsymbol{k}) f_0(\boldsymbol{k}) \left(f_0(\boldsymbol{k}) + 1\right) \boldsymbol{v}^i(\boldsymbol{k}) \boldsymbol{v}^j(\boldsymbol{k}) d\boldsymbol{k} \tag{3.16}$$

where usually the phonon energy is substituted by the angular phonon frequency as $E(\boldsymbol{k}) = \hbar\omega(\boldsymbol{k})$. Moreover, it is common to obtain the total κ_l as a summation of the contributions of each phonon mode.

In the studies of Part II we will compute the lattice thermal conductivity using the ShengBTE code [60].

Finally, now that we have defined the different transport coefficients, we can see how they are coupled in a thermoelectric material. A thermoelectric material is characterized by showing a large thermoelectric effect [61], i.e., a thermoelectric material can generate an electric potential ΔV from a temperature gradient ∇T (and vice versa) as:

$$\Delta V = -S_s \nabla T. \tag{3.17}$$

Therefore, this class of materials present potential applicability in the area of efficient energy management. As shown in eq. (3.17), a high Seebeck coefficient S_s is required in order to have a good thermoelectric. However, this is not the only quantity to pay attention when designing a good thermoelectric.

When a temperature gradient is imposed to a thermoelectric material, its charge carriers tend to diffuse from the hot end to the cold end. A net charge is formed at the cold side (negative in the case of electrons and positive for holes). This produces an electrostatic potential. Thus, an equilibrium is reached between the chemical potential for diffusion and the electrostatic repulsion of the total net charge at the cold end. A large thermoelectric effect will be developed if the material is able to maintain the thermal gradient, i.e., if it presents a low thermal conductivity κ, and also if it shows a high carrier mobility, i.e., if it presents a high electrical conductivity σ. The coupling between the different transport coefficients that defines a good thermoelectric is introduced through the so-called thermoelectric figure of merit zT as

$$zT = \frac{S_s^2 \sigma}{\kappa} T. \tag{3.18}$$

Therefore, the goal when designing a good thermoelectric is to maximize the figure of merit. Moreover, note that a good thermoelectric contains only a single type of carrier, it will be either a n-type or a p-type semiconductor. This is due to the fact that if we had electron and hole conduction at the same time, the net charge at the cold end would be zero and the induced electric field would not arise.

In this chapter we have introduced the fundamental concept of density of states and how it is used along distribution functions to compute some of the properties that describe a material in equilibrium. Moreover, we have presented the Boltzmann transport equation that allows to define and compute different transport coefficients. The ingredients to find a good thermoelectric material were also exposed. All this provides the connection between the nano and the macroscale of a material.

Part II

Studies on Crystalline Transition Metal Compounds

USC UNIVERSIDADE DE SANTIAGO DE COMPOSTELA

USC
UNIVERSIDADE
DE SANTIAGO
DE COMPOSTELA

4 Transport Properties of $SrTiO_3$

$SrTiO_3$ has been proposed as a prototypical example of complex oxide where many different properties can be studied. In particular, when doped, it has been reported to be a good thermoelectric material. The Seebeck coefficient and the lattice thermal conductivity are the fundamental transport properties that determine this thermoelectric behaviour. In this chapter we analyze how the thermopower and the lattice thermal conductivity of $SrTiO_3$ depend on the electronic and crystal structure and how those transport properties can be tuned by structural distortions. The analysis related to the thermopower can be found in [I] from the List of Publications, where we show a way to include the effect of the orbital degeneracy on the thermopower. The study related to the lattice thermal conductivity is exposed on [III] and we found there what are the main features that determine the thermal conductivity of $SrTiO_3$. Both studies could be used as a basis to understand similar compounds.

4.1 Introduction

Complex oxides have become a major platform for discovering new fundamental physical properties of materials and for their applications in devices. In particular, transition metal oxides have become an interesting playground to search for new materials with enhanced thermoelectric (TE) properties. Their synthesis is affordable in many cases, they are chemically stable, they can be nanostructured in the form of films [62], nanoparticles [63] and nanowires [64], and they span a huge range of chemical compositions and doping [65].

In standard semiconductors, the parameters entering the TE figure of merit (eq. (3.18)), namely the electrical conductivity, the Seebeck coefficient and the thermal conductivity (in particular its electronic component) are usually coupled [66] so that improving the electrical conductivity has a negative effect in the Seebeck coefficient and the thermal conductivity, and vice versa. Many different routes have been proposed to optimize the figure of merit [67, 68]. Transition metal oxides, with their flexible d electrons, should be more permeable to changes and tunability of their electronic structure with

strain [69] and nanostructuring [70] than standard sp semiconductors. d electron systems show many different phases as a product of the coupling between lattice, spin, charge and orbital degrees of freedom [5], which could help tuning the band structure at will and modify the TE response in the desired direction. Examples of oxides with promising TE properties are the family of misfit layered cobaltates [71, 72] and also doped $SrTiO_3$ (STO) [73] and its nanostructures [74].

The cubic perovskite structure has always been a paradigmatic example. In particular, $SrTiO_3$ serves as a template for all sorts of oxide-based nanostructures since many other oxides can be grown on top of it, but also because of its own intriguing physical properties. It is a quantum paraelectric material that undergoes a structural transition at 105 K [75]. This is a tetragonal (low-temperature) to cubic (higher temperature) transition accompanied by an octahedral rotation existing in the low-temperature phase. It also becomes superconducting at 300 mK when doped [76]. Its nanostructures have shown all sorts of interesting physical properties: two-dimensional electron gas [62], ferromagnetism [77], superconductivity [78], a tunable Rashba effect [79], etc. Moreover, the influence of various sorts of strain have been thoroughly studied, in particular the appearance of a ferroelectric-like phase on the tensile strain limit has been predicted [80, 81] but not fully demonstrated experimentally so far. Apart from that, a Poiseuille flow of phonons was recently identified on STO at low temperatures [82]. Moreover, due to its potential as an energy harvesting material, the thermoelectric properties of STO have been profusely studied [74, 83].

One way to enhance the TE response of a material is, on the one hand, to decouple the electronic components. This has been suggested to be achieved via strain engineering [84]. On the other hand we can play with the phonon part of the thermal conductivity [85–88], which in contrast is the least studied factor from a computational point of view [89].

In this chapter we will see how the thermopower and the lattice thermal conductivity of STO are coupled to the electronic and crystal structure. The analysis related to the thermopower can be found in [I], while in Ref. [III] we expose the study focused on the lattice thermal conductivity. In principle, the findings obtained for STO should provide a general platform for understanding similar mechanisms that occur in other perovskite-related oxides of interest for TE and thermal transport applications.

4.2 Thermopower of $SrTiO_3$

In the past, strain has been proposed as a natural way to produce band engineering in oxides [90] and hence a possible route to tune the thermopower of STO. In principle, in a cubic system strain has a detrimental effect by reducing orbital degeneracy, thus reducing the thermopower, particularly at high temperatures [83]. To explore quantitatively the effects of strain and its related symmetry breaking in the actual values of the thermopower for typical oxides, we have chosen to model this using a very simple cubic perovskite oxide,

the STO, that is naturally n-doped. Those electrons will populate the t_{2g} bands which will respond to strain in different ways depending on its magnitude, its sign, but more importantly, also depending on the doping level. We will analyze in detail the effects of strain in terms of disturbing the electronic degeneracies in a t_{2g} electron system and how these affect the thermopower and the effective mass of the system.

4.2.1 Computational Methods

Ab initio electronic structure calculations based on the density functional theory (DFT) [17, 18] have been performed using an all-electron full potential code (WIEN2K [30]) on $SrTiO_3$.

The exchange-correlation term is parametrized depending on the case. We have used the generalized gradient approximation (GGA) in the Wu-Cohen [91] scheme for structural optimizations (volume optimizations). For the electronic structure calculations we have used the semilocal potential developed by Tran and Blaha as a modification of the Becke-Johnson potential [22]. As explained in the first chapter, this method typically allows the calculation of band gaps with an accuracy similar to the much more expensive GW or hybrid methods [92], and in particular for $SrTiO_3$ it gives an accurate band gap [83]. However, effective masses are not improved with respect to standard LDA/GGA functionals [93].

The calculations were performed with a converged k-mesh and a value of $R_{mt}K_{max}$= 7.0. Spin-orbit coupling (SOC) was introduced in a second variational manner using the scalar relativistic approximation [23, 25]. The R_{mt} values used were in a.u.: 2.50 for Sr, 1.86 for Ti and 1.69 for O when studying $SrTiO_3$.

Transport properties have been calculated using the BoltzTrap [59] code. This solves Boltzmann transport equation from first-principles calculations within the constant relaxation time approximation. This strategy will allow us to obtain the Seebeck coefficient at different temperatures, which is, within that approximation, independent of the scattering time. These calculations require an even finer k-mesh for the Brillouin zone integrations ($25 \times 25 \times 25$ is the converged grid).

We have simulated the effects of both tensile and compressive strains on $SrTiO_3$ by fixing the a lattice parameter to that of several well-known systems typically used as substrates for thin film deposition (LAO: a=3.820 Å, LSAT: a=3.868 Å, STO: a= 3.905 Å, DSO: a= 3.942 Å, GSO: a= 3.968 Å) [83, 94, 95] and relaxing the c lattice parameter. We have thus explored how the electronic band structure evolves under different degrees of strain.

4.2.2 Thermopower Modeling

In this subsection we will provide an expression for the thermopower as a function of temperature and strain and analyze the different temperature regimes. We will obtain the Seebeck coefficient for different strain situations from DFT calculations and interpret

the results we get in terms of a simple model in order to make predictions easier. In the model that we propose, we have simplified the expression proposed by Kubo for the thermopower [96]. Within this formalism, the equation to solve in order to obtain the Seebeck coefficient is the following:

$$S = \frac{S^{(2)}/S^{(1)} + \mu/e}{T} \tag{4.1}$$

where μ is the chemical potential, e the absolute value of the electron charge, T the temperature and $S^{(2)}$ and $S^{(1)}$ are integrals of time correlation functions. We will not go further in the discussion of these integrals since their shape makes them impractical when calculating transport properties in most cases. For this reason, in our model, we will replace these integrals by a simpler function of temperature.

Equation (4.1) can be split in two parts. The term $S^{(2)}/TS^{(1)}$ is the energy-transport term, while μ/Te is the entropy term, that will dominate at high temperature [97]. We can assume that the thermopower will follow the simple expression:

$$S = \frac{A}{T + T_0} + S_{(T\to\infty)} \tag{4.2}$$

where the first term on the right is dominant at low temperatures and corresponds to the energy-transport term, whereas the second term, that is associated to the entropy term, dominates at high enough temperature.

In the following subsections we will discuss in more detail the meaning of each term separately and the parameters that appear in our model.

Low temperature Seebeck coefficient

To interpret the origin and shape of the energy-transport term, we will make use of the results obtained from our ab initio calculations solving the Boltzmann transport equations to obtain the values of the constants A and T_0 and try to provide a physical interpretation for them. This will be fit to the following expression:

$$S = \frac{A}{T + T_0'} + B \tag{4.3}$$

in order to obtain the value of the parameter A, that accounts for the temperature dependence of the energy-transport term.

The T_0 parameter is introduced in our model to make the Seebeck coefficient to be zero when temperature is zero. From eq. (4.2) it is easy to see that:

$$T_0 = \frac{-A}{S_{(T\to\infty)}} \tag{4.4}$$

Let us now try to analyze the physical meaning of the A parameter relating it to the effective mass m^*. Our aim is not to give an exact value for the effective mass (since this

would be a band-dependent and largely anisotropic in momentum space tensor [98]) from A, but just analyzing its variation with strain.

On the one hand, thermopower's Mott formula for semiconductors [99] has a similar shape to that of the model we are considering:

$$S_{Mott} = \frac{E_F - E_c}{eT} - \frac{k_B}{e} a_c \tag{4.5}$$

where E_F is the Fermi level, E_c the minimum in energy of the conduction band (it will be at the Γ point in STO), k_B the Boltzmann constant and a_c is a constant that depends on the material. Comparing with our model:

$$A = \frac{E_F - E_c}{e} \tag{4.6}$$

On the other hand, if we consider an energy band with a parabolic dispersion:

$$E(k) = E_c + \frac{\hbar k^2}{2m^*} \tag{4.7}$$

it can be shown that the Fermi level is given by [100]:

$$E_F = E_c + \left(\frac{3n}{\pi}\right)^{2/3} \left(\frac{h}{8m^*}\right) \tag{4.8}$$

where n is the carrier concentration and h the Planck constant. Equation (4.8) is the usual expression of the Fermi energy as a function of the carrier concentration for electrons in parabolic bands.

We can now consider together eq. (4.6) and eq. (4.8). Straightforward algebra allows to obtain an expression for the effective mass m^* in terms of the parameter A, that we can obtain from a fit to our ab initio calculations of the thermopower:

$$m^* = \left[\frac{\left(\frac{3n}{\pi}\right)^{2/3} \left(\frac{h}{8m_0}\right)}{Ae}\right] m_0 \tag{4.9}$$

where m_0 is the bare electron mass. As we have previously mentioned , this effective mass corresponds to a simplified parabolic band picture, but it would be helpful to analyze its dependence with strain. It is important to remark that the effective mass could be highly dependent on SOC because this effect changes substantially the low-doping electronic structure. With this in mind, we will include it in all our calculations.

High temperature Seebeck coefficient

In this part, we will explain where the high temperature Seebeck coefficient comes from. In Ref. [97] an equation that relates the thermopower S at high temperatures to the number of possible configurations g is deduced:

$$S_{(T\to\infty)} = -\frac{k_B}{e}\frac{\partial \log g}{\partial N} \tag{4.10}$$

where k_B is the Boltzmann constant, e is the electron charge and N is the number of electrons. In this paper the authors obtain the Seebeck coefficient in different situations. We will show some of the results in order to clarify the equation that we will use.

For a system of N spinless fermions with N_A sites to be occupied, the number of possible configurations g is:

$$g = \frac{N_A!}{N!(N_A - N)!} \tag{4.11}$$

using equation (4.10), the so-called Heikes formula is obtained:

$$S_{(T\to\infty)} = -\frac{k_B}{e}\log\left[\frac{(1-\eta)}{\eta}\right] \tag{4.12}$$

where $\eta = N/N_A$. We want now to find an equation similar to (4.12), but for the case of fermions with spin. We will be interested in the case in which the repulsion energy between fermions (for our purpose these fermions will be electrons) is larger than the thermal energy, so in each site there can be just one particle. The number of possible configurations is the one seen for spinless fermions (4.11) multiplied by a 2^N factor that takes into account the spin degeneracy. Hence, we get:

$$g = \frac{N_A!}{N!(N_A - N)!}2^N \tag{4.13}$$

so the Seebeck coefficient that we obtain is:

$$S_{(T\to\infty)} = -\frac{k_B}{e}\log\left[2\frac{(1-\eta)}{\eta}\right] \tag{4.14}$$

Now that we have seen how to introduce the spin degeneracy, we are in the position to expand equation (4.13) to account for the t_{2g} orbital degeneracy that occurs at the bottom of the conduction band in electron-doped STO. We will introduce heuristically a factor $f_{t_{2g}}$ in eq. (4.13), that weighs the t_{2g} degeneracy in a similar way as the factor 2 does for the spin degeneracy:

$$g = \frac{N_A!}{N!(N_A - N)!}2^N f_{t_{2g}}^N \tag{4.15}$$

so inserting this in equation (4.10) we obtain:

$$S_{(T\to\infty)} = -\frac{k_B}{e}\log\left[2f_{t_{2g}}\frac{(1-\eta)}{\eta}\right] \tag{4.16}$$

but we have not talked about the shape of this factor $f_{t_{2g}}$ yet. Our goal is to find an expression that reproduces the degeneracy behavior in different strain situations. We

will model it as a function of the number of electrons in the d_{xy} orbital, N_{xy} and the total number of electrons in the t_{2g} manifold, $N_{t_{2g}}$. Figure 4.1 shows the three limiting cases we will have to consider in order to model the degeneracy in every case. The unstrained case implies all t_{2g} bands are degenerate, and hence there is a triple orbital degeneracy. If tensile (compressive) strain occurs, the d_{xy} (xz/yz) band/(s) lies (lie) lower in energy and then a single (double) degeneracy occurs.

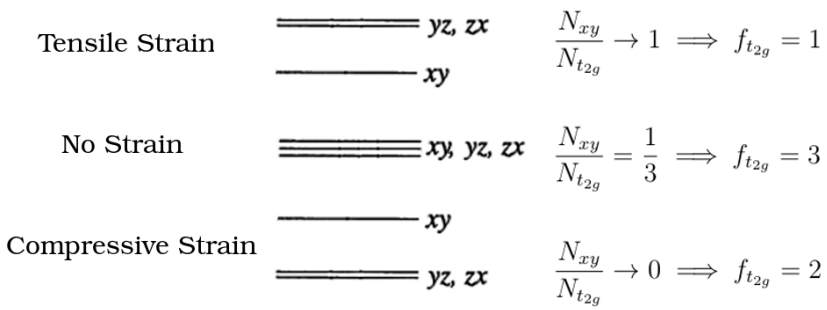


Figure 4.1: We show the three limiting cases for the t_{2g} degeneracy. In the case without strain (middle panel), all the orbitals are degenerate ($f_{t_{2g}} = 3$). If strain is applied, degeneracy is broken towards having a lower-lying singlet (tensile strain: $f_{t_{2g}} = 1$, top panel) or a lower-lying doublet (compressive strain: $f_{t_{2g}} = 2$, bottom panel).

So we encounter that the factor $f_{t_{2g}}$ must be a function of $x = N_{xy}/N_{t_{2g}}$, its value must be contained in the interval $[1, 3]$, and the maximum being equal to 3 at $x = 1/3$. Considering all these facts, we are going to fit the points shown in Fig. 4.1 to the following function (we chose a Gaussian because it is the simplest smooth function that one can think of that has only one adjustable extremum in the $[1, 3]$ interval):

$$f_{t_{2g}} = \gamma + \frac{\alpha}{\beta\sqrt{\frac{\pi}{2}}} e^{-2\left(\frac{(x-1/3)}{\beta}\right)^2} \tag{4.17}$$

where the constants α, β and γ are completely determined by the three limiting cases shown in Fig. 4.1. A plot of the factor as a function of x can be seen in Fig. 4.2.

In some previous works the weight of the degeneracy in the thermopower has been studied [101]. Considering eq. 4.16 and the range of values that the degeneracy factor $f_{t_{2g}}$ can have ($[1, 3]$), the maximum variation in S that can be introduced due to the degeneracy $\Delta S^{max}_{(T\to\infty)}$ is:

$$\Delta S^{max}_{(T\to\infty)} = -\frac{k_B}{e}(\log[3] - \log[1]) \sim -95\ \mu V/K \tag{4.18}$$

However, in any realistic situation, the modification will not be that large.

We have found an analytical function for the high temperature thermopower from a statistical calculation. A degeneracy factor for the t_{2g} manifold was introduced as a

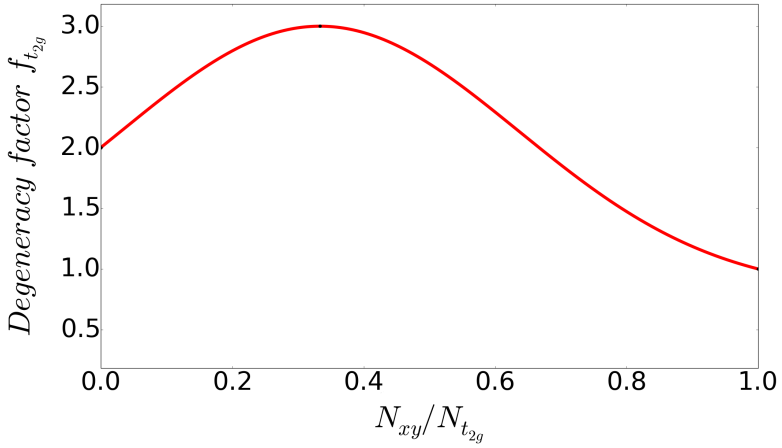


Figure 4.2: $f_{t_{2g}}$ function that results from eq. 4.17. This degeneracy factor fulfills the three limiting cases analyzed in Fig. 4.1 for the effect of strain in a t_{2g} electron system. It accounts for the orbital degeneracy of the system as a function of strain. N_{xy} and $N_{t_{2g}}$ need to be determined ab initio.

function of $N_{xy}/N_{t_{2g}}$. This procedure will make possible to calculate the entropy-related term $S_{(T\to\infty)}$ from our DFT calculations just by computing $N_{xy}/N_{t_{2g}}$ for each strain introduced in the STO structure.

What we have done so far is being able to decouple the influence in thermopower variations with strain that comes from electronic degeneracies and from band structure modifications (such as effective mass changes in a parabolic-band description), that strain will also introduce.

4.2.3 Results of the Model on $SrTiO_3$

We have run calculations in $SrTiO_3$ simulating different strain situations by fixing the lattice parameter a to that of the different standard perovskite substrates mentioned in the computational procedures section. For each a, we have optimized the lattice parameter c. We have not considered oxygen octahedral tilts, since this kind of distortions are hardly dependent on the impurity introduced as dopant. Therefore, we have limited our analysis to a cell volume distortion caused by biaxial strain. We have found that tensile (compressive) strain increases (reduces) the unit cell volume (as shown in Fig. 4.3. This has been experimentally reported previously for other oxides [102] and also for this system [103]. In Fig. 4.3 we plot the evolution of the unit cell volume with strain. We observe that, tensile strain leads to an increase in unit cell volume. The volume reduction that occurs for compressive strain leads to a smaller Ti-Ti distance, which increases the hopping integrals and hence leads to an increased bandwidth. This bandwidth increase should be related to a decrease in effective mass.

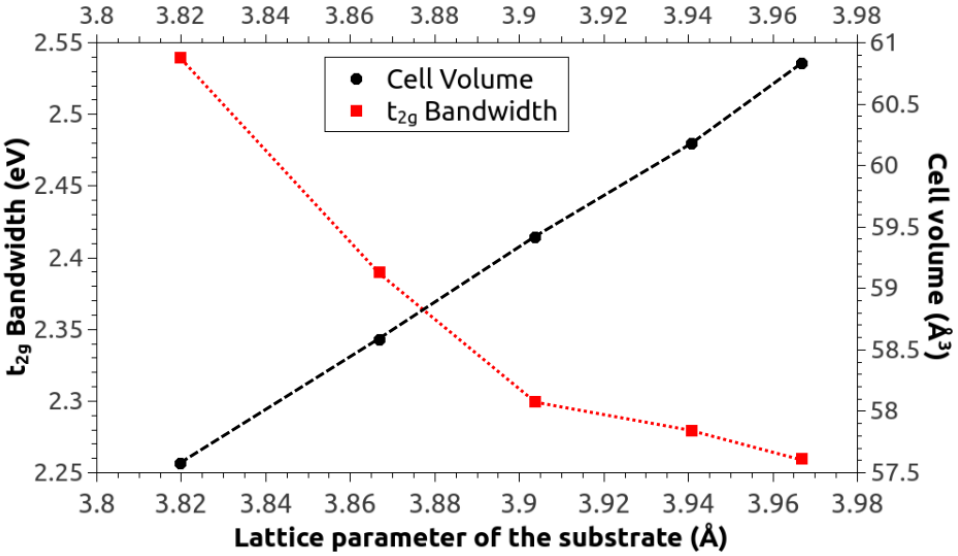


Figure 4.3: Bandwidth and unit cell volume for different strain situations. We see that bandwidth decreases with volume and volume is increased as positive (tensile) biaxial strain is applied.

With these structures we have performed electronic structure calculations including spin-orbit coupling with the TB-mBJ exchange-correlation potential, that allows to give an accurate band gap without additional computational cost. Figure 4.4 shows the band structures (only the conduction bands close to its bottom) for different strain situations together with the corresponding DOS's on the same energy scale. GSO corresponds to the tensile strain limit and LAO to the compressive one. We can observe that the former leads, as explained above, to a reduction of the t_{2g} bandwidth, together with some shifts in the DOS peaks. The bottom of the conduction band is at Γ. We can see also that the position of the unoccupied t_{2g} bands is higher in energy for compressive strain and lower for the tensile strain case.

Figure 4.5 shows the energy bandgap variation with cell volume and hence with strain. It can be seen that an increase in the lattice parameter of the substrate produces a decrease in the energy bandgap.

We have calculated the number of electrons in the d_{xy} orbital, N_{xy} and the total number of electrons in the t_{2g} manifold, $N_{t_{2g}}$. Both values were obtained by integrating inside the Ti muffin-tin sphere. We will assume that the degree of localization will be identical for the three t_{2g} orbitals and hence integrating inside the muffin-tin spheres is sufficient for our purposes since we are only interested in the ratio. This ratio is needed to obtain the degeneracy factor $f_{t_{2g}}$ and consequently the thermopower at high temperature $S_{(T\to\infty)}$ as a function of doping.

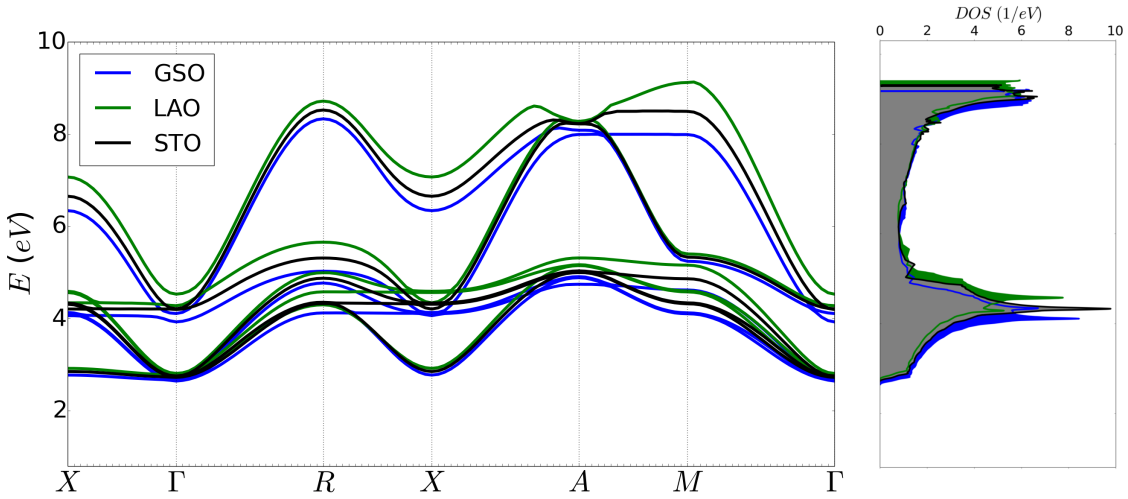


Figure 4.4: Band structure representation and density of states (DOS) calculated for different strain values. It can be seen how the bandwidth increases for compressive strain and decreases for tensile strain.

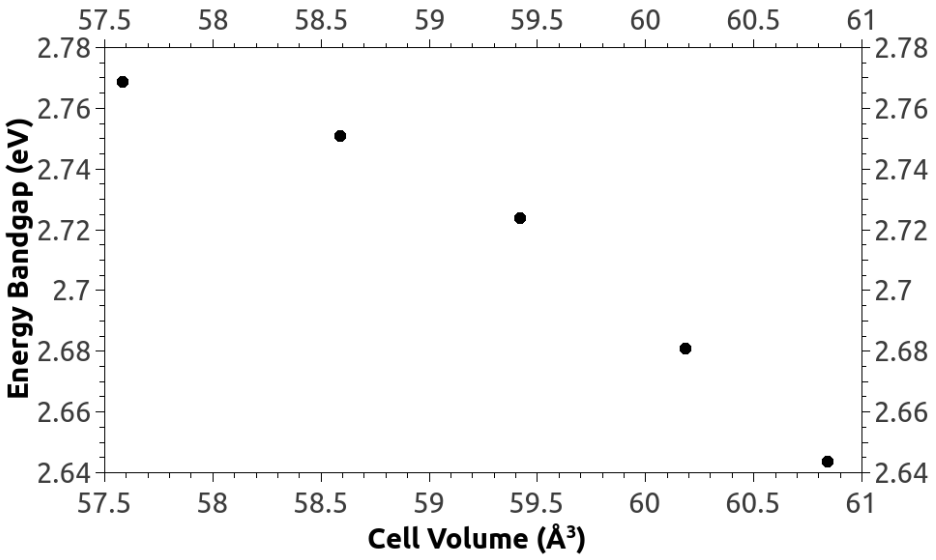


Figure 4.5: Energy bandgap variation with cell volume. We see that tensile strain decreases the energy gap.

Figure 4.6 shows the degeneracy factor dependence with doping for the different strain situations analyzed. We can see there, as a function of electron doping (in terms

of electrons doped per unit cell, or Nb atoms substituting Ti, thus adding one extra electron to the conduction band per dopant). We can see that at low doping, the three limiting cases we discussed above are obtained (in the pure single-ion picture), with the unstrained case having threefold degeneracy and the compressive or tensile strain cases tending to a twofold degenerate state or a singlet, respectively. As doping increases, the t_{2g} bands become more heavily populated and the actual band splittings become less and less important. Above 5% doping, the degeneracy factor becomes very close to 3, almost independent of strain. This illustrates that, even though in principle strain can tune degeneracies (by removing them), thermopower at high temperatures might not be affected if doping is substantial. This limit will of course depend on the system, but for STO we see that it is obtained (within a rigid band approximation) at values which are on the order of those sought for in the case of TE applications ($\sim 10^{20}$ cm^{-3}). The important point to notice here is that the effect of strain on STO will not damage the TE efficiency at high temperature by reducing orbital degeneracies, when working at those high doping levels we are discussing.

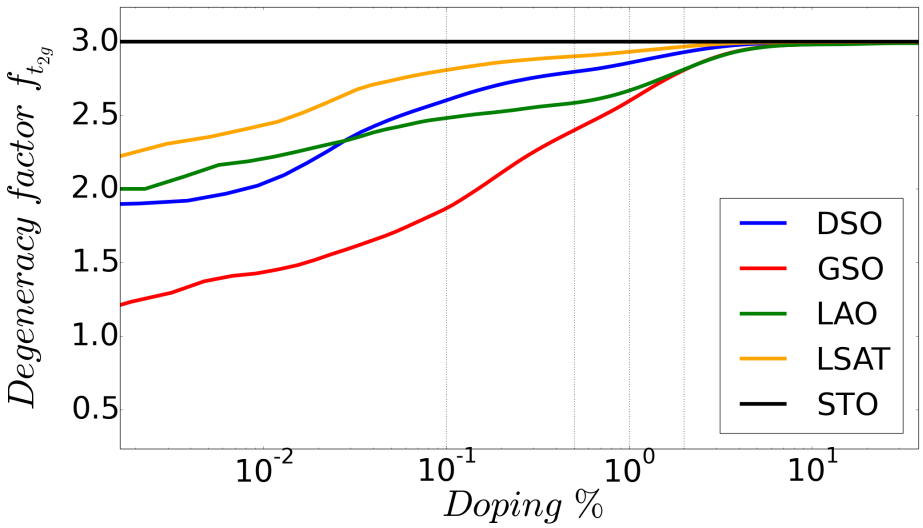


Figure 4.6: Degeneracy factor as a function of doping. In the low doping regime the degeneracy factors collapse to the three limiting cases exposed in Fig. 4.1, so they become largely dependent on strain. As we increase the doping level the factor becomes strain independent and tends to 3 as the t_{2g} bands become more populated. Our calculations show that this occurs between 2-5 % Nb-doping. In the case of unstrained STO we see that the degeneracy factor is completely independent of the doping level since there is always a triple degeneracy in that case. This figure suggests that degeneracy effects vanish above ∼5% doping.

Introducing the results for the degeneracy factor $f_{t_{2g}}$ in eq. (4.16), we can obtain the thermopower at high temperature $S_{(T\to\infty)}$ as a function of doping for the five strain situ-

ations that we are analyzing. Once $S_{(T\to\infty)}$ is computed, we have to solve the Boltzmann transport equations to obtain the parameter A. After that, we are in the position to get the value of T_0 using eq. (4.4) and consequently determine the three parameters of our model (eq. (4.2)). We must warn the reader that the Boltzmann transport equations used to compute the parameter A would be less accurate at lower temperatures (in particular the phonon drag term is not included). Consequently, we will restrict our conclusions to analyze the evolution with strain and not focus too much on the actual values predicted for the thermopower. Also, discrepancies with experimental values could be due to the use of the constant relaxation time approximation which is used routinely but could have its limitations [104].

Figure 4.7 shows six representations of the thermopower obtained using the model that we propose (eq. (4.2)) at different doping levels for the five strain cases analyzed, utilizing the values of the parameters that we have just calculated. We can see that the high temperature thermopower decreases in absolute value as we increase the doping level, as one would expect. The parameters A, $S_{(T\to\infty)}$, T_0 and also the obtained effective masses are summarized in Table 4.1.

Figure 4.8 shows the dependence that effective masses have with strain for the high doping regime. We can observe there that the theoretical effective masses obtained increase their value as doping increases. However, eq. (4.9) proposed to obtain the effective masses from parameter A is just a mechanism to get the effective mass tendency with strain. As we have said, it will only be valid in the high doping regime so we will focus on analyzing the evolution of the effective mass with strain but not so much on its actual doping dependence, since this will be quite dependent on the type of dopant. This feature is analyzed in Ref. [105] concluding that the effective mass will also depend on the kind of defect introduced to dope STO and the kind of distortions these introduce in the lattice.

Coming back to Fig. 4.7, we can analyze now each doping regime, we see that for low doping levels the strain tendency is given by the high temperature Seebeck $S_{(T\to\infty)}$, i.e. we see in Fig. 4.7, for 0.1% doping ($\sim 1.7\times10^{19}$ cm^{-3}) that the Seebeck evolution with temperature follows the same strain dependence than $S_{(T\to\infty)}$. The unstrained case (with a equal to that of STO) is the one that has the largest Seebeck value (in absolute value) at any temperature. Meanwhile, at high doping levels, greater than or equal to 2%, according to the results shown in Fig. 4.6, $S_{(T\to\infty)}$ stops being strain dependent. Consequently, the only dependence on strain in the evolution of the Seebeck with temperature comes from the A parameter. We can easily check that the curves in the 2%, 4% and 50% doping levels ($\sim 3.3\times10^{20}$, $\sim 6.6\times10^{20}$ and $\sim 8.4\times10^{21}$ cm^{-3} respectively) follow the strain dependence given by parameter A in Table 4.1, i.e., the inverse behaviour that effective masses have with strain (see Fig. 4.8). This comes about due to the fact that $f_{t_{2g}}$ becomes very close to 3 and strain independent at those doping levels. Hence, the only changes to the thermopower occur via variations of the energy-transport term, in which (for high doping regimes of 2% or more) the thermopower is enhanced (in absolute value) by tensile strain.

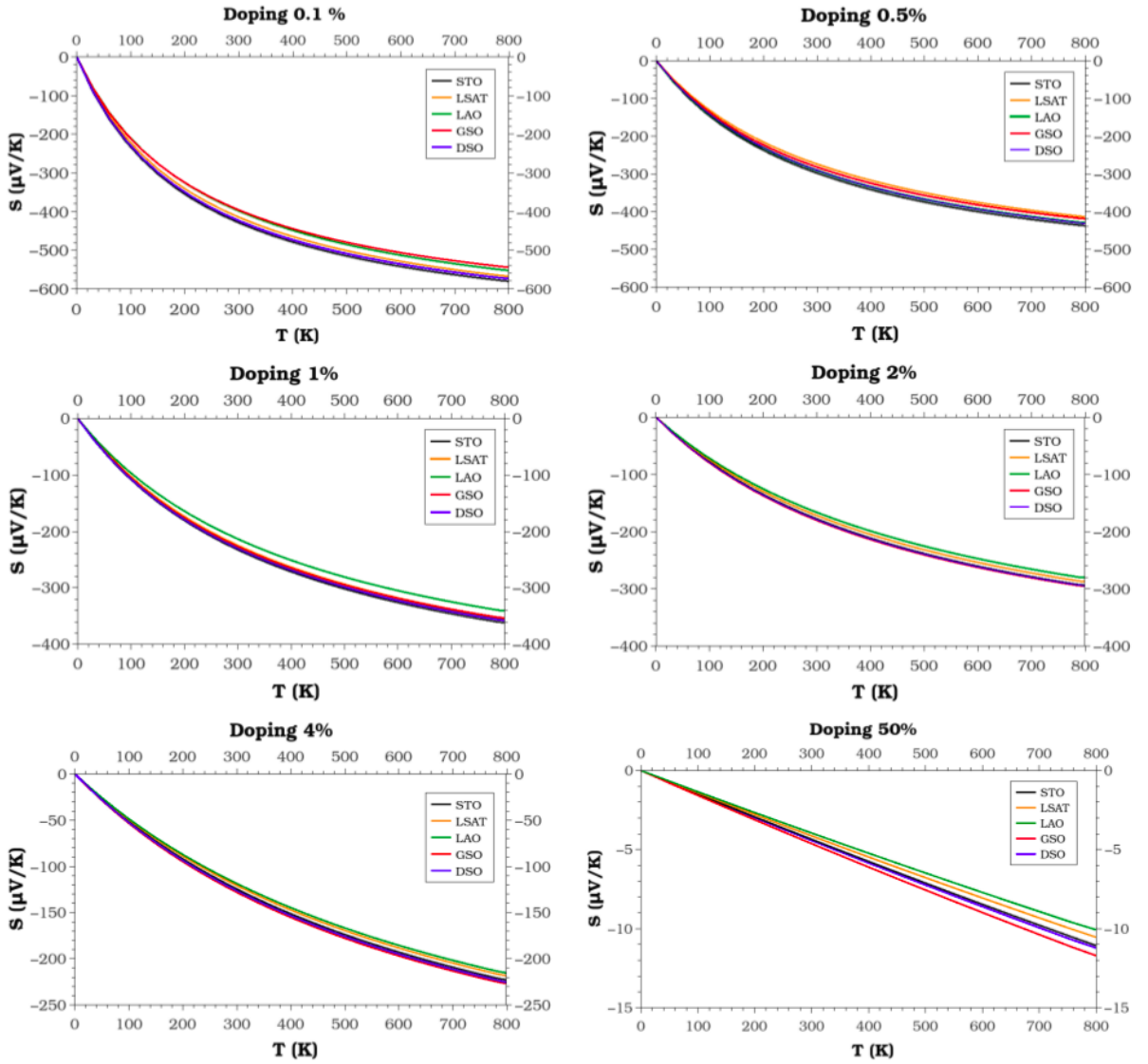


Figure 4.7: Representation of the Seebeck coefficient as a function of temperature using eq. (4.2) for six different doping regimes. The parameters obtained in each case are compiled in Table 4.1. It can be seen that in the low-doping regime (below 2.0%) the entropy-related term dominates the evolution with strain, leading to a reduction in the Seebeck coefficient (in magnitude) caused by any kind of strain. However, for high doping, it is the low temperature (energy-transport term) thermopower the one that dominates the strain tendency because $S_{(T\to\infty)}$ becomes strain independent (see Fig. 4.6). In that case, we see that tensile strain increases the thermopower (in magnitude).

Table 4.1: Model's parameters for the six representative doping values shown in Fig. 4.7. Values for the effective masses m^*/m_0 obtained using eq. (4.9) are also shown.

Doping 0.1%	A (μV)	$S_{(T\to\infty)}$ $(\mu V/K)$	T_0 (K)	m^*/m_0
GSO	163000	-703	232	0.145
DSO	158000	-730	217	0.150
STO	159000	-737	215	0.151
LSAT	166000	-730	228	0.145
LAO	174000	-720	242	0.140

Doping 0.5%	A (μV)	$S_{(T\to\infty)}$ $(\mu V/K)$	T_0 (K)	m^*/m_0
GSO	195000	-592	329	0.353
DSO	199000	-605	323	0.348
STO	190000	-609	312	0.368
LSAT	199000	-607	328	0.354
LAO	210000	-596	352	0.341

Doping 1.0%	A (μV)	$S_{(T\to\infty)}$ $(\mu V/K)$	T_0 (K)	m^*/m_0
GSO	215000	-533	403	0.509
DSO	215000	-537	400	0.513
STO	219000	-545	403	0.506
LSAT	230000	-543	423	0.489
LAO	240000	-534	450	0.473

Doping 2.0%	A (μV)	$S_{(T\to\infty)}$ $(\mu V/K)$	T_0 (K)	m^*/m_0
GSO	241000	-481	501	0.720
DSO	245000	-483	508	0.714
STO	252000	-486	519	0.700
LSAT	265000	-485	546	0.672
LAO	272000	-481	567	0.661

Doping 4.0%	A (μV)	$S_{(T\to\infty)}$ $(\mu V/K)$	T_0 (K)	m^*/m_0
GSO	296000	-425	696	0.932
DSO	303000	-426	711	0.917
STO	311000	-427	729	0.899
LSAT	325000	-427	761	0.870
LAO	330000	-425	775	0.868

Doping 50.0%	A (μV)	$S_{(T\to\infty)}$ $(\mu V/K)$	T_0 (K)	m^*/m_0
GSO	1490000	-154	9690	0.995
DSO	1560000	-154	10100	0.957
STO	1590000	-154	10300	0.949
LSAT	1670000	-154	10900	0.910
LAO	1750000	-154	11400	0.878

In order to analyze these trends in more detail, we have obtained the effective masses and its strain and doping dependence (see Table 4.1). Despite the fact that we show the effective masses calculated in six doping cases, it is hard to analyze its strain dependence away from the high doping limit. At 2% doping, we can observe that the effective mass is larger for the unit cells with a larger volume (volume increases for tensile strain). Increasing the volume leads to a reduction in the hopping parameter, smaller band widths and hence a larger effective mass [106]. Above 2% doping, such dependence with strain of the effective mass is retained. For lower doping values, the dependence with strain is more complex due to the partial involvement of different bands. The effective mass increases monotonously with doping and it reaches values close to 1.0 m_0 at about 50% doping. In

that doping region, a single parabolic band picture makes more sense than at low doping, where the sole concept of a single effective mass where all the bands contribute in a similar fashion is more difficult to identify.

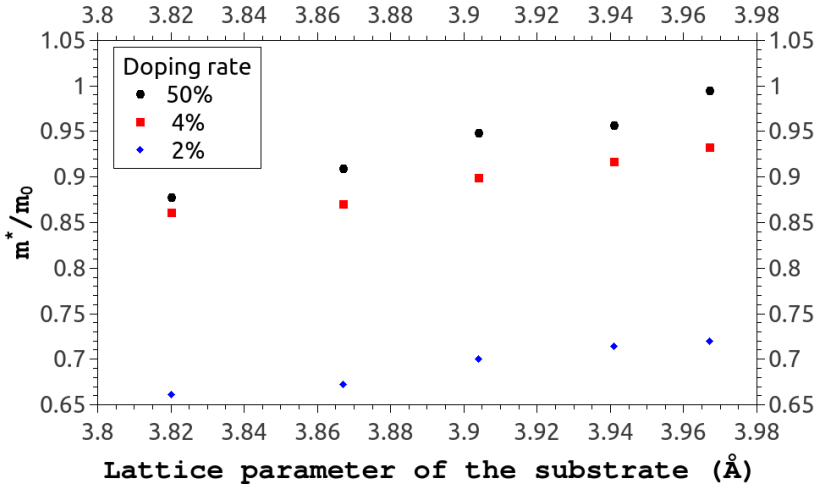


Figure 4.8: Effective mass as a function of strain in the high-doping regime. Effective mass increases (decreases) with tensile (compressive) strain and barely changes once all the bands become populated. The limit of 50% doping, even though beyond the validity of the rigid band approximation is shown as the limiting case found in $LaAlO_3$/STO interfaces.

In Fig. 4.9 we can see a comparison between the thermopower calculated using BoltzTraP (energy-transport term) and the prediction using our model, in which the entropy term is included. This plot reinforces the idea that low doping regimes (0.1%) the degeneracy has a great effect on the thermopower evolution with strain (degeneracy is different for each strain value). However, the trend with strain obtained for high doping regimes (4%) retains that of the energy-transport term (BoltzTraP) and is independent of the entropy term (degeneracy is independent of strain).

In Ref. [98] Janotti et al. analyze the directional effective masses dependency with strain. In order to compare with their data, we can obtain a mean effective mass m^*_{ave} performing a harmonic mean of the directional effective masses $m_{\Gamma-X}$ (parallel) and $m_{\Gamma-\overline{X}}$ (perpendicular to the strain direction) given in this article and we can compare these m^*_{ave} with the effective masses we have obtained for 2% doping. In our calculations LSAT corresponds to biaxial strain -1.0%, STO to 0.0% and DSO to $+1.0\%$. The results are summarized in Table 4.2. Their results, when analyzed this way, agree with ours in the strain dependence of the effective mass. However, the actual values are largely doping dependent, as we have discussed here.

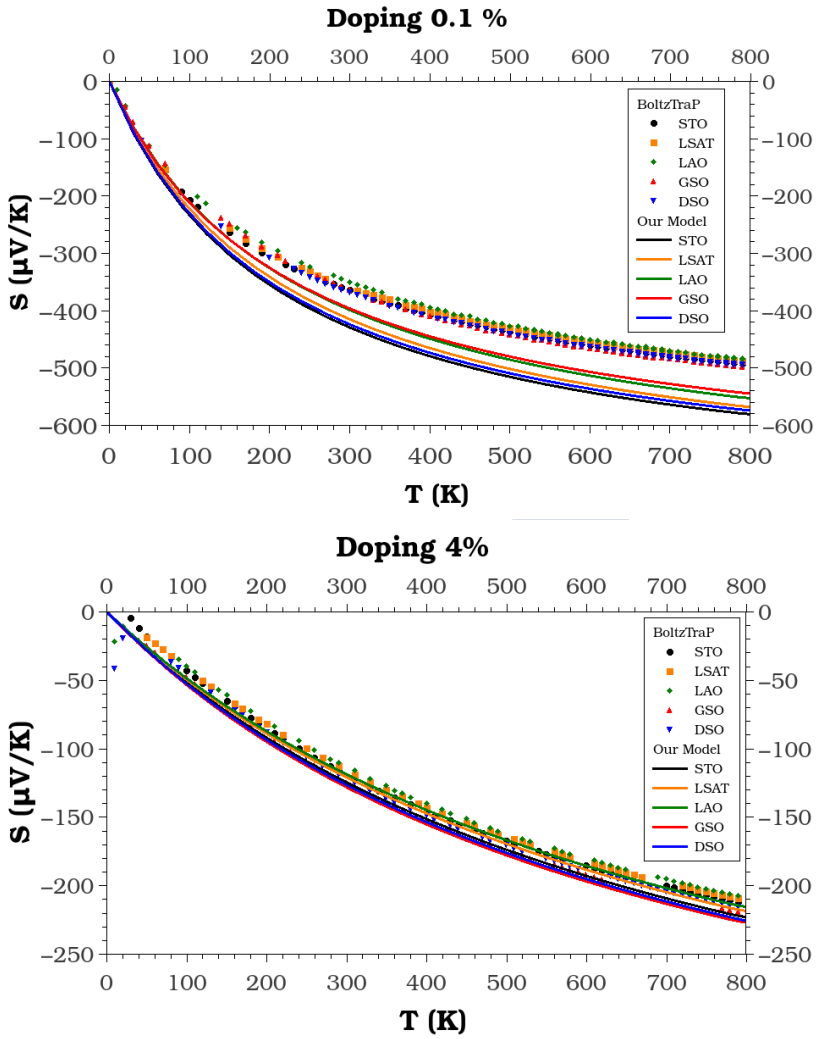


Figure 4.9: BoltzTraP calculations vs our model predictions for different doping regimes. In the high doping regime our model predicts the same tendency with strain than that given by BoltzTraP. However, in the low-doping regime, our model prediction disagrees with that given by the BoltzTraP due to the introduction of the degeneracy term.

The effective masses are slightly larger in our model than the ones provided in Ref. [98]. We are comparing our calculations at 2% doping level with the effective masses calculated from the inverse of the second derivative of the first conduction band in their case. However, the strain tendency is the same for both calculations. In view of the last two columns of Table 4.2 we can conclude that the mean effective mass in bulk STO increases (decreases) with positive (negative) biaxial strain. The same dependence is obtained in Ref. [105] where they found that an increase of the effective mass produces an increase of the thermopower.

Strain	$m_{\Gamma-X}$	$m_{\Gamma-\overline{X}}$	m^*_{ave}	Our m^* (2% doping)
-1.0%	0.67	0.40	0.547	0.672
0.0%	0.55	0.55	0.550	0.700
$+1.0\%$	0.42	2.2	0.575	0.714

Table 4.2: Comparison between the effective masses obtained by A. Janotti et al. [98] and the ones from our model at 2% doping. The masses are given in units of the free electron mass m_0. As we explain in the text, the actual values for the effective masses are largely doping dependent, but the evolution with strain we obtain is retained, and consistent with previous results in the literature.

A similar analysis can be performed to compare with previous literature the Seebeck dependence with strain that we have obtained from our model. In Ref. [107] Daifeng Zou et al. calculate the strain dependence of the thermopower in different directions (parallel and perpendicular to the strain plane). A harmonic mean value of their results provides the same strain dependence that we have obtained from our model, i.e., tensile strain enhances the thermopower.

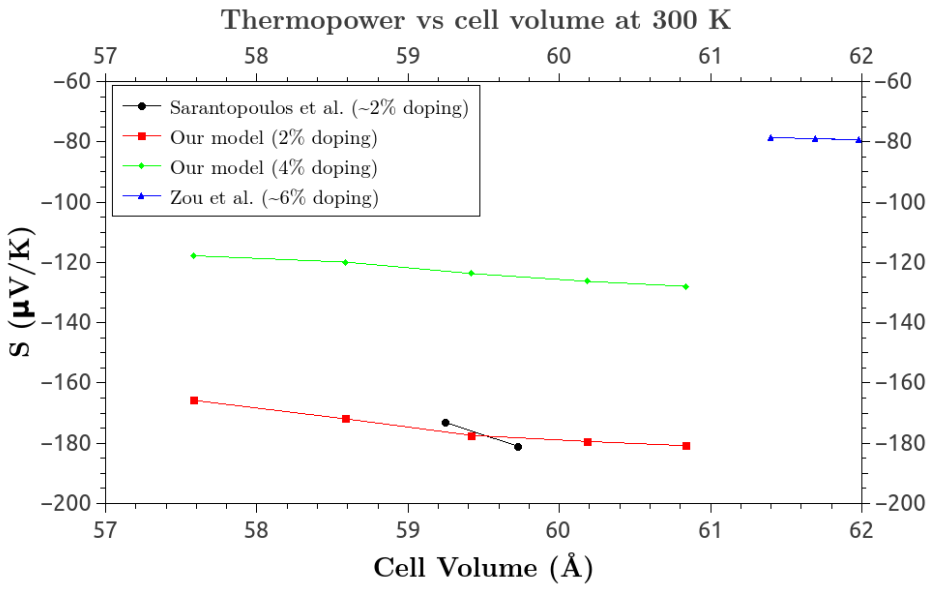


Figure 4.10: Seebeck coefficient dependence with the cell volume at 300 K in the high doping regime. An increase in the cell volume produces an increase in absolute value of the thermopower. We show values predicted by our model and others from the literature (both experimental and theoretical).

Figure 4.10 shows the thermopower dependence with the cell volume. The mean values obtained from Ref. [107] are plotted. They show the same dependence with volume that our model predicts. We have also included experimental data from Ref. [83].

They show a good agreement with our predictions. They confirm that an increase in the cell volume produces an increase in absolute value of the thermopower in the high doping regime, where the degeneracy dependence is quenched. Experimental points from Sarantopoulos et al. [83] have not exactly the same doping value, 2.0% for the greater cell volume and 2.2% for the other. However, they are inside the experimental error, and compare well with the results of our model.

The Seebeck coefficient dependence with strain is crucial when fine-tuning the TE properties of oxides, which often comes about due to nanostructurization, where strain is a key factor. The simple model we have put forward, supported by ab initio calculations, allows to account separately for the different factors that influence the thermopower. In principle, one could naively think that applying strain simply destroys the t_{2g} degeneracy ruining the high temperature Seebeck coefficient, but we can see from our calculations on STO that this effect is small since the usual degrees of strain attained experimentally do not fully break the t_{2g} degeneracy, in particular at substantial doping ($\geq 10^{20}$ cm^{-3}), as is required for TE applications [108]. We can see that band effects such as band alignment modifications, doping levels and effective masses are much more important in affecting the Seebeck. Of course, the doping limit that leads to washing away the orbital degeneracies will be largely dependent on the system.

4.3 Lattice Thermal Conductivity of $SrTiO_3$

As we have stated in the introduction of this chapter, the phonon part of a system can also be tuned to modify its TE and thermal transport properties. In this section, we analyze from a theoretical point of view how different structural distortions affect the thermal conductivity of STO. In the past, several strategies have been proposed to tune the thermal conductivity of STO: nanostructuring [109, 110], application of external electric fields [111], substitution of different kind of cations [82, 112–117], oxygen vacancies [118–120], etc. Yet despite all this, there are interesting fundamental questions one can ask about heat transport in STO: what are the main mechanisms that determine its thermal conductivity? How can we tune them by modifying its structure? In this section we will try to answer them.

We will follow this plan: first, we will identify which are the main features that determine its thermal conductivity. Then, we will see how those get modified when a particular distortion is applied to the structure. We have performed this analysis in both the high temperature cubic phase and the low temperature tetragonal one that occur in STO. The results obtained in this study can serve as a platform for drawing a more general conclusion in complex oxides and their nanostructures, as well as a guidance to interpret experimental results.

4.3.1 Computational Methods

We have performed first principles calculations to compute the lattice thermal conductivity (κ) for STO in its cubic and tetragonal phases by iteratively solving the linearized Boltzmann transport equation of phonons with the ShengBTE package [60]. Converged phonon momenta q meshes of $15 \times 15 \times 15$ were used for solving the transport equation. In order to calculate κ, stable structures (i.e., phonon band structures without imaginary frequencies) are required. Thus, two different methods were used to compute each phase. We have also used two different codes for each method. We have checked that both codes provide compatible results.

For the high temperature $Pm\bar{3}m$ cubic phase which is unstable at 0 K, *ab initio* Molecular Dynamic (aiMD) calculations were performed as implemented in the VASP code [36] in order to stabilize the cubic phase that occurs at high temperature. The simulations were carried out in a $2 \times 2 \times 2$ supercell (which was checked to be big enough to converge the thermal conductivity) in the canonical ensemble at 300 K during 20000 steps of 1 fs following equilibration. The generalized gradient approximation (GGA) in Perdew-Burke-Ernzerhof (PBE) scheme [19] was used for the exchange-correlation term within the projector augmented wave (PAW) method. The choice of the functional was based on previous studies on lattice dynamics of STO [121]. We have also checked that the results that we have obtained with it are in agreement with experiments. The tolerance in the forces was 10^{-4} eV/Å, and the cutoff energy for the planewave basis set was 410 eV. We have used the temperature-dependent effective potential (TDEP) method [51] to extract the effective interatomic force constants (IFCs) that best describe the anharmonic Born-Oppenheimer potential energy surface at a given temperature from the set of supercells with displacements generated in the aiMD.

For the low-temperature $I4/mcm$ tetragonal phase, we have performed first principles Density Functional Theory (DFT) calculations [17, 18] with the PAW method as implemented in the QUANTUM ESPRESSO code [35]. The GGA in the revised PBE scheme [122] was used for the exchange-correlation term. The harmonic IFCs were calculated using density-functional perturbation theory (DFPT) [35, 123]. The third-order anharmonic IFCs were computed using the real-space supercell approach [60] with a $3 \times 3 \times 3$ supercell. The single cell was the 10-atom primitive cell that corresponds to the low-temperature $I4/mcm$ tetragonal phase. All the calculations were performed in a converged k-mesh with a plane-wave energy cutoff of 60 Ry for the kinetic energy and 240 Ry for the charge density. The longitudinal optical-transverse optical (LO-TO) splitting was included using the dielectric constant and Born effective charges calculated from linear response DFPT.

4.3.2 Results and Discussion

Figure 4.11 shows the kind of structures we will be considering in this work, based on the perovskite structure. We will analyze first the high temperature phase. We will identify the main sources that determine the thermal conductivity of STO. Then, we will

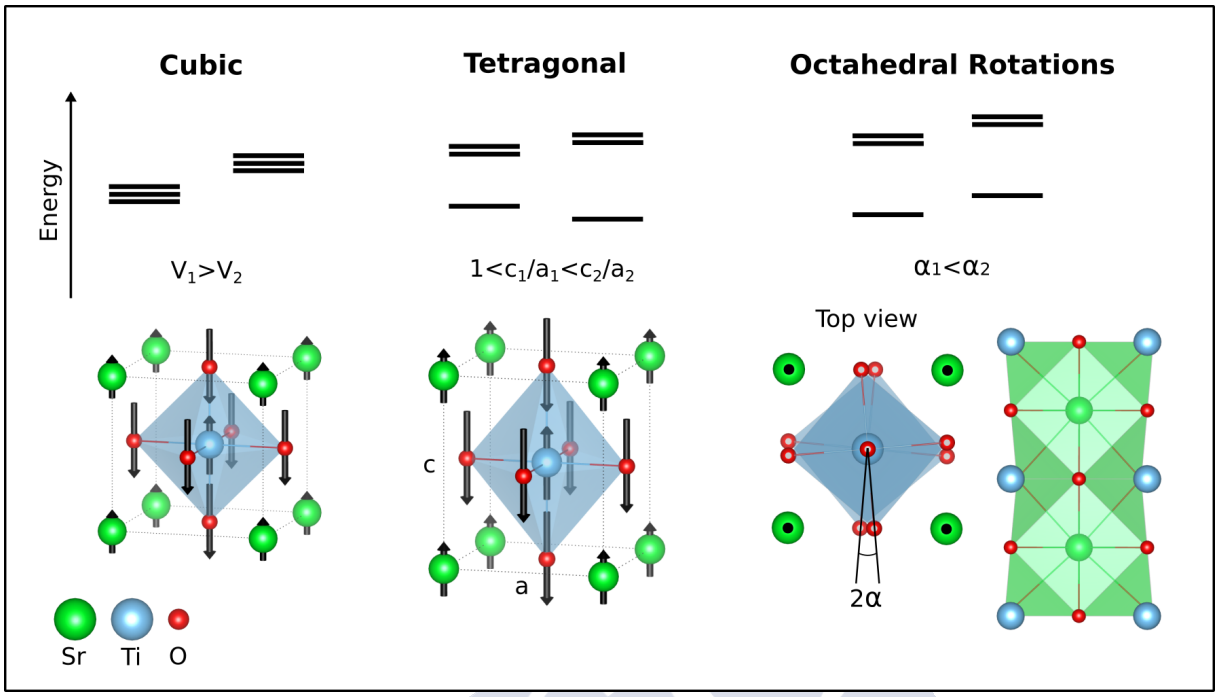


Figure 4.11: Energetic scheme of the polar modes that tune the thermal conductivity. Sr (Ti, O) atoms depicted in green (blue, red). Black arrows illustrate the atomic displacement in the polar mode. For the cubic phase, since the three lattice parameters are equal, the mode is triply degenerate. Decreasing the volume of the unit cell increases the frequency of the mode and hence the thermal conductivity is enhanced. The tetragonal distortion breaks the triple degeneracy. For $c/a > 1$, the polar mode along the z-axis lowers its frequency due to the bond length increase between the Ti atom and the apical O atoms of the octahedra. Increasing the c/a ratio increases the gap between xy and z-axis modes, thus reducing the thermal conductivity. The octahedral rotations keep the volume of the octahedra constant. However, the Sr-O bond length is reduced. This causes an increase in the frequency of the mode producing an increase in the thermal conductivity.

proceed to analyze the low temperature phase and how different distortions modify the thermal conductivity.

The high temperature $Pm\bar{3}m$ phase

First, we start analyzing the lattice thermal conductivity in the cubic phase. This phase is the stable one at high temperatures. We have imposed the experimental lattice parameter of cubic STO, $a_0 = 3.905$ Å[83]. The calculation of the phonon band structure of this phase from DFPT produces imaginary frequencies at the R point of the Brillouin zone as may be expected. These unstable modes are related to the octahedral rotations that appear at low temperatures [124]. Figure 4.12 shows the phonon dispersion for cubic

STO computed using aiMD. As we have already mentioned, this method allows to stabilize the high temperature phase, permitting us to compute the thermal conductivity in the cubic phase. Its calculated value is 13.4 W/mK which is in reasonable agreement with the one reported by experiments (11 (W/mK) at 300 K in Ref. [II]). The small overestimation in our calculation may perhaps be due to the lack of impurities and boundary scattering in our calculations as opposed to the experimental case.

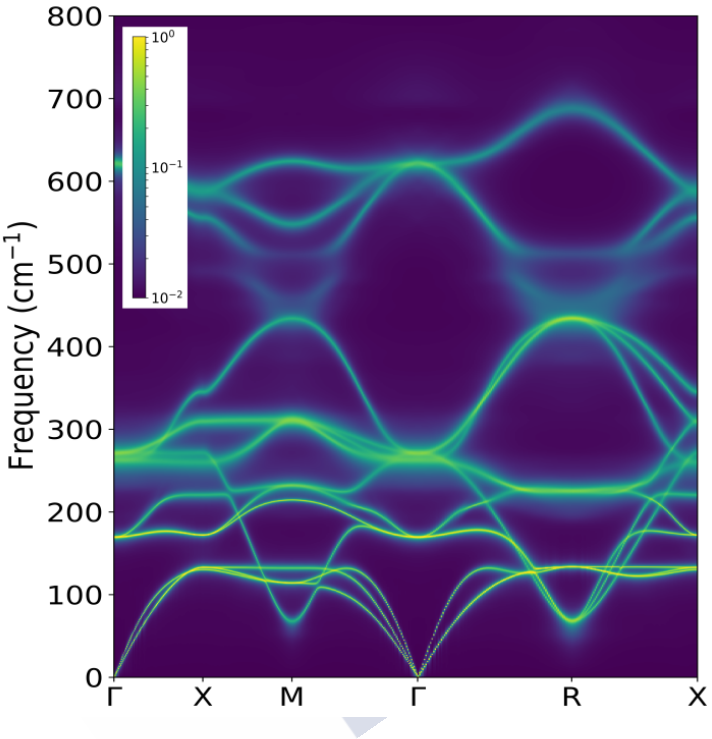


Figure 4.12: Phonon lineshape in the $Pm\bar{3}m$ phase at 300 K. The intensity of the bands represents the likelihood of exciting a particular phonon. The high peaks of the intensity are found at the acoustic bands and at the polar modes around 200 cm^{-1}.

In order to identify the modes that contribute most to the thermal transport, we have computed and plotted in Fig. 4.12 the phonon band structure with the so-called lineshape (eq. (1.64)). As we have introduced in Chapter 1, the lineshape corresponds to the one-phonon neutron scattering cross section that can be measured in inelastic neutron scattering experiments. The frequency axis is the probing energy and the intensity represents the likelihood of exciting a phonon at a given energy and momentum. The lineshape is related to the imaginary part of the phonon self-energy, which can be computed via the third order force constants [125–127]. The most intense and sharp peaks in the lineshape provide the most active phonon modes in the sense of the longest lifetimes. Therefore, they will be the ones that contribute most to the thermal transport. In the case of STO, we can see in Fig. 4.12, that they correspond to the acoustic bands and to the triply degenerate polar mode depicted in Fig. 4.11 (the modes below 250 cm^{-1}). The order

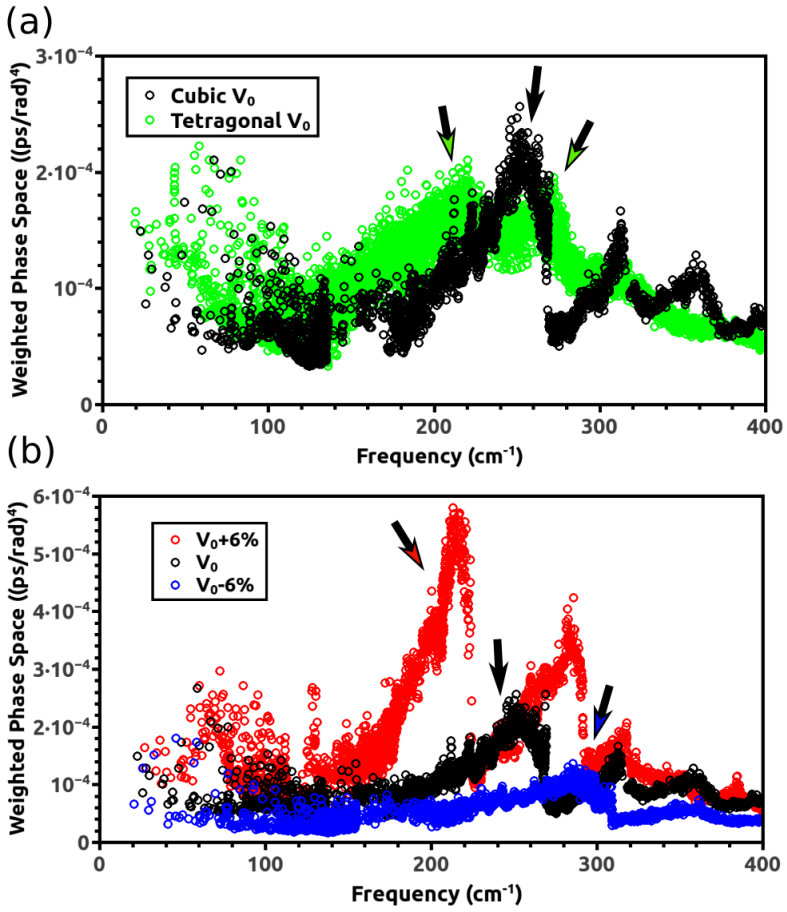


Figure 4.13: Weighted phase space for the high temperature phase at 300 K as a function of frequency. An increase in the weighted phase space is related to an increase in the anharmonic scattering rate, thus decreasing the thermal conductivity. The arrows indicate the peaks associated to the polar modes that tune the thermal conductivity. (a) Comparison between cubic (black) and tetragonal (green) structures. (b) Evolution with the unit cell volume.

of magnitude of the STO thermal conductivity is given by the dispersion of the acoustic bands, since these modes are the main heat carriers, but also tuned by the polar modes. The mean group velocity associated to the acoustic modes at 300 K that we have obtained is 5.24 km/s, which is in good agreement with previous experiments [II].

In Fig. 4.13 we have plotted the weighted phase space, as defined in [128]; it will help us to identify the main sources of scattering that tune the thermal conductivity of STO. The weighted phase space provides the scattering rate as a function of frequency weighted by the harmonic frequencies. Therefore, it is very sensitive to the phonon spectra and hence can be used to identify the modes responsible for the stronger scattering processes.

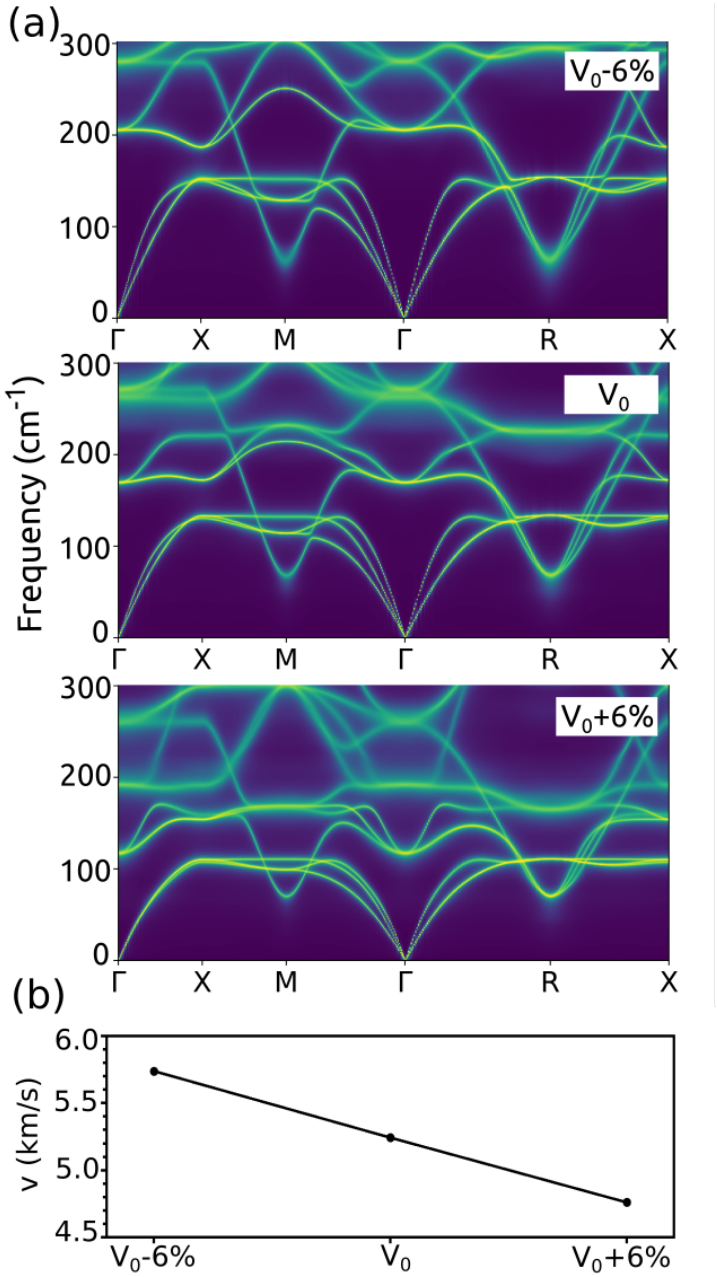


Figure 4.14: (a)Phonon lineshape for three different volumes in the $Pm\bar{3}m$ phase at 300 K. From top panel to bottom we present an increase in the volume of the unit cell, V_0 being the experimental unit cell volume. At the Γ point and between $100 - 200$ cm^{-1}, we identify the triply degenerate polar mode. Increasing the volume decreases the frequency of the polar mode. The band dispersion of the acoustic modes increases when reducing the volume. (b) Phonon mean group velocity of the acoustic bands as a function of the unit cell volume.

It also helps to analyze how the scattering rate is modified when different distortions, that change the phonon spectra, are applied to the structure. In the case of cubic STO at 300 K, we can see in Fig. 4.13a (black dots) that the weighted phase space has a peak around 250 cm^{-1}. At this frequency, this peak is associated to the scattering processes of the polar modes. So, we can conclude that the polar modes shown in Fig. 4.11 are the main source of scattering in STO. This triply degenerate polar mode was previously identified, using other methods, as one of the main sources of phonon-phonon scattering [111, 121]. Apart from that, in a recent work, this mode was also reported to be electron-phonon active [129].

The subsequent discussions will be based on how the acoustic and polar modes evolve under different distortions. In particular shifting the polar modes to lower frequency may be expected to scatter more strongly acoustic phonons lowering the thermal conductivity.

Figure 4.14a shows the lineshape for three different unit cell volumes at 300 K for a cubic structure. We can observe that a decrease in the volume of the unit cell increases the dispersion of the acoustic bands. This is translated into an increase of the mean group velocity of the acoustic bands (Fig. 4.14b). A reduction of the unit cell volume also increases the frequency of the triply degenerate polar mode due to the reduction of the Ti-O bond length. This increase in the frequency (depicted in Fig. 4.11) reduces the phonon scattering, as can be seen in Fig. 4.13b, where a clear reduction of the phase space peak occurs by reducing the unit cell volume. Hence, both effects on the acoustic and polar modes produce an increase in the thermal conductivity. The calculated values are: 7.6, 13.4 and 18.0 W/mK for the largest unit cell volume to the smallest one, respectively. This increase of the thermal conductivity when the volume of the unit cell is reduced is in agreement with previous experiments on other family of oxides that report an increase of κ when pressure is applied [130].

Figure 4.15 shows the lineshape computed at 300 K when a tetragonal distortion is applied. This distortion keeps the volume of the unit cell constant and equal to the experimental one, while the c/a ratio was kept fixed at 1.06. We can see that the triple degeneracy of the polar mode is broken as explained in Fig. 4.11. Since the c lattice parameter becomes larger it will increase the bond length of the Ti with the apical O atoms of the octahedra, reducing the frequency of the mode along the z-axis as shown in Fig. 4.15. Moreover, due to the increase of the c lattice parameter and the decrease of a, the acoustic modes change their dispersion as compared to the cubic case. The calculated lattice thermal conductivity is $\kappa_{xx} = \kappa_{yy} = 10.4$, $\kappa_{zz} = 8.0$ W/mK. We see that the tetragonal distortion breaks the triple degeneracy of the κ-tensor and reduces the thermal conductivity at 300 K. The degeneracy break of the polar mode is the main responsible for decreasing the thermal conductivity. In Fig. 4.13a we can see how the peak associated to the polar modes is divided in two peaks (green dots) when a tetragonal distortion is applied. The difference that we observe between cubic and tetragonal thermal conductivity would be diminished taking into account the volume reduction that occurs in the cubic to tetragonal phase transition, which produces an increase on the thermal conductivity. Furthermore, we will see in the next subsection that including the octahedral rotations in

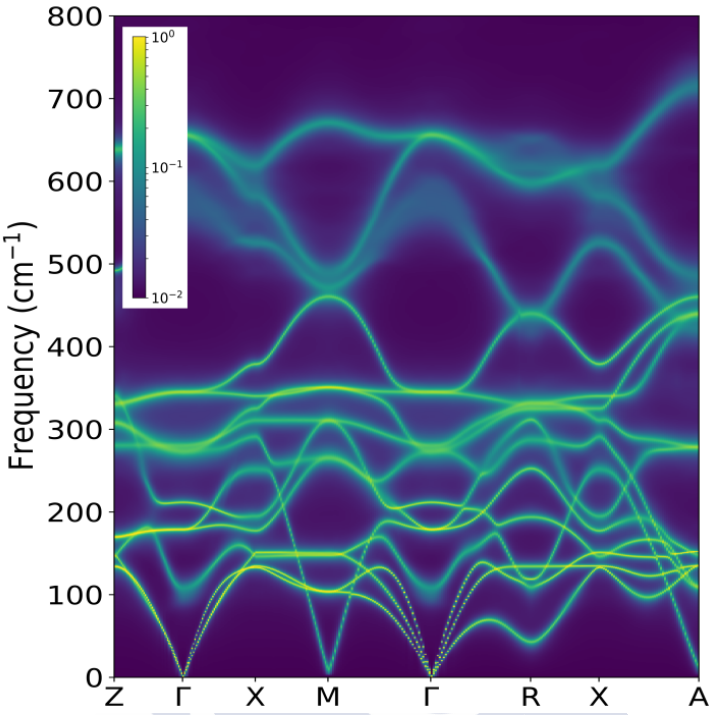


Figure 4.15: Phonon lineshape for a tetragonal distortion of the cubic phase at 300 K ($c/a = 1.06$). The triple degeneracy of the polar mode is broken due to this distortion as explained in Fig. 4.11. There is a softening of the polar mode along the z-axis.

the tetragonal phase will increase the thermal conductivity. Thus, the difference obtained between both phases would be reduced by including these effects.

The low temperature $I4/mcm$ phase

Below 105 K, STO undergoes a phase transition from the cubic $Pm\overline{3}m$ space group to the tetragonal $I4/mcm$ [75]. This tetragonal phase is characterized by the stretching of the unit cell and also by a TiO_6 octahedra antiphase rotation along the c axis [131]. The structure of this phase is depicted in Fig. 4.11. We have optimized the lattice parameters and the atomic positions. We have then applied different structural distortions and study how they affect the phonon dispersion and also the thermal conductivity. We will see that, as obtained for the high temperature cubic phase, the polar modes play a fundamental role in the heat transport. The optimized structure that we have obtained has $a_0 = 3.868$ Å, $c_0 = 3.935$ Å, lattice parameters and $\alpha_0 = 6.6°$ octahedral rotation angle in agreement with previous calculations [124]. Both c_0/a_0 ratio and α_0 are overestimated by GGA compared to experimental values [132]. Since the optimized structure is a stable structure at 0 K, we can perform the study using DFT calculations. Small distortions to this structure can be applied without introducing imaginary frequencies in the phonon spectrum that would invalidate our analysis. In this subsection we will study the effect on

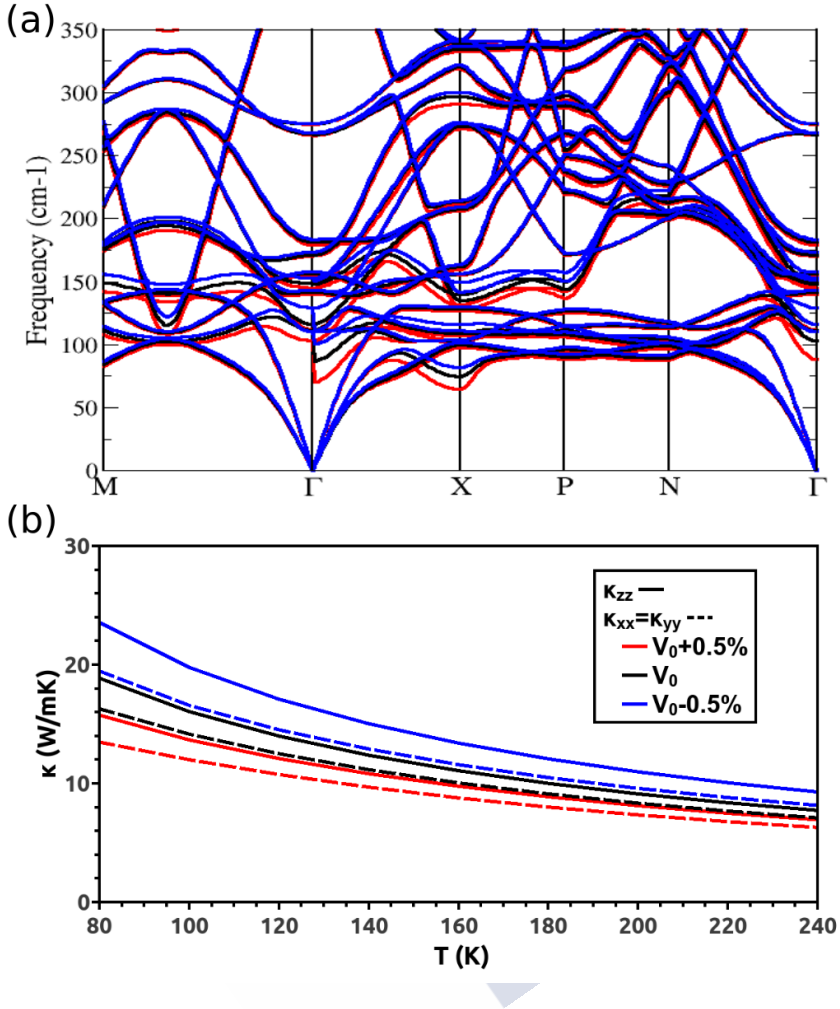


Figure 4.16: Results for the variation of the unit cell volume in the $I4/mcm$ phase. Octahedral rotation angle and c/a ratio are kept constant. (a) Phonon band structure for three different volumes, in red the largest and in blue the smallest, V_0 is the optimized unit cell volume. An increase in the volume reduces the frequency of the polar modes and the phonon dispersion of the acoustic modes increases. (b) Thermal conductivity as a function of temperature. An increase in the volume reduces the thermal conductivity.

the spectrum and the thermal conductivity of unit cell volume, c/a ratio and octahedral rotation angle. We will keep two of these parameters constant while varying the third one to try to decouple their effects. Note that we will plot the thermal conductivity of this low temperature phase for temperatures above 105 K, the temperature of the structural phase transition. We do this to better visualize the variations in κ with each distortion. Moreover, below 80 K the thermal conductivity is not plotted since it is dominated by the sample dependent boundary scattering. Therefore, the realistic temperature range for the computed κ is between 80 and 105 K.

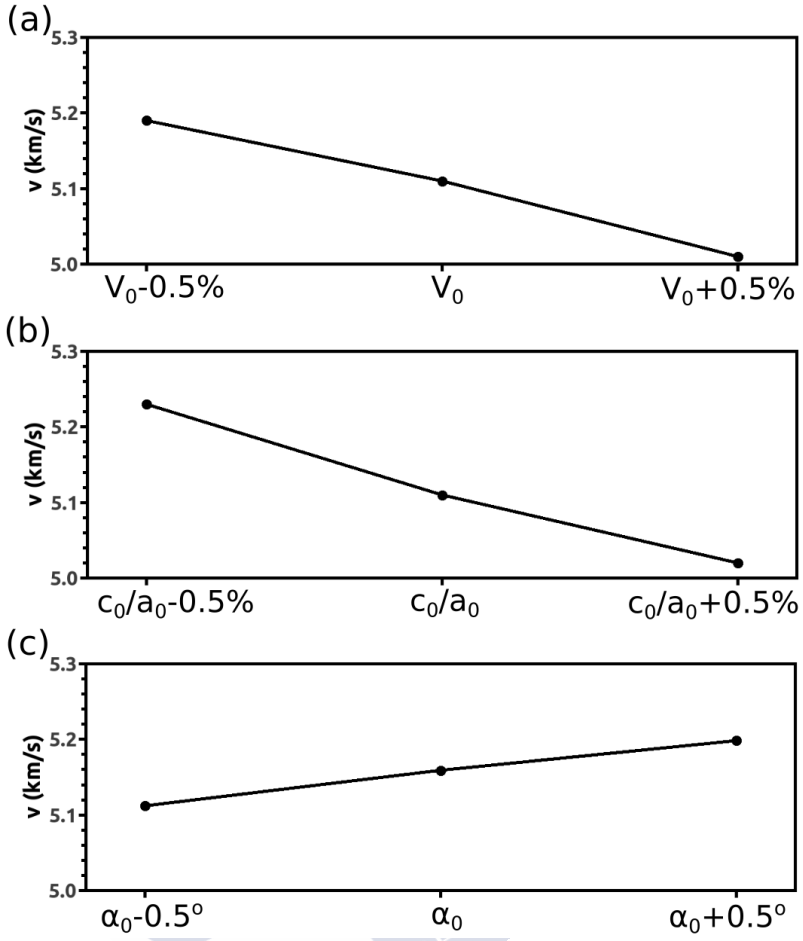


Figure 4.17: Mean group velocity of the acoustic modes for the low temperature phase. Its increase produces an increase of the thermal conductivity. (a) Evolution with the unit cell volume, (b) c/a ratio and (c) octahedral rotation angle.

Figure 4.16a shows the phonon dispersion for three different volumes of the unit cell. We can see that a reduction of the volume increases the dispersion of the acoustic bands, thus increasing the group velocity of the compound (Fig. 4.17a). We can also see that the polar modes increase their frequency when the volume is reduced. This causes a reduction of the phonon-phonon interaction. Figure 4.18a shows how the peak of the weighted phase space associated to the polar modes decreases when the volume is reduced. These two consequences in the phonon spectrum act in a positive way increasing the thermal conductivity when reducing the volume (see Fig. 4.16b). This trend is in agreement with the result obtained for the high temperature cubic phase. The thermal conductivity at 100 K for the optimized structure is $\kappa_{zz} = 16.1\ W/mK$ and $\kappa_{xx} = \kappa_{yy} = 14.2\ W/mK$. Considering that V_0 is overestimated by GGA, these are in pretty good agreement with the experimental value [II] from the List of Publications and also with previous calculations

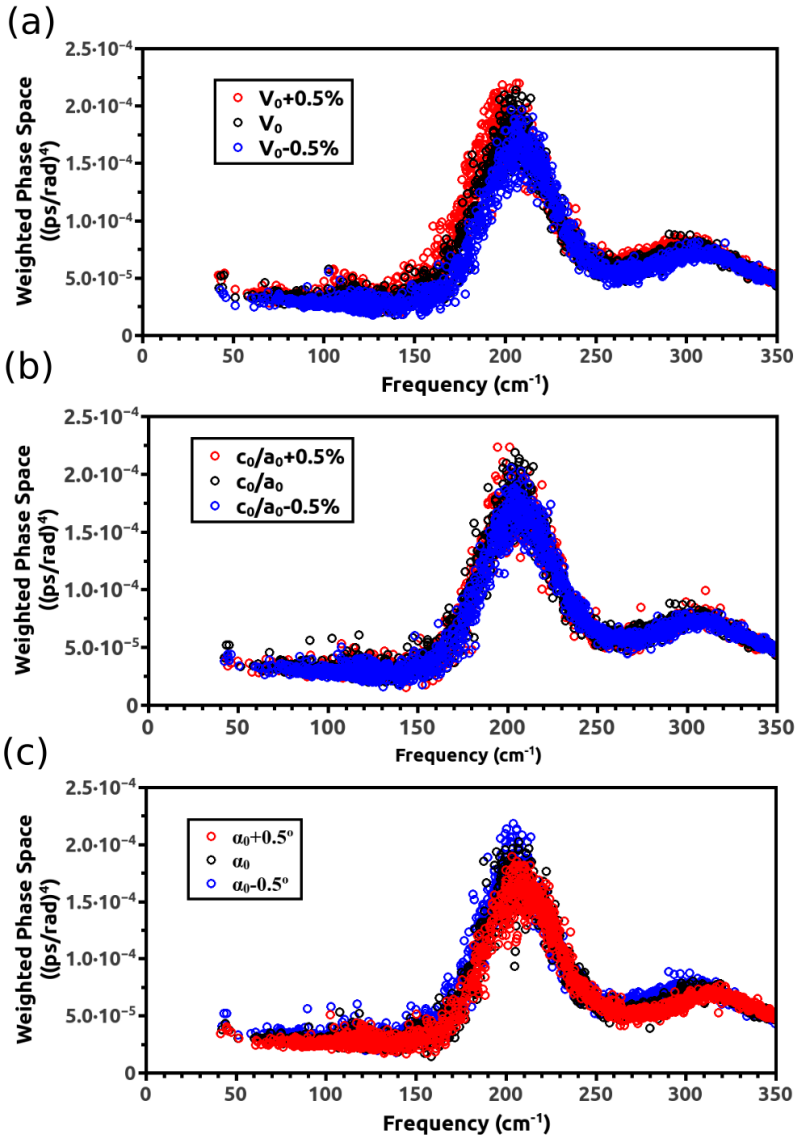


Figure 4.18: Weighted phase space for the low temperature phase at 80 K as a function of frequency. The high peak around 200 cm^{-1} is associated to the polar modes. Its increase produces an increase of the anharmonic scattering rate and hence a reduction of the thermal conductivity (a) evolution with the unit cell volume, (b) c/a ratio and (c) octahedral rotation angle.

[111]. We see that a decrease in 1% in the unit cell volume produces an increase of around 30% on the thermal conductivity.

Figure 4.19a shows the phonon dispersion for three different c/a ratios. We can see that a reduction of the c/a ratio increases the dispersion of the acoustic bands, thus increasing the group velocity of the compound (Fig. 4.17b). We can also see that the

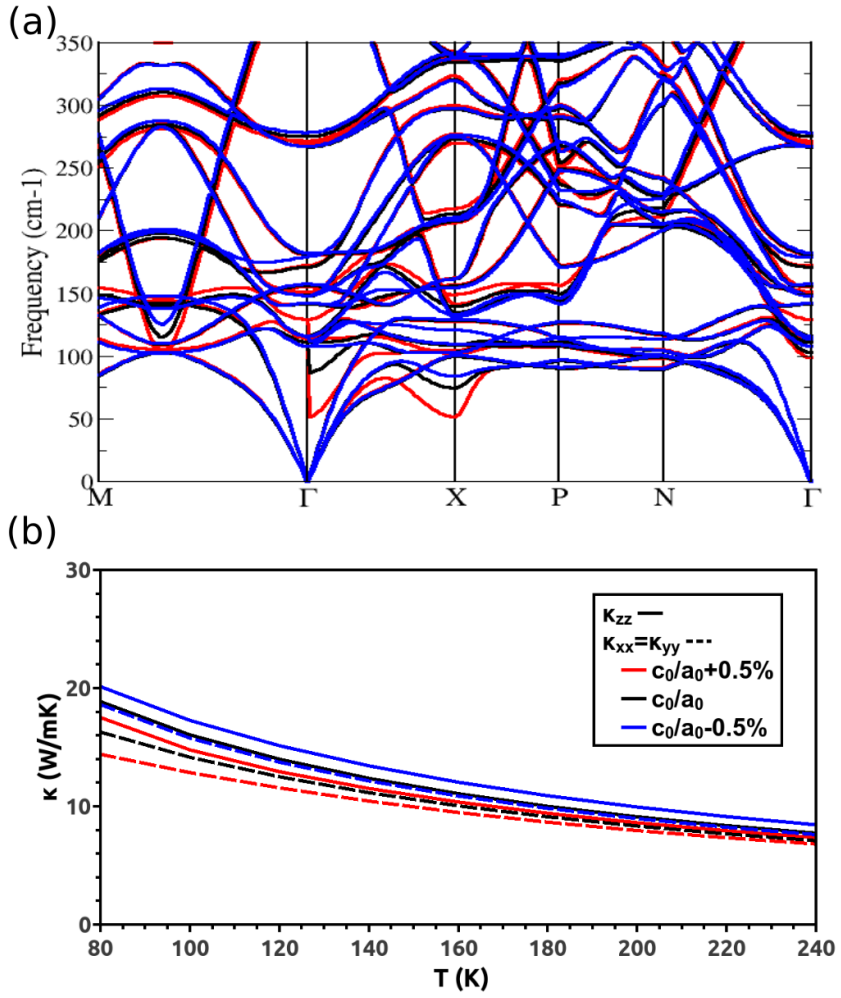


Figure 4.19: Results for variation of the c/a ratio in the $I4/mcm$ phase. Unit cell volume and octahedral rotation angle are kept constant. (a) Phonon band structure for three different c/a ratios, in red the largest and in blue the smallest, c_0/a_0 is the optimized c/a ratio. The acoustic bands undergo a softening, mostly at the X point, when the c/a ratio is increased. At the Γ point, we see that an increase of the c/a ratio increases the gap between the xy and z-axis polar modes. (b) Thermal conductivity as a function of temperature. Increasing the c/a ratio lowers the thermal conductivity.

z-axis polar mode softens when the c/a ratio is increased. Moreover, the energy gap between this polar mode and the other doubly degenerate polar mode increases with c/a (see Fig. 4.11). Figure 4.19b shows the increase of the thermal conductivity when c/a is reduced. We observe that a decrease of 1% in the c/a ratio produces an increase of around 14% on the thermal conductivity. The effect of the c/a ratio on the thermal conductivity is relatively smaller compared to the effect of the unit cell volume. The reason for this is that one polar mode softens and the doubly degenerate ones raise their frequency in the

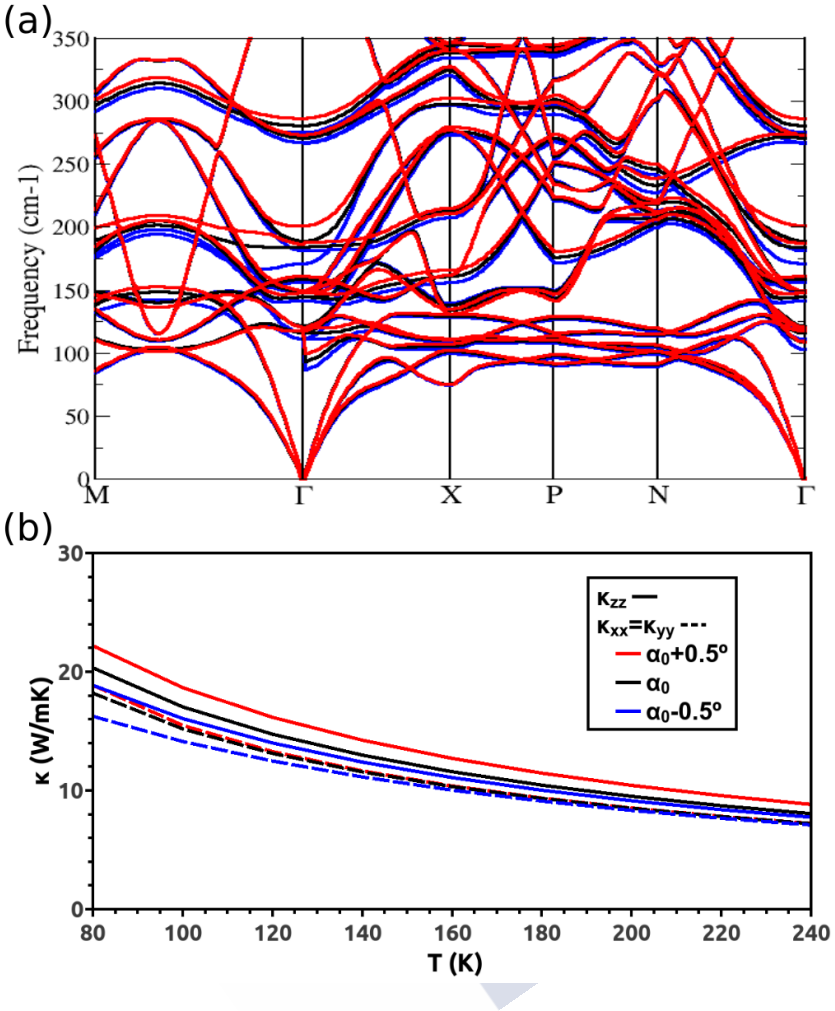


Figure 4.20: Results for the variation of the octahedral rotation angle in the $I4/mcm$ phase. Unit cell volume and c/a ratio are kept constant. (a) Phonon band structure for three different angles, in red the largest and in blue the smallest, α_0 is the optimized rotation angle. An increase in the angle increases the frequency of the polar modes. (b) Thermal conductivity as a function of temperature. Increasing the angle raises the thermal conductivity.

case of the c/a distortion, while the three polar modes soften when modifying the volume (see Fig. 4.11), increasing the phonon-phonon scattering and having a larger effect on κ.

Figure 4.20a shows the phonon dispersion for three different octahedral rotation angles α. We can see that increasing α has not a big effect on the dispersion of the acoustic bands, compared to the aforementioned volume distortions or varying the c/a ratio. Mean group velocities of the acoustic modes increase with the angle, but barely compared to the other distortions. We can also see that the z-axis polar mode softens when α is reduced (see Fig. 4.11). Figure 4.20b shows the increase of the thermal conductivity when α is

increased. This can be understood in terms of the evolution of the weighted phase space with the octahedral angle. Its increase causes a reduction of the peak. We observe that an increase of 1° in α produces an increase of around 14% on κ_{zz} while only 3% on $\kappa_{xx} = \kappa_{yy}$. The effect of varying α on the thermal conductivity is lower compared to the effect of the two other distortions we have considered and analyzed. The main reason for this is that the acoustic bands are barely modified by α, since there is no change in the lattice parameters.

The competition between the antiferrodistortive (octahedral rotations) and ferroelectric phases was already studied in literature, by suppressing the rotations one can in principle achieve a ferroelectric phase [133–135]. This could be achieved via strain engineering since different octahedral rotation patterns and angles can be obtained [136]. We have shown here the coupling between the octahedral rotations and the polar mode responsible for ferrolectricity and also the effect that this has on the thermal conductivity of STO.

4.4 Conclusions

In this chapter we have described two independent works on transport properties of $SrTiO_3$. They are presented together due to the applicability of STO as a thermoelectric material.

In the first work we have analyzed the thermopower of STO and its strain dependence for different n-doping levels, being able to decouple the different origins of these dependencies: those coming from electronic degeneracies and entropy-related terms from those coming from the actual modifications of the band structure. We have proposed a simplified model for the Seebeck coefficient and applied it to analyze the thermopower strain dependency of STO. We have obtained that in the low-doping regime the electron degeneracy dominates the Seebeck so any kind of strain decreases the thermopower, while at high doping the cell volume effect dominates, i.e., increasing volume (tensile strain) leads to an increase in the Seebeck.

In the second work we have analyzed the thermal conductivity of STO. We have studied the main sources of thermal transport and how these are modified when a distortion is introduced in the structure. We have analyzed both the high temperature cubic phase and the low temperature tetragonal one. We have identified the acoustic bands and the low-energy triply degenerate polar mode as the main heat carriers. Reduction of the unit cell volume or the c/a ratio (i.e., approaching a cubic structure) are found to increase the lattice thermal conductivity. The octahedral rotation angle was found to be strongly coupled to the phonon-active polar modes. We report that an increase of this angle raises the thermal conductivity.

Considering together both works, we can figure out some conclusions about the thermoelectric response of this material. We have seen that in order to optimize this response we need to increase the thermopower and reduce the lattice thermal conductivity as much

as possible. These two requirements can be satisfied by increasing the volume of the unit cell via nanostructural engineering. Moreover, the insertion of octahedral rotations in the system is expected to affect the thermoelectric response in a detrimental way.

The studies that we have performed in this chapter for STO could be extended and used to understand the thermopower and the thermal conductivity of similar perovskite-based oxides. They provide a guide to design new experiments and nanostructures based on a wide variety of oxides.

USC UNIVERSIDADE DE SANTIAGO DE COMPOSTELA

5 Ferromagnetic and Insulating Behavior of $LaCoO_3$

In this chapter we show that the oxygen vacancies observed experimentally in thin films of $LaCoO_3$ subject to tensile strain when grown on top of $SrTiO_3$ are thermodynamically stable. By using DFT calculations, we show that oxygen vacancies on the order of 6% forming chains perpendicular to the (001) direction are more stable than the stoichiometric solution. This leads to magnetic Co^{2+} ions surrounding the vacancies that couple ferromagnetically. The remaining Co^{3+} cations in an octahedral environment are non magnetic. The gap leading to a ferromagnetic insulating phase occurs naturally and we provide a simple ionic picture to explain the resulting electronic structure. The work presented in this chapter can be found in Ref. [IV] from the List of Publications.

5.1 Introduction

In this chapter we continue with the study of oxides, entering now into the field of magnets. In the previous chapter, when analyzing $SrTiO_3$, we mentioned that this compound is widely used to form nanostructures in combination with other oxides. We will see here that when $LaCoO_3$ is grown on top of it as a thin film, a ferromagnetic insulating phase arises in the cobaltate.

Ferromagnetic insulators (FMI) and in particular ferromagnetic oxides are uncommon materials. The usual situation is that a ferromagnetic coupling occurs together with metallic behavior. In the case of oxides, the most common situation for insulators is that they order antiferromagnetically. However, several examples of ferromagnetic insulating oxides do exist, such as spinels [137, 138], perovskite-based $La_{1-x}Sr_xMnO_3$ [139], La_2CoMnO_6 [140], etc, which are of extreme importance in the fabrication of spintronic devices [141–144]. Due to their technological relevance and rarity, it is interesting to explore and clarify the properties of one of such systems. This could help in designing other oxides with similar improved properties.

$LaCoO_3$ (LCO) is a very intriguing insulator with a not-completely understood spin-

state transition [145–150], and also an interesting excitonic behavior [151]. In its bulk form it presents a diamagnetic response at low temperatures, all the Co^{3+} cations being in a non-magnetic low-spin state, with all its 6 electrons occupying the lower-lying t_{2g} levels. As temperature rises, a crossover to other spin states occurs leading to an increase in the magnetic susceptibility [152]. However, when LCO is grown as a thin film on a substrate that induces epitaxial strain on it, a ferromagnetic phase appears at low temperatures. In case the substrate is $SrTiO_3$ (STO), it is characterized by a saturation magnetization close to 0.8 μ_B/Co and a T_c of about 80 K [153–157]. Early explanations discussed this magnetic ordering as arising in a stoichiometric strained form of LCO from a spin-state ordering formed by a Co^{3+} HS-LS alternating pattern [153–155, 158, 159]. However, more recent experiments have shown that epitaxial strain induces the formation of oxygen vacancy planes. The off-stoichiometry changes the electron count and leads to magnetic moments on some Co atoms that eventually couple ferromagnetically [156, 160–162].

In Ref. [160] a combination of atomically resolved Z-contrast imaging and electron-energy-loss spectroscopy is used to prove that, when LCO is grown on STO (001), oxygen vacancy planes are formed perpendicular to the substrate with a repetition of one vacancy plane every three unit cells. This pattern has also been interpreted as coming from a kind of spin-state ordering providing the contrast [163].

Taking those images as a basis for our calculations, here we present a DFT study on the possible oxygen-vacancy configurations consistent with the Z-contrast imaging pictures published by various groups in different samples, grown by physical methods such as pulsed laser deposition [156, 160] or by chemical methods such as polymer assisted deposition [157] that could account for the ferromagnetic insulating behavior found experimentally.

Our total energy calculations in the various possible configurations allow to understand the amount of vacancies that are stable, what environments for the neighboring cations these produce, how the local moments couple and the resulting electronic structure. Thus, our work helps clarifying the origin of the insulating behavior found in these thin films.

5.2 Computational Methods

Ab initio electronic structure calculations based on Density Functional Theory (DFT) [17, 18] have been performed using an all-electron full potential code (WIEN2K [30]) on LCO. The exchange-correlation term is parametrized depending on the case:

We have used the generalized gradient approximation (GGA) in the Perdew-Burke-Ernzerhof [19] scheme for structural optimizations and to compute the energetics of the different configurations of LCO. These calculations were performed with a converged k-mesh and a value of $R_{mt}K_{max}$= 5.0. The R_{mt} values used were in a.u.: 1.80 for La, 1.40 for Co and 1.11 for O when studying LCO energetics. The need to compare energetics

considering the O_2 molecule explains the choice of such small R_{mt} values. In order to compute the energy of the O_2 molecule, an fcc lattice was used with the molecule at the center and a large enough unit cell so the bond-length is converged and it gives a value of 1.20 Å, which compares reasonably well with the experimental O-O bond length of 1.21 Å[164].

Correlation effects in the Co d manifold were included with the LDA+U method ($U = 7$ eV, $J = 0.7$ eV) in order to find a good description of the magnetic moments of the Co cations, their couplings and the overall electronic structure [20]. A mapping of U between 4 eV and 8 eV was carried out to determine the energy term E_e in eq. (5.1). A converged k-mesh and a value of $R_{mt}K_{max}$= 6.0 were used. The R_{mt} values used in that case were in a.u.: 2.33 for La, 1.83 for Co and 1.62 for O. The atomic magnetic moment values quoted below correspond to this kind of calculation.

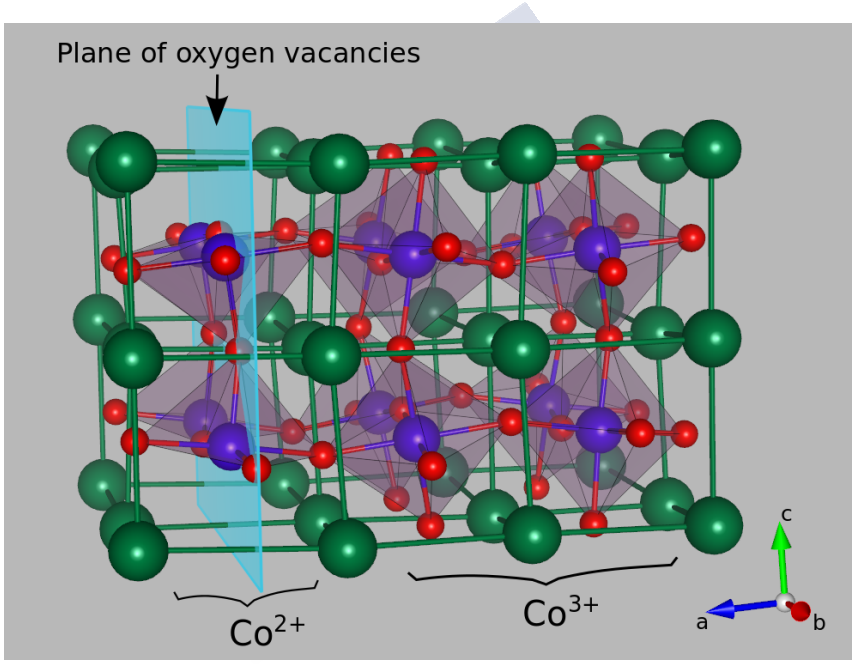


Figure 5.1: Unit cell representation of $La_{12}Co_{12}O_{36-n}$ used in the calculations. La in green, Co in purple and O in red. The blue plane corresponds to the plane in which the oxygen vacancies are imposed. Notice that this plane is parallel to the *bc* plane and perpendicular to the interfacial plane *ab*. In the ground state configuration, Co^{2+} cations occur in the plane of O-vacancies while the other Co atoms are Co^{3+}.

5.3 Results and Discussion

We have divided the study in two main parts: structural characterization and electronic structure and magnetic properties of tetragonally strained LCO. First, we need

to understand how many oxygen vacancies appear and how they are distributed. Once the structural ground state is found, we proceed to describe the electronic structure and magnetic properties that result from that ground state configuration.

5.3.1 Structural Characterization

In this section, we have characterized the structural properties of LCO when it has tetragonal symmetry and the in-plane lattice parameters are those of STO, thus mimicking the epitaxial strain effect introduced in an LCO film when grown on an STO substrate. We have performed a systematic study that allows to determine the optimal oxygen vacancy concentration as well as their distribution in the plane of vacancies. The unit cell that we have considered is shown in Fig. 5.1. Its stoichiometry is $La_{12}Co_{12}O_{36-n}$ where n is the number of oxygen vacancies. We have fixed the lattice parameters a and b to reproduce the in-plane strain due to STO (3.905 Å) [83]. Parameter c was left free for optimization. As Fig. 5.1 shows, the c direction is the (001) growth direction in the standard experiments with thin LCO films on a cubic perovskite substrate. We have allowed all the possible octahedral rotations that occur in bulk LCO and fully relaxed all the atomic coordinates.

We have introduced one plane including O vacancies out of every 3 La-rich planes, as it is observed in experiments, such as Ref. [156] (see Fig. 5.1, light blue plane). In our study, we have performed calculations for 10 different oxygen-vacancy configurations, as described in Fig. 5.2. The number of possible configurations increases with the number of oxygen vacancies, that is one of the reasons why we stop the analysis in 2 vacancies. Also, with 3 vacancies or more we could not figure out a simple ionic model that would yield a ferromagnetic insulating state at the same time as providing a magnetic moment close to the experimental value. However, we foresee that we have found a 2-oxygen-vacancy configuration that is in agreement with the experimental data. For choosing the different configurations we have taken into account the tetragonal symmetry of the system, considering that a basal O is different than an apical one, but retaining xy-symmetry for the analysis.

In order to compute the energy E of each configuration we have used the following equation [165–167]:

$$E = E_{conf} + \frac{n}{2}E_{O_2} - 2nE_e - E_{0_vac} \tag{5.1}$$

where E_{conf} is the energy of one of the configurations shown in Fig. 5.2 (the effect of charged vacancies is not included in this term). E_{O_2} is the energy of the O_2 molecule, calculated as described in the Computational Methods section, and n the number of vacancies. E_e is the term that provides the energy due to the charged vacancies. It is computed as the difference in energy between the top of the valence band of the configuration that we are calculating and the top of the valence band of the configuration without vacancies (0_vac). In order to set a common zero of energies for each case, we chose the energy of an oxygen $1s$ orbital that lies away from the vacancy plane. The factor 2 is the

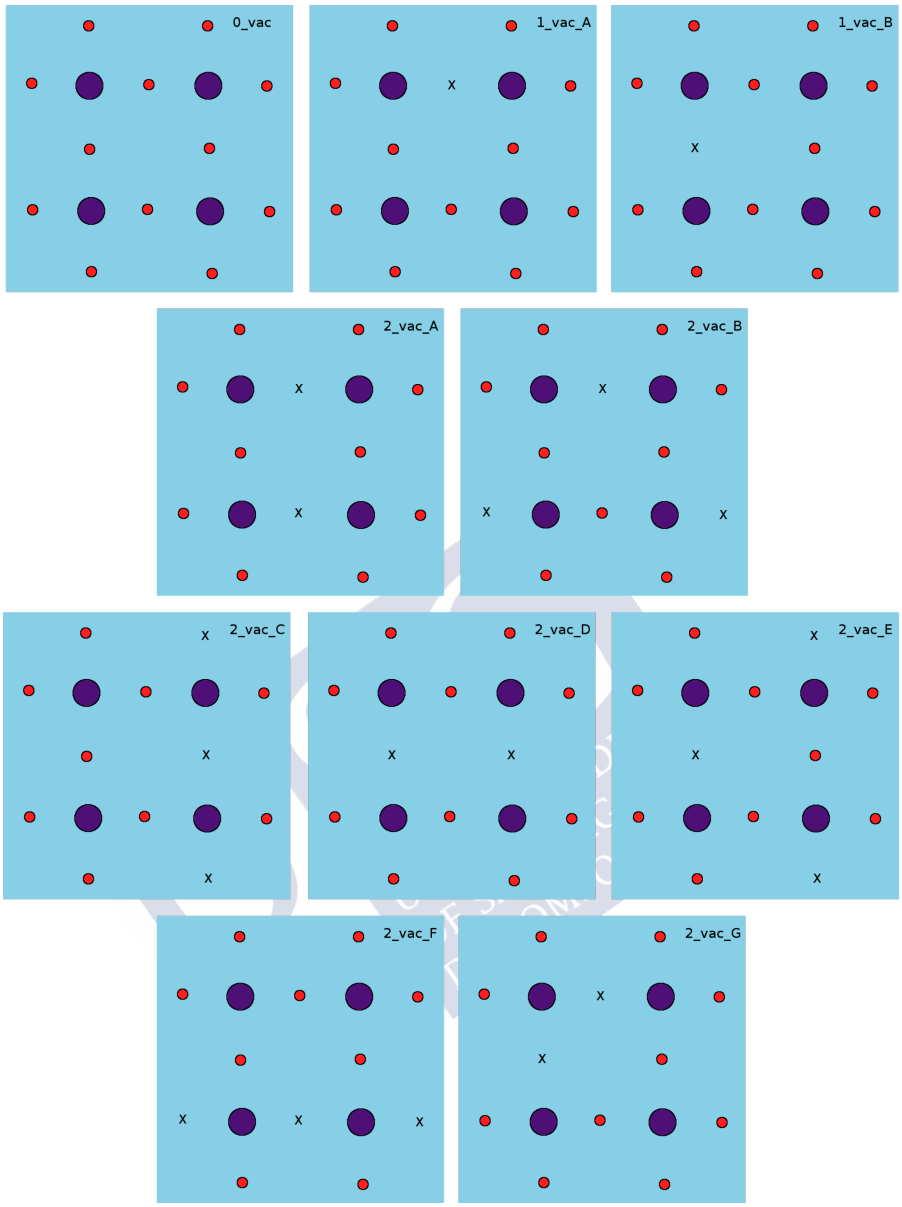


Figure 5.2: Ten different oxygen-vacancy configurations, all of them projected on the blue plane described in Fig. 5.1. Co is in purple, O in red and the vacancies are represented by a cross. In each panel, the O on the left hand side are equivalent to those on the right and the bottom to the top ones. 0_vac stands for LCO without vacancies, 1_vac_A and 1_vac_B correspond to the two different possibilities when one O vacancy is introduced, 2_vac_A, 2_vac_B, 2_vac_C, 2_vac_D, 2_vac_E, 2_vac_F and 2_vac_G are the seven two-O-vacancy configurations. The horizontal coordinate corresponds to the b parameter and the vertical one to c.

charge, supposing they become fully ionized, as is found in other oxides [136]. Finally, E_{0_vac} is the energy of the configuration without vacancies 0_vac, this term represents the zero of energies when obtaining E from eq. (5.1). We have assumed that all the vacancies form O_2 and we have also neglected the electrostatic interaction between the homogeneous background charge and the charged vacancies. This assumption was made considering previous works [165–167] and the fact that the most stable compound for the oxygen element is the O_2 molecule.

All terms in eq. (5.1) were calculated using the GGA scheme, but E_e was computed using the LDA+U scheme for various U values, since GGA leads to metallic solutions and the LDA+U method allows to compare the band alignment between two realistic insulating solutions, both for the stoichiometric and non-stoichiometric systems.

The results for the energy of each oxygen-vacancy configuration using eq. (5.1) are shown in Fig. 5.3. We observe that only the configuration 2_vac_D is more stable than the one without vacancies. This corresponds to chains of oxygen vacancies perpendicular to the (001) and contained in the plane of vacancies (see Fig. 5.2).

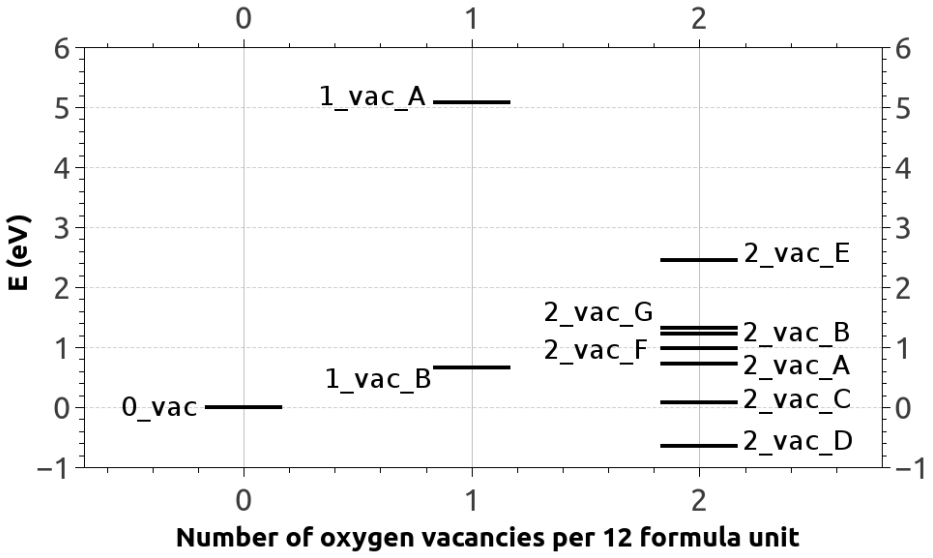


Figure 5.3: Energetics for the different oxygen-vacancy configurations computed using eq. (5.1). We can see that the most stable configuration is the 2_vac_D. This configuration corresponds to vacancy chains perpendicular to the (001) direction and contained in the vacancy plane. Only results with $U = 7\ eV$ are presented in this figure.

Before analyzing in detail configuration 2_vac_D, which is the ground state, we can explore the other configurations. For the case without vacancies, the system is a non-magnetic insulator. We also see that this configuration is quite stable compared to the others that present oxygen vacancies (2_vac_D is the only configuration with vacancies

that is more stable than the stoichiometric solution). If we put an eye now on the two configurations with one vacancy, we will realize that one of them is much more stable than the other. The difference in energy between them is a sizable 0.37 eV/Co. This result suggests us that in the case of adding a second vacancy, it could be energetically favorable to include it in an equivalent position to configuration 1_vac_B, i.e, forming chains perpendicular to the (001) direction. We have demonstrated this statement calculating the energy for the 7 possible 2-vacancy configurations. As we have said 2_vac_D gives a stable solution. All the other $n = 2$ cases are also FMI solutions, but higher in energy, except 2_vac_C, which is a ferromagnetic metal. We have tried several values of U in a wide range, but an energy gap was not opened for that particular configuration.

Table 5.1: Energies (in eV) for the different configurations at different values of U. The zero of energies is represented by the configuration without vacancies. It can be observed that configuration 2_vac_D is a robust ground state in a wide range of values of U. It is the only configuration that is stable for $U \geq 5.5\ eV$.

U (eV)	**4.1**	**5.5**	**6.8**	**8.2**
1_vac_A	5.78	5.40	5.08	5.16
1_vac_B	1.33	0.96	0.66	0.70
2_vac_A	2.29	1.44	0.72	0.87
2_vac_B	2.61	1.60	1.23	1.43
2_vac_C	1.00	-0.16	0.08	0.47
2_vac_D	1.93	**-0.24**	**-0.64**	**-0.41**
2_vac_E	3.13	2.41	2.45	2.90
2_vac_F	1.38	1.10	0.99	1.56
2_vac_G	2.61	1.62	1.33	1.75

Table 5.1 shows a summary of all the energetics of the configurations considered as a function of U for four selected values of U. We can see that the only stable solution that includes O-vacancies is the one we have analyzed thoroughly in the paper: configuration 2_vac_D. We see that it is the ground state for a wide range of U values, $U \geq 5.5\ eV$. The typical U values utilized for this kind of cobaltates in similar calculations are in the range of $6 - 8\ eV$ [159, 168, 169]. Thus, our calculations show a robust trend indicating that configuration 2_vac_D is indeed the ground state of the system.

Figure 5.4 shows that there is a range of U values where 2_vac_D becomes stable, and such U is within that range. We have also seen that configuration 2_vac_D is a robust ground state in a wide range of U values above 5.5 eV. We will determine the origin of this stabilization in the next subsection as a change in the electronic structure produced by the electronic correlations.

If we analyze in more detail the structure of the 2_vac_D configuration that we have obtained from our calculations, we find the following characteristics that can be

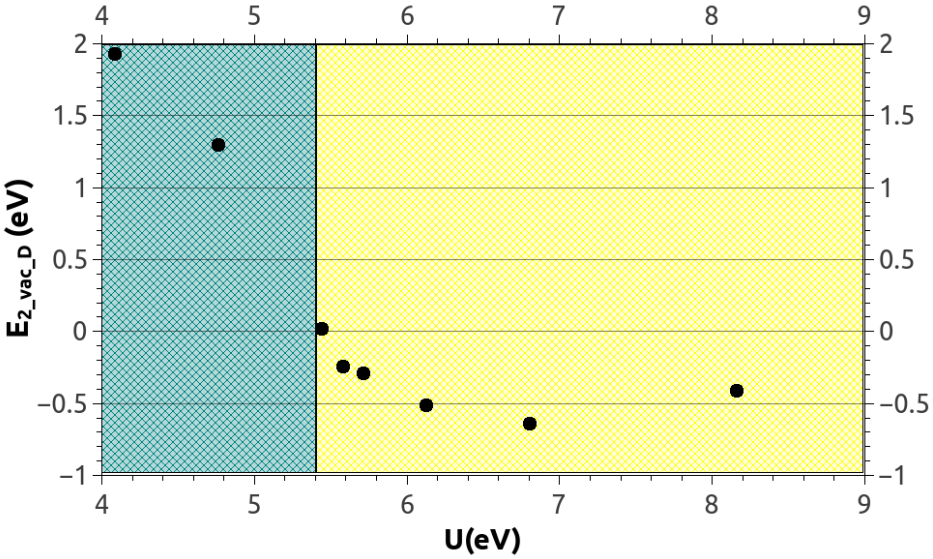


Figure 5.4: Energy of the 2_vac_D configuration as a function of U computed using eq. (5.1). The zero of energies would be the stoichiometric solution without vacancies. We observe that for values of $U > 5.5\ eV$ the configuration labeled 2_vac_D becomes stable.

compared with the experimental results reported in Ref. [156]. The lattice parameter along the (001) direction undergoes a contraction compared to the bulk value of LCO. We have obtained $c = 3.810$ Å, which is in reasonable agreement with the experimental value $c = 3.767$ Å[156]. The distance between LaO planes parallel to the plane of oxygen vacancies depends on whether one considers the distance between two LaO planes that contain the plane of vacancies or two stoichiometric planes. In the former case, with the plane of oxygen vacancies inside, we found that the distance is 4.02 Å. In the other case we found it is 3.85 Å. Experimentally, the same trend is observed but with a larger ratio [160]. Therefore, we have found in this subsection a configuration of oxygen vacancies that agrees with the experimental microscopy data obtained for LCO films grown on STO.

5.3.2 Electronic Structure and Magnetic behavior

We analyze now the electronic structure of configuration 2_vac_D. As we have already said, this presents a ferromagnetic-insulator behavior and is found to be a ground state. We will try first to explain the simple ionic model that accounts for the magnetic moments observed and its consistency with the ab initio calculations of the partial density of states (DOS) of the Co atoms shown in Fig. 5.5. In it, we can see the 3 types of Co atoms that appear in the converged solution: a non-magnetic Co atom six-fold coordinated and two magnetic Co atoms with 5-fold oxygen coordination, one with a higher

value of the magnetic moment than the other.

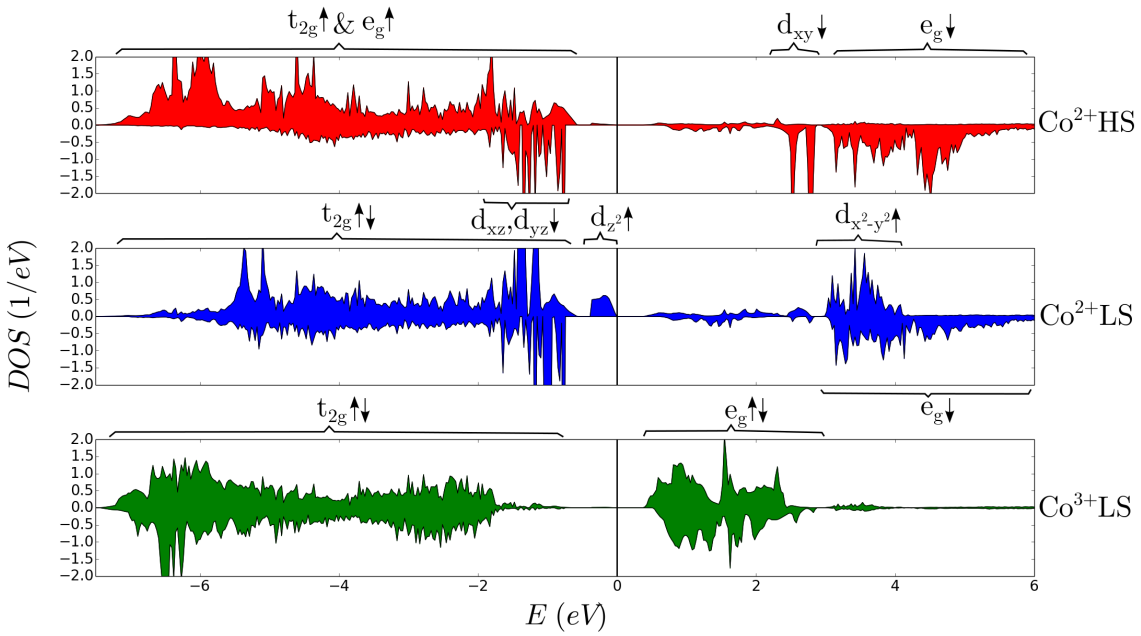


Figure 5.5: Partial DOS for Co^{2+} HS, Co^{2+} LS and Co^{3+} LS computed in the LDA+U scheme, for $U = 7\ eV$. The Fermi level is set to the zero of energies. Upper panel, Co^{2+} HS: the t_{2g} and the e_g majority-spin states are occupied, and also the d_{xz}, d_{yz} minority orbitals. Middle panel, Co^{2+} LS: the t_{2g} majority and minority orbitals are occupied and so is the d_{z^2} majority. Lower panel, Co^{3+} LS: the t_{2g} majority and minority orbitals are occupied.

From an ionic picture, if we consider the unit cell shown in Fig. 5.1, we have La^{3+}, O^{2-} and Co^{3+} for the stoichiometric compound without vacancies. The t_{2g} orbitals of Co^{3+}, which are in an octahedral environment, are occupied in the low-spin (LS) state, see Fig. 5.6 panel c), which gives rise to a zero magnetic moment and an insulating state caused by crystal-field splitting between the Co t_{2g} and e_g levels that leads to a gap opening around the Fermi level in the simple diamagnetic configuration.

If we remove now two oxygens from the unit cell (Fig. 5.1), we have the stoichiometry $La_{12}Co_{12}O_{34}$. Structurally, there are four Co atoms that are five-fold coordinated and the remaining eight Co cations are six-fold octahedrally coordinated and remain non-magnetic, suggesting they retain the original 3+ valence. A simple electron count would naively imply that the other 4 Co atoms are Co^{2+} cations. These are in a five-oxygen environment, that could be analyzed in an ionic picture as an octahedral environment distorted along the z-axis. Such distortion breaks the degeneracy of the t_{2g} and the e_g levels as sketched in Fig. 5.6. The coordinate system that we use to analyze the electronic structure is local to each Co atom with z lying along the O-Co-vacancy direction. Our

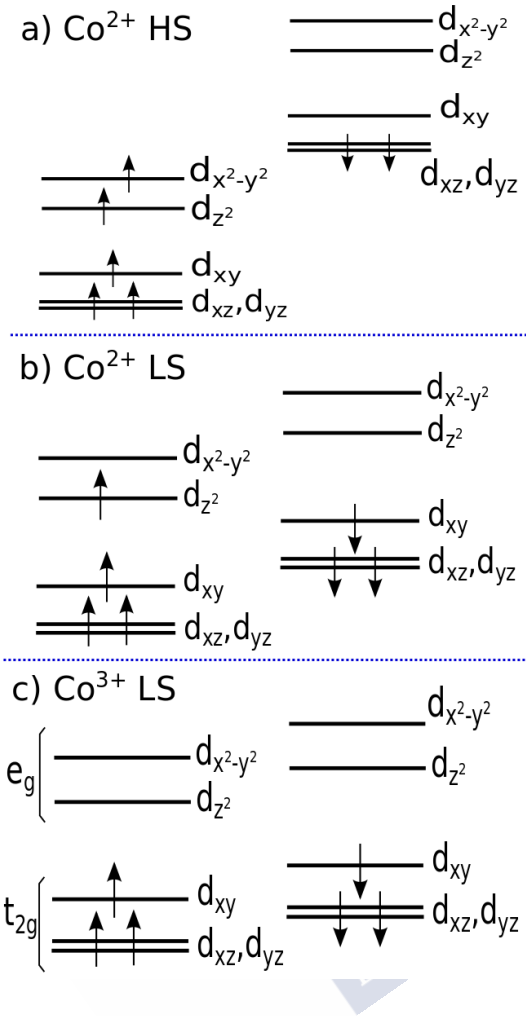


Figure 5.6: Ionic model for Co^{2+} HS, Co^{2+} LS and Co^{3+} LS. a) Co^{2+} HS: the t_{2g} and the e_g majority states are occupied, and also the d_{xz}, d_{yz} minority orbitals. b) Co^{2+} LS: the t_{2g} majority and minority orbitals are occupied and also the d_{z^2} majority. c) Co^{3+} LS: the t_{2g} majority and minority orbitals are occupied.

calculations show that the magnetic moment values are consistent with an ionic picture where half of these Co^{2+} cations are in the LS state (in the 2_vac_D panel of Fig. 5.2 the Co atoms on the left side), and the other half in the HS state (the ones on the right side). The actual values for the magnetic moments inside the muffin-tin spheres obtained from our calculations are approximately 0.8 and 2.4 μ_B, which account for the ionic values plus substantial hybridizations. Taking into account Fig. 5.6: for the case of Co^{2+} LS (Fig. 5.6 b)), we observe that the t_{2g} bands are fully occupied and there is one extra electron occupying the lower-lying e_g state, which is of d_{z^2} parentage due to the missing apical oxygen. Thus, the LS Co^{2+} cations are in an $S = 1/2$ state. In the case of Co^{2+} HS (Fig. 5.6 a)), the majority channel is fully occupied, i.e., the t_{2g} and the e_g majority states are

occupied, there are two minority t_{2g} electrons occupying the lower-lying doublet xz/yz, which is split from the higher-lying xy orbital due to the missing apical oxygen in the five-fold-coordinated environment. This leads to $S = 3/2$ HS state. This simple ionic picture can be observed to be approximately reproduced (with substantial hybridizations, as is common in transition metal oxides) in the partial DOS for each inequivalent Co cation shown in Fig. 5.5. In this figure we show that the DFT calculations can be understood with the simplistic ionic model sketched in Fig. 5.6. The labels in Fig. 5.5 help to see the correspondence with the ionic model. Spectroscopy data confirm that most of the sample is Co^{3+} non-magnetic and that some magnetic Co^{2+} exist [156]. The data do not discard the existence of Co^{3+} HS yet they cannot confirm it. Our calculations show that Co^{3+} HS does not appear. No analysis of the possible existence of Co^{2+} LS that our calculations predict is provided in Ref. [156], thus our calculations are in principle consistent with spectroscopic evidences.

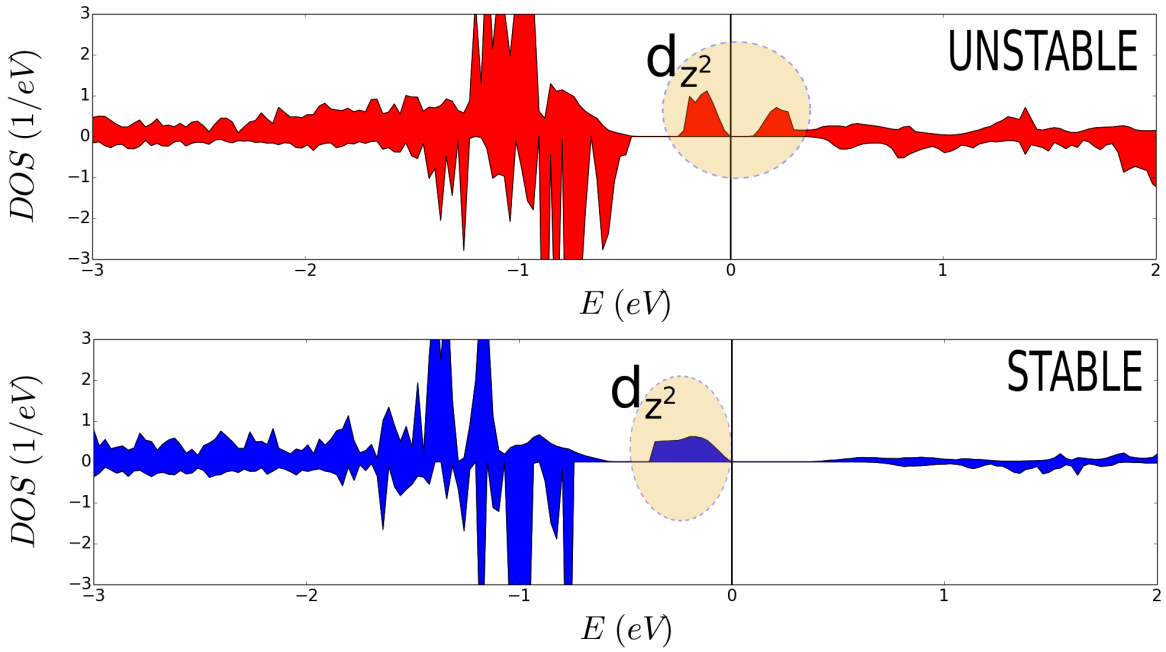


Figure 5.7: Partial DOS Co^{2+} LS for two different values of U, 4 and 7 eV respectively. Upper panel: we observe that the d_{z^2} orbital (highlighted in yellow) is not fully occupied which results in a solution that is not the ground state. Lower panel: we observe in this case that the d_{z^2} orbital is fully occupied, which stabilizes the 2_vac_D configuration to become the ground state.

The total spin magnetic moment in this solution is 0.67 μ_B/Co. If we now include spin-orbit coupling in the calculations, the total ordered moment obtained as the sum of $l_z + 2s_z$ is about 0.8 μ_B/Co, since the magnetic Co cations present a non-negligible orbital

angular momentum that becomes partially unquenched. This is in reasonable agreement with the saturation magnetization of the LCO thin films obtained experimentally of about 0.85 μ_B/Co [156]. We also observe in Fig. 5.5 that the energy gap is between the d_{z^2} orbital of the Co^{2+} LS (top of the valence band) and the e_g of the Co^{3+} LS (bottom of the conduction band). Of course the particular value of the gap will depend on the value of U chosen for the LDA+U calculations. In particular, for the DOS presented in Fig. 5.5, the value used was 7 eV.

In the previous subsection we stated that for values of U less than 5.5 eV the 2_vac_D configuration was not stable. This can be analyzed through the change in the electronic structure that occurs when comparing the low-U and high-U solutions. Plots of the partial DOS of Co^{2+} LS for two different values of U, one for an unstable case and another one for the stable case are shown in Fig. 5.7. We can see that the d_{z^2} orbital of the Co^{2+} LS is not fully occupied for the unstable case, while it becomes totally occupied for the stable case at larger U values. This change in the electronic structure is correlated with the stabilization of the 2_vac_D configuration. Therefore, according to our results, the insulating properties of these films occur naturally due to the additional band splittings introduced by the non-octahedral environments and the correlation energy of the d electrons.

Table 5.2: Energy of the whole unit cell (12 Co atoms) for the different magnetic configurations. They are all referred to E_{FM}.

	Energy (eV)
E_{FM}	0.0
E_{AFM1}	2.1
E_{AFM2}	0.5
E_{AFM3}	2.2
E_{AFM4}	1.9
E_{AFM5}	2.2

Finally, let us analyze the magnetic order that occurs in LCO. In order to do so, we have performed calculations on different magnetic configurations in the ground state structural configuration 2_vac_D. These configurations are shown in Fig. 5.8. The corresponding magnetic exchange coupling constants we have introduced into a Heisenberg model of the system are depicted as the various J's. The energies of each magnetic configuration are shown in Table 5.2. They are all referred to the energy of the ferromagnetic (FM) configuration E_{FM}, which is taken as zero. Total energy is given for the whole unit cell (12 Co atoms in total). The arrangement of the Co^{2+} HS and LS is preserved for all the magnetic configurations and the geometry of the structure is not changed. We see that the FM configuration is the most stable.

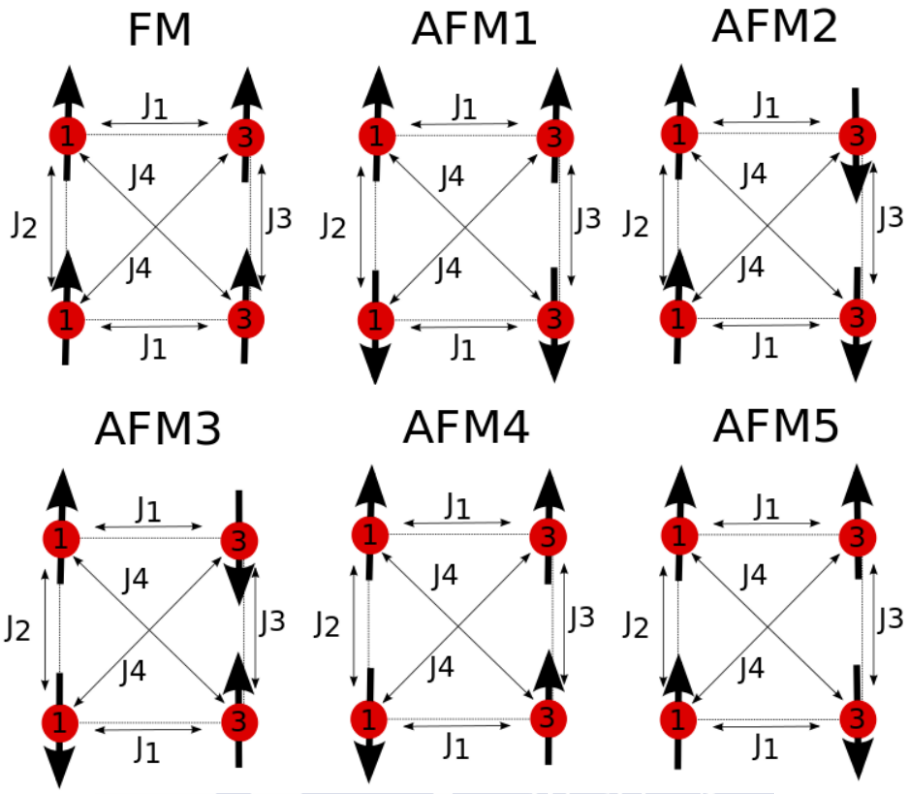


Figure 5.8: Ferromagnetic and antiferromagnetic configurations of the 2_vac_D in the plane of O-vacancies. The spin direction of each Co is depicted with arrows. The exchange interactions are labeled with J_1, J_2, J_3 and J_4. The numbers inside the red circles represent the modulus of the magnetization for each Co atom (1 and 3 μ_B) in the corresponding ionic limit.

Moreover, we can obtain the value of the different exchange interactions as a function of the energies of the magnetic configurations:

$$\begin{aligned} J_1 &= \frac{E_{AFM2} + E_{AFM3} - E_{AFM1} - E_{FM}}{24} = 300K \\ J_2 &= \frac{E_{AFM1} + E_{AFM3} + 2(E_{AFM4} - E_{AFM5}) - E_{AFM2} - E_{FM}}{8} = 4600K \\ J_3 &= \frac{E_{AFM1} + E_{AFM3} - 2(E_{AFM4} - E_{AFM5}) - E_{AFM2} - E_{FM}}{72} = 730K \\ J_4 &= \frac{E_{AFM1} + E_{AFM2} - E_{AFM3} - E_{FM}}{24} = 150K \end{aligned} \tag{5.2}$$

We observe from eqs. (8.1) that all the the exchange interactions (J's) are positive, which entails a ferromagnetic order according to our sign convention.

We have characterized in this section the electronic structure of the 2_vac_D configuration. We have related the calculated DOS to a simple ionic model that explains both the ferromagnetic ordering with a consistent value of the total magnetic moment and the insulating behavior.

5.4 Conclusions

In this chapter we have analyzed the ferromagnetic-insulating behavior of LCO when it is grown on (001) STO. We have used DFT calculations to analyze the electronic structure properties of LCO under tensile strain and for various stoichiometries including different oxygen vacancy configurations and concentrations.

We have found that the ground state of LCO when it is grown on STO is given by an off-stoichiometry of the form $LaCoO_{2.83}$ produced by about 6% oxygen vacancies. We have shown that the vacancies form chains perpendicular to the (001) direction and are contained in the plane perpendicular to the film/substrate interface, consistent with experimental findings. Other structural features like the distance between La layers or the lattice parameter in the (001) direction agree with the experimental measurements.

We found that the Co atoms that lie in the plane of vacancies are a mixture of Co^{2+} LS and Co^{2+} HS. The total magnetic moment is in close agreement with experimental measurements. The ferromagnetic insulating behavior of the film is readily obtained as a ground state, the gap opening occurring naturally in that electron count due to the appearing crystal field splittings together with the addition of a reasonable U value. Our ab initio total energy calculations confirm that all the nearest-neighbor magnetic exchange couplings are indeed ferromagnetic.

In conclusion, we can say that the strain introduced by STO on LCO favors the presence of O-vacancy chains perpendicular to the (001) direction. Ferromagnetism arises from the inclusion of those vacancy chains and can be explained with an ionic model. The results presented in this work could lead to a better understanding and the eventual design of other ferromagnetic-insulator oxides in which oxygen vacancies could play an important role.

6 Sr-doping on Infinite-layer Nickelates

Just a year ago before the pandemic, Sr-doped $NdNiO_2$ was found to be a high temperature superconductor. This so-pursued result has opened the possibility to study nickelates as cuprates analogs. In this chapter we study the effect of Sr-doping in the electronic and magnetic properties of infinite-layer nickelates as well as the nature of the holes. Our results show that doping induces a cuprate-like character on infinite-layer nickelates. The work presented here can be found in Ref. [V] from the List of Publications and it is part of a collaboration with Antía Botana's group.

6.1 Introduction

One of the major achievements in the field of oxides was the discovery of high-temperature superconductors (HTS) in 1986 [170]. Since then, many different strategies have been taken to try to decipher the origin of HTS [171]. Cuprate nanostructuring in which CuO_2 layers are arranged with different dopants in multiple ways has been probably the most studied route. However, a more illuminating approach could be to substitute Cu^{2+} with isoelectronic Ni^{1+}: d^9 [172]. This nickel oxidation state is reported to occur in infinite layered nickelates of the form $RNiO_2$ (where R= La, Nd) [173–177]. It took more than 30 years to experimentally achieve a doped infinite-layer nickelate [178]. In 2019, Sr-doped $NdNiO_2$ was reported to be a superconductor with $T_c \sim 15$ K and a dome-shaped doping dependence as occurs for cuprates [179]. In this chapter we will analyze from first principles how the electronic structure and magnetism of infinite-layer nickelates is affected by Sr doping.

The parent phase of 112 nickelates (at d^9 filling), i.e. the stoichiometric phase, is quite different from that of cuprates. Experimental measurements show that $RNiO_2$ family is metallic and no antiferromagnetic order is found [173–176]. Apart from that, and unlike cuprates, previous electronic-structure calculations on $RNiO_2$ compounds report the presence of low-lying R-5d states crossing the Fermi level. Specifically, the Ni $3d_{z^2}$ and R $5d_{z^2}$ hybridization creates a small spherical electron pocket centered at the Γ point, and the Ni $3d_{z^2}$ and R d_{xy} hybridization creates another electron pocket at the corners of the Brillouin zone. Electrons occupying these pockets originate from the otherwise filled

Ni $3d_{z^2}$ band, resulting in additional holes in the Ni 3d band. This is the phenomenon we will call self-doping and results in a formal electron count for the Ni of $d^{8+\delta}$. Moreover, since Ni is left to the Cu in the periodic table, it presents an increased charge-transfer energy [180–184] (twice as large than a prototypical cuprate value). However, both in cuprates and infinite-layer nickelates superconductivity appears upon hole doping, so a relevant question to address is how do the above parameters change upon doping as well as the nature of holes.

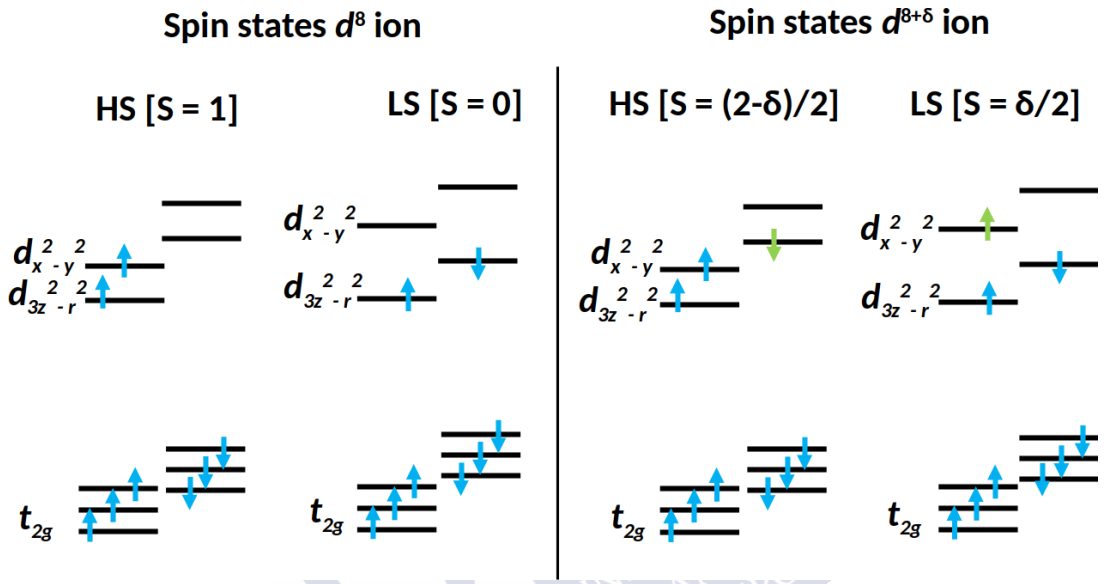


Figure 6.1: Schematic representation of the energy level diagrams for high-spin and low-spin states of $Ni^{2+}(d^8)$(left) and $Ni^{2+\delta}(d^{8+\delta})$(right) ion in a square-planar environment. t_{2g} label refers to non-degenerate xy, xz, yz orbitals for simplicity. Green arrows refer to a partial occupation of that particular orbital.

In the parent phase of cuprates the Cu^{2+} ions have an active $d_{x^2-y^2}$ orbital hybridized with the p orbitals of the neighboring in-plane oxygens [5]. One may expect that when doping with holes, a Cu^{3+} (d^8) will arise from the initial Cu^{2+} (d^9). However, Cu^{3+} is an oxidation state with negative charge-transfer gap and instead holes predominantly go to the O-p orbitals, that is, the state $Cu^{2+}(d^9)\underline{L}$ (where $\underline{L}$ stands for a ligand hole, e.g., hole on oxygen). This allows the formation of Zhang-Rice singlets [185]. As we have already said, in the case of nickelates the charge-transfer energy is much larger [181] leading to a dominant Ni^{2+} state with holes residing on the Ni, rather than in the O-p band. Ni^{2+} can be in two different spin states, as depicted in Fig. 6.1: either a low-spin state (LS) if the electron from the higher-lying $d_{x^2-y^2}$ orbital is removed, resulting in a configuration $(t_{2g})^6$ $(d_{z^2})^2$ configuration with S=0; or a high-spin (HS) state if the electron from the d_{z^2} orbital is removed, in which case the resulting configuration is $(t_{2g})^6$ $(d_{z^2})^1$ $(d_{x^2-y^2})^1$ with S = 1 [186, 187]. It was recently argued that hole-doping infinite layer nickelates

should produce Ni^{2+} with spin S = 1 [188–190]. However, in this study we find from *ab initio* calculations including explicit Sr-doping in $RNiO_2$ (R= La, Nd) supercells, that a low-spin state (S=0) is preferred instead due to the large crystal field splitting of the e_g states in the square planar environment. This is consistent with what is found in other square planar layered nickelates [186, 191–194]. We also find that upon hole doping, the electronic structure of infinite layer nickelates becomes more cuprate-like with reduced charge transfer energy and suppressed self-doping.

6.2 Computational Methods

In order to check chemical pressure effects, we have performed Density Funtional Theory (DFT) calculations [17, 18] in both $LaNiO_2$ (with a= 3.96 Å, c= 3.37 Å), and $NdNiO_2$ (a= 3.92 Å, c= 3.28 Å), which are two experimentally available members of the family of infinite-layer nickelates. Supercells of size 2×2, 3×3 and 4×4 relative to the primitive P4/mmm cell were employed to study the effect of 11% and 25% Sr doping in both $LaNiO_2$ and $NdNiO_2$. They give rise to an average Ni-d filling of 8.75, 8.89 and 8.75, respectively (with 4 Sr dopants in the unit cell clustered around a particular Ni atom in the latter, which becomes nominally a Ni^{2+}). The corresponding structures are shown in Fig. 6.2.

In order to speed up structural relaxations, the Sr-doped supercells were fully relaxed using the pseudo-potential method as implemented in the Vienna *ab-initio* simulation package (VASP) code [36] within Perdew-Burke-Ernzerhof version of the generalized gradient approximation (GGA) [19]. However, for an accurate treatment of the d-electrons, the subsequent electronic structure calculations were performed using the all-electron, full potential WIEN2k code [30], which is based on the augmented plane wave plus local orbitals (APW+lo) basis set. The electron correlations beyond GGA at Ni sites were taken into account through LDA+U calculations [20]. Two LDA+U double-counting schemes were used: the 'fully localized limit' (FLL) and the 'around mean field' (AMF) [195, 196]. For both schemes, we have studied the evolution of the electronic structure with increasing U (U_{Ni}= 1.4 to 6 eV, J= 0.8 eV). In spin-polarized calculations both ferromagnetic (FM) and antiferromagnetic (AFM) orders were considered. The muffin-tin radii used were 2.5 a.u for La, 2.46 a.u. for Sr, 1.96 a.u for Ni and 1.69 a.u. for O.

6.3 Electronic Structure and Magnetism

$RNiO_2$ materials are formed by NiO_2 planes (with 180° O-Ni-O bond angles) that are separated by a single layer of R ions (see Fig. 6.2). Upon Sr-doping the structures experience a small increase in volume with respect to the parent materials ∼ 1-2 % for doping levels up to 25%. This trend could be expected since Sr^{2+} is larger than La^{3+} and Nd^{3+}. Moreover, for the doped structures a slight deviation in bond-lengths and bond-angles appears after structural relaxation. In particular, there is a distortion of the

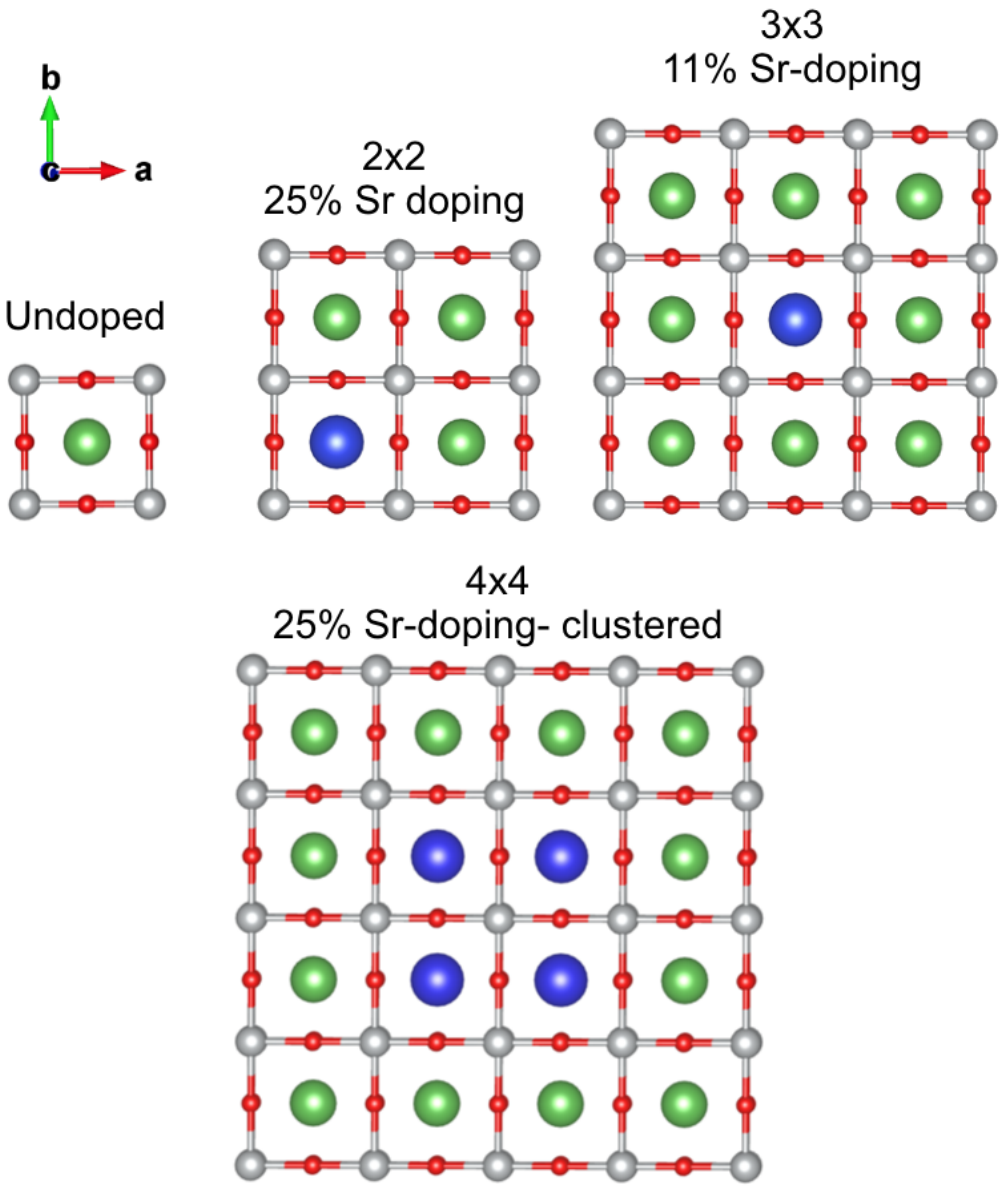


Figure 6.2: Crystal structure of undoped $RNiO_2$ (R=La, Nd) (a) and Sr-doped $RNiO_2$ supercells of different size 2×2 (b), 3×3 (c), and 4×4, corresponding, respectively, to average Ni-d fillings: 8.75, 8.89 and 8.75. R atoms in green, Sr-atoms in blue, oxygen atoms in red, Ni atoms in gray. Note that (d) corresponds to a particular type of 25% Sr-doping, where all the Sr dopants are clustered around a particular Ni cation, that one can study as the closest possible approximation to a nominally Ni^{2+} impurity.

Ni-O distances in the NiO_2 planes consisting of a modulation of the Ni-O bond length: shorter around the Ni ions closer to a Ni^{2+} state, those proximate to the Sr atoms (1.95-1.96 Å) and longer around Ni ions closer to a Ni^{3+} state (1.98-1.99 Å), those away from the dopants. There is also a significant buckling close to the Sr-substituted atom with Ni-O-Ni bond angles $\sim 175°$.

Using those relaxed Sr-doped $RNiO_2$ supercells (Fig. 6.2) we have performed a full study of the stability of different spin states. For the 2×2, 3×3, and 4×4 supercells we have effective d fillings of $d^{8.75}$ $d^{8.89}$, and clustered-$d^{8.75}$, respectively. In the smaller cells (2×2, 3×3), two possible spin states can occur in Sr-doped $RNiO_2$. The (on average) $d^{8+\delta}$ cations sit in a square planar environment that leads to a large splitting between the $d_{x^2-y^2}$ and d_{z^2} bands. The crystal field splitting (Δ_{cf}) within the e_g states can be then comparable to the Hund's rule coupling (J_H); if the former is larger, a low spin (LS) state (with S= $\delta/2$ and a moment δ per nickel) develops and if the latter is larger, a high spin (HS) state would be more stable (with S= (2-δ)/2 and a moment 2-δ per nickel). In contrast, in a large enough cell, a d^8 configuration can be stabilized for the Ni clustered by the Sr dopants. In this case δ would be effectively zero and hence a HS state with S=1 or a LS state with S=0 could be obtained for that specific Ni atom surrounded by first neighbor Sr atoms. This distinction is depicted in Fig. 6.1 with the HS and LS states leading to drastically different properties: the former is non-cuprate like (in that the d_{z^2} states are the dominant ones around the Fermi level) and the latter is more cuprate-like (in that the $d_{x^2-y^2}$ states dominate around the Fermi level). We note that for either LS and HS $d^{8+\delta}$ cases, an AFM coupling between neighboring Ni atoms is always preferred, mediated by the close to half-filling $d_{x^2-y^2}$ band. An AFM state for undoped $RNiO_2$ materials has also been shown to be energetically favored in the absence of fluctuations [181, 182, 197], even though an AFM ordered state is experimentally not observed [176]. As proposed in Ref. [197] this might suggest that it is a metastable but physically inaccessible phase in $RNiO_2$ materials.

The energetics for the HS and LS spin states in the different supercells have been analyzed within two different LDA+U schemes: around mean field (AMF) and fully localized limit (FLL). Moreover, the possible effect of chemical pressure in the stability of HS vs LS state was taken into account by performing calculations for both La112 and Nd112. We have also studied the evolution with U of the energy differences as it is also expected that a large U would tend to favor the HS state. Figure 6.3 shows a summary of the phase diagram for the two possible (HS and LS) states as a function of U for AMF and FLL schemes, for both $LaNiO_2$ and $NdNiO_2$ at two different Sr doping levels- 25% (2×2 supercell), and 11% (3×3 supercell). Within the AMF LDA+U flavor, the LS state is favored, independent of the chosen U value. The FLL flavor also favors the LS state at low values of U, whereas at high values of U the high-spin solution is favored. There is a well-known tendency of these different LDA+U flavors to make LS (AMF) or HS (FLL) more stable, respectively [198]. This is a direct consequence of the double counting term in the AMF scheme giving magnetic states a larger energy penalty than FLL does. For the 2 × 2 and 3 × 3 cells, the magnetic moments inside the muffin-tin spheres are

consistent with the above description in terms of Ni-$d^{8+\delta}$ ions with μ=(2-δ)μ_B for the HS state and μ=$\delta\mu_B$ for the LS state with $\delta \sim$ 0.8-0.9. We note that within FLL, at low U values a HS state cannot be obtained, whereas at high U values (above 4.2 eV), a LS state cannot be converged. Within AMF, at low U values a HS state cannot be obtained either. The only remarkable difference observed upon a change in R in Fig. 6.3 is that for $NdNiO_2$, the transition to a HS state within the FLL scheme occurs at a slightly larger U when compared to the La material. This result can be well understood considering that the Nd-based unit cell is smaller, and the LS state tends to be typically favored at smaller volumes [191].

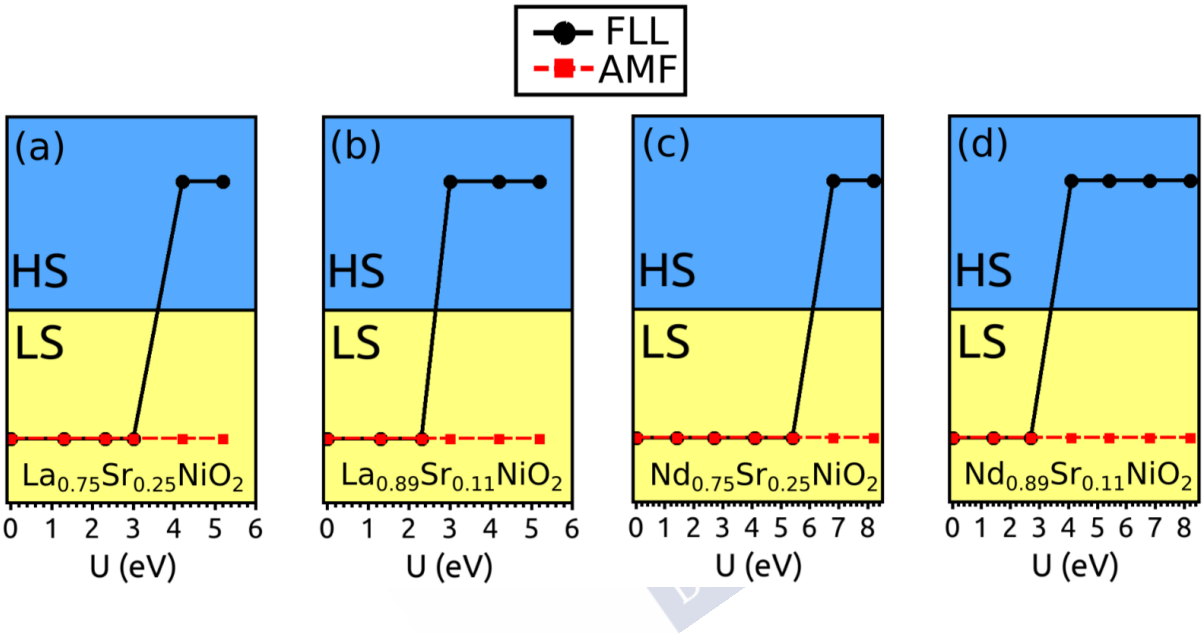


Figure 6.3: Evolution of the lowest-energy spin state (either HS or LS states) with U for the two types of LDA+U schemes: FLL (fully localized limit) and AMF (around mean field). Results indicate that only at large U and only for the FLL functional, the HS state could be stabilized, otherwise the LS state is more stable for both dopings studied for the La and Nd cases.

These trends are consistent with earlier results on the trilayer members of the layered nickelate family [186, 191]. Given that in square planar trilayer nickelates (with the Pr variant also being metallic) the AMF scheme was deemed to provide a better description of the electronic structure in comparison to experiments, the same can likely be anticipated for metallic infinite-layer systems so these results suggest that indeed a LS state would be the most stable situation for these smaller cells.

Using these AMF-LS results for 2×2 and 3×3 Sr-doped cells, at an effective U= 5 eV we analyze the evolution of the La-d, O-p and Ni-d orbital-resolved densities of states (DOS) upon increasing Sr-doping (see Fig. 6.4). We show the DOS of $LaNiO_2$ but an identical picture is obtained for its Nd-counterpart. In a simplified picture, hole-doping

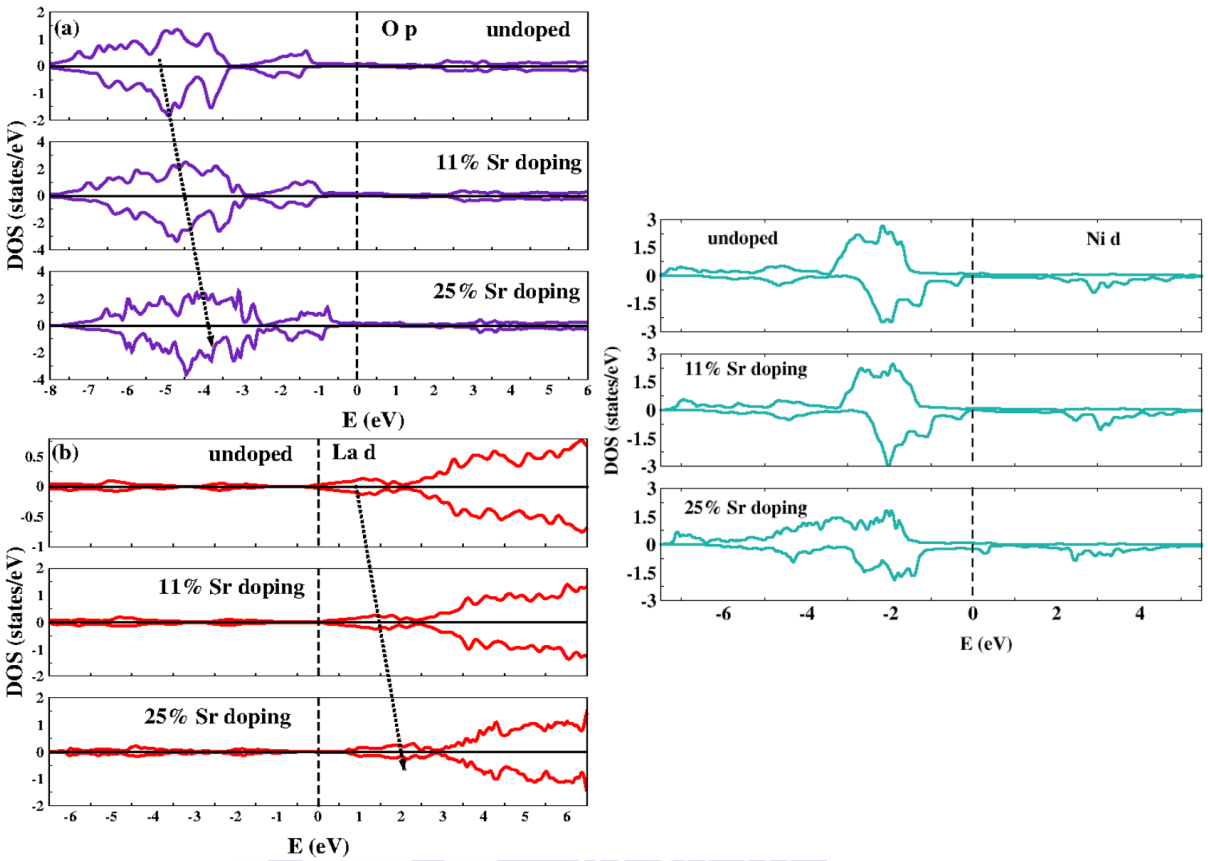


Figure 6.4: Evolution of the orbital resolved DOS for O-p, La-d, and Ni-d states upon increasing Sr-doping in $LaNiO_2$. We see that, as Sr doping is introduced, the centroid of the Ni-d bands does not significantly change while the O-p bands move closer to the Fermi level, effectively reducing the charge-transfer energy. The La d bands move away from the Fermi level, reducing the self-doping effect.

would simply shift down the Fermi level, but this is a self-doped system, and hence moving the La-d bands to higher energies would reduce the self-doping effect as a function of Sr doping. We describe how this mechanism works analyzing the actual DOS plots in which the La-d character at E_F can be seen to decrease with doping, as the La-d bands clearly shift to higher energies. Thus, reducing the self-doping effect and giving a more pure single-band cuprate-like picture. Reinforcing this picture, O-p states are pushed towards the Fermi level with doping. As the centroid of the Ni-d bands does not get shifted noticeably, this reduces the $p-d$ energy splitting (charge-transfer energy) by more than 1 eV when going from the undoped compound to 25% Sr-doping.

The doping effect on the Ni-d states is more complicated to analyze. On the one hand, Sr introduces holes but on the other, it reduces the self-doping effect from the La-d electron pocket that now moves away from the Fermi level. The overall result is a lower

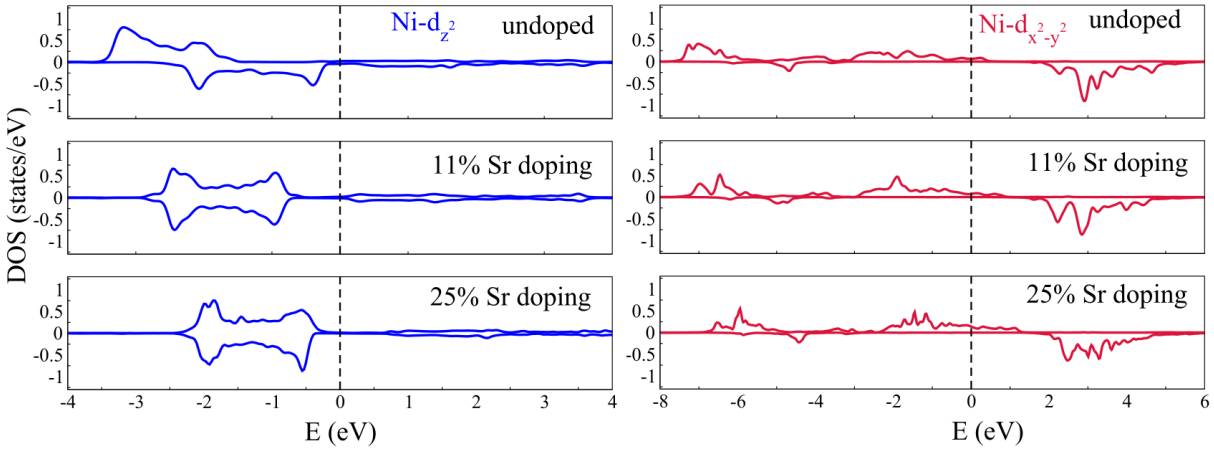


Figure 6.5: Evolution of the orbital resolved DOS for Ni-d_{z^2} and Ni-$d_{x^2-y^2}$ states upon increasing Sr-doping in $LaNiO_2$, obtained using the AMF scheme with U= 5 eV.

weight of the Ni d_{z^2} band around the Fermi level as Sr-doping is introduced, leaving a dominant $d_{x^2-y^2}$ contribution that makes Sr-doped 112 nickelates a more cuprate-like, single-band system (see Fig. 6.5). All of the above described trends imply that, as Sr dopants are introduced in $RNiO_2$ materials, some of their electronic-structure features become closer to those of the cuprates: low-spin dopant states, reduced charge-transfer energy, and a single Ni $d_{x^2-y^2}$ band around the Fermi level.

Finally, the 4×4 supercells with an average $d^{8.75}$ filling given by a 25% Sr substitution that allow, via clustering of all the Sr dopants, for one Ni in the cell to be nominally d^8 (the Ni atom completely surrounded by first-neighbor Sr cations in Fig. 6.2). In this scenario, we find that a LS ($S = 0$) state is preferred in both $RNiO_2$ (R= La, Nd), for the Ni ion surrounded by Sr atoms even within FLL. In the AMF scheme the low-spin solution is not only the lowest in energy, but a high-spin solution does not even exist, as attempts to start the self-consistency procedure with a S=1 state of Ni^{2+} ion lead to a vanishing magnetic moment. The rest of the Ni atoms preserve the expected magnetic moments. Figure 6.6 contrasts the orbital resolved density of states for the nominally d^8 Ni cation (that is surrounded by Sr atoms) in both a LS state and a HS state in this 4×4 supercell within FLL. We choose once again to show calculations for Sr-doped $LaNiO_2$ but the situation is identical in the Nd-material. In the low-spin state the t_{2g}^6 $d_{z^2}^2$ configuration is clear with the two $d_{x^2-y^2}$ orbitals remaining unoccupied for both spin channels. In the high-spin case, the t_{2g} orbitals are also completely occupied, but now one electron occupies the majority spin d_{z^2} and $d_{x^2-y^2}$ orbitals. The LS state for the Ni^{2+} is strongly connected to a reduction in the d_{z^2} character around the Fermi level. This can be seen in Fig. 6.6 where the Ni d_{z^2} band crossing the Fermi level for the HS state becomes fully occupied, well below the Fermi level for the LS state. This effect is concomitant with the reduction of the La-d self-doping effect upon increasing Sr-doping

described above. Overall, the stable LS state solution we find gives then rise to an explicit cuprate-like scenario with planes of S=1/2 ions that are lightly doped with mobile low-spin S=0 ions, a configuration that is directly analogous to the low-spin S=0 Cu^{3+} ion situation, mediated by O-p holes as explained above.

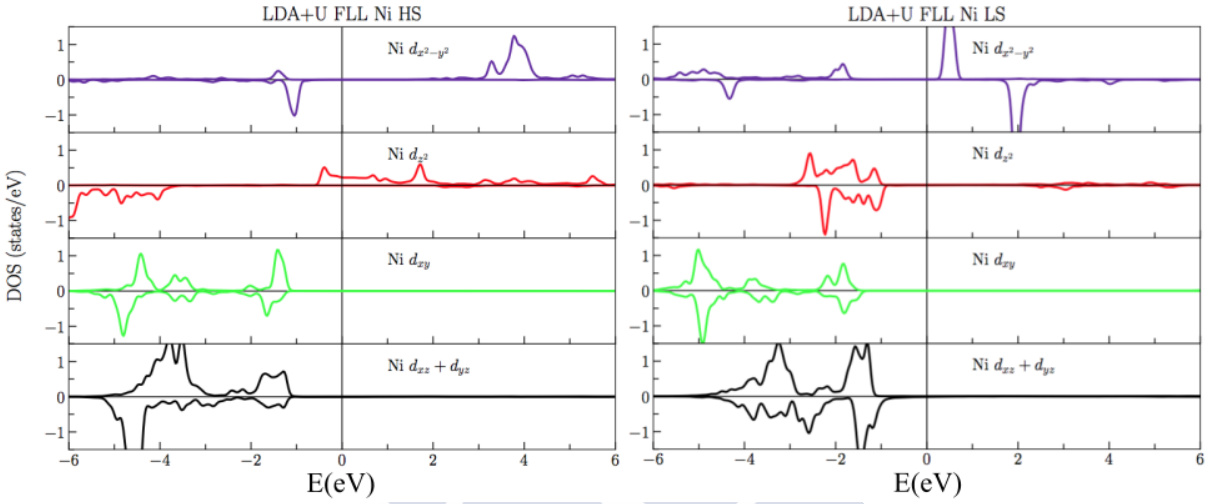


Figure 6.6: DOS of the nominally Ni^{2+} dopant in the 4×4 supercell with 25% Sr-doping in the two different spin states studied. HS (LS) configuration is shown in the left (right) panel. It can be noticed that the lower-energy LS configuration leads to a depletion of Ni d_{z^2} states around the Fermi level.

We note that in other intensively studied nickelates (such as in La_2NiO_4) the high-spin (S=1) configuration of Ni^{2+} is favored [199, 200] and not the low-spin (S=0) configuration as we find here. La_2NiO_4 is structurally different to $RNiO_2$ as it preserves apical oxygen atoms and has an octahedral environment for its Ni^{2+} cations. We show here that if the Ni^{2+} ions are forced into a square planar local environment as happens in the 112 materials, they prefer a low-spin d^8 (S=0) cuprate-like state instead, in agreement with recent experimental reports [201].

6.4 Conclusions

In this chapter we have analyzed how Sr-doping affects the electronic structure and magnetic state of infinite-layer nickelates $RNiO_2$ (R= La, Nd).

We have found that including Sr reduces the self-doping effect by shifting the rare-earth d bands up in energy away from the Fermi level. This leads to a more single-band-like picture, with the Ni $d_{x^2-y^2}$ band dominating. We have also analyzed the magnetic spin configuration as a function of doping (11% or 25%) and rare-earth cation in the framework of LDA+U calculations with two different double-counting methods. In any

case, a low-spin Ni^{2+} state is found to be the lower energy solution. Moreover, Sr-doping highly reduces the charge transfer energy between the Ni and O atoms.

Our study shows substantial changes in the electronic structure of these nickelates upon Sr-doping. A cuprate-like electronic structure and magnetic state is obtained when doping these compounds. Therefore, this result suggests a cuprate-like description of the superconducting state that arises in doped infinite-layer nickelates.

7 Spectroscopy of Cs_2CuCl_4

In this chapter we study the electronic structure of Cs_2CuCl_4. This material has been discussed in the framework of frustrated antiferromagnet quantum spin liquids. A combined set of experimental techniques and Density Functional Theory has allowed us to determine the spectrum of this compound. This is mainly determined by the crystal field splitting that Cu^{2+} ions feel when they are placed in the strongly distorted tetrahedral environment of this compound. This unpublished work is part of a collaboration led by Dr. Santiago Blanco-Canosa.

7.1 Introduction

In the previous chapter we have analyzed the electronic structure and magnetic properties of infinite-layer nickelates. We found that when doped with Sr their electronic structure can be understood to resemble that of the high-temperature superconducting cuprates. In this chapter we continue analyzing materials with promising exotic behaviour. However, we abandon at this point the study of oxides just before focusing on van der Waals layered materials in the next chapter. Therefore, this work will serve as an interlude between oxides and van der Waals transition metal compounds. It will also highlight the ability to combine experiment and theory to determine the electronic structure of a material.

Quantum spin liquids (QSL) were hypothesized to occur in nature by Philip Anderson in 1973 [202]. This is a state of matter in which the electrons' spins remain fluid-like, i.e., fluctuating without entering in a long-range order phase, even at 0 K [203]. Interestingly, the excitations of a QSL, known as spinons, are fractional, leading to a characteristic transport behaviour. Geometrically frustrated spin textures, like triangular, Kagomè and honeycomb lattices, are considered to be the most promising systems to find a QSL [204]. The magnetic order and its excitations will be determined by the competition between the different sign of the exchange interactions on the frustrated spin lattice.

Among the solids showing frustrated magnetism, significant attention has been drown to Cs_2CuCl_4 due to the experimental observations that report a two-dimensional QSL phase by means of specific heat measurements [205], electron spin resonance (ESR) [206]

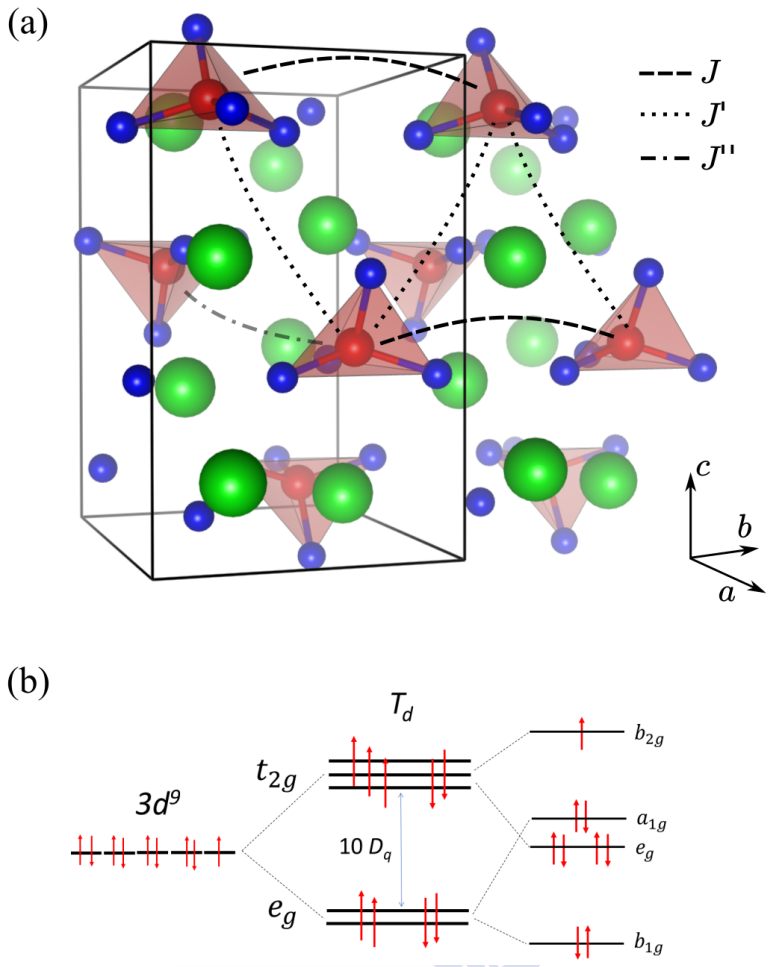


Figure 7.1: (a) Orthorhombic unit cell of Cs_2CuCl_4. Green, red and blue balls denote Cs, Cu and Cl atoms, respectively. The tetrahedral coordination of Cu is highlighted. The magnetic exchange interactions commented in the text have been depicted. (b) Crystal field splitting of the Cu^{2+} ions in the distorted tetrahedral environment, where the e_g orbitals lower their energy with respect to the t_{2g}. The Jahn-Teller distortion further splits the energy levels with b_{1g} ($d_{x^2-y^2}$), e_g (d_{xz},d_{yz}), a_{1g} (d_{z^2}) and b_{2g} (d_{xy}) symmetries.

and neutron scattering [207], which uncovered an extensive two-spinon continuum. The ESR and neutron scattering measurements revealed a weaker interchain exchange coupling, J'/k_B= 1.4 K, between Cu atoms than the intrachain interaction, J/k_B=4.7 K, along b axis [208] (see Fig. 7.1a). Moreover, interlayer coupling in Cs_2CuCl_4 is smaller than J and J' by more than one order of magnitude, J''= 0.13 K, in good agreement with the theoretical description of quasi-1D weakly coupled S=1/2 Heisenberg chains [209].[1]

[1]Be aware that in the literature antiferromagnetic exchange constants are commonly defined as positive when dealing with QSL models.

Besides, central to the study of spin exchange interactions in frustrated magnets is the precise knowledge of the crystal-field ground state symmetry and hopping energies of the $S = 1/2$ Cu^{2+} ions. In fact, the experimental determination of the crystal field and Jahn-Teller splittings, Δ^{CF} and Δ^{JT} has remained elusive. Moreover, the orbital occupation is commonly inferred from the oxidation state in an ionic picture, but is usually limited in covalent systems, where the strong overlap between d and p bands gives rise to charge transfer effects [210]. Indeed, the most noticeable effect of the different orbital occupation is highlighted in the manganese perovskites, $RMnO_3$ (R= rare earth) [211] and cobaltates [146], where the ground state properties are strongly influenced by the site symmetry of the transition metal ion and the electronic rearrangement within the d-shell [212].

Experimentally, the crystal field splitting, especially in $4f$ systems, has been measured by inelastic neutron scattering [213, 214], but the information is sometimes hampered by phonons or small amount of crystals. In transition metal compounds, X-ray absorption spectroscopy (XAS) is traditionally used to probe the magnitude of the crystalline electric field splittings in the $3d$ shell [215] and the degree of the $3d$ hybridization in the ground state. Nevertheless, the multiplet effects are often hindered by the metal-ligand hybridization, which smears out the splittings of the $3d$ states. Therefore, a comprehensive determination of the different energy scales is usually a tedious task and relies on several complementary techniques.

On the other hand, band structure calculations have reported the electronic properties of Cs_2CuCl_4 and predicted a strong dependence on the Jahn-Teller distortion, Δ^{JT}, as a function of the correlation exchange functional [216]. However, a direct comparison between theory and experiment is still missing.

In this work, we have circumvented these drawbacks by combining resonant inelastic X-ray scattering (RIXS), Density Functional Theory (DFT) and cluster calculations, which allows us to provide a satisfactory and comprehensive description of the Cs_2CuCl_4 electronic spectrum.

7.2 Experimental and Computational Methods

Single crystals of Cs_2CuCl_4 were grown by our experimental colleagues Dr. F. Rodríguez and Dr. S. Blanco-Canosa. The quality of the single crystals was checked by X-ray diffraction, resulting in lattices parameters a= 9.77 Å, b= 7.61 Å, c = 12.41 Å, and inelastic Raman scattering [217]. DFT calculations [17, 18] were performed using the all-electron, full-potential WIEN2K code [30] based on the augmented plane wave plus local orbital (APW+lo) basis set. The generalized gradient approximation (GGA) in the Perdew-Burke-Ernzerhof [19] scheme was used for the exchange correlation functional, with a fully converged k-mesh of $R_{mt}K_{max}$=7.0 and muffin-tin radii of 2.5, 2.22, 1.91 a.u. for Cs, Cu and Cl, respectively. RIXS experiments were performed by Dr. S Blanco-Canosa at the U41-PEAXIS beamline at BESSY II at 20 K and combined energy resolution, $\Delta E \approx 150$ meV.

7.3 Results and Discussion

The crystal structure of Cs_2CuCl_4 is orthorhombic with space group *Pnma*. Each Cu^{2+} atom is surrounded by 4 Cl^- ions in a distorted tetrahedral coordination (Fig. 7.1a) which splits the *d*-levels into low energy 2-fold e_g and high energy 3-fold degenerate t_{2g} orbitals (Fig. 7.1b). The isolated $CuCl_4^{2-}$ tetrahedra units are further Jahn-Teller distorted towards a lower symmetry D_{2d} point group [218]. This environment provides a spatially anisotropic spin-1/2 triangular antiferromagnet of Cu-Cl chains on a geometrical *bc* plane, bonded by Cl^- ions along the *a* direction. Our magnetic susceptibility measurements show no trace of magnetic order down to 5 K, which is in good agreement with a weakly frustrated magnet [219].

Figure 7.2 summarizes the DFT results of Cs_2CuCl_4 for the simple unit cell depicted in Fig. 7.1a. Only the ferromagnetic state was considered, since there is only one inequivalent Cu atom. Calculations assuming a non-magnetic ground state directly give a non physical metallic solution. We have found that calculations on a $1 \times 2 \times 1$ supercell provide an antiferromagnetic order as the lower energy solution for the ground state, in agreement with the report of Foyevtsova et al. [216]. Nevertheless, we have opted for the ferromagnetic ground state in the simple cell, since our aim is not the determination of the magnetic order and does not have a substantial effect on the electronic energy levels. Therefore, the ferromagnetic solution allows for an easier visualization of the electronic structure and the direct comparison between DFT and the RIXS spectra. Between -4 and 0 eV (Fig. 7.2a) the DOS shows a clear contribution of the Cu $3d$ and Cl $3p$ bands, while the Cs bands do not contribute to the DOS at the Fermi level and, therefore, do not hybridize with Cu. The Cu and Cl bands are separated from the next unoccupied states by a gap of 4.5 eV, having mostly Cs character. We call this charge transfer gap and corresponds to the energy difference between the $[CuCl_4]^{2-}$ cluster and the Cs^+ ions. Note that it must be differentiated from the *traditional* charge transfer gap defined between the transition metal *d* and the ligand *p* states in oxides [220]. On the other hand, the *d-d* gap appears below 1 eV and represents the energy gap between the Fermi level and the empty d_{xy} band.

Figure 7.2b delves into the band structure of Cs_2CuCl_4. Bonding and antibonding bands show up between -4 and -3 eV and between -1 and 1 eV, respectively. The untangled electronic band structure gives a clue about the breaking of the orbital degeneracy sketched in Fig. 7.1b. In a tetrahedral coordination, the $3d^9$ electronic configuration splits the crystal field generated by Cl^- ions surrounding a Cu^{2+} ion into the energetically lower Cu e_g ($d_{x^2-y^2}$ and d_{z^2}) doublet and higher Cu t_{2g} triplet (d_{xy}, d_{xz}, and d_{yz}). Owing to the Jahn-Teller-like uniaxial distortion of the tetrahedron, the t_{2g} triplet is further split into the doubly degenerated d_{xz}, d_{yz} states (e_g irreducible representation) and the half-filled d_{xy} states (b_{2g}), and the $d_{x^2-y^2}$ (b_{1g}) and d_{z^2} (a_{1g}) become also energetically nonequivalent (Fig. 7.1b).

Having carried out a theoretical description of the electronic structure of Cs_2CuCl_4, we proceed with the experimental analysis of the RIXS spectra.

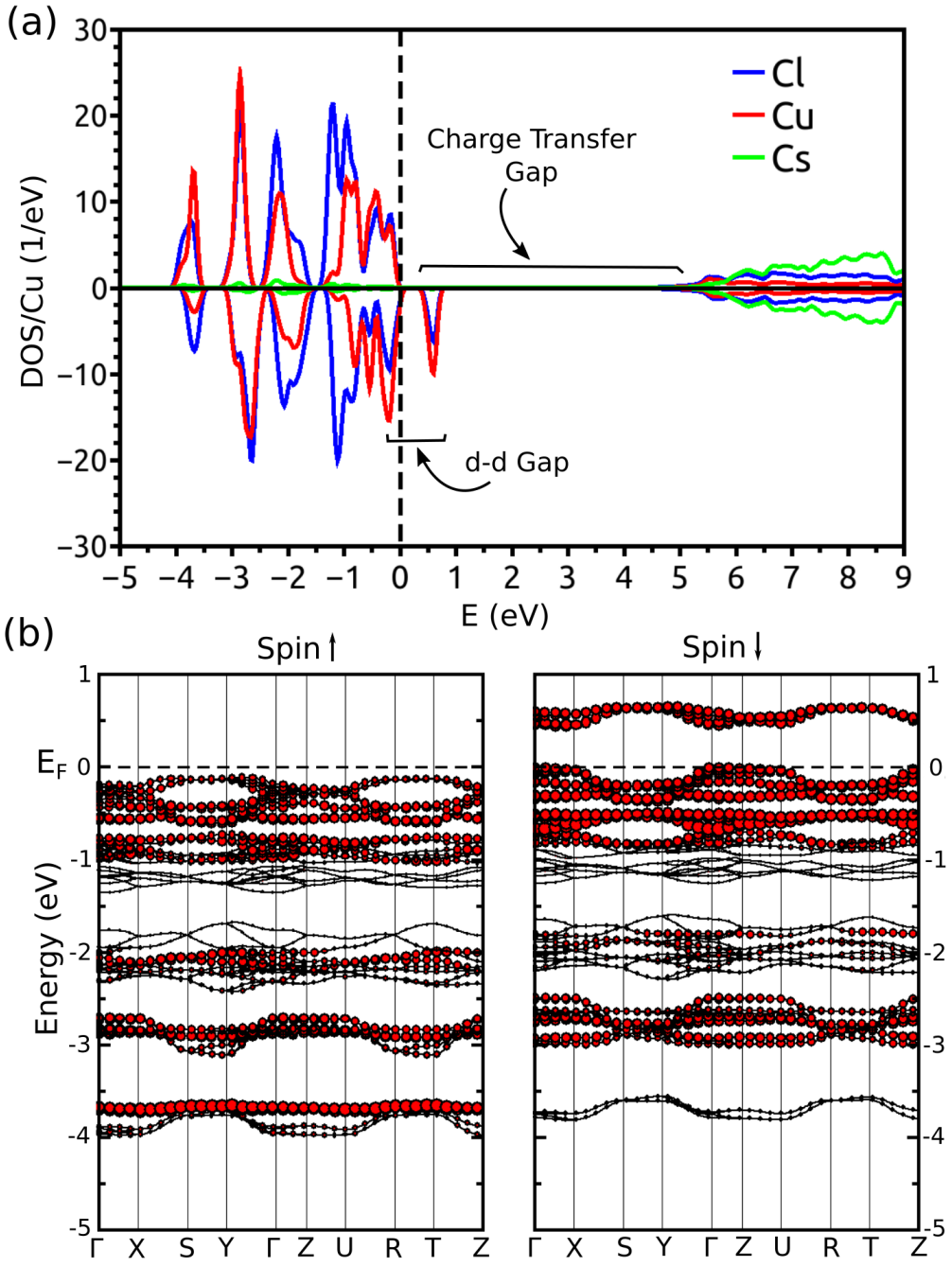


Figure 7.2: (a) Projected DFT density of states (DOS) for the ferromagnetic structure of Cs_2CuCl_4, Cs (Cu, Cl) atom in green (red, blue). Both charge transfer and *d*-*d* energy gaps have been highlighted. (b) Energy bands for the majority (minority) spin channel on the left (right) panel. The *d*-orbital character of the Cu atom is depicted as red circles.

The fast improvement of the RIXS instrumentation in energy resolution of soft X-ray RIXS has allowed to study the low energy electronic properties of correlated oxides, giving detailed information of collective magnetic, charge and orbital excitations in oxides [221]. Figure 7.3b illustrates the case of the Cu^{2+} ion with a $3d^9$ electronic configuration in a tetrahedral crystal field (T_d), with a hole in an $|xy\rangle$ state. In the initial step of the RIXS process, a photon resonant at the Cu L_3 edge ($2p \rightarrow 3d$ transition) is excited from the ground state, $|i\rangle$, into the $3d$ shell (intermediate state, $|n\rangle$) filling the $|xy\rangle$ orbital and creating an excited core-hole state. In the final step ($|f\rangle$), the core hole is annihilated via decay towards the ground state (elastic scattering, E_{loss}=0 eV) or an excited state (magnons, phonons, d-d transitions) [222].

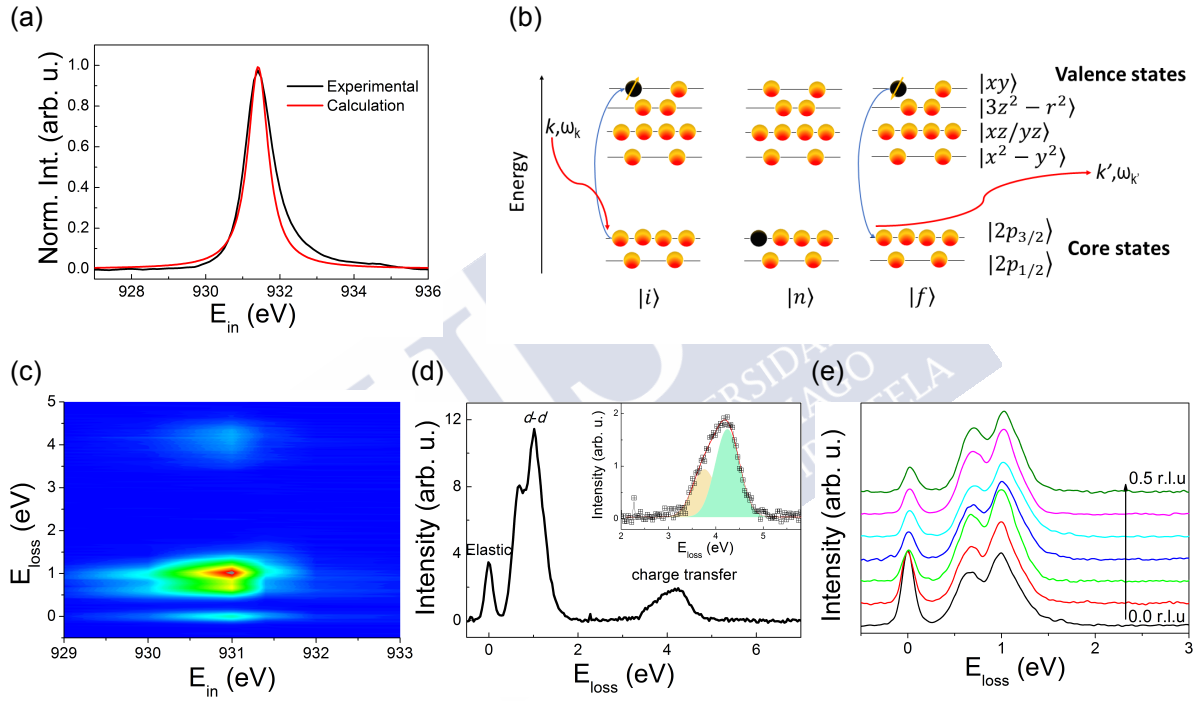


Figure 7.3: (a) Experimental (black) and calculated (red) X-ray absorption (XAS) of Cs_2CuCl_4. (b) Schematics of the RIXS process showing the initial, intermediate and final steps. (c) RIXS map plotting the energy loss, E_{loss}, against the incoming energy, E_{in}, for Cs_2CuCl_4 at 20 K. The maximum intensity of the inelastic features appears at E_{in}= 931 eV. (d) Close up view of the RIXS scan at E_{in}=931 eV, highlighting the elastic, d-d excitations and the charge gap in the inset. (e) In-plane momentum dependence of the d-d excitations, showing no orbital dispersion.

Figure 7.3c displays the incident energy (E_{in}) vs energy loss (E_{loss}) RIXS map. The maximum intensity of the resonant features is observed at E_{in}= 931 eV (Fig. 7.3d), 0.5 eV below the maximum of the L_3 absorption edge (Figure 7.3a), which consists on a feature-less absorption band. In nice agreement with the DFT calculations, the charge transfer

excitations resulting from the $[CuCl_4]^{2-}$ cluster to the Cs $6s$ states are observed as a broad band at E_{loss}= 4 eV, matching the optical gap observed by absorption spectroscopy [223]. As shown in the inset of Fig. 7.3d, this charge transfer gap displays 2 broad bands at 3.7 and 4.2 eV, corresponding to transitions from the Fermi level and the d_{xy} orbital above the Fermi level (Fig. 7.2b) to the upper Cs $6s$ bands. The region between E_{loss}=0.5-1.2 eV (matching the energy difference between the 2 broad charge transfer bands) corresponds to the so called optically forbidden crystal field *d-d* excitations, as widely reported in superconducting cuprates [221], and identified in the DFT calculations below ≈1 eV. The orbital assignment of these excitations was verified by comparing their energy with the DFT calculations. Considering that the $3d$ and $3p$ bands of Cu and Cl atoms are disentangled in energy from the rest of the bands (Fig. 7.2b), an expansion of the Bloch manifold can be performed in real space in terms of *localized Wannier functions*. The 68 Bloch bands in the energy window between -5 and 1 eV have been used to generate the localized and atom centered Wannier functions spanning such Bloch manifold [224]. A symmetry analysis of those Wannier functions allows to identify how the crystal field splitting affects the Cu $3d$ orbitals. As shown in Fig. 7.1b, we found that the $d_{x^2-y^2}$ (b_{1g}) and the d_{xy} (b_{2g}) orbitals correspond to the lowest and highest energy levels, respectively. Apart from that, the strong orthorhombic distortion of the tetragonal environment inverts the energy levels of the doubly degenerate d_{xz} and d_{yz} (e_g) and d_{z^2} (a_{1g}). Therefore, *d-d* transitions originate from the decay of an electron from the $d_{x^2-y^2}$, d_{z^2}, d_{xz} and d_{yz} orbitals due to the broken degeneracy of the $3d$ states.

To better understand the *d-d* excitations in the RIXS spectra, we have adopted the *hole* language, where the ground state represents a hole in the d_{xy} orbital, hence, a d_{yz} orbital excitation corresponds to moving a hole from the d_{xy} to the d_{yz} orbital. Within the energy resolution of our experimental setup, we can discriminate the 3 orbital intratomic transitions; 2 sharp excitations at 0.67 and 1.02 eV, respectively and a shoulder at 1.21 eV (see Fig. 7.4b). Having considered only the tetrahedral point group, T_d, this would result in a $10D_q$ value of 0.45 eV. Further, we see no orbital dispersion (Fig. 7.3e) indicating highly localized *d-d* excitations, as expected due to the strongly ionic character of Cs_2CuCl_4 compound. Since these orbital *d-d* excitations are intra-atomic and well localized, they can be simulated within a full-multiplet calculation considering a single site of a Cu^{2+} ion of the D_{4h} point group, isomorphic with the D_{2d} [225], which is exemplified by a regular tetrahedron elongated along one of its C_2 axes. The RIXS simulations were carried out by Dr. S. Blanco-Canosa with the Quanty code [226, 227] including the Coulomb interactions and multiplet effects leaving free the radial integrals D_q (crystal field splitting), D_s and D_τ (distortions of the tetrahedra), which are the splitting terms for the Y_2^0 and Y_4^0 spherical harmonics, as input parameters in the calculation. Figure 7.4a displays the calculated RIXS map for Cu^{2+} within the D_{4h} point group. The 3 orbital transitions corresponding to the $d_{x^2-y^2}$, d_{z^2} and doubly degenerate d_{xz}, d_{yz} orbitals are clearly identified. As shown in Fig. 7.4b, the experimental and theoretical RIXS spectra is fairly well reproduced after normalization to the same height of the *d-d* features, with an additional instrumental and experimental broadening of 0.1 and 0.25 eV, respectively.

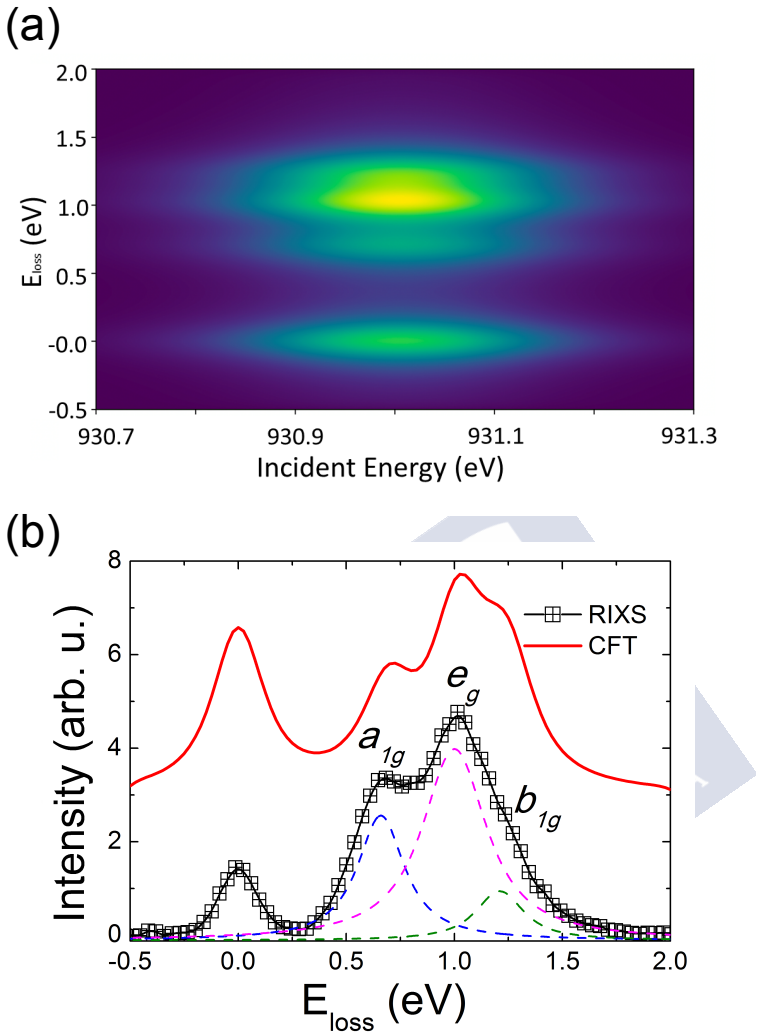


Figure 7.4: (a) Calculated RIXS intensity map within the CFT theory, highlighting the crystal field excitations. (b) Comparison of the experimental and theoretical RIXS spectrum for 931 eV incident energy. Labeled are the *d*-*d* transitions. The calculated RIXS spectrum is vertically shifted for clarity.

From the simulation, we obtain D_q=-0.120 eV, D_s=0.085 eV and D_τ=-0.165 eV. The signs and relative magnitudes of D_q, D_s and D_τ depend upon the nature of the distortion undergone by the tetrahedron and indicate a proximity to a square planar geometry. The negative values of D_q and D_τ account for the stabilization of the b_{1g} state ($d_{x^2-y^2}$ orbital) as the ground state, followed by the e_g doublet (d_{xz}/d_{yz} orbitals), in agreement with the *wannierization* of the DFT bands. Besides, the ground state is 2-fold degenerate with spin and orbital quantum numbers $\langle S_z \rangle = \pm 1/2$ and $\langle L_z \rangle = \pm 0.31$ and orbital occupations

N_{Cu}= 9.0 and N_{Cl}=6.0 electrons, which agree with the strong ionic character of the Cu^{2+} and Cl^{-} bond. To confirm the validity of the crystal field parameters, Dr. Blanco-Canosa simulated the XAS spectrum of Cs_2CuCl_4 using the same atomic Hartree-Fock values as for the RIXS simulations and without any other adjustable parameter (see Figure 7.3a). The calculation is rather satisfactory and nicely models the experimental XAS spectrum of Cs_2CuCl_4. Therefore, we have fully characterized the electronic spectrum of this compound.

7.4 Conclusions

In this chapter we have carried out a detailed spectroscopic study of the geometrically frustrated quantum spin liquid Cs_2CuCl_4. We have found a good agreement between experiments, cluster calculations and DFT results. We have been able to resolve the crystal field splittings, obtaining the values of D_q, D_s and D_τ that reproduce reasonably well the RIXS spectrum and have shown that the *charge transfer gap*, commonly seen in the RIXS experiments, corresponds here to the energy gap between the $[CuCl_4]^{2-}$ cluster and the Cs^{1+} *s* states. Moreover, we find that the inelastic spectrum describes a strongly ionic character of the Cu-Cl bond , which might be the reason for the lack of dispersion of the *d-d* excitations, unlike the orbiton dispersion observed in cuprates with a high degree of covalency [228, 229].

USC UNIVERSIDADE DE SANTIAGO DE COMPOSTELA

USC
UNIVERSIDADE
DE SANTIAGO
DE COMPOSTELA

8 Cr-based van der Waals Ferromagnets

Van der Waals compounds provide an excellent platform to study low-dimensional properties. In particular, magnetism in that limit has attracted a great deal of attention due to their numerous applications. In this chapter, we present a comparative theoretical and experimental study of the electronic structure and magnetic properties of the two-dimensional van der Waals ferromagnets $CrBr_3$ and $Cr_2Ge_2Te_6$. Dimensionality effects are studied by applying pressure on both systems. We found that their dissimilar electronic structure leads to a different magnetic behaviour. This work can be found in Ref. [VI] from the List of Publications.

8.1 Introduction

At this point of the thesis, we initiate the study of transition-metal layered van der Waals materials. This kind of compounds allows to reach the low dimensional limit, where the d electrons of the transition metal might prompt to emergent phenomena.

Since the successful synthesis of graphene in 2004 [230], two-dimensional (2D) materials have continuously increased their academic and technological relevance, and many other materials like transition metal dichalcogenides [231], boron nitride (BN) [232], or phosphorene [233], have been profusely studied. Besides, 2D materials can exhibit multitude of exotic properties when combined in heterostructures [234, 235].

In this last decade, long-range ferromagnetic (FM) order in several atomic-thick materials, such as $FePS_3$, CrI_3 and Fe_3GeTe_2, has been reported [236–238]. The advent of long-range 2D ferromagnetism brings about new transport phenomena in two dimensions, like tunneling magnetoresistance [239, 240] and electrical switching of magnetic states [241], promoting 2D ferromagnets as versatile platforms for engineering new quantum states and device functionalities.

Cr-based van der Waals ferromagnets have gained attention over the past years due to their high magnetic moment and Curie temperature (T_C). In these compounds, magnetic order is determined by different exchange paths. For instance, the isotropic in-plane magnetic coupling J_{in} in transition metal dichalcogenides (TMDs), di- and trihalides and phosphosulfides, is determined by the competition between metal-metal direct exchange

and indirect exchange mediated by the anions [42]. These exchange paths have been found to be highly dependent on the crystal [242] and electronic structure [243], and different strategies have been proposed to tune them [244, 245]. Therefore, the stabilization of 2D magnetic order requires a comprehensive understanding of the electronic structure and magnetic exchange interactions of their 3D van der Waals parent compounds.

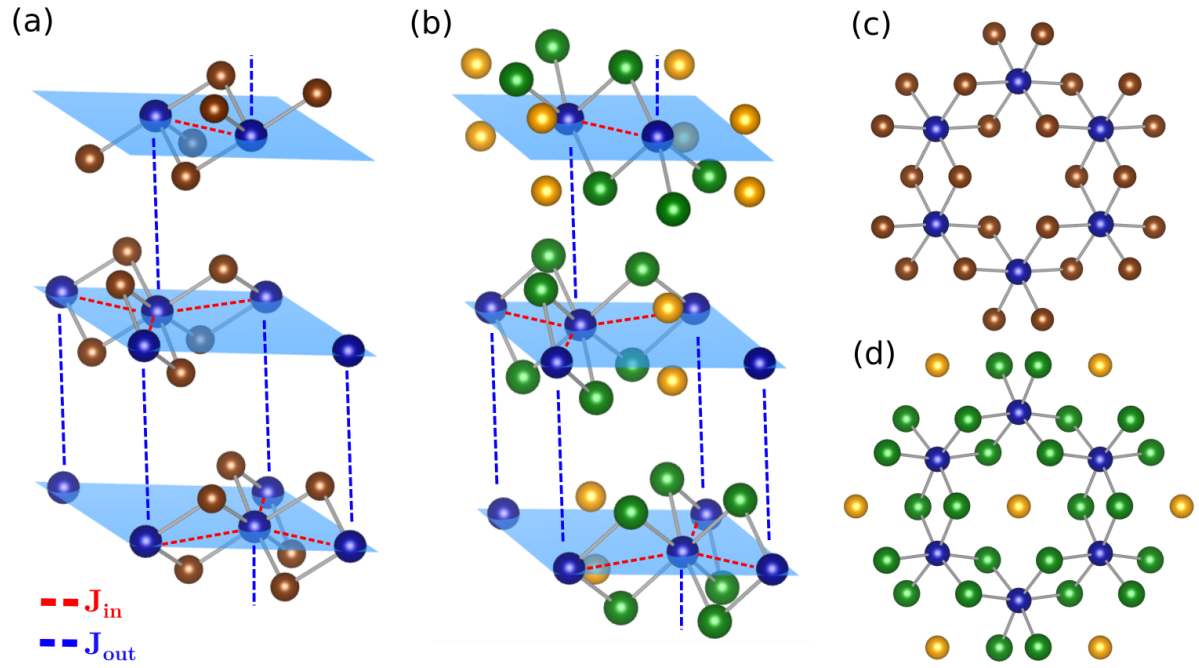


Figure 8.1: Unit cells of (a) $CrBr_3$ and (b) $Cr_2Ge_2Te_6$. Cr atom in blue, Br atom in brown, Ge atom in yellow and Te atom in green. Different exchange constants are considered: an in-plane J_{in} that takes into account both the direct Cr-Cr exchange and the superexchange via Br or Te, and the out-of-plane J_{out} that couples out-of-plane Cr-Cr neighbours. (c) and (d) show the top view of $CrBr_3$ and $Cr_2Ge_2Te_6$ unit cells, respectively.

In this chapter, we combine *ab-initio* calculations and high-pressure experiments on single crystals of $CrBr_3$ and $Cr_2Ge_2Te_6$. These two Cr-based van der Waals compounds crystallize in a lamellar structure with hexagonal symmetry (space group no. 148), forming a honeycomb network of edge-sharing octahedra, stacked with van der Waals voids separating the Cr^{3+}-rich planes, as shown in Fig. 8.1. Both compounds retain their bulk ferromagnetism down to the single layer limit, T_C=34 K for $CrBr_3$ and T_C=61 K for $Cr_2Ge_2Te_6$, with an out-of-plane easy axis [246–249]. This magnetic anisotropy is necessary to circumvent the restrictions of the Mermin-Wagner theorem, leading to a long-range FM order at the monolayer limit.[1] We will explore, in a comparative way, the electronic

[1]The Mermin-Wagner theorem establishes that a continuous symmetry cannot be spontaneously broken at finite temperature in systems with sufficiently short-range interactions in dimensions $D \leq 2$ [250]. Thus, long-range fluctuations arise with little or no energy cost (massless Goldstone modes) that

structure and the pressure dependence of the in- and out-of-plane exchange interactions, J_{in} and J_{out}, (shown in Fig. 8.1) of $CrBr_3$ and $Cr_2Ge_2Te_6$. We will find that they present a different electronic structure character. We will see that this feature results in a dissimilar pressure evolution of the magnetic transition temperatures in each compound. Thus, highlighting the crucial role of the electronic band structure in the pursuit for new materials retaining a large Curie temperature down to the monolayer limit.

8.2 Experimental and Computational Methods

Density Functional Theory (DFT) calculations [17, 18] were performed using the all-electron, full potential code WIEN2K [30] based on the augmented plane wave plus local orbital (APW+lo) basis set. For the structural relaxations, in particular the computation of the lattice parameters at different pressures, special exchange-correlation functionals were needed to deal with the out-of-plane van-der-Waals-type interactions [251]. The exchange-correlation term chosen to compute the exchange parameters was the generalized gradient approximation (GGA) in the Perdew-Burke-Ernzerhof scheme, which is found to provide a good description of the electronic structure and magnetism [19]. A fully-converged k-mesh, $R_{mt}K_{max}$= 7.0 and muffin-tin radii of 2.42 a.u. for Cr, 2.07 a.u. for Ge, 2.19 a.u. for Br and 2.38 a.u. for Te, were used in the calculations. Besides, the Curie temperature (T_C) at each pressure was obtained by solving the nearest-neighbour Heisenberg model generated using the computed exchange constants. We have applied periodic boundary conditions, 10^6 steps in total and a set of 864 particles. The Heisenberg model was solved using the Monte Carlo Metropolis algorithm [43]. The T_C was obtained by fitting the magnetization curves as explained in Ref. [252].

Regarding the experimental details. They were performed by our colleagues: Drs. S. Blanco-Canosa, H. Babu-Vasili, P. Gargiani, Hongze Li, Jian-Shi Zhou and F. Rivadulla. Single crystals of $CrBr_3$ and $Cr_2Ge_2Te_6$ were synthesized from the purely elemental starting materials and provided by HQ Graphene. The quality of the crystals was confirmed by X-ray diffraction and X-ray photoemission spectroscopy (XPS). X-ray absorption (XAS) and X-ray magnetic circular dichroism (XMCD) measurements up to 6 Tesla were performed at Cr $L_{2,3}$ edge at the BOREAS BL29 beamline at ALBA synchrotron [253]. Magnetic measurements under pressure up to P=1 GPa were performed in a Be-Cu cell, using a silicon oil as pressure medium, inside a MPMS SQUID from Quantum Design. The pressure was monitored *in situ* through the superconducting transition of a Sn pressure gauge. X-ray diffraction under pressure was carried out in a diamond anvil cell using 4:1 methanol:ethanol as pressure media. The pressure dependence of the lattice volume up to 5 GPa was fitted to the Birch-Murnaghan equation.

ruin the long-range ordered phase. For our purposes, that will be the case of 2D ferromagnetic phases. We will come back in more detail to this theorem in the next chapter, and how to circumvent it. In this chapter it will not apply since we will deal with 3D systems.

8.3 Electronic Structure

In this Section we will analyze the electronic structure for both compounds. Figure 8.2 shows the density of states computed with DFT for $CrBr_3$ and $Cr_2Ge_2Te_6$. In both cases, the electronic structure of Cr can be well described as a Cr^{3+}:d^3 cation with S=3/2, the majority-spin t_{2g} bands being fully occupied.

On the one hand, for $CrBr_3$, the states just below and above the Fermi level have dominant Cr d character, thus suggesting a Mott insulator behaviour with a d-d energy gap (top panel in Fig. 8.2a). This result is in agreement with previous photoluminescence experiments [249].

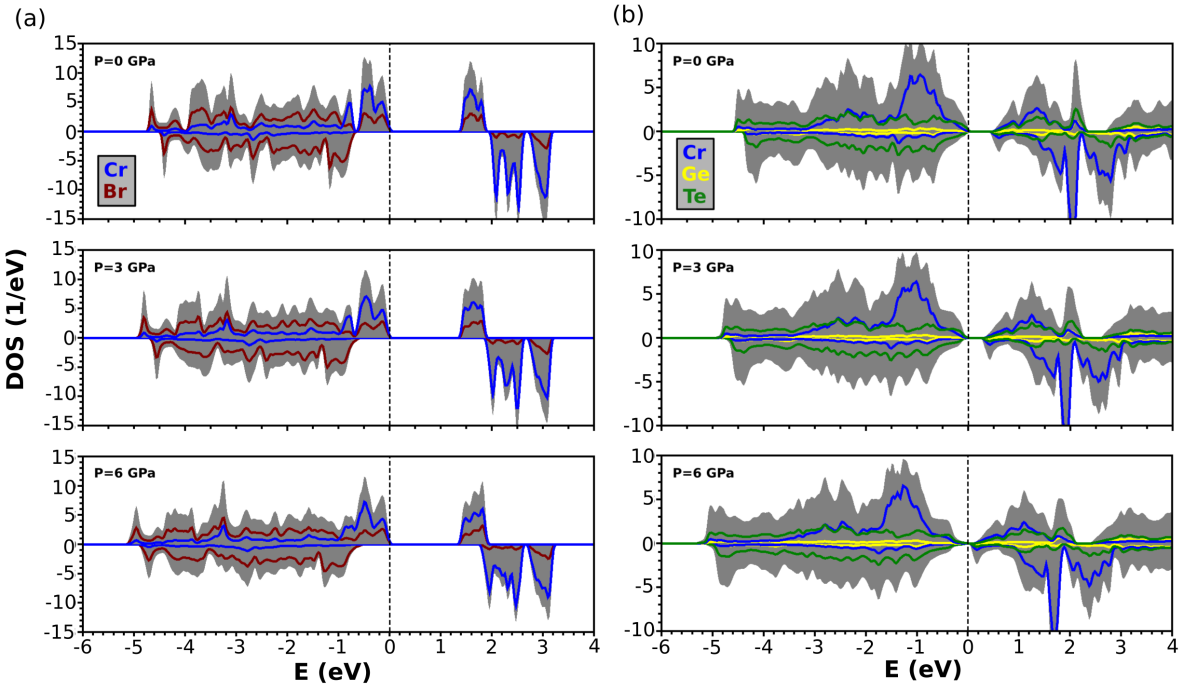


Figure 8.2: Density of states as a function of pressure. The shaded area represents the total DOS, in positive (negative) the majority (minority) spin channel. Fermi energy was set to zero. (a) Partial density of states (DOS) of the Cr d (blue) and Br p (brown) states. The energy gap has d-d character. (b) Partial density of states (DOS) of the Cr d (blue), Ge p (yellow) and Te p (green) states. Note the large bandwidth of the Te p states leading to a substantial charge transfer; the larger weight at the Fermi level is due to Te p bands. The gap closes completely at high pressure in this case.

On the other hand, for $Cr_2Ge_2Te_6$, the states just below the Fermi level are very broad and have dominant Te p character. A p-d energy gap is observed for this material, which suggests a charge transfer insulator behaviour. Ge atoms do not play a substantial role in the electronic structure, with a vanishing contribution close to the Fermi level (top panel in Fig. 8.2b).

We can analyze now the effect on the electronic structure of each system when pressure is included. In order to do so, both systems are fully relaxed at different volumes (including the lattice parameters, c/a ratio and the internal positions). The Birch-Murnaghan equation is used to obtain the pressure value at each volume [254]. Figure 8.2 shows the DOS and the partial DOS (pDOS) as a function of pressure for both compounds. In Fig. 8.2a we see that $CrBr_3$ does not undergo a substantial modification of its electronic structure with pressure. The d-d energy gap observed at P=0 GPa is preserved when pressure is raised up to 6 GPa. However, Fig. 8.2b shows how the p-d energy gap of $Cr_2Ge_2Te_6$ closes as pressure is increased. Therefore, our calculations predict that $Cr_2Ge_2Te_6$ undergoes an insulator to metal transition at high pressure. This can be better seen in Fig. 8.3a, where the energy gap is plotted as a function of pressure for both compounds. The values of the band gaps presented here were obtained using GGA, which has a tendency to underestimate them. This is less so when dealing with crystal-field gaps [255]. Yet, the pressure evolution should be correct in any case.

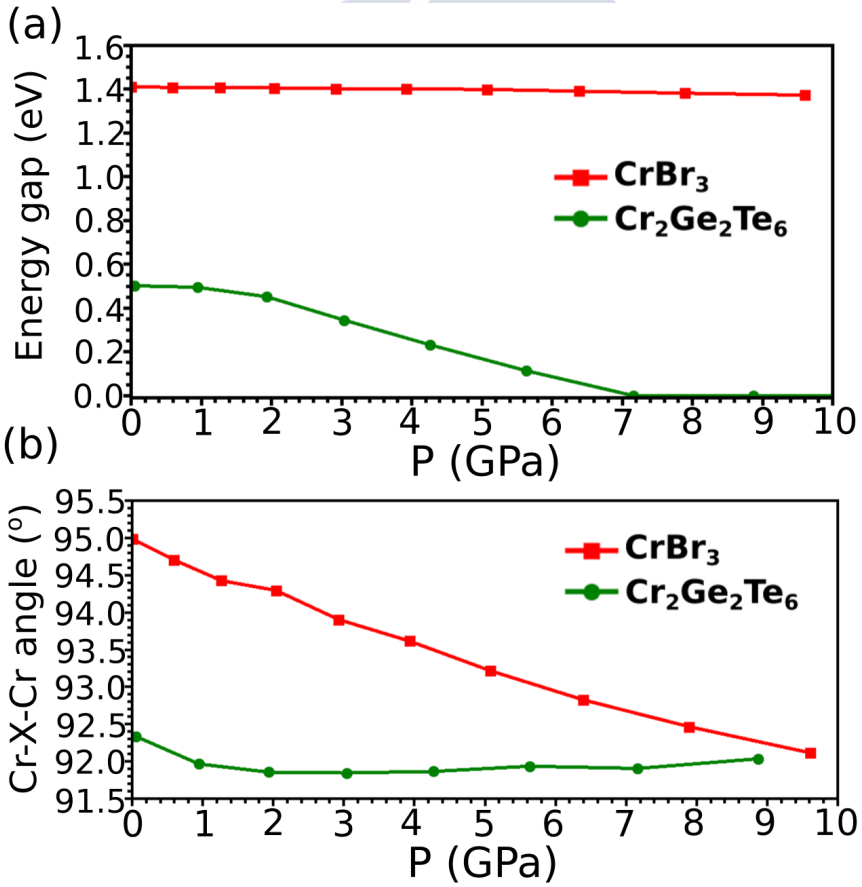


Figure 8.3: (a) Calculated energy gap as a function of pressure for both compounds, obtained using the GGA exchange-correlation functional. (b) Evolution of the Cr-X-Cr angle as a function of pressure. X represents Br or Te atoms.

Apart from that, in Fig. 8.3b the pressure dependence of the cation-anion-cation angle is plotted. While for the Mott insulator $CrBr_3$ the angle shows a monotonic decrease up to 10 GPa, in $Cr_2Ge_2Te_6$ the angle remains constant in the whole range of pressures up to 10 GPa. Hence, external pressure modifies the internal structure of $CrBr_3$, while in $Cr_2Ge_2Te_6$, there is a pressure-induced insulator-to-metal transition as a consequence of the closing of the energy gap due to the change in the Te-Cr distance and not the Cr-Te-Cr angle, which remains roughly unchanged.

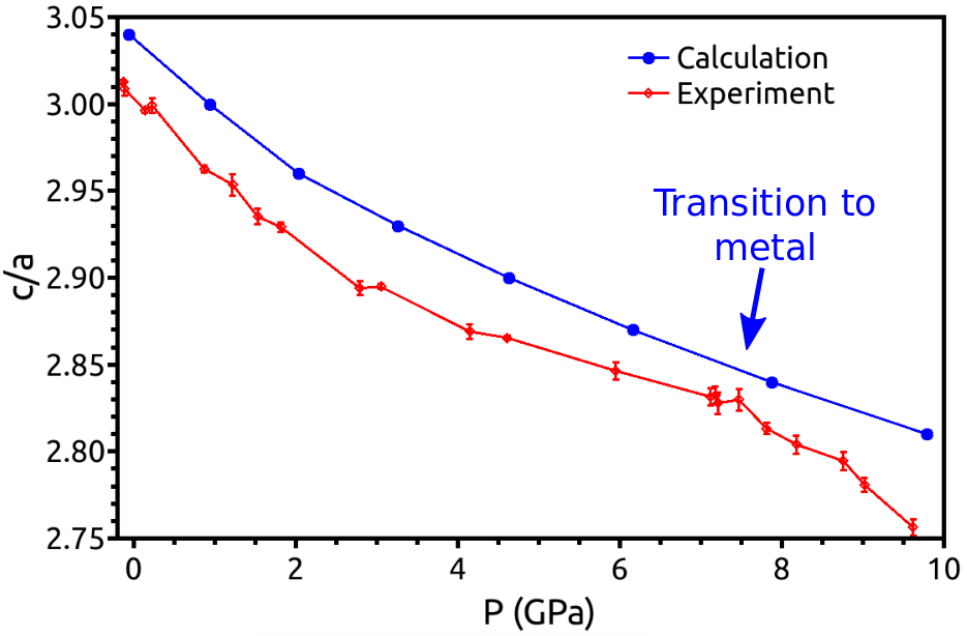


Figure 8.4: Comparison of the high pressure XRD data with the results of our ab initio calculation for the c/a ratio of $Cr_2Ge_2Te_6$. DFT predicts a transition to a metallic state around the same pressure that XRD data shows a peak.

In order to shed light on the nature of the pressure-induced metal-insulator transition predicted by our DFT calculations for $Cr_2Ge_2Te_6$, we have performed high pressure X-ray diffraction (XRD) measurements. In Fig. 8.4, we plot the pressure dependence of the ratio of the lattice parameters, c/a ratio, showing a sudden decrease above 7 GPa, suggesting a structural transition. This pressure coincides with the collapse of the electronic gap, as predicted by our *ab initio* calculations. The insulator-to-metal transition observed in our DFT calculations was obtained assuming that the symmetry of the lattice remains unchanged upon pressure. Pressure-induced structural phase transitions and amorphizations have been observed before by means of high pressure X-ray diffraction between 18 and 30 GPa for $Cr_2Ge_2Te_6$. However, no structural anomalies were reported at pressures relevant in this work [256]. Despite the high pressure X-ray data shows a structural transition, whether this structural transition is accompanied with a softening of the lattice on approaching the pressure where the insulator to metal transition is

predicted or a mere structural change to a lower symmetry semiconducting state, cannot be concluded from our data. However, in the 2021 APS March Meeting, Prof. Yoshiya Uwatoko reported the experimental finding of the insulator-to-metal transition that we have predicted for this compound [257].

8.4 Magnetic Properties

Now that we have seen that each compound presents a different electronic structure character, leading to a different evolution with pressure, we can analyze how the ferromagnetic order evolves. Considering the results of the previous section for the electronic structure, we might expect that also the magnetic behaviour is going to be different for each compound. In fact, that is what we have obtained from our experiments.

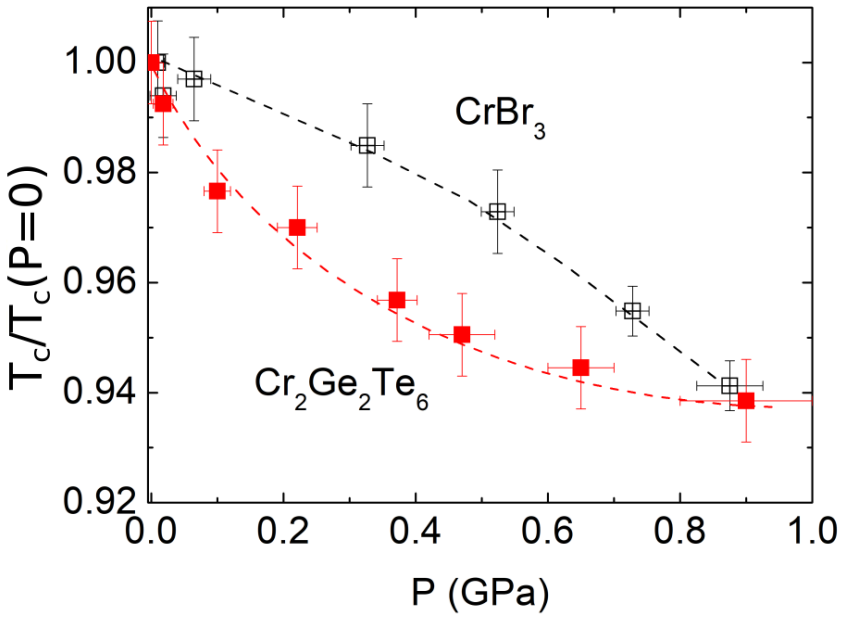


Figure 8.5: Experimental pressure dependence of the normalized Curie temperature for $Cr_2Ge_2Te_6$ and $CrBr_3$. A different trend between both compounds can be easily identified.

Figure 8.5 displays the evolution of the magnetic transition temperature of $CrBr_3$ and $Cr_2Ge_2Te_6$ up to 1 GPa. A normalized Curie temperature is represented in order to better compare the trends for both compounds. At zero pressure, the magnetic transitions appear as an upturn in the magnetization upon cooling at 37 and 63 K for $CrBr_3$ and $Cr_2Ge_2Te_6$ respectively, following a Curie-Weiss behavior at $T>T_C$. As seen in the raw data and summarized in Fig. 8.5, the T_C of both compounds decreases as pressure is applied, in agreement with previous reports [258, 259] and at odds with the expectations for the pressure dependence of the exchange interaction in a localized magnetic system [260]. Our data also shows a different trend for $T_C(P)$. While the critical temperature

of $CrBr_3$ displays a slightly convex decay, the decrease observed in $Cr_2Ge_2Te_6$ is concave and shows a clear tendency to saturation at the highest pressures analyzed in this work.

Our aim now will be to provide an explanation from a theoretical point of view for the different experimental trends observed in Fig. 8.5. As described in the previous chapter, the electronic structure shows largely ionic Cr^{3+}: S= 3/2 cations with a half-filled spin-polarized t_{2g} manifold. This leads to a significant gap opening at the Fermi level for $Cr_2Ge_2Te_6$ and $CrBr_3$, even at the LDA/GGA level, without the need to introduce strong correlation effects in the calculations. In a first approximation, this indicates that the magnetic semiconductor limit could be applicable to understand the pressure dependence of these systems.[2] However, even if the system can be described in the localized limit, various different exchange interactions compete, responding differently to pressure, and this leads to the complex pressure dependence of T_C observed experimentally. The different energy contributions to the magnetic ground state can be modelled separately by considering the nearest-neighbour J_{in} and the J_{out} exchange couplings in a Heisenberg-like Hamiltonian. The different J's are shown in Fig. 8.1, with the J_{in} and J_{out} depicted as broken red and blue lines, and the Cr^{3+} cations surrounded by edge-sharing trigonally distorted octahedra. Four more exchange paths including second and third nearest neighbours have been included in previous works [261]. Nevertheless, as we will discuss, our simple Heisenberg-type model suffices to explain the magnetic order as a function of pressure in these compounds. J_{in} is the sum of two exchange contributions, the direct Cr-Cr exchange across the octahedral edge, which is antiferromagnetic (AF) between two half-filled t_{2g} bands, and the indirect Cr-(Br or Te)-Cr superexchange at approximately 90-degrees. According to Goodenough-Kanamori-Anderson rules, the indirect exchange, cation-anion-cation, can be either FM or AF, depending on the strength of the delocalization and correlation superexchange effects [42]. At zero pressure, our results show that $J_{in} = 27.5$ K and $J_{out} = 12$ K for $Cr_2Ge_2Te_6$ and $J_{in} = 28.5$ K and $J_{out} = 6$ K for $CrBr_3$. These values were obtained by fitting total energy differences computed *ab initio* between the magnetic configurations shown in Fig. 8.6 to a Heisenberg-type Hamiltonian.

The following equations can be obtained for the magnetic exchange constants as a function of the energy of the magnetic configurations shown in Fig. 8.6:

$$\begin{aligned} J_{out} =& \frac{E_{AFM1} - E_{FM1}}{27} \\ J_{in} =& \frac{1}{3}\left(\frac{2(E_{AFM2} - E_{FM2})}{27} - J_{out}\right), \end{aligned} \tag{8.1}$$

where E_{FM1}, E_{AFM1}, E_{FM2} and E_{AFM2} are the energies of the magnetic configurations shown in Fig. 8.6. We can also calculate the pressure dependence of both J_{in} and J_{out}. This is shown in Figs. 8.7a and and 8.7b. At first glance we can notice that all J's are

[2]Note that for the case of $Cr_2Ge_2Te_6$ we have only performed this analysis at pressures where the system remains a semiconductor.

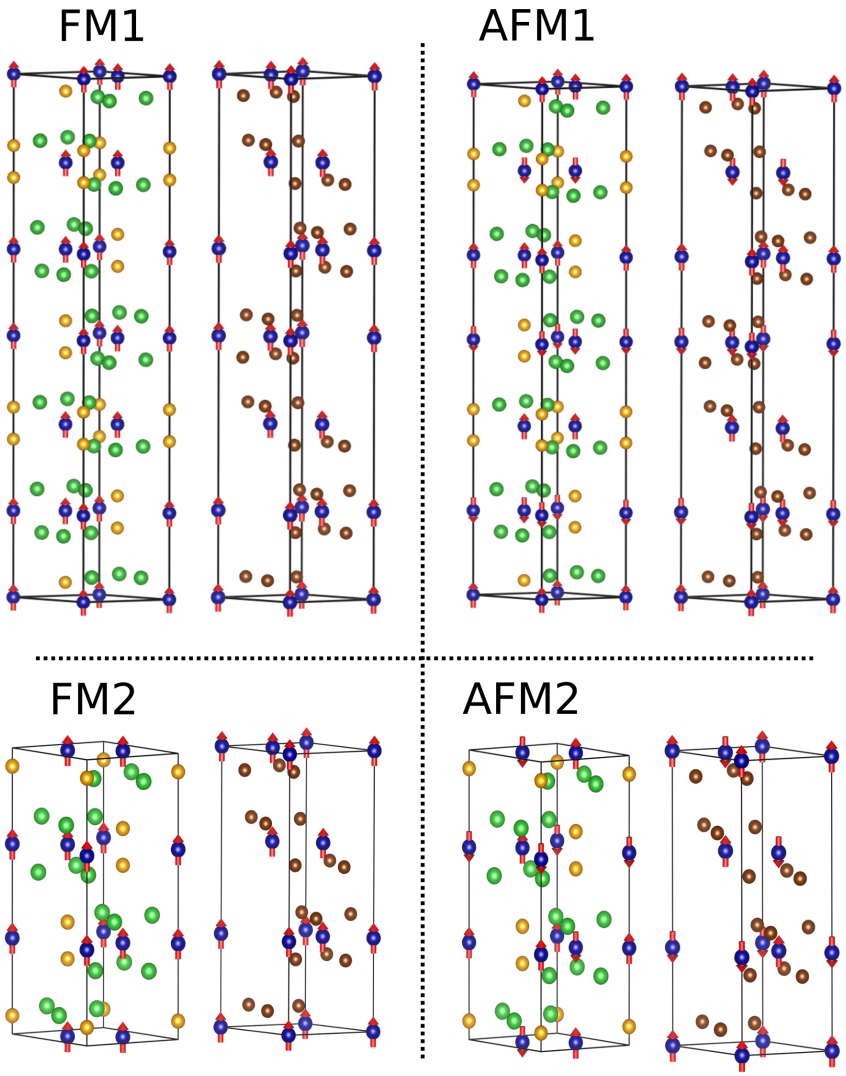


Figure 8.6: Magnetic configurations used to compute the magnetic exchange constants. Cr atom in blue, Br atom in brown, Ge atom in yellow and Te atom in green.

positive, which explains the FM order observed in the experiments for both compounds. But let us further analyze the magnetic behaviour.

With the calculated values of the magnetic exchange constants, we have set up a Heisenberg-type Hamiltonian of interacting spins, and solved it using a classical Monte Carlo simulation. This allowed us to obtain a theoretical T_C and its evolution with pressure. At 0 GPa the theoretical Curie temperatures are 77 K for $Cr_2Ge_2Te_6$ and 69 K for $CrBr_3$, this small overestimation is in the range of acceptable values for GGA. Note that for the Br compound the overestimation is bigger compared to the experimental value.

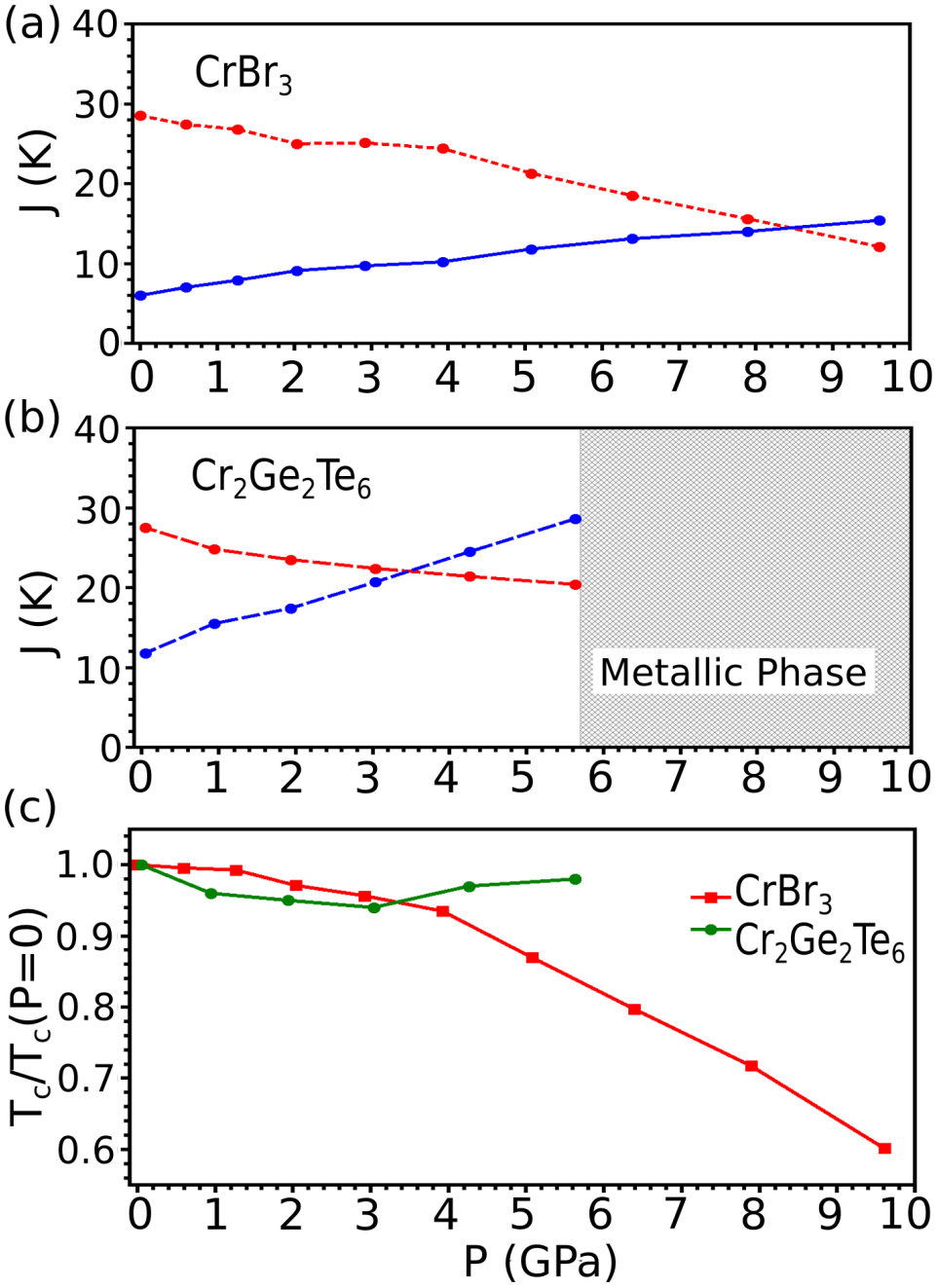


Figure 8.7: (a) and (b) values of the exchange constants extracted using a Heisenberg-type Hamiltonian for $CrBr_3$ and for $Cr_2Ge_2Te_6$, respectively. J_{out} in blue, J_{in} in red. The out-of-plane coupling becomes larger as pressure is applied. (c) Evolution of the normalized transition temperature with pressure obtained from the Monte-Carlo simulation.

The Mott-insulator character of $CrBr_3$ might explain it, since the electronic correlations play a major role in this kind of systems and the GGA treatment underestimates them.

Despite the overestimation of the absolute value of magnetic exchange constants, the actual pressure dependence of the calculated T_C is in good agreement with the observed experimental trend, as it can be seen from a comparison between Figs. 8.5 and 8.7c. Again, the theoretical values are normalized to the T_C at ambient pressure for better comparison. In the Heisenberg-type Hamiltonian we have included an anisotropic term as in Ref. [261], since it was reported that for $Cr_2Ge_2Te_6$ this term changes its sign with pressure [262]. However, no influence on the value of T_C or its pressure dependence was observed due to the much smaller energy scale of that anisotropic term.

For $CrBr_3$, J_{out} increases with pressure while J_{in} decreases (Fig. 8.7a). Since $J_{in} > J_{out}$ and the number of Cr in-plane neighbours is greater than the out-of-plane, the trend of T_C(P) is governed by J_{in}. Therefore, decreasing J_{in} produces the decrease of T_C as pressure increases, in agreement with the experimental values in Fig. 8.5. On the other hand, for $Cr_2Ge_2Te_6$, J_{out} increases with pressure, while, initially, J_{in} decreases and saturates at higher pressure just before entering into the metallic phase (see Fig. 8.7b). Therefore, J_{in} dominates the change of T_C at low pressures, but J_{out} becomes the dominant term at higher pressures. This is in agreement with the experimental evolution presented for the T_C with pressure (Fig. 8.5). Further experimental measurements at higher pressures should confirm the minimum in T_C predicted in our calculations. In fact, Prof. Yoshiya Uwatoko reports in his March Meeting talk this minimum and a significant increase of the Curie Temperature in the metallic phase [257].

8.5 Conclusions

In this chapter we have explored pressure effects on the electronic, magnetic and structural properties of $CrBr_3$ and $Cr_2Ge_2Te_6$ by a combination of experimental and computational approaches.

We found that $CrBr_3$ is a Mott-Hubbard like insulator with a *d*-*d* energy gap. It follows that the system remains insulating under pressure. On the other hand, the energy gap of $Cr_2Ge_2Te_6$ is found to have *p*-*d* character, which leads to a charge transfer insulating behaviour. Our calculations predict an insulator-to-metal transition to occur at around 6 GPa, which might be related to the structural transition observed in the high pressure X-ray experiments. This different electronic structure character of each compound and its evolution with pressure are found to determine the pressure dependence of the Curie temperature and the magnetic exchange interactions in $Cr_2Ge_2Te_6$ and $CrBr_3$. The experimental observation yields a reduction of the Curie temperature as pressure is applied, but with a different trend for each compound. *Ab initio* calculations reveal that the microscopic origin for this trend relies on the different pressure dependence of the in- and out-of-plane magnetic exchange couplings.

This work sheds light on the competition of the different types of exchanges that may occur in similar quasi-two-dimensional magnetic materials. Long-range order depends on the type of spin-spin interactions, which themselves compete with intrinsic fluctuations

and determine the magnetic anisotropy and the stability of the long-range magnetic order at the monolayer limit. We have seen that in Cr-based van der Waals structures, these spin-spin interactions (and their competitions) are strongly dependent on the evolution of the electronic structure with pressure and, therefore reciprocally, on the dimensionality.

USC UNIVERSIDADE DE SANTIAGO DE COMPOSTELA

9 Ferromagnetism and Charge Density Waves in TMDs

In this chapter we focus on the study of transition metal dichalcogenides (TMDs). These compounds are promising candidates to show long-range ferromagnetic order in the single-layer limit. Moreover, it is known that many TMDs develop a charge density wave (CDW) order at low temperatures. Here, we will study the interplay between both the magnetic and the structural orders of two TMD, $CrTe_2$ and VSe_2. While $CrTe_2$ presents a Heisenberg-like ferromagnetism where magnetic moments can be considered well localized, VSe_2 tends to an itinerant behaviour. The effect of the CDW on the ferromagnetic order of each compound will be analyzed, and a different trend will be found. While in $CrTe_2$ the CDW produces the stabilization of the long-range ferromagnetic order, in VSe_2 the CDW has a detrimental effect, quenching ferromagnetism. This chapter summarizes and presents together two independent works that can be found in Refs. [VII] and [VIII] from the List of Publications for $CrTe_2$ and VSe_2, respectively.

9.1 Introduction

In the previous chapter we started studying van der Waals materials with the aim of unveiling the origin of two dimensional (2D) ferromagnets. Low dimensional ordered phases have been boosted by the discovery of 2D ferroelectrics and ferromagnets in the last decade [261, 263]. In particular, the latter kind of systems has gained attention due to the multiple applications that it could prompt in other research areas: spintronics, experiments on quantum anomalous Hall effect, tunneling magneto resistance, spin valves, etc [264].

We have already mentioned in Chapter 8 some systems where 2D ferromagnetism has been observed [236–238]. In this chapter we pay attention to the family of layered transition metal dichalcogenides (TMDs) [265, 266]. The formula unit of these compounds is MX_2, where M corresponds to a transition metal and X to a chalcogen atom. The transition metal in the structure provides the d-electrons that might lead to a non-zero magnetic

moment, and eventually to long-range ferromagnetic order. Layered compounds bonded via van der Waals interactions allow an accurate control of the material thickness, thus making possible to achieve the 2D limit by different techniques, for instance: mechanical exfoliation, chemical vapor deposition and layer-by-layer Molecular Beam Epitaxy (MBE) [267–269].

Many of the properties that TMDs have in the bulk structure are present in the 2D limit, like charge density wave or superconducting phases [270, 271]. As we have anticipated in the previous chapter, long-range ferromagnetic order in 2D systems is possible if the restrictions imposed by the Mermin-Wagner theorem are circumvented [250]. Let us recall that the Mermin-Wagner theorem establishes that spin-rotational invariance cannot be spontaneously broken at finite temperature in systems with sufficiently short-range interactions in dimensions $D \leq 2$, thus, forbidding long-range ferromagnetic order. Long-range fluctuations arise with little or no energy cost (massless Goldstone modes) that ruin the long-range ordered phase. There are ways to overcome the restrictions of the theorem. For instance, this can be done by applying an external field or force such as a magnetic field or strain. But, more interestingly, it can also be achieved intrinsically by a strong magnetic anisotropy in the crystal driven by spin-orbit coupling (SOC) or, as we will see here, by the emergence of a charge density wave (CDW) phase. But, what do we understand by a CDW?

A CDW phase corresponds to a *static* modulation of the conduction electronic density of a system. Due to the static character of this electronic modulation a crystal lattice distortion is also produced. Therefore, we can think of a CDW as a structural transition in which the crystal symmetry is lowered, i.e., the system evolves from a given space group to a subgroup contained in the former. The original idea of CDW transitions was proposed by Peierls for a 1D chain of atoms [57]. A metal-insulator transition occurs accompanied by a lattice distortion known as Peierls dimerization. The lattice parameter of the unit cell doubles its size. A divergence in the electronic susceptibility (Lindhard response function) at $k = \pi/2a$ occurs due to the perfect nesting condition in 1D. This produces a softening in the phonon spectra known as a Kohn anomaly, i.e., the phonon at the corresponding wavevector becomes imaginary leading to the lattice distortion [272]. However, the driving force of CDW transitions has been under discussion over the past years. In higher dimensional systems, electron-phonon interactions have been highlighted as the main mechanism producing the transition, other than the purely electronic picture considered in 1D systems [273].

CDW phases have been reported to emerge in many TMDs at low temperatures, specially when reaching the 2D limit of these compounds [274–279]. CDW phases can have a great impact in other many-body properties, in particular in the ferromagnetic (FM) order. In this chapter we will analyze two different TMD compounds, namely $CrTe_2$ and VSe_2. At high temperature both crystallize in the trigonal phase known as 1T, space group number 164 ($P\bar{3}m1$). This high temperature phase is what we will refer to as the normal state (NS), in order to distinguish it from the low-temperature CDW phase that might arise in these compounds. In bulk, experiments show $CrTe_2$ is a high temperature

ferromagnet with the magnetic moments pointing in-plane, while VSe_2 is non-magnetic. Apart from that, in the former compound no evidence of a CDW phase has been reported, while VSe_2 develops a low-temperature CDW. The monolayer limit of both compounds is an active area of research, specially VSe_2 where an enhancement of the CDW order and the emergence of 2D ferromagnetism have been reported [280]. However, the appearance of strong FM order has been highly debated during the last years. Mostly, in terms of the interplay between the CDW phase and the incipient itinerant FM behaviour that might occur. On the other hand, the monolayer limit of $CrTe_2$ has not been studied yet. The strong ferromagnetic behavior observed in bulk makes $CrTe_2$ an excellent candidate to achieve 2D ferromagnetism. However, the in-plane magnetic moments and the more Heisenberg-like character of this compound challenge to circumvent the Mermin-Wagner theorem, thus achieving long-range FM order. Apart from that, nothing is known about the emergence of other structural phases at low temperatures that could play a role in the magnetic properties. In this chapter we will try to shed light on all these questions.

9.2 Computational Methods

We have performed *ab initio* electronic structure calculations based on Density Functional Theory DFT [17, 18] using the all-electron full potential code (WIEN2K [30]) on $CrTe_2$ and VSe_2. In $CrTe_2$ the exchange-correlation term used for the bulk and monolayer structures was the generalized gradient approximation (GGA) in the Perdew-Burke-Ernzerhof [19] scheme. These calculations were performed with a converged k-mesh and a value of $R_{mt}K_{max}$=7.0. The R_{mt} values used were 2.39 and 2.50 in a.u. for Cr and Te respectively. In VSe_2 the exchange-correlation term for the bulk structure was GGA in the Perdew-Burke-Ernzerhof [19] scheme. The LDA+U method was used for the 2D case [20]. The calculations were carried out with a converged k-mesh and a value of $R_{mt}K_{max}$= 7.0 and a R_{mt} value of 2.12 a. u. for both V and Se.

The magnetic anisotropy energy (*MAE*) of $CrTe_2$ was computed introducing spin-orbit coupling (SOC) in a second variational manner using the scalar relativistic approximation [23, 25]. The harmonic phonon spectrum of monolayer $CrTe_2$ was computed using the real-space supercell approach [49]. Scanning tunneling microscope (STM) images of the monolayer were calculated using a density of 5×10^{-5} $e^-/\text{Å}^3$ associated to the constant current. They were represented using the XCrySDen code [281].

Transport properties of bulk VSe_2 were obtained with the *BoltzTrap* code [59] using a denser k-mesh, and solving the Boltzmann transport equation within the constant relaxation time approximation.

9.3 The case of $CrTe_2$

We start analyzing $CrTe_2$. As we have said this TMD crystallizes in a 1T-phase in which the Cr-rich hexagonal planes are sandwiched by Te-rich layers. $CrTe_2$ layers of this

form are stacked via van der Waals interactions (see Fig. 9.1a). This compound shows a room temperature ferromagnetic phase with a Curie temperature of 310 K and magnetic moments aligned parallel to the layers [282]. The transition above room temperature makes $CrTe_2$ a highly interesting material from the technological point of view.

As we have mentioned in the introduction, in order to achieve a 2D FM long-range order, magnetic anisotropy is needed to overcome the Mermin-Wagner theorem. Therefore, the magnetic moments pointing in-plane that are found in the bulk compound might prevent 2D ferromagnetism in the monolayer. Our first goal will be to analyze engineering strategies, such as strain, to align the magnetic moments perpendicular to van der Waals planes for the bulk structure. In order to compute the magnetic anisotropy energy, that allow us to determine the magnetization direction of the system, we introduced SOC in our calculations for an in-plane magnetization direction and an out-of-plane direction. Then, we define the MAE as:

$$MAE = E_{In} - E_{Out}, \tag{9.1}$$

where E_{In} is the energy per metal atom when the magnetization is set along an in-plane direction (parallel to the Cr layers), while E_{Out} is calculated considering the magnetization points along the out-of-plane direction (perpendicular to the Cr-rich layers). Positive values of the MAE in our convention mean that magnetic moments point perpendicular to the Cr layers. After analyzing the bulk structure we continue with the monolayer. There, apart from examining the magnetic properties, a detailed study of the structure will be performed.

9.3.1 The Bulk

The starting point for the bulk analysis is the experimental structure [282]. We see from a computational point of view how the effect of strain affects the alignment of the magnetic moments. The idea is to modify the off-plane lattice parameter c and fully relax the atomic positions. We have also done this for different values of the in-plane lattice parameter a. We introduced SOC and compute the MAE for each structure as given by eq. (9.1). Therefore, we obtain this way a structural mapping of the MAE. The summary of these calculations is shown in Fig. 9.2.

We can see that the out-of-plane direction is a trigonal axis for the Te_6 octahedron surrounding the Cr cations (Fig. 9.1a). Thus, a crystal field analysis shows that stretching (compressing) the octahedra along this axis leads to a splitting of the otherwise degenerate t_{2g} triplet into a lower(higher-)-lying doublet (so-called e_g^*) and a higher(lower-)-lying singlet (a_{1g}) [5]. As reported from experiments [282], our calculations show that for the experimental values of the lattice parameters, the magnetization points in the plane. We can analyze now the effect of strain in the MAE shown in Fig. 9.2. If the Cr layers get closer to each other, i.e., the lattice parameter c is reduced, the MAE turns positive. This suggests that with a high enough uniaxial pressure that approaches Cr layers together, bulk $CrTe_2$ will present an out-of-plane magnetization direction. Similarly, if the system

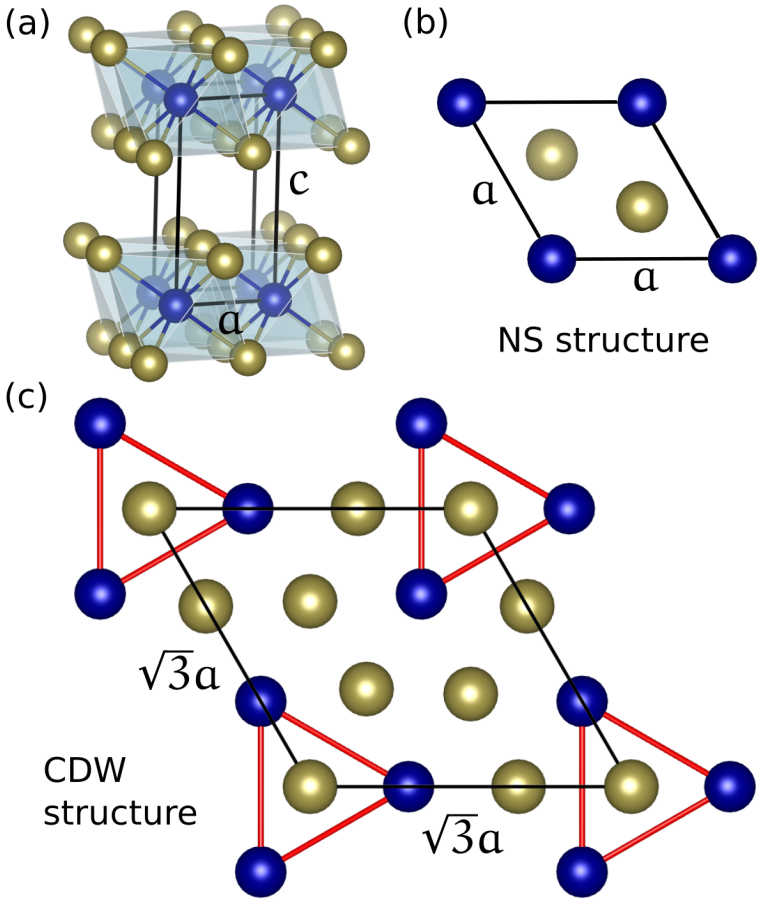


Figure 9.1: $CrTe_2$ structures used in this study. Cr (Te) atoms in blue (gold). (a) Unit cell in bulk. $CrTe_2$ layers are bonded via van der Waals interactions. Cr atoms are octahedrally coordinated by Te atoms. The off-plane direction is a trigonal axis. (b) Top view of monolayer NS (normal state) structure, the single unit cell is depicted by the black rhombus. It contains just 1 Cr and 2 Te atoms. (c) Top view of monolayer CDW structure, a $\sqrt{3} \times \sqrt{3}$ supercell is required to describe its unit cell (black rhombus). Groups of three Cr atoms are formed by Cr-nearest-neighbour stretching (red triangles).

approaches the monolayer limit, i.e., Cr layers get separate and the lattice parameter c is increased, the magnetic moments also tend to point out-of-plane, but only for larger lattice parameter a values. In fact, without it, the magnetic moments will stay pointing in-plane (negative values of the MAE). Therefore, a high enough trigonal tensile strain together with an increase in the lattice parameter a, as shown in Fig. 9.2, lead us to expect long-range ferromagnetic order at the 2D limit. This is what motivates a further detailed study of the monolayer.

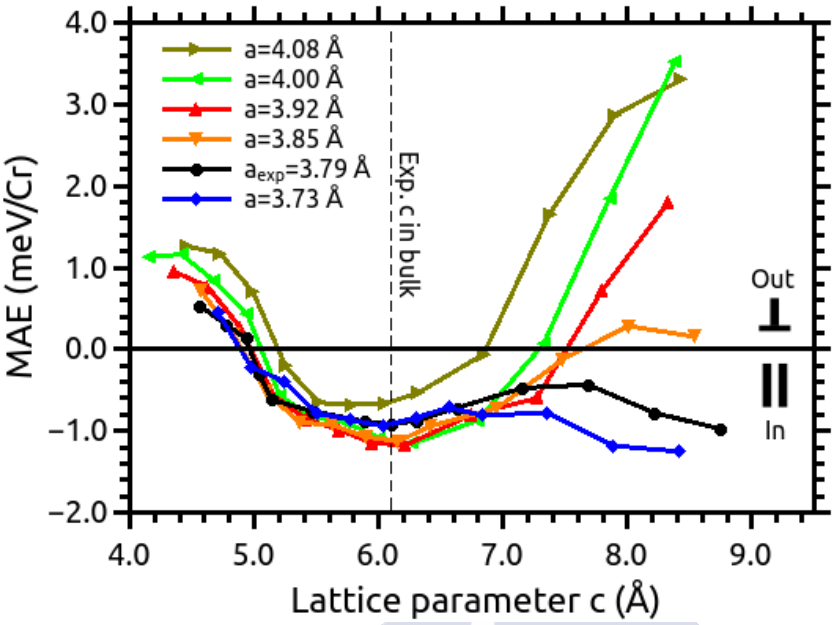


Figure 9.2: Magnetic anisotropy energy (MAE) as a function of the lattice constant c (out-of-plane) for different lattice constant a (in-plane) values for bulk $CrTe_2$. Positive MAE indicates moments point out of the plane. Decreasing the lattice parameter c drives the magnetic moments to point perpendicular to the $CrTe_2$ layers for any value of a analyzed. Increasing the lattice parameter c drives the magnetic moments to point perpendicular to the Cr layers when the lattice parameter a is also increased compared to the experimental value.

9.3.2 The Monolayer

As stated in the introduction, previous studies report the enhancement or even the emergence of a CDW phase in many TMDs when the 2D limit is reached [274–279]. Because of this fact, we have analyzed if a CDW state emerges when going to the monolayer limit of $CrTe_2$. To do so, we have performed phonon band structure calculations in the normal state (NS) structure of the monolayer. Figure 9.1b shows the NS structure and its unit cell. This NS structure has a perfect hexagonal arrangement of the Cr atoms as in bulk (space group no. 164), but with the Te atoms fully relaxed in the monolayer limit. In this state, each Cr atom has 6 Cr neighbours at the same distance and the unit cell can be reduced to the one depicted in Fig. 9.1b as a black rhombus. If a CDW phase is the ground state of the system, the phonon band structure must show unstable modes at certain q-points related to the supercell structure in which the CDW is described [272]. Figure 9.3a shows the phonon band structure for NS monolayer $CrTe_2$. A clear instability is observed at the K point (1/3,1/3) in reciprocal space, which suggests a $\sqrt{3} \times \sqrt{3}$ supercell rotated 60° to describe the CDW state. Note that an instability in the harmonic spectrum is just an indication (not a proof) of the existence of a CDW phase. The intro-

duction of anharmonicities could lead the NS to stabilize, i.e. quenching the appearance of the CDW phase [277]. Therefore, without including anharmonic effects, the route that we have to follow to demonstrate the existence of the CDW in monolayer is to find a modulated structure lower in energy than the NS structure that presents stable phonon modes.

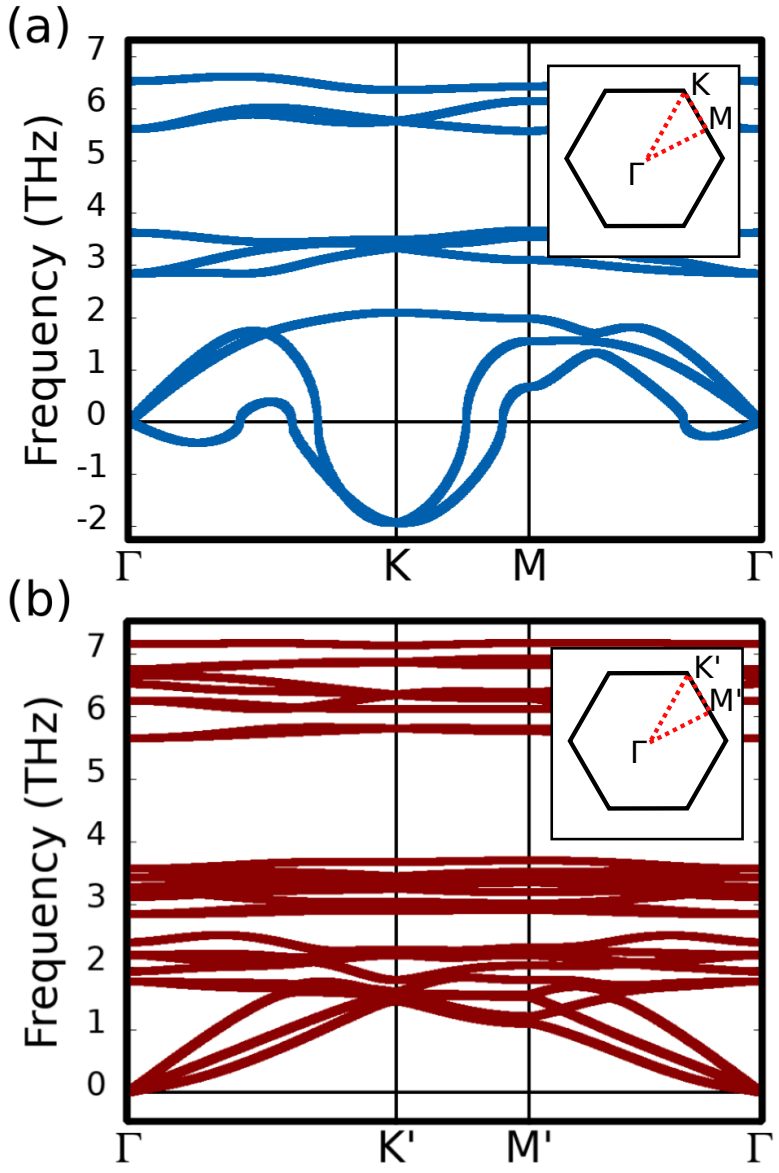


Figure 9.3: $CrTe_2$ phonon band structures in the monolayer limit. (a) For the NS unit cell structural instabilities appear around the K point in the form of imaginary phonon modes. (b) For the CDW unit cell no instabilities are observed, this is a dynamically stable structure. Brillouin zones along high symmetry paths are included in the insets.

Motivated by the harmonic instability at the K point, we have generated a $\sqrt{3} \times \sqrt{3}$ supercell as the one shown in Fig. 9.1c. We have optimized all the atomic positions in it. The result is a reconstruction of the atomic distances. Compared to the NS structure, in which each Cr atom has 6 equidistant Cr neighbours, in the CDW structure each Cr has two short and 4 long Cr-Cr bonds, i.e. a triangular modulation like the one shown in red in Fig. 9.1c appears in the structure. Modulations like this due to the CDW are known to produce new peaks in the X-Ray diffraction pattern [283]. However, this experimental technique does not allow to measure the structural reconstruction that happens in 2D materials. Therefore, we have computed the constant current STM images for the NS (Fig. 9.4a) and the CDW (Fig. 9.4b) structures. In these images, the white dots are associated to the top-layer Te atoms that form the Te-Cr-Te sandwich of the 2D material. For the NS case, all of the Te atoms present the same intensity. However, in the CDW case, some of the white dots are brighter and bigger. These dots are the ones associated to the Te atoms that lie inside the red triangle in Fig. 9.1c. The stretching of the Cr atoms forming the triangle make these Te atoms come out of the plane. This leads to an increase in the intensity and size observed in the STM image. A symmetry analysis of the CDW structure allows us to identify that the structure corresponds to the space group no. 157, which is a subgroup of the NS structure symmetry (space group no. 164). Note that this subgroup has no inversion symmetry along the z-direction. Thus, this CDW breaks inversion symmetry, just like the Janus monolayers, but without imposing substitutional doping to one of the Te sub-layers [284, 285].

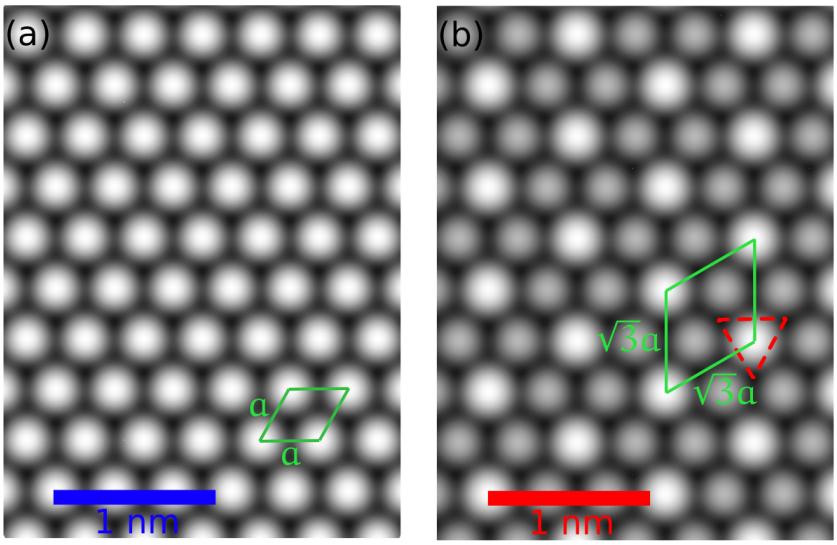


Figure 9.4: Computed STM images for monolayer $CrTe_2$ (a) in the NS and (b) in the CDW phase. Each white dot is associated to a Te atom in the top layer that forms the Te-Cr-Te monolayer. Unit cells for each phase can be identified (green rhombuses). In the CDW image, an enhancement in the intensity of some Te atoms is produced due to the Cr-nearest-neighbour stretching (red triangle in Fig. 9.1).

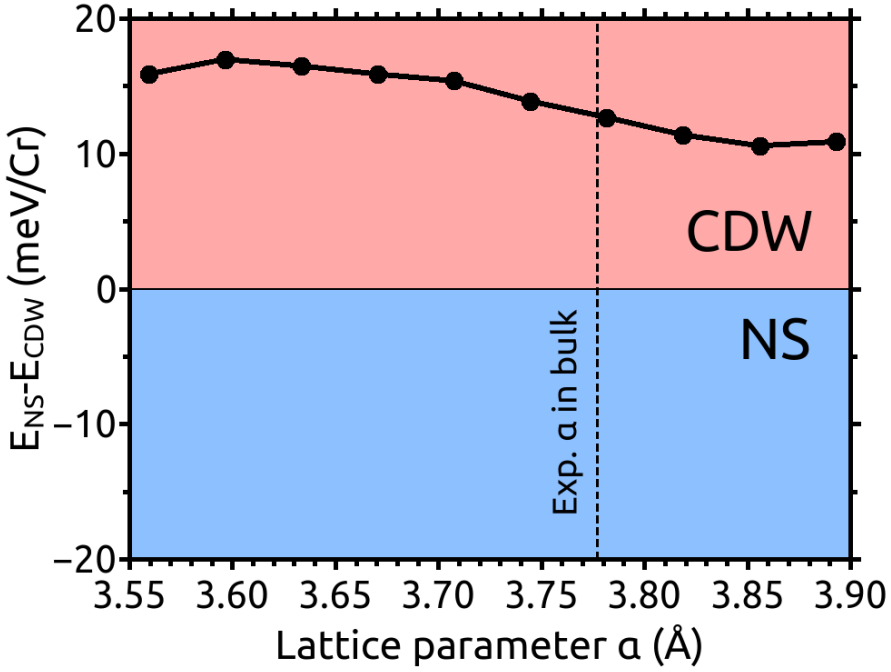


Figure 9.5: Energy difference between the NS structure and the CDW structure as a function of the a lattice parameter for monolayer $CrTe_2$. Positive values in this difference imply that the CDW phase is more stable than the NS.

We have to demonstrate now that the CDW supercell corresponds to the ground state at low temperatures for $CrTe_2$ monolayer. In order to do that we have computed the total energies of both the NS and the CDW structures using DFT calculations. This allows to determine which structure is energetically preferred at 0 K. Figure 9.5 shows the energy difference between the NS and the CDW structure as a function of the lattice parameter a. The experimental value of a in bulk [282] is plotted for comparison. Our DFT calculations show that in the monolayer limit the optimized lattice parameter a is 2% smaller than the experimental value in bulk, within the uncertainty range for a DFT calculation. Consequently, the overall conclusions obtained for the experimental value are the same as the ones for the optimized value. We observe that the CDW phase is more stable than the NS at any lattice parameter studied. In particular, for the experimental case, the energy difference is ~ 14 meV/Cr atom. A reliable proof that practically guarantees that the CDW structure that we have obtained is the ground state structure is a harmonic calculation of the phonon spectra. The phonon band structure for the CDW structure is shown in Fig. 9.3b. We can clearly see that this structure does not show dynamic instabilities in the form of imaginary phonon modes in the phonon band structure, and hence it provides the ground state for monolayer $CrTe_2$. Note that the labels of the reciprocal space in Fig. 9.3b have been primed to emphasize that the first Brillouin zone is reduced in the CDW phase. Apart from that, we have identified

an optical mode in the CDW structure that drives this phase to the NS one. This mode has a frequency of 1.96 THz and could eventually be activated to switch between both phases.

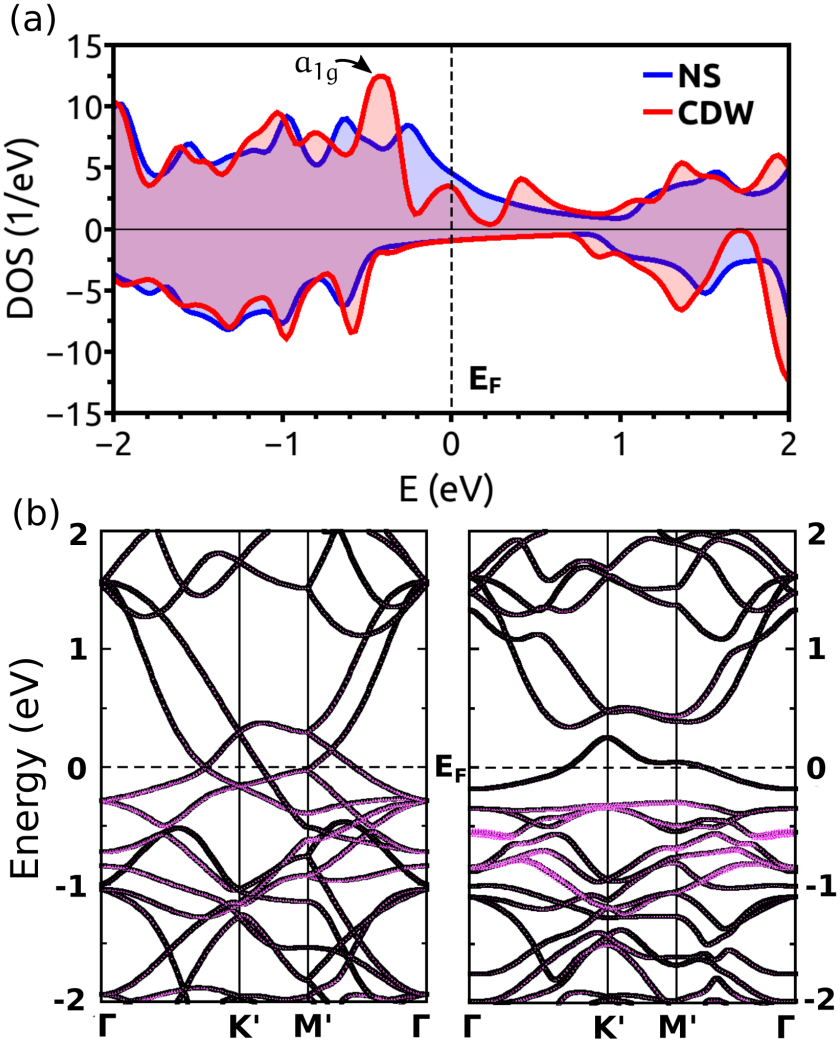


Figure 9.6: (a) Density of states (DOS) as a function of energy for the NS structure in blue and the CDW one in red. The majority (minority) spin channel is represented as positive (negative). (b) Band structures for the majority spin channels. Left (right) panel for the NS (CDW) structure. The a_{1g} orbital character is highlighted in pink.

Having proved that a CDW phase at low temperatures emerges on $CrTe_2$ monolayer, we can analyze its effect on the electronic structure and the FM order of this compound. Typically, the occurrence of a CDW phase leads to the opening of electronic gaps or pseudogaps (energy gaps at certain k-points) in the vicinity of the Fermi level [279, 286, 287]. In order to see the rearrangement that the electronic structure of $CrTe_2$ undergoes

within the CDW phase, we have computed the electronic density of states (DOS) and the band structures for both phases. Figure 9.6a shows the DOS for the NS (CDW) phase in blue (red) near the Fermi level. As discussed in the previous subsection for the bulk case, the octahedral environment around the Cr atoms is trigonally distorted and hence the d-orbitals split into 3 sets of energy levels, one a_{1g} singlet and two (e_g and e_g^*) doublets. The occupation of the a_{1g} and two electrons in the wider e_g^* bands in the majority spin channel leads to a total magnetic moment of 3 μ_B/Cr, corresponding to an approximate Cr^{3+} valence, but with a high degree of hybridization with Te-p orbitals, which produces the observed metallic state. However, a Heisenberg picture for the magnetism can be applied. The minority spin channel presents roughly no occupied Cr d states (apart from some bonding character in the Te p bands). In Fig. 9.6a, in the majority channel, we can see that gaps are opened around the Fermi level as a consequence of the CDW (shown in red). We can better see this in the band structure (Fig. 9.6b) in which the majority spin channels are represented. On the left (right) panel, the NS (CDW) band structure is shown. Both phases were computed in the $\sqrt{3} \times \sqrt{3}$ supercell for better comparison. The atomic rearrangement in the CDW causes a band hybridization that opens a gap below and above the Fermi level leaving a flat single band crossing the Fermi level. This depletion of states around the Fermi level reduces the total energy of the system, making the CDW structure the ground state solution. We can also see that the a_{1g} orbital, whose character is represented in pink in Fig. 9.6b, gets more localized. This result can also be identified as a peak in the DOS just below the Fermi level for the CDW case (Fig. 9.6a).

Regarding the magnetic properties of the system, we have already stated that monolayer $CrTe_2$ presents a magnetization of 3 μ_B per Cr atom in which a Heisenberg picture holds. In the bulk case, the system is a room-temperature ferromagnet in which the in-plane magnetic exchange couplings (the ones relevant in the 2D limit) are ferromagnetic. Considering previous works in which the dimensionality effect is studied for similar Cr van der Waals compounds like Ref. [288], or the study in Ref. [VI] that we have presented in the previous chapter, the in-plane magnetic exchange couplings remain ferromagnetic in monolayer $CrTe_2$. The question that arises now is if the moments are long-range ordered in the 2D limit, thus providing a ferromagnetic state. In order to check this, we have computed the MAE as given by eq. (9.1). Fig. 9.7 shows the MAE as a function of strain for the NS and the CDW phases. An out-of-plane MAE (positive values in our convention) circumvents the restrictions of the Mermin-Wagner theorem leading to long-range ferromagnetic order to be stable at finite temperatures.

In Fig 9.7 we observe that for the experimental value of the in-plane lattice constant, a long-range FM order is on the verge of being feasible. A very small tensile strain produces a spin reorientation for the CDW phase with the solution with an out-of-plane magnetization being stable. A substantially larger tensile strain is required to produce the same effect in the NS structure. It can be seen that the CDW phase has a higher tendency to have the magnetic moments aligned perpendicular to the layer, i.e. every MAE value for the CDW is more positive (or less negative) than the corresponding one in the NS. This tendency for the moments to get oriented out of plane is accompanied of

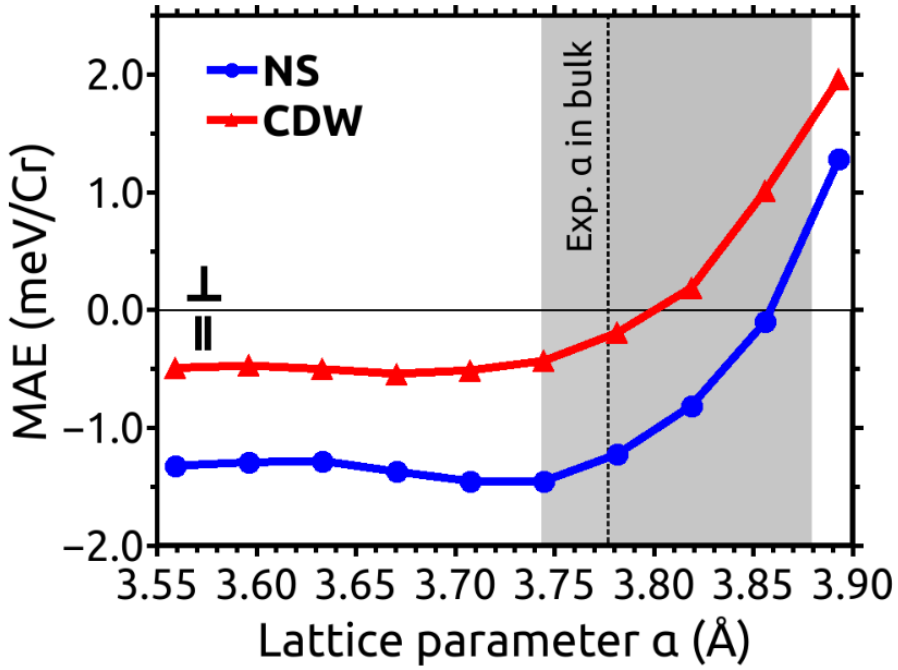


Figure 9.7: *MAE* as a function of the lattice parameter a for 2D $CrTe_2$. The CDW phase and tensile strain drive the magnetic moments to point perpendicular to the monolayer. In the shaded area we could control the ferromagnetic order via strain or phase transition.

a stronger moment localization in the CDW phase, as we can see in the band structure analyzed above. When tensile strain is applied, the states also become more localized. Bandwidths are reduced by an increase of the inter-atomic bond length which causes a reduction of the in-plane hopping. In this respect, tensile strain operates in the same direction as the CDW does. Therefore, we can see that for the case of $CrTe_2$ the CDW favours the FM order.

We saw in the previous subsection that for $CrTe_2$ in the bulk, strain is also a mechanism responsible for producing an out-of-plane orientation of the magnetization in this compound. In particular, enlarging the in-plane lattice parameter (reducing the Cr d bandwidth, and producing a stronger electronic localization) increases the tendency for the magnetic moments to point out of the plane. This kind of out-of-plane to in-plane magnetic moment reorientation has been observed in similar (bulk) van der Waals ferromagnets like $Cr_2Ge_2Te_6$ when pressure is applied [262]. The effect of pressure goes in the opposite direction than tensile strain. It reduces the lattice parameter, thus increasing the bandwidth (or delocalization) of the d orbitals and hence driving the moments parallel to the layers. Thus, we found that this relationship between magnetocrystalline anisotropy and moment orientation in trigonally distorted Cr^{3+}-based 2D magnets is somewhat general.

We observe that for the experimental value of the lattice parameter a, ferromagnetic order is on the verge of stability in the CDW phase. Small values of strain could lead the system to become ordered, and vice versa. Thus, strain provides an effective way to control 2D ferromagnetism in monolayer $CrTe_2$. Apart from this mechanism, it can also be controlled by activating the 1.96 THz phonon mode that we have identified in the previous section. This would drive the CDW phase to the NS one, thus quenching the magnetic order. This prompts a route to switch between both phases in a controlled way via infrared pulses, in a similar way to what has been done before for the ferroelectric phase of $SrTiO_3$ [289]. The shaded area in grey in Fig. 9.7 provides the range of lattice parameter values in which we could control the ferromagnetic order of 2D $CrTe_2$.

9.4 The case of VSe_2

We continue this chapter analyzing VSe_2. As happens to $CrTe_2$, VSe_2 crystallizes in the 1T-phase (space group $P\bar{3}m1$) at high temperatures. However, as many other TMDs [274, 275] VSe_2 shows a CDW phase below 110 K [276]. This phase transition in bulk has been experimentally identified by transport and X-ray diffraction measurements [283, 290, 291]. The modulation of the CDW is commensurate to a $4a \times 4a \times 3c$ supercell [290, 292, 293]. Recently, electron-phonon coupling was shown to be the driving mechanism of this transition and van der Waals interactions were found to be essential to correctly describe the transition temperature of this compound [294]. The CDW phase is accompanied by the opening of pseudogaps at certain k-points of the Fermi surface [295]. Apart from that, experiments have reported a non-magnetic behaviour in bulk [290, 295–297]. However, DFT calculations previous to our work in 2018 had predicted a FM solution for this system, both in bulk and in the monolayer [298–301]. In our analysis (Ref. [VIII]) we reconcile this disagreement between theory and experiments by highlighting the importance of the CDW phase to correctly address the non-magnetic behaviour of VSe_2.

The monolayer limit of VSe_2 is most subtle. A vast amount of studies have been performed since we started working in this system in 2017. The transition temperature of the CDW (T_{CDW}) is found to be highly dependent on the number of layers in a non-monotonic way [267, 302, 303]. In the 2D limit different CDW orders with different modulations have been reported. The most sounded modulations are a $\sqrt{3}a \times \sqrt{7}a$ with $T_{CDW} \sim 220$ K [270, 304] and a $4a \times 4a$ with $T_{CDW} \sim 140$ K [268, 305, 306] and $T_{CDW} \sim 186$ K [307]. But other modulations have also been shown [305, 306, 308, 309]. Such a plethora of different results is also accompanied by the report of different electronic and magnetic properties for VSe_2 in the monolayer limit. A transition to an insulating state at low temperatures has been reported by some works [268–270, 305, 306, 308], while others have not observed it [304, 306, 307]. Apart from that, a controversial high temperature FM order was reported [267, 280]. However, many other works have claimed the absence of such magnetic state [268, 270, 304–306, 308]. Therefore, the results exposed above suggest a sample dependence on preparation methods, sizes and environment for the monolayer.

This leads to different reconstructions of the CDW phase and hence to different electronic and magnetic properties. A theoretical analysis clarifying once and for all the intrinsic properties of VSe_2 monolayer is still needed.

In this study, we highlight the role played by the CDW phase quenching the FM order. We start analyzing the bulk structure where the CDW order is clear. We show then that the CDW phase has also a detrimental effect on the magnetic order of the monolayer. Due to the itinerant-electron character of VSe_2, we will discuss its magnetic order in the framework of the phenomenological Stoner model [55]. The Stoner theory compares the energy gained by the system via a spin splitting to the kinetic energy cost produced by displacing minority-spin electrons into a higher-energy majority-spin band. Only when the overall energy gets reduced, an itinerant electron system becomes spontaneously magnetic. The Stoner criterion can be summarized as:

$$\text{Stoner criterion} \begin{cases} \text{FM, if } \mathrm{I} \cdot \mathrm{DOS}(\mathrm{E_F}) > 1 \\ \text{Non} - \text{magnetic, otherwise} \end{cases} \tag{9.2}$$

where I is the exchange energy between the Bloch d-band electrons, the so-called Stoner parameter [310], and $\mathrm{DOS}(\mathrm{E}_F)$ is the electronic density of states at the Fermi level when the system is spin degenerate in energy. Typical itinerant ferromagnets such as Fe, Ni and Co present values of $\mathrm{I{\cdot}DOS}(\mathrm{E}_F)$ ranging from 2.5 to 3 [311]. The criterion will be used to study the proximity of VSe_2 to the ferromagnetic order.

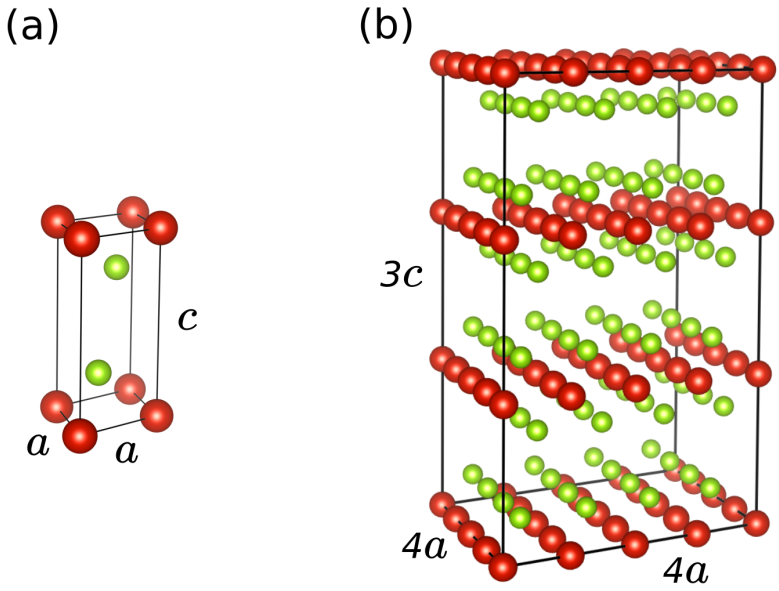


Figure 9.8: $VSe_{2.0}$ bulk structures. V (Se) atoms are represented as big red (green) spheres. (a) NS structure in the $P\bar{3}m1$ space group. (b) 4a × 4a × 3c supercell of the CDW state.

9.4.1 The Bulk

As mentioned above, bulk VSe_2 develops a CDW phase below 110 K [290, 291]. This result is confirmed in the experiments performed by Dr. Blanco-Canosa shown in Figs. 9.9a and 9.9b. We can identify the CDW transition as a kink in the magnetic susceptibility; at 110 K for $VSe_{2.0}$ and 55 K for $VSe_{1.8}$, evidencing the drop in transition temperature upon introducing Se defects. Figures 9.9c and 9.9d show the magnetization curves as a function of the magnetic field and temperature. Neither the magnetization of $VSe_{2.0}$ nor $VSe_{1.8}$ saturates at 6 T. Taking into account the higher density of vacancies in $VSe_{1.8}$, the small hysteresis observed in $VSe_{2.0}$ could arise from Kondo impurities [312] or phase slippage of the CDW [313]. Further X-ray magnetic circular dichroism (XMCD) experiments confirm that the small magnetic signal observed for $VSe_{2.0}$ comes from Kondo impurities.[1] Therefore, experiments show no evidence of a magnetic phase in bulk VSe_2.

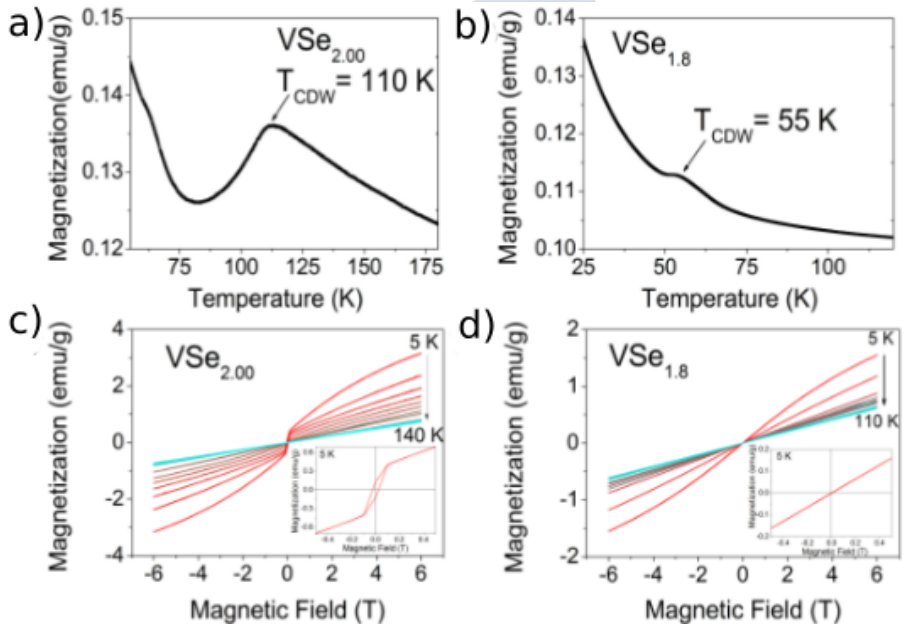


Figure 9.9: (a-b) Temperature dependence of the magnetization for stoichiometric $VSe_{2.0}$ and Se-deficient $VSe_{1.8}$ single crystals. The charge density wave transition temperature (T_{CDW}) is signaled by a kink in the magnetization curve. (c-d) Magnetization vs field for $VSe_{2.0}$ and $VSe_{1.8}$ single crystals. Inset, zoom-in of the low field magnetization highlighting the small magnetic signal for $VSe_{2.0}$, not observed in $VSe_{1.8}$.

As previously said, earlier DFT calculations had predicted a FM solution for this system, both in bulk and in the monolayer [298–301]. However, none of those had included the effect of the CDW phase in the analysis of the magnetic properties, as we did in Ref. [VIII]. This consideration will be crucial to reconcile experiments and theory.

[1] A detailed description about the experiments can be seen in Ref. [VIII].

In order to obtain a deep understanding of the electronic and magnetic ordering in single crystals of $VSe_{2.0}$, we have carried out *ab initio* calculations, both in the normal (NS) and CDW state. ARPES and X-ray diffraction [290] have found a 3-dimensional CDW below 110 K, leading to the opening of a pseudo-gap at the Fermi level at ($\frac{1}{4}$, $\frac{1}{4}$, $\frac{1}{3}$) reciprocal lattice units [286]. To take this into account in our calculations, we have computed a $4a \times 4a \times 3c$ supercell. The unit cells of each phase are shown in Fig. 9.8. The introduction of a periodic lattice distortion may affect the calculated DOS at the Fermi level and hence the magnetic properties of this itinerant electron system.

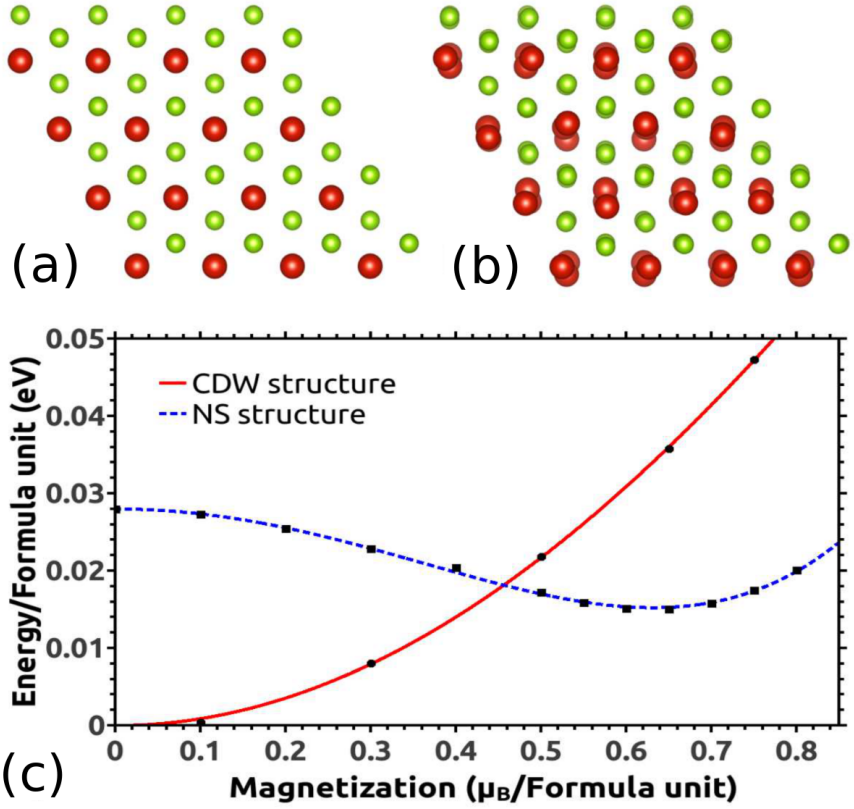


Figure 9.10: Top view of $VSe_{2.0}$ bulk structures. V (Se) atoms are represented as big red (green) spheres. a) NS structure in the $P\bar{3}m1$ space group. b) A modulated 4a × 4a × 3c supercell of the CDW state. c) Energy as a function of the magnetization for the bulk $VSe_{2.0}$ for the NS structure (blue line) and CDW state (red line).

We have relaxed the lattice parameters and the atomic positions in the $4a \times 4a \times 3c$ supercell. This allowed us to obtain the low temperature, CDW state. The optimized atomic positions taking into account the new lattice periodicity [290], are plotted in Fig. 9.10b, showing that the short-range hexagonal symmetry is lost. The CDW structure calculated *ab-initio* is 28 meV per formula unit more stable than the NS structure resulting in a strong reduction of the DOS at the Fermi level (Fig. 9.11b).

We can plot the energy (E) *vs* magnetization (M) curves to see how the new structure affects the magnetic order of VSe_2. We can see in Fig. 9.10c that, while in the NS state the minimum is at 0.6 μ_B per V atom indicating a FM solution for this structure, in the low temperature CDW state the minimum-energy configuration is non-magnetic. Therefore, Fig. 9.10c shows how the CDW phase is the ground state and how it quenches the FM order predicted in the NS structure.

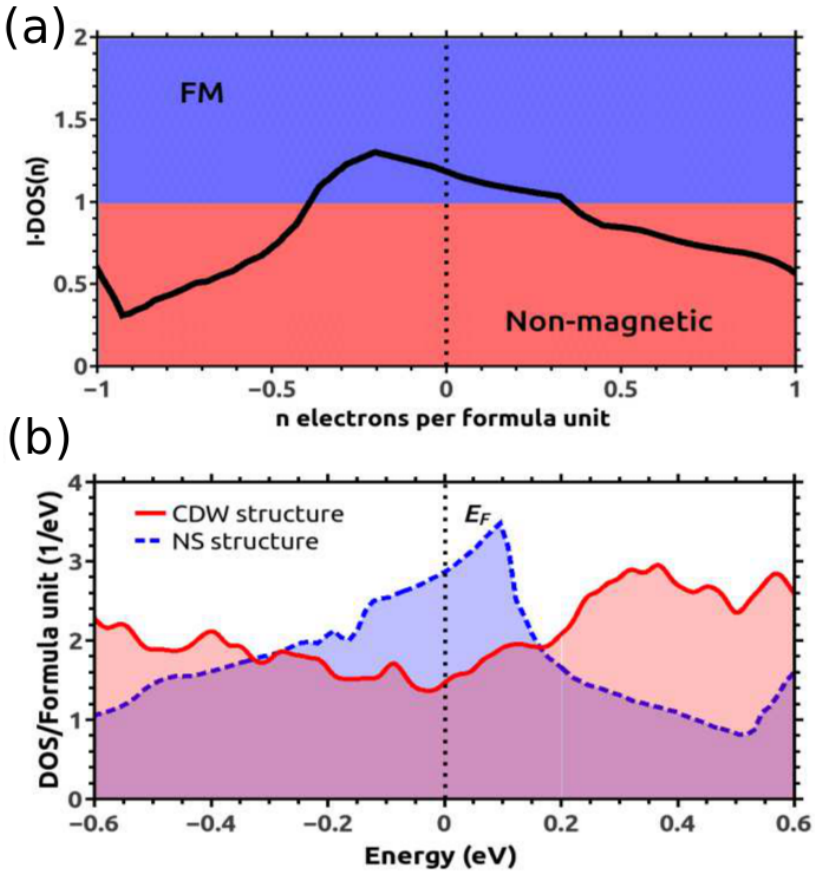


Figure 9.11: a) Stoner criterion applied for the NS structure as a function of the number of electrons introduced per formula unit. In the NS, VSe_2 is FM but close to a non-magnetic state. b) DOS around the Fermi level for the bulk structures. Red (blue), DOS of the CDW (NS) state, showing a reduction of the DOS in the CDW state.

We can further analyze the proximity of VSe_2 to a magnetic state using the Stoner criterion (eq. (9.2)). We can obtain the Stoner parameter I for the bulk NS structure from a fitting of the energy *vs* magnetization curve (blue line in Fig. 9.10c) to:

$$E = (1 - IDOS(E_F))/DOS(E_F)M^2 + kM^4, \tag{9.3}$$

where k is a fitting parameter independent of I [310]. This allows us to analyze the Stoner criterion for the NS VSe_2. Moreover, we can perform the analysis as a function

of the carrier concentration, or number of electrons per formula unit n. At the Fermi level $n = 0$, $n > 0$ ($n < 0$) implies hole (electron) doping. The carrier concentration was calculated using a rigid-band approximation by integrating the total DOS of the non-magnetic calculation. In Fig. 9.11a, we show that the Stoner criterion for FM is satisfied for -0.5<n<0.5. However, any perturbation to this system leads to a small reduction in the DOS at the Fermi level and to a non-magnetic state. Recall that typical itinerant ferromagnets such as Fe, Ni and Co present values of I·DOS(E_F) ranging from 2.5 to 3 [311]. Previous *ab initio* studies had shown that a reduction of the FM moment can be achieved by strain engineering [299]. Here, we have shown that the CDW state is responsible of a substantial reduction of the DOS at the Fermi level (Fig. 9.11b) that suffices to unfulfill the Stoner criterion and quench the FM order of bulk VSe_2.

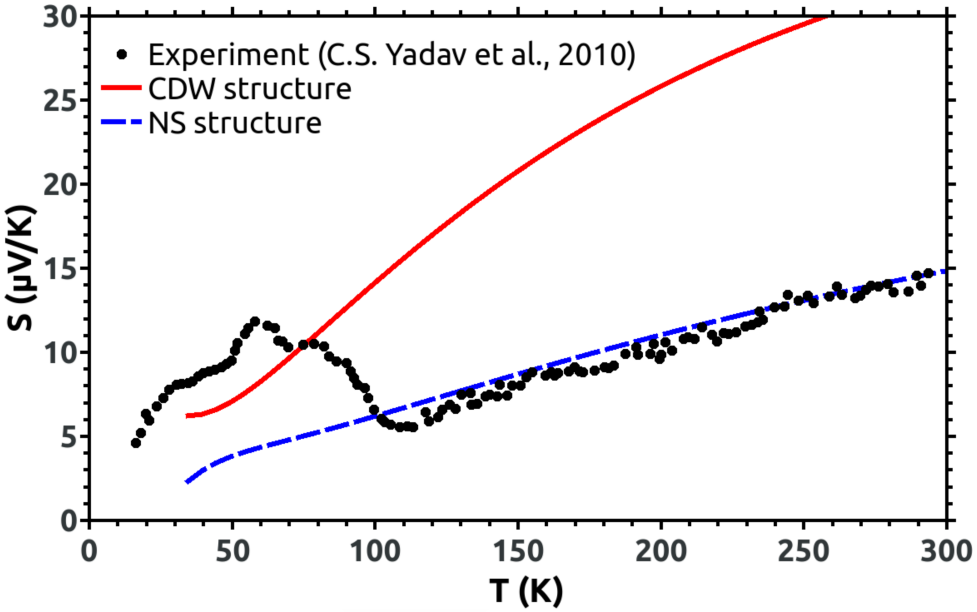


Figure 9.12: Thermopower as a function of temperature for bulk VSe_2. The black points show the experimental measurements from Ref. [291]. The red and blue lines show the calculated thermopower for the $4a \times 4a \times 3c$ supercell (CDW state) and for the $P\bar{3}m1$ cell (normal state).

Finally, before swiping to the analysis of the monolayer, we have mentioned that a way to identify CDW transitions is by means of jumps in transport properties as a function of temperature. Therefore, let us see how the CDW structure that we have obtained affects a transport property. In particular, the thermopower, since as we said in Part I is one of the transport properties that we can compute with most accuracy. Experimentally, a significant enhancement in the Seebeck effect is observed at the transition from the NS at high temperatures to the CDW state below 110 K, due to the opening of a pseudo-gap at the Fermi level. In Fig. 9.12 the computed thermopower of both the NS (blue dashed line) and the CDW (red line) structures is compared to the ones in the literature [291]

(black points). Despite the coarse fitting at low temperature, an enhancement of the thermopower with respect to the NS is also obtained in the theoretical simulations within the constant scattering time approximation. This is further evidence for the reliability of modelling bulk VSe_2 in its CDW phase using a $4a \times 4a \times 3c$ supercell.

9.4.2 The Monolayer

By the time we performed our analysis in Ref. [VIII], a controversial high temperature FM order had recently been reported [280]. Soon after that, many different works, including ours, claimed against that finding [268, 270, 304–306, 308]. Our experiments performed on high quality monolayers of $VSe_{2.0}$ grown on HOPG and Si-C show no evidence of magnetism in the range of 300 and 5 K. From a theoretical point of view our analysis of the monolayer might be considered old-fashioned and should be updated. However, the main idea showing the detrimental effect of the CDW introduced on the magnetic order of VSe_2 is still valid. In 2018 the modulation of the CDW phase was not clear [268–270] (it remains unclear today). Moreover, some ARPES experiments claimed that a full gap was opened in the monolayer at low temperatures [268, 270, 304]. All that muddled results hindered our theoretical study in [VIII]. Therefore, our aim with the DFT calculations that we presented there was to explain the physical mechanism that the monolayer undergoes rather than looking for perfect agreement with controversial experimental data. This helped to highlight the importance of the CDW phase when analyzing the electronic and magnetic properties of VSe_2 in the monolayer too.

We present calculations on a $2a \times 2a$ supercell since it was computationally affordable. This allows us to understand the possible electronic reconstructions that may occur in the 2D limit when a periodic lattice distortion takes place, shedding light on how both the FM quenching and the full-gap opening occur. We have taken into account that in the monolayer limit the hopping parameter, t, between layers vanishes and, hence, the ratio between the *on-site* Coulomb repulsion and hopping, U/t, increases. In order to include the electron interactions that become stronger, we have performed LDA+U calculations. Figure 9.13a shows the evolution of the energy gap in the whole Brillouin zone as a function of U for a fully relaxed $2a \times 2a$ supercell of the monolayer. At reduced values of U, a metallic FM structure is stable. However, for U greater than 2.7 eV a non-magnetic CDW is formed and, consequently, an energy gap appears in the whole Brillouin zone, in agreement with experiments [270]. The calculated band structures for the non-magnetic-monolayer NS and CDW state are shown in Fig. 9.13c. If no structural instability is present, the d-band crossing at the Fermi level and the high density of states (blue dashed line in Fig. 9.13d) lead to a FM metallic state. Nevertheless, the structural transition associated to the CDW, depicted in Fig. 9.13b, drives the system towards a Peierls-like distortion with a tetramerization among 4 V atoms. A comparison between the DOS of the NS structures both for the bulk and the monolayer reveals that decreasing dimensionality increases the DOS at the Fermi level, the bands become flatter due to the absence of the off-plane hopping. In general, for itinerant systems, this would

be a mechanism to enhance the stability of a FM phase. However, due to the CDW state, the 4 d-bands in the $2a \times 2a$ supercell hybridize forming 2 bonding and 2 antibonding bands (right side of Fig. 9.13(b) opening an energy gap (red line in Fig. 9.13(d)) with a concomitant quenching of the FM moment.

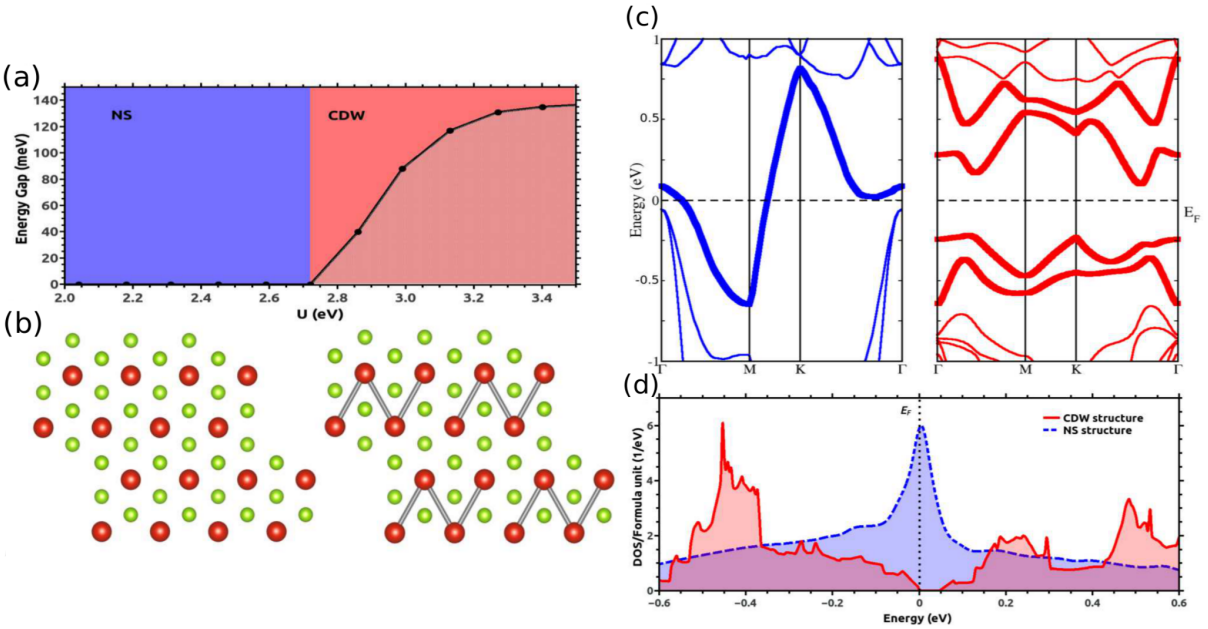


Figure 9.13: Results for the monolayer. (a) Mapping on U. The structure was fully optimized for each value of the Coulomb repulsion. At low values, the metallic FM NS structure is the most stable. For U> 2.7 eV, a non-magnetic gap opens and the CDW stabilizes. (b) Structure schemes: NS on the left, each V atom has 6 neighbors at the same distance. CDW on the right, a tetramer is formed in a $2a \times 2a$ supercell. The tetramer bonds are depicted in gray. (c) Band structures: On the left the NS, a d-band crosses the Fermi level producing a FM metallic state. On the right the CDW, the tetramer is formed by two bonding and two antibonding bands, opening a gap and quenching the magnetic moment. (d) Comparison of the DOS of the NS monolayer VSe_2 (blue dashed line) with the CDW state (red line).

Apart from that, in order to study from an *ab initio* perspective the effect of strain and Se vacancies in the monolayer limit, we have computed the DOS for different strain values and also carried out similar calculations including Se vacancies in a V:Se ratio similar to our single-crystal experiments (Fig. 9.14). We have performed calculations in the NS and shown that the DOS is not substantially increased (mostly reduced) with respect to the unstrained-stoichiometric NS monolayer $VSe_{2.0}$. The effect of strain and Se vacancies can be seen in Fig. 9.14(a-b), suggesting that neither strain nor Se vacancies will induce an intrinsic FM state in single-layer $VSe_{2.0}$, as discussed above in our experiments for the bulk case.

Despite our DFT calculations find a drop of DOS at the Fermi level discarding a possible FM state, the effect of intrinsic disorder in monolayer VSe_2 has to be carefully studied experimentally, since high density of vacancies, anti-sites, substitutions, edges and grain boundaries can dominate the materials' properties. The proximity to a magnetic ground state for VSe_2 monolayer allows to look for engineering strategies to get a 2D ferromagnet. For instance, a FM phase of about 0.4 μ_B per V atom was reported for the monolayer when hybridized with a Co atomic overlayer [314]. This finding highlights that monolayers of VSe_2 can be manipulated to tailor new magnetic ground states.

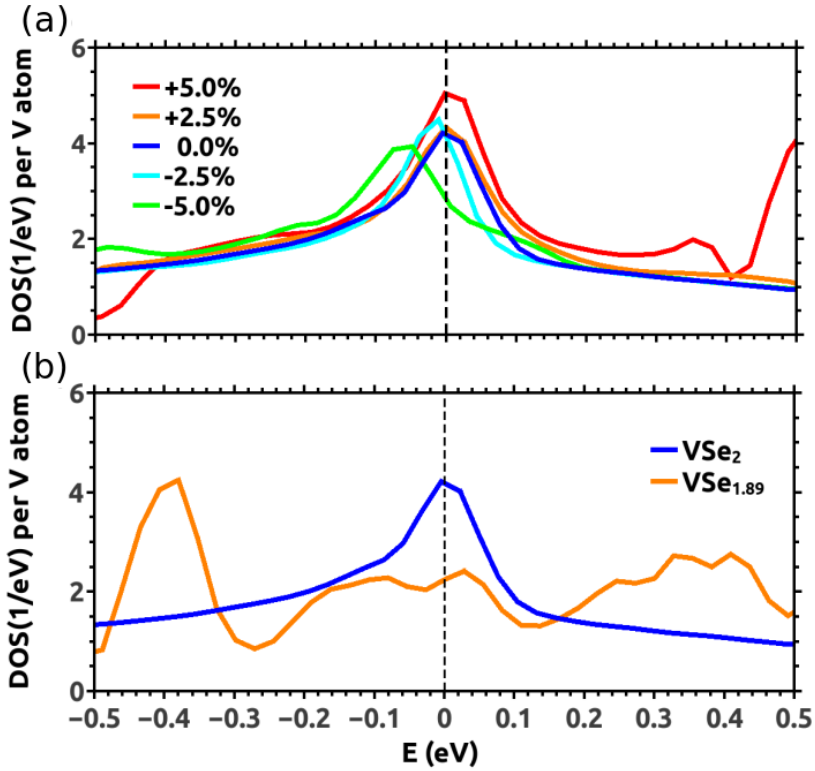


Figure 9.14: Calculated DOS for the monolayer. (a) DOS for different strain values of the lattice parameter for the monolayer single-unit cell. A substantial change in the DOS at the Fermi level is not observed. (b) Effect of Se vacancies on VSe_2 DOS. Including vacancies reduces the density of states at the Fermi level and hence decreases the possibility of having a FM phase.

Soon after our work, first principles calculations of the CDW structure of monolayer VSe_2 reported that a CDW phase with a non-magnetic supercell modulation of $\sqrt{3}a \times \sqrt{7}a$, compatible with experiments, was more stable than the FM NS structure [304]. This reinforced our result indicating a clear competition of ferromagnetism and the CDW phase in the monolayer limit of VSe_2. However, as mentioned in the introduction of this section, there is still work to do from a theoretical and computational point of view to unveil the intrinsic CDW order and magnetic properties of VSe_2.

9.5 Conclusions

In this chapter we have analyzed the interplay between CDW phases and FM order for two different layered TMDs, $CrTe_2$ and VSe_2.

We focus first in $CrTe_2$, a room-temperature ferromagnet in the bulk with the magnetic moments pointing in-plane. This is discussed in the framework of a Heisenberg ferromagnet. We show how different distortions can be applied to drive the moments out-of-plane. After that, a detailed description of the monolayer limit was presented. We find and fully characterize a CDW phase that emerges at low temperatures. We provide guidance for experimental identification of such a phase. Moreover, the optical phonon mode responsible for the transition between the CDW and the NS phases is given, showing a way to switch between phases. The analysis of the electronic structure showed that the CDW phase opens pseudogaps around the Fermi level and localizes the d orbitals. This is found to drive the magnetic moments to point perpendicular to the monolayer, thus, overcoming the constraints imposed by the Mermin-Wagner theorem and producing long-range ferromagnetic order in the 2D limit. Tensile strain is also found to increase the localization of the d orbitals and hence produce ferromagnetism in both phases.

In the second study we focus on VSe_2, a non-magnetic compound in bulk that develops a CDW phase at low temperatures. This compound is discussed in the framework of an itinerant ferromagnet. We show that the CDW phases quenches the ferromagnetic order in bulk. This result reconciles the experiments with previous DFT calculations where the effect of the CDW was not taken into account. Moreover, we show that the low temperature phase that we found is able to explain the kink in the thermopower observed in experiments due to the structural transition. The study of the monolayer is still an active area of research, that deserves further theoretical consideration. Its closeness to a magnetic instability makes VSe_2 to be highly affected by its sample preparation and external conditions. However, our analysis helps to determine that a FM order in VSe_2 monolayer is also affected in a detrimental way by the presence of a CDW phase.

To sum up, our work in this chapter provides additional understanding for the interplay between different competing phases in low-dimensional materials and gives fundamental insight in order to find 2D ferromagnetism in TMDs and related systems. We have highlighted here the importance that the structure has in providing a good description of the magnetic properties of these compounds. A hand-wavy comparison between both systems tells us that while the emergence of a CDW drives $CrTe_2$ to a long-range FM order in the single-layer limit, in VSe_2 the opposite effect is obtained, and the CDW quenches magnetism. This result could be related to the different ferromagnetic character, Heisenberg and Stoner, in which these compounds have been framed. However, further experimental and theoretical studies have to be performed in order to clarify this gross generalization.

10 Topological Transitions in $BaSn_2$

In this work we perform a theoretical analysis on $BaSn_2$, a topological nodal-line semimetal when spin-orbit coupling is not taken into account. We use this system as a theoretical playground to study topological transitions. We report a topological-to-topological transition when uniaxial pressure is applied to this system. We provide insight into the microscopic mechanism that produces this kind of transitions and pave the way to experimentally test them. The work presented in this chapter can be found in [IX].

10.1 Introduction

In this last chapter we are going to study from a theoretical point of view $BaSn_2$. The first thing that one might be wondering is why this compound? Where is the transition metal element? How does it fit in this thesis? Well, analogously as it happens to transition metal compounds, the d electrons of the Ba atom are found to play a fundamental role in its physical properties. In particular, d electrons will be relevant to explain a topological transition this compound undergoes when uniaxial pressure is applied. Apart from that, $BaSn_2$ is a van der Waals layered compound, in line with the previous chapters. Hence, this work will provide a little bite on topological materials, a novel topic in the last decade.

The concept of topology has introduced a different perspective to look at materials. As we presented in Part I, topological invariants can be defined for a given system. These characterize the electronic structure of that material as trivial or topologically non-trivial. Systems will be now referred to, within this framework, as trivial or topological, respectively. This field was initiated with the discovery of topological insulators [315] followed by topological semimetals [316]. Inside the latter category, topological nodal-line semimetals (NLSM) are three dimensional systems in which the valence and conduction bands near the Fermi level cross each other forming a one-dimensional loop in momentum space [317, 318]. These crossings produce robust drumhead-like surface states, prompting the possibility to study strongly correlated surface phases such as superconductivity or ferromagnetism [319–321].

Topological nodal lines have been reported in the family of ZrSiX materials (where X corresponds to a chalcogen atom) [322–324]. In recent studies, it has been shown that pressure can induce topological phase transitions in these nodal-line semimetals. In the case of ZrSiS pressure induces a topological nontrivial-to-trivial transition [325]. It has been attributed to a weak lattice distortion by nonhydrostatic compression in which crystal symmetries are not preserved [326]. In a different way, infrared spectroscopy experiments have suggested that ZrSiTe undergoes two phase transitions at 4.1 and 6.5 GPa [327]. Raman spectroscopy and X-ray diffraction measurements as well as calculations have found that they correspond to Lifshitz transitions, i.e., transitions in which the topology of the Fermi surface changes without breaking any lattice symmetry. Interlayer interactions caused by pressure are found to be responsible for those transitions [328]. However, their topological character cannot be elucidated from these experiments. Therefore, some questions arise regarding the topological nature of those transitions. Can they appear in other family of materials that contain a nodal line? Does pressure always reduce the non-trivial character of the compound or is it possible to find a different transition in terms of topology?

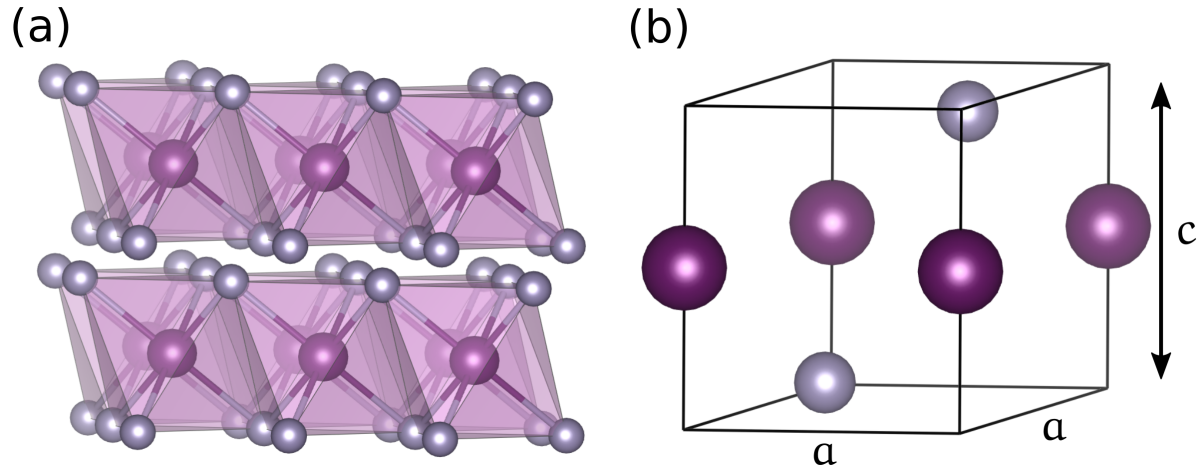


Figure 10.1: Crystal structure of $BaSn_2$, Ba (Sn) atoms in purple (grey). (a) Side view of the layered structure of $BaSn_2$, where Sn atoms octahedrally coordinate the Ba cations. (b) Unit cell of $BaSn_2$. Uniaxial pressure is applied along the depicted off-plane c direction.

$BaSn_2$ belongs to the family of alkaline-earth stannides, germanides, and silicides. It has been reported to be a strong topological insulator with a bulk band gap of about 200 meV [329]. However, in the absence of spin-orbit coupling (SOC) $BaSn_2$ becomes a Dirac nodal-line semimetal [330]. Although $BaSn_2$ displays a non negligible SOC coupling in reality, $BaSn_2$ in absence of SOC constitutes an ideal system to analyze the possibility of pressure-induced topological phase transitions from a theoretical point of view, as it offers some advantages compared to more realistic NLSMs: it is a layered nodal line semimetal at ambient pressure that crystallizes in the space group no. 164 (Fig. 10.1a),

and the effects of pressure can be easily analyzed. Also, it is a well known system from an *ab initio* perspective [330]. For these reasons, we will use $BaSn_2$ as a representative model system to discuss possible scenarios of topological phase transitions driven by pressure other than the ZrSiX family. In this study, we will combine first principles calculations and a model Hamiltonian. This procedure will allow us to provide evidence of a topological-to-topological pressure induced transition, explain its microscopic origin and give experimental guidance to identify it.

10.2 Computational Methods

In the first part of the analysis, we have performed first principles electronic structure Density Functional Theory (DFT) calculations [17, 18] on $BaSn_2$ using the all-electron full potential code (WIEN2K) [30]. The exchange-correlation term was the generalized gradient approximation (GGA) in the Perdew-Burke-Ernzerhof [19] scheme, which properly describes the electronic structure of this system [329, 330]. The calculations were carried out with a converged k-mesh and a value of $R_{mt}K_{max}$= 7.0 and a R_{mt} value of 2.5 a. u. for both Ba and Sn. Uniaxial pressure was imposed by fixing the experimental [331] lattice parameter a = 4.652 Å constant and compressing the c lattice parameter (Fig. 10.1b).

In the second part we have built a pressure-dependent tight-binding (TB) Hamiltonian that mimics the DFT calculations. We have used the `PythTB` [40] and `Pybinding` [41] packages to perform the calculations with our TB Hamiltonian. We have also included a magnetic field (B) in our TB Hamiltonian through a Peierls flux with 80 unit cells in each direction. The kernel polynomial method [332] was used to compute the DOS as a function of the applied magnetic field (Fig. 10.10).

10.3 Results and Discussion

We have divided this section in two subsections. In the first one the DFT calculations are shown, providing evidence of a pressure-induced transition in $BaSn_2$. In the second subsection, the model Hamiltonian is defined and used to provide further analysis on the topological character of the transition as well as the experimental hallmark associated to it.

10.3.1 DFT Calculations

We start computing the pressure dependence of the lattice parameter c. The crystal symmetry is fixed for all the calculations. Figure 10.2 shows the linear fitting of the lattice parameter c as a function of uniaxial pressure and the black points correspond to the DFT calculations. The linear fitting allows us to obtain c as a function of pressure P given in GPa, $c = 5.717 - 0.136P$ Å.

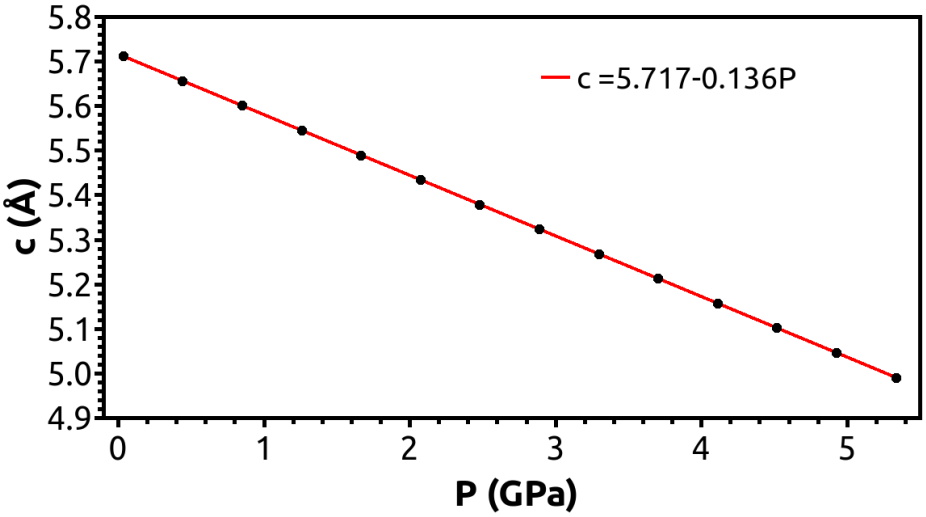


Figure 10.2: Linear fitting of lattice parameter c as a function of pressure.

We can compute now the evolution of the electronic band structure as a function of uniaxial pressure. Figure 10.3 shows the DFT band structures of $BaSn_2$ for the two different pressure regimes that we have identified (SOC is not included). The orbital character of the bands is shown in different colors. We start analyzing the low-pressure phase that we will call T1. In Fig. 10.3a we can see that a band crossing appears in the A-H line. We can notice from the orbital character of the bands that a band inversion occurs between the p_z (in red) and s (in blue) orbitals of the Sn atoms at that crossing point. Ba d orbitals (in green in the band structure calculation) are fully unoccupied. Moreover, it can be confirmed by the Fermi surface (Fig. 10.4a) that this crossing point corresponds to a topological snake-like nodal line around the A point, with an axis parallel to the z-direction. This low-pressure phase and the non-trivial topological character of the snake-like nodal line has already been studied in detail in Ref. [330].

For uniaxial pressures greater than 4 GPa a second crossing point appears along the K-M symmetry line (Fig. 10.3b). We can see that the orbital character of the bands involved in this second crossing is Sn p_z and Ba d, which suggests that a transition to a different phase (T2) might have taken place. The calculation of the Fermi surface (Fig. 10.4b) shows that this new crossing corresponds to a nodal line around the M point. The plane where this new nodal line lives is leaned 45° with respect to the z-direction. Since the M point has three arms, three new nodal lines emerge in this new T2 phase.

Note that when SOC is included in these calculations, band crossings are opened and lead to topological insulating states in both phases. Figure 10.5 shows the DFT band structure when SOC is included. SOC was introduced in a second variational manner using the scalar relativistic approximation [23, 25]. At low pressures the band crossing point at the A-H segment (related to the nodal-line) opens and the system becomes a

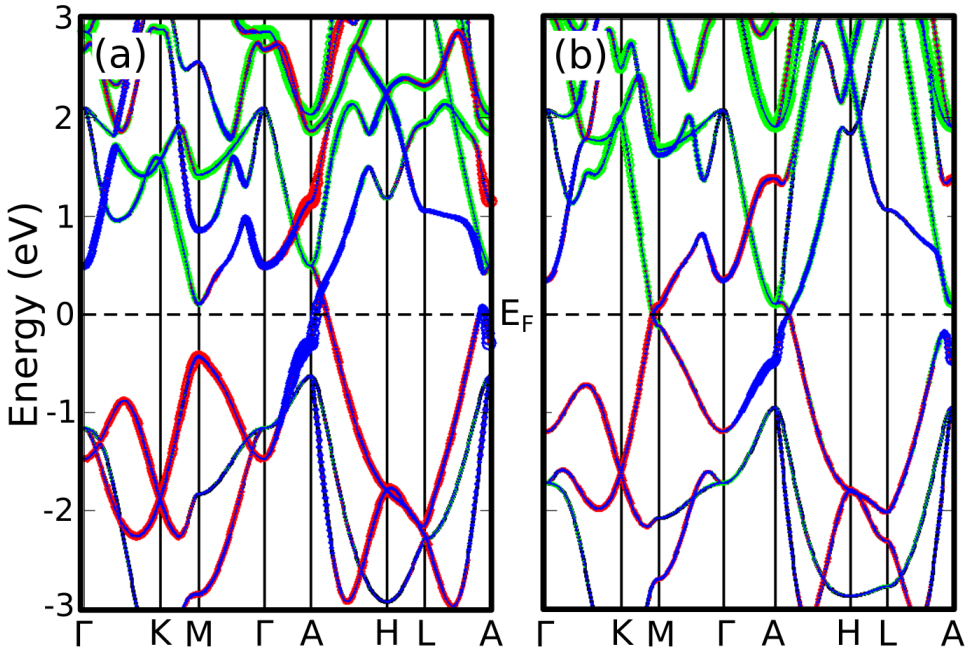


Figure 10.3: DFT band structures for $BaSn_2$. The orbital character is highlighted in colors: Sn s in blue, Sn p_z in red and Ba d in green. The Fermi level is set at zero. (a) Band structure for $P = 0$ GPa (T1), there is one band crossing point in the A-H line. (b) Band structure for $P = 6$ GPa (T2), a second band crossing appears near the M point.

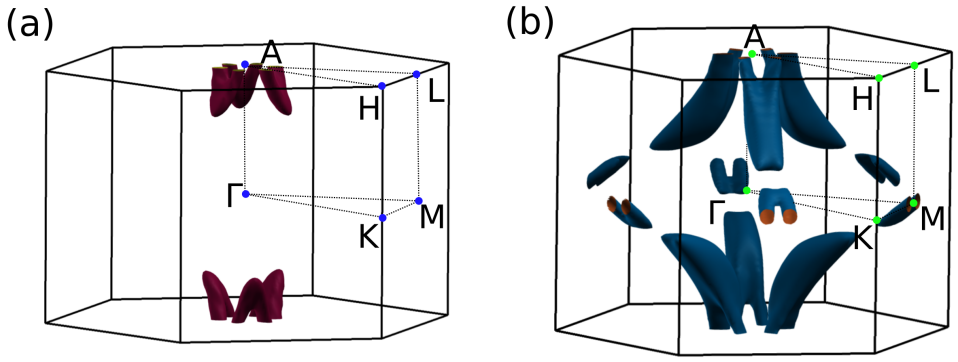


Figure 10.4: DFT Fermi surfaces for $BaSn_2$: (a) for $P = 0$ GPa (T1), it presents a snake-like nodal line around the A point, (b) for $P = 6$ GPa (T2), new nodal lines emerge around the M points.

topological insulator (Fig. 10.5a). For pressures greater than 4 GPa, the crossing around the M point (related to the second nodal-line that appears in the absence of SOC) also opens (Fig. 10.5b). Therefore, the effect of SOC in both phases is to switch the system into a topological insulator.

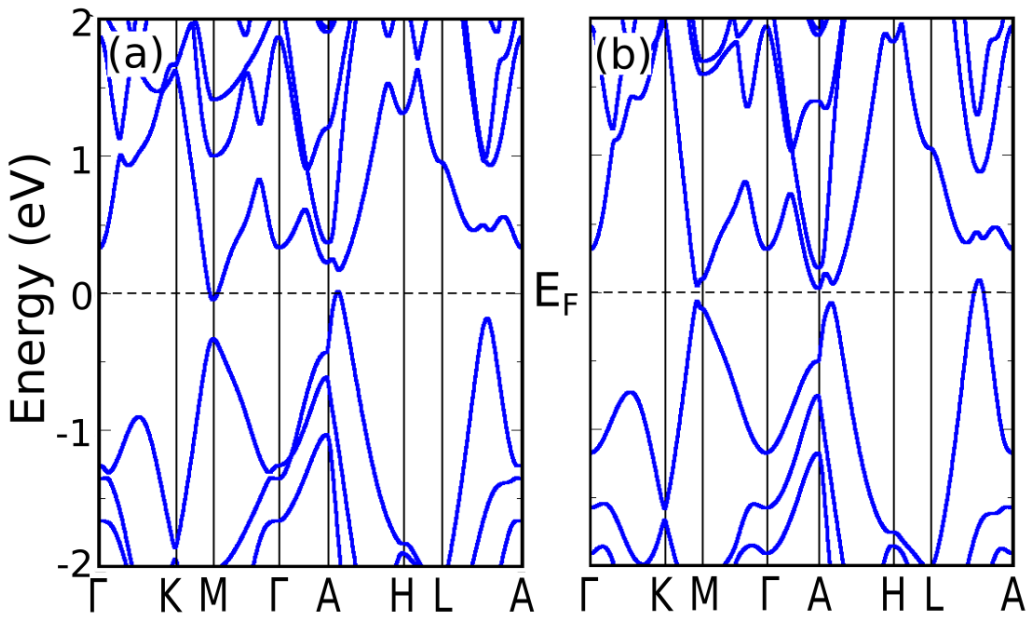


Figure 10.5: DFT band structures for $BaSn_2$ including SOC. (a) Band structure for P=0 GPa (T1). (b) Band structure for P=6 GPa (T2)

Since we are interested in analyzing NLSM transitions, we will focus in the case where SOC is absent. Our aim now is to determine the topological character of the new nodal lines that emerge around the M points when pressure is applied.

10.3.2 Tight-binding Model

In order to study the topological features and the microscopic origin of the transition, we have constructed a TB Hamiltonian as a function of uniaxial pressure. The model was built considering that the unit cell of $BaSn_2$ has the following lattice-parameter dependence with uniaxial pressure P: $a = b = 4.652$ and $c = 5.717 - 0.136P$ Å with P in GPa. The atomic positions in the unit cell are: Ba (0,0,1/2c), Sn1 (2/3a, 1/3a, 0.895c) and Sn2 (1/3a, 1/3a, 0.105c). The Hamiltonian comprises the s and p orbitals of the two Sn atoms in the unit cell and the d orbitals of the Ba atom. Thus, we have thirteen orbitals in total. The on-site energies U of each orbital are given by:

$$\begin{aligned} U_s &= -5.25 + 0.04P \\ U_{p_{x,y}} &= 0.97 + 0.04P \\ U_{p_z} &= 0.57 + 0.04P \\ U_{d_{z^2}} &= 2.75 + 0.04P \\ U_{d_{xz,yz}} &= 3.63 + 0.04P \\ U_{d_{xy,x^2-y^2}} &= 3.04 + 0.04P, \end{aligned} \tag{10.1}$$

in eV and the hopping parameters t between different orbitals are given by:

$$
\begin{aligned}
&t_{ss} = 0.4 \\
&t_{p_s p_z} = 0.35 \\
&t_{p_s p_{x,y}} = 1.3 \\
&t_{p_z p_z} = 0.2 \\
&t_{p_{x,y} p_{x,y},\sigma} = 2.0 \\
&t_{p_{x,y} p_{x,y},\pi} = 0.65 \\
&t_{p_{x,y} p_z} = 0.85 \\
&t_{d_{z^2} p_z} = 0.7 \\
&t_{d_{xz,yz} p_z} = 0.7 + 0.2P \\
&t_{d_{xy,x^2-y^2} p_z} = 0.05 \\
&t_{d_{z^2} p_{x,y}} = 0.7 \\
&t_{d_{xz,yz} p_{x,y},\sigma} = 0.3 \\
&t_{d_{xz,yz} p_{x,y},\pi} = 0.22 \\
&t_{d_{xy,x^2-y^2} p_{x,y},\sigma} = 0.24 \\
&t_{d_{xy,x^2-y^2} p_{x,y},\pi} = 0.21
\end{aligned}
\tag{10.2}
$$

in eV. Note the σ and π bonding type in some of the hopping parameters. Be aware that these hopping energies have to be multiplied by the Slater-Koster parameters that take into account the relative position between orbitals [39].

We can see that the TB Hamiltonian mimics the DFT band structure as a function of pressure. Figure 10.6 shows the computed TB band structures for two given pressures below ($P = 0$ GPa) and above ($P = 6$ GPa) the transition. The constructed TB model reproduces fairly well the obtained DFT band structures close to the Fermi level in both phases. Moreover, the analysis of the TB band crossings is shown in Fig. 10.7, and it can be seen that, in agreement with the DFT calculations of the previous subsection, the TB Hamiltonian correctly predicts a snake-like nodal line around the A point for low pressure. For pressures greater than 4 GPa new nodal lines arise around the M points. Again, these are leaned 45° with respect to the z-direction.

Once we have shown that the TB Hamiltonian we have modelled reproduces well the DFT calculations around the Fermi level, we can start using it to analyze the topological features of $BaSn_2$ in both phases.

The first thing to notice from the hopping parameters shown in eq. 10.2 is that in this TB model the only parameters that depend on pressure are the hopping energies between the Ba d_{xz} and d_{yz} with the Sn p_z orbitals as $t_{d_{xz}p_z} = t_{d_{yz}p_z} = 0.7 + 0.2P$. Therefore, the phase transition that is observed with pressure must be governed by this particular hopping. It has been previously reported that an increase of interlayer interactions without breaking any crystal symmetry might be responsible of the appearance of Lifshitz

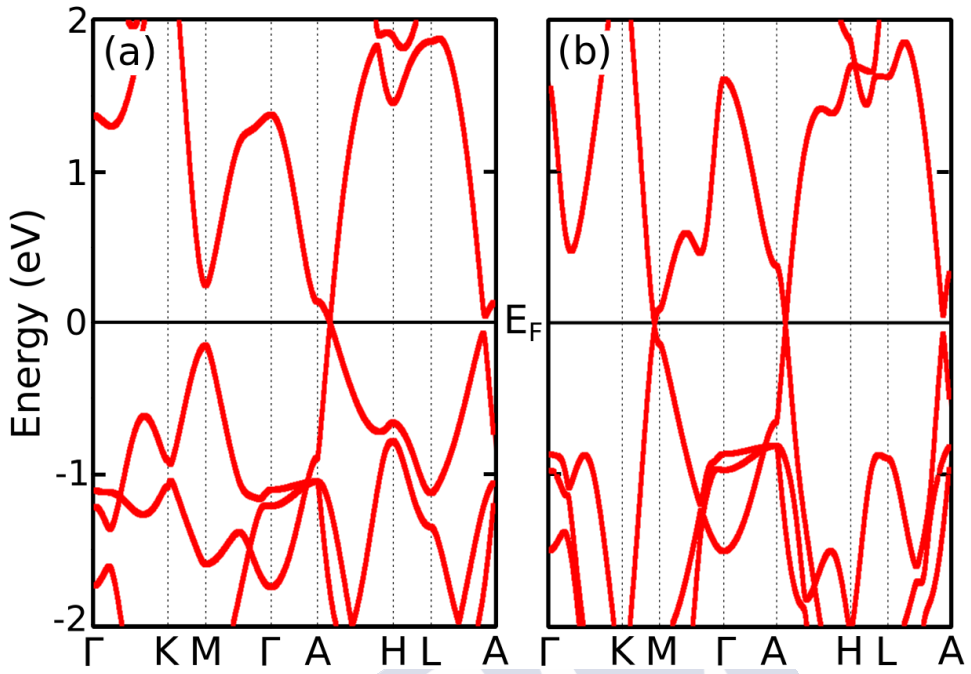


Figure 10.6: Tight-binding model band structures for $BaSn_2$ (a) for P=0 GPa (T1), the first band crossing point at the A-H line is well reproduced by the model, (b) for P=6 GPa (T2), the second band crossing near the M point is also reproduced.

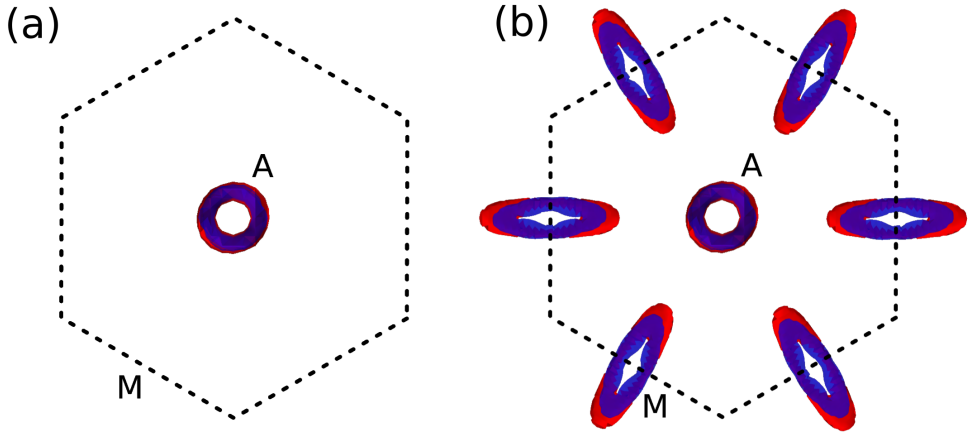


Figure 10.7: Top view of the TB band touchings within the first Brillouin zone at the Fermi level. The valence (conduction) band is shown in red (blue): (a) for P=0 GPa (T1), the snake-like nodal line is formed around the A point, (b) for P=6 GPa (T2), new nodal lines appear around the M points.

transitions in ZiSiTe [328]. Here we find that pressure changes hopping processes within the same Sn-Ba-Sn layer leading to the appearance of a new topological nodal line, without breaking the PT symmetry responsible of the stability of the nodal lines. This is at

odds to the case of ZrSiS, where it is found that a topological nontrivial-to-trivial phase transition takes place due to a crystal symmetry breaking [326].

We now analyze the topological character of the nodal lines. In Chapter 2 we define quantities in the reciprocal space such as a the Berry curvature (eq. (2.17)) or the Berry flux (eq. (2.18)) that are gauge invariant and allow to determine the topological character of a given electronic structure. A formulation in real space in terms of Wannier functions can also be given.

Wannier functions $w_{i\boldsymbol{n}}$ are orthonormal localized functions that span the same space as the eigenstates of a given set of Bloch bands $u_{i,\boldsymbol{k}} = \sum_j U_{ji}(\boldsymbol{k}) u_{j,\boldsymbol{k}}$, where $U_{ji}(\boldsymbol{k})$ is a $\boldsymbol{k}$-dependent unitary transformation [333]. The Wannier functions are defined as:

$$w_{i\boldsymbol{n}}(\boldsymbol{r}) = \frac{1}{\Omega_{1BZ}} \int_{1BZ} d\boldsymbol{k} e^{i\boldsymbol{k}\cdot(\boldsymbol{r}-\boldsymbol{T}_n)} u_{i,\boldsymbol{k}}. \tag{10.3}$$

where $\boldsymbol{n}$ corresponds to the real space unit cell. Wannier functions are not uniquely defined. A different degree of localization can be obtained in terms of the relative phases and amplitudes of the Bloch functions. In crystals with dimension greater than one hybrid Wannier functions can be defined. These are localized along one direction, for instance z, and extended in the other perpendicular directions (x and y). For a crystal with lattice parameter c along the z direction the hybrid Wannier functions are constructed as:

$$w_{inc}(k_x, k_y) = \frac{c}{2\pi} \int_0^{2\pi} dk_z e^{ik_z(z-nc)} u_{i,\boldsymbol{k}}, \tag{10.4}$$

where nc corresponds to the real space unit cell in the z-direction. We can obtain the expectation value of $\hat{z}$ in the first unit cell, i.e. $nc = 0$. This is known as the Wannier charge center along the z direction:

$$z_i(k_x, k_y) = \langle w_{i0}(k_x, k_y) | \, z \, | w_{i0}(k_x, k_y) \rangle = \frac{c}{2\pi} \int_0^{2\pi} dk_z \, \langle u_{i,\boldsymbol{k}} | \, i\partial_{k_z} \, | u_{i,\boldsymbol{k}} \rangle \,, \tag{10.5}$$

where we can identify the integrand in eq. (10.5) as the Berry connection in a one dimensional space. Therefore, the sum of the Wannier charge centers over the occupied subspace along the z direction $\mathrm{WCC}_z(k_x, k_y) = \sum_i z_i(k_x, k_y)$ is equal (up to a factor of 2π) to the total Berry phase of the occupied Bloch functions accumulated along the k_z direction, which has to be either 0 or π for an arbitrary loop in the Brillouin zone [334, 335]. Thus, in units of c, the $\mathrm{WCC}_z(k_x, k_y)$ is expected to be quantized as either 0 or 1/2 and in a NLSM a jump of 1/2 will appear when passing through a projected non-trivial nodal line, i.e. $\mathrm{WCC}_z(k_x, k_y)$ is a topological invariant. We have reformulated the analysis of the topology in terms of Wannier charge centers, which is more convenient when dealing with a real space TB model as we are doing.

Coming back to our analysis in $BaSn_2$, we have computed the sum of the Wannier charge centers along a high symmetry path in the k_x-k_y plane over the z-direction ($\mathrm{WCC}_z(k_x, k_y)$). At low pressure there is only one nodal line around the A point, which

produces a jump of 1/2 in $\mathrm{WCC}_z(k_x, k_y)$ when crossing it (see Fig. 10.8a). This confirms the topological character of that nodal line, as already reported in Ref. [330]. In the high pressure regime new nodal lines emerge around the M points. Figure 10.8b shows that they produce a jump of $-1/2$ in $\mathrm{WCC}_z(k_x, k_y)$. This is a proof of the non-trivial character also for these nodal lines. Note, however, that nodal lines around the M points have opposite sign to that around A. Since the M point has 3 branches it contributes three times. Adding contributions from all the nodal lines, at high pressures the system behaves as it would have two nodal lines, i.e. this phase transition has increased the amount of topological nodal lines by 1.

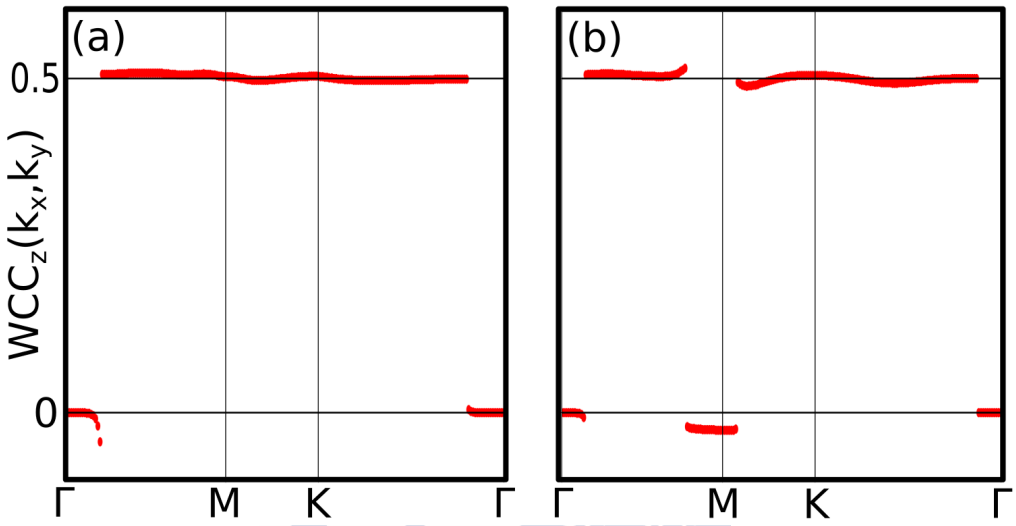


Figure 10.8: Wannier charge centers (a) For P=0 GPa (T1), around the Γ point and due to the snake-like nodal line a jump of 0.5 happens. (b) For P=6 GPa (T2), due to the new topological nodal line a second jump of -0.5 appears around the M point.

It is important to remember that topological phase transitions are subject to energy considerations to take place as other phase transitions. In the present case, as we are neglecting SOC, the system is spin-rotational invariant, so the symmetry protecting the nodal line at ambient pressure is the combination of inversion and time-reversal symmetries. As this symmetry is not removed during the transition, as can be easily concluded from the fact that the initial nodal line remains unaltered, and the same combined symmetry protects the second nodal line appearing after $P = 4$ GPa. Then, only energetic considerations are behind this topological phase transition.

As mentioned above, one important feature of the topological NLSM is the appearance of robust surface states. The TB Hamiltonian allows to compute them for each phase separately. Figure 10.9a shows the energy states of a 50-layer structure stacked along the z-direction for the T1 phase, i.e. at low pressures. The colormap represents the expectation value of the position operator along the z-direction, in blue (red) the bottom (top) layer and in grey the bulk states. We can see the crossings related to the topological

nodal line that appears in the bulk. The edge states fill the space outside the projected nodal line around Γ. This behavior is a consequence of the 1D atomic chains with time-reversal and spatial inversion symmetries [330]. In the high pressure T2 phase (Fig. 10.9b) new crossings, related to the new topological nodal line, appear around the M point for the bulk states. In this phase, the surface states get modified by the presence of the new nodal line projected around M. As in the low pressure phase, inside the nodal line the surface states are not present. Moreover, the dispersion of all surface states is increased by uniaxial pressure. In the T1 phase the bandwidth of the surface state is about 0.2 eV, while in the T2 phase it increases to more than 1 eV. Note also that the surface states are highly sensitive to the kind of truncation imposed to the structure. Here we chose to terminate with a Sn-rich plane for our calculations, but different cuts can be used to obtain surface states inside or outside the projected nodal loop as explained in Ref. [330].

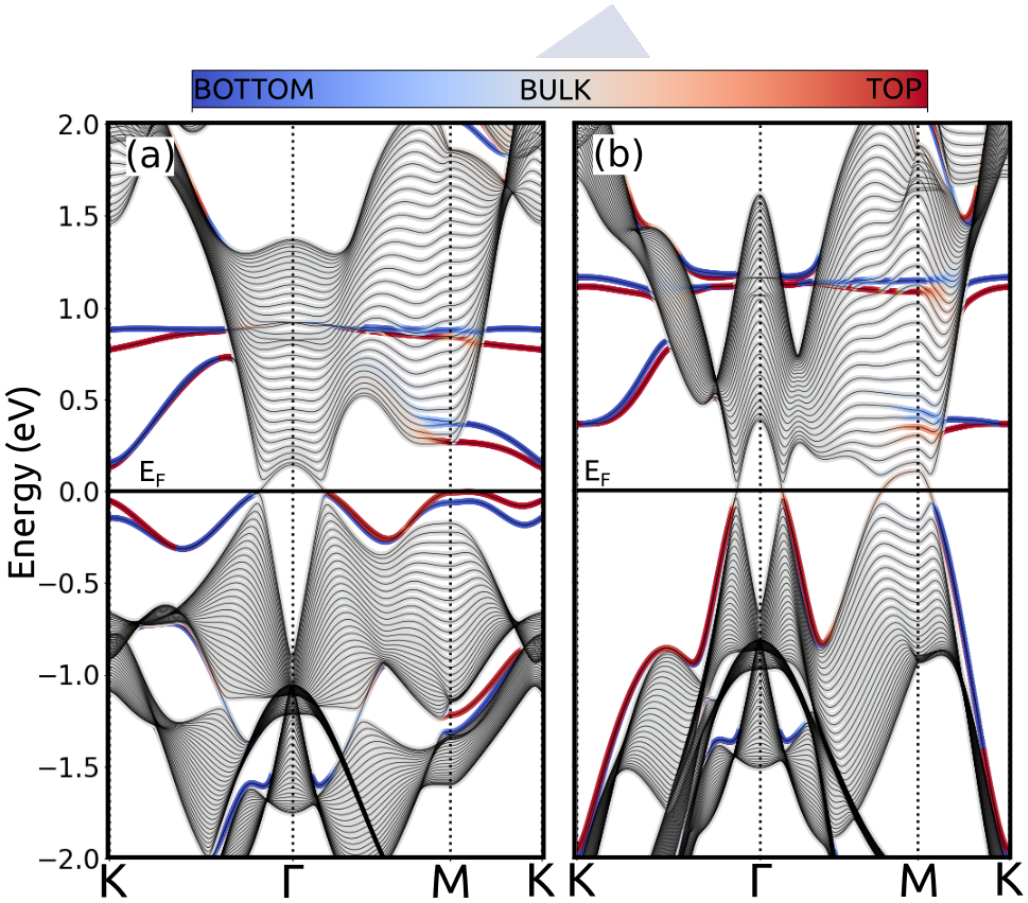


Figure 10.9: Energy states in a 50-layer structure stacked along the z-direction (Sn-dangling bond terminated). The colormap represents the expectation value of the position operator along the z-direction, in blue (red) the bottom (top) layer and in grey the bulk states. (a) For P=0 (T1), the surface states fill the region outside the projected nodal line around the Γ point (b) For P=6 GPa (T2), the surface states get opened around the M point due to the new nodal lines.

Finally, let us provide some experimental guidance in order to identify the topological-to-topological phase transition that we have found. Magnetotransport measurements are the most extended experimental tests employed to analyze the topological character of NLSM through the analysis of the corresponding Landau level fan diagrams. It is also known that the same information can be obtained from quantum oscillations in the density of states (DOS) [336–338]. Together with the Berry phase contribution to the phase of the quantum oscillations, non-trivial topological phases in NLSM are characterized by the appearance of zero-energy Landau levels [339] in the presence of a magnetic field. The orbits associated to this zero-energy Landau level would be in turn responsible for the presence of a non-trivial Berry phase in the Landau level fan diagram. Therefore, in order to check that, we have included a magnetic field (B) in our TB Hamiltonian.

In the low-pressure regime T1, there is only one nodal loop, lying in the OZ plane. When the magnetic field is applied perpendicular to the nodal line ($\theta = 0$), no zero-energy modes are present since all the magnetic oscillations are trivial (Fig. 10.10a). However, when the field is applied perpendicular to the OZ plane ($\theta = \pi/2$) the DOS associated to a zero-energy Landau level is observed (Fig. 10.10c). These results are in agreement and equivalent to those of a single nodal line lying in the k_x-k_y plane produced by a cubic lattice [337].

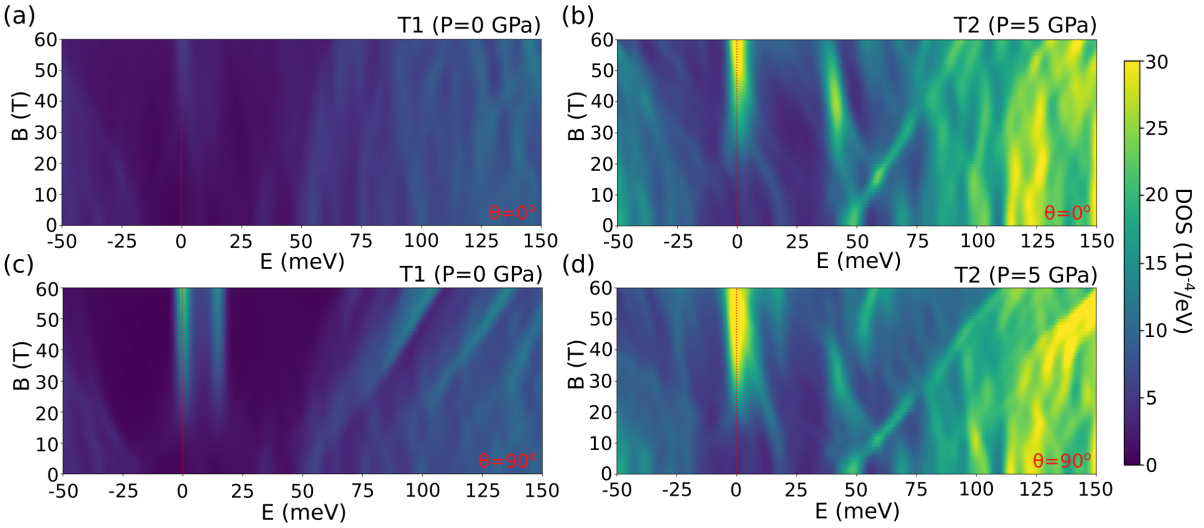


Figure 10.10: Colormap of the density of states as a function of an applied magnetic field B along the z-direction (a,b) and perpendicular to it (c,d) for the T1 phase (a,c) and for the T2 phase (b,d). Magnetic oscillations and zero-energy modes are analyzed in the text.

In the high-pressure phase T2, new nodal lines tilted $\pi/4$ with respect to the OZ-direction are present around the M points. Thus, when the magnetic field is applied along the OZ-direction ($\theta = 0$) only the contribution from these new nodal lines is observed in the DOS at zero energy (Fig. 10.10b). The presence of this zero-energy mode is related with the nontrivial Berry phase that can be measured by the analysis of

the quantum oscillations in magnetotransport. Thus, for a given tilting angle θ where the magneto-oscillations look trivial, the appearance of another nodal line with different tilting angle with respect to the magnetic field will generate topologically nontrivial magneto-oscillations. Therefore, it provides a way to directly observe the topological transition described in the present work. When the magnetic field B is applied perpendicular to the OZ plane ($\theta = \pi/2$), the original nodal line and the new ones contribute to the DOS at $E = 0$. Since both zero-energy modes correspond to an extreme orbit that dominates the amplitude of the quantum oscillations, we expect a substantial increase in the magneto-oscillation amplitude (Fig. 10.10d). We are focusing on the qualitative analysis of the pressure-induced topological phase transitions in NLSM, a fully quantitative analysis of the topological character of the quantum oscillations goes beyond the scope of the present work. However, we can obtain more quantitative results by focusing on the features of the zero-energy DOS of each phase.

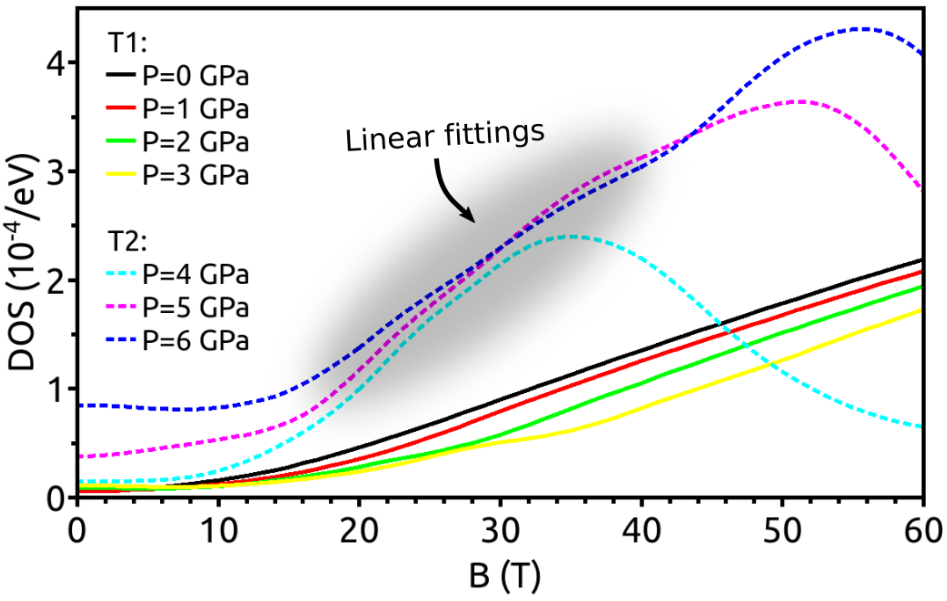


Figure 10.11: Zero-energy modes for different pressures as a function of the magnetic field. Linear fittings were performed for each phase. The ratio between slopes is 1.98, demonstrating the existence of a topological-to-topological phase transition (see text).

Figure 10.11 shows the DOS at zero energy as a function of B, for $\theta = \pi/2$ and for different pressure values. Both phases can be identified in this plot. While in the T1 phase there is only one nodal line contributing to the DOS at the Fermi level, in the T2 phase the emergence of 3 new nodal lines with opposite sign (as previously shown in the $WCC_z(k_x, k_y)$ analysis) makes the system behave as it would have 2 independent nodal lines. Therefore, the DOS at the Fermi level in the T2 phase is expected to be two times that in the T1 phase. To check whether this argument is correct, we have performed

linear fittings of the DOS as a function of B. While the dependence of the DOS with B in the T1 phase is almost linear since there is only 1 nodal line, the behavior in the T2 phase appears to be more complex as there are multiple nodal lines oriented along different directions. For this reason, we have restricted the fittings to a range of values in which the DOS shows a linear trend (shaded area in Fig. 10.11). We have also averaged the slopes of each phase to reduce the uncertainty. We have obtained a ratio between the slope of phase T2 (s_{T2}) and T1 (s_{T1}) of $s_{T2}/s_{T1} = 1.98 \simeq 2$. Therefore, this demonstrates a clear signature of the topological-to-topological phase transition.

As we have stated in the introduction of this chapter, it has been widely reported, both theoretically and experimentally, that pressure can induce changes in the Fermi surface of different materials [340–343], and in some cases pressure has been found to modify the topological character of the compound. For instance, it has been shown that pressure can induce a transition to a nontrivial topological phase from a trivial one [344–350]. The opposite case has been reported too. Pressure is able to induce a transition from topological to trivial in which topological objects such as nodal pairs [351] or nodal lines are annihilated [325]. In this work, we report a different kind of transition (topological-to-topological) in $BaSn_2$ when SOC is neglected. Using $BaSn_2$ as a model, we have shown that pressure can increase the number of topological nodal lines in an already nontrivial compound. Multiorbital character of the bands and crystal symmetry preservation have been found to be key factors to increase the number of topological nodal lines.

10.4 Conclusions

In this chapter we have performed a combined set of DFT and TB model calculations in $BaSn_2$. We have found that the number of topological nodal lines increases when uniaxial pressure is applied to the system. Therefore, highlighting the existence of a topological-to-topological phase transition at around 4 GPa. The microscopic origin of such transition was explained, claiming that Ba d electrons play a fundamental role on it. We have also proposed a way to experimentally test this kind of transitions by means of magnetotransport measurements.

Final Remarks and Outlook

> "The only true wisdom is in knowing you know nothing."
>
> — Socrates

In this thesis we have studied from a theoretical point of view the interplay between the electronic, magnetic and structural degrees of freedom in crystalline transition metal compounds. We have started setting up the basics to describe materials at the nanoscale. We have seen that this entails a many-body problem in which electrons and nuclei are the fundamental particles. Their interactions produce the emergence of collective phenomena and determine the properties of the material at the macroscale.

In the first part, we have explained the *ab initio* approach to solve that quantum problem. We have provided different approximations and methods to simplify and make the many-body system tractable. In order to do so, the fundamental concept of symmetry was highlighted. We have also introduced the connection between the nano and the macro scale description of a material through statistical mechanics and transport properties. In the second part we have applied all that theory to study different transition metal compounds. This family of compounds presents a huge variety of different properties, and hence, forms an ideal platform to get fundamental knowledge of materials. In particular, we have mainly focused on oxides and layered van der Waals materials. The reason for this is their huge versatility to be synthesized and nanostructured in different forms. We have started analyzing the transport properties of $SrTiO_3$, a material that we have discussed in the frame of thermoelectrics. We then explain the ferromagnetic and insulating behaviour of $LaCoO_3$ when grown on top of $SrTiO_3$. Then, the effect of doping was analyzed in infinite-layer nickelates leading to an analogous electronic structure to that of the high-temperature-superconducting cuprates. After that, we have exposed how the spectrum of Cs_2CuCl_4 can be described in combination of experiments and theory. The next work was devoted to present a comparative study between the electronic and magnetic properties of $CrBr_3$ and $Cr_2Ge_2Te_6$, two Cr-based van der Waals ferromagnets with similar structure. Later, we analyzed the interplay between ferromagnetic and charge density wave phases in $CrTe_2$ and VSe_2. Two transition metal dichalcogenides in which ferromagnetic order is discussed in a different framework. The final chapter was dedicated to study a topological-

to-topological phase transition in $BaSn_2$. The partially filled d electrons are found to play a major role to explain the miscellaneous phenomena encountered in crystalline transition metal compounds.

All the works presented in this thesis represent illustrative examples of the state-of-the-art research in Solid State Physics. They help to achieve fundamental understanding in this wide field. However, this is just the tip of the iceberg. There are a lot of investigations to be carried out. Finding the best thermoelectric material and controlling heat transport at will remains an active area. Achieving ordered phases at room temperature such as ferroelectricity or ferromagnetism continue to be a fundamental goal, in particular in the 2D limit. Finding a proper description to explain exotic phenomena like spin-liquids or superconductivity remains elusive. Studying the interplay between dimensionality effect and the electronic, magnetic and structural properties of solids keeps on being a need to comprehend the many-body emergent phenomena. The renewed role of topology in condensed matter is far from being totally understood. Many other physical properties that we have not talked about deserve to be considered. From a theoretical point of view, the methods used in this thesis might not be enough to accomplish those aims. Electron correlation continues to be an ambitious corner stone to be properly described. New approaches should be studied and developed to achieve it. In spite of this overwhelming work to be done, in this thesis we have paved the way for future research in this area. We have tried to remark the importance of having always in mind the full many-body problem. Nuclei and electrons, both together, play a fundamental role to explain the electronic, magnetic and structural properties of materials.

USC UNIVERSIDADE DE SANTIAGO DE COMPOSTELA

Acknowledgements

This PhD thesis would not have been possible without the presence of many people. In the following lines I will try to thank them.

I have to start thanking my PhD supervisor, Prof. Víctor Pardo, for sharing with me all his knowledge during these years. If I can consider myself a scientist is thanks to him. From the very beginning he gave me the freedom to think by myself while at the same time he provided valuable advice to develop my career. Víctor is not only an excellent colleague and teacher, but, most importantly, he is an example of the personal and scientific ethics that should be in academia.

I would like to acknowledge all my group mates over these years: Pablo, Juan, Cris, Iván, Dani, Jan, and David. It has been a pleasure to work along you and I wish you the best. I want to express my gratitude to the professors in the area of Electromagnetism: Javier, Daniel, Jorge and Alfonso, who have shared with me their teaching experience. Also to Marisol and Rafa who have always helped me with everything I have needed.

During this period of life I have got the opportunity to contact and visit some scientific groups. The closest one, here in Santiago de Compostela, was the group led by Prof. Francisco Rivadulla. Fran is another of those representative examples of what a scientist should be. A proof of that is the wonderful people he teams with that I have the pleasure to meet: Elías, Lucía, Alex, Eric, David and Carlos. I have to thank Prof. David Singh for giving me the chance to visit his group in Columbia, Missouri. It was a great experience from which I want to thank Akshay, Tushar, Zongliang, Kristen, Zark, Aditya and the rest of the group mates there. Thanks to Prof. Ion Errea who has allowed me to work in is lovely group for three months. He is an outstanding professional from whom I have learnt not only new scientific ideas but also how a group should be managed. I want to thank my mates there, specially Josu and David. Of course, I have to thank my flatmate in Donosti, Nekane. This visit would not have been the same without your company.

Special thanks to Dr. Santiago Blanco Canosa. Santi is probably the most devoted scientist I have met. He has been like a second supervisor for me, but also a hard working student to supervise. He has coined this thesis as *The París de Noia Thesis*[1] due to the diverse content that has been exposed on it. Great part of that rich variety is his fault. Thank you Santi for sharing your ideas.

[1]For the non galicians, *París de Noia* is a galician music group that plays in summer festivities a selection of hits that everyone enjoys.

Finally I would like to say a few words in my mother tongue to those who are always there, out of the scientific world, taking care and supporting, family and friends.

Gustaríame agradecer dun xeito especial aos que sempre están pendentes dun, sen importar a distancia. A miña nai por preocupase constantemente de min e ser un exemplo de traballo e dedicación. A meu pai por estar sempre disposto a axudar no que faga falta sendo un exemplo de boa persoa. A Davi por ser simplemente o mellor irmán do mundo e un referente ao que mirarse. A meus tíos e tías Fon, Fran, Ali, Rafa, Lin e Francisco por pasar tanto tempo comigo ensinándome moitas das cousas que sei. A meus primos pequenos Sandra, Óscar e Fonsi por manterme en contacto cos anos que van pasando e non van volver. A miñas avóas Julia e Mila e a meu avó Adolfo por coidarme de pequeno, construíndo esa verdadeira patria que é a infancia.

Tamén querería adicar unhas palabras a esas persoas marabillosas que un se vai atopando e que chama amigos. Aos da infancia Alex, Carmen, Diego, Alicia e Alberto por terme aturado dende ben novo e estar sempre aí cando un volve ao Carballiño. Aos do Clemente, cos cales vivín os meus primeiros (e non tan primeiros) anos na Universidade. Gustaríame destacar a Filloas poloa boa sintonía que tiven con el estes anos. Mención tamén para o grupo de doutorandos do IGFAE que acolleu a este físico aplicado nos seus contubernios. Remato acordándome dos meus queridos físicos Pablo, Pedro, Alejandro e Parga *feat.* Rosalía. Tiven a sorte de compartir con vos un fogar durante estes 4 anos de tese no que xurdiron moitas vivencias inesquecibles. O pronóstico indica que nos distanciaremos nos próximos anos, pero teño a certeza de que faremos o imposible por volver a xuntarnos.

"Se queres ir máis rápido, camiña só.
Pero se o que queres e chegar máis
lonxe, vai acompañado."

— Proverbio africano

List of Publications

In this appendix I include a detailed description of the articles I have authored. All the Journals in which they have been published allow the authors to reproduce their content in dissertations. Moreover, all the coauthors have given their consent to used the articles in this thesis. Note that articles [I] and [II] are prior to this thesis. However, they were included here because their results were used in the analyses that we have performed. Article [I] is described in section 4.2, while article [II] is simply cited in section 4.3.

[I] Ab initio study of the strain dependence of thermopower in electron-doped $SrTiO_3$, *Journal of Physics: Condensed Matter* 29 065501 (2017)

Authors
Adolfo O. Fumega[*ab] and Victor Pardo[*ab]

[a] Departamento de Física Aplicada, Universidade de Santiago de Compostela, E-15782 Campus Sur s/n, Santiago de Compostela, Spain.
[b] Instituto de Investigacións Tecnolóxicas, Universidade de Santiago de Compostela, E-15782 Campus Sur s/n, Santiago de Compostela, Spain.

PhD student contribution: First and corresponding author

Journal information
Journal Name: Journal of Physics: Condensed Matter **Publisher:** IOP Science
ISSN: 0953-8984 **DOI:** https://doi.org/10.1088/1361-648X/29/6/065501
Impact factor in 2016-2017: 2.678 **Quartile in Material Science:** Q2
Reproduced in this thesis with standard author permissions from the IOP Science **Chapter:** 4

[II] Analysis of the temperature dependence of the thermal conductivity of insulating single crystal oxides, *APL Materials* 4, 104815 (2016)

Authors
E. Langenberg,[a] E. Ferreiro-Vila,[a] V. Leborán,[a] A. O. Fumega,[b] V. Pardo,[b] and F. Rivadulla[*a]

[a] CIQUS, Centro de Investigación en Química Biolóxica e Materiais Moleculares, and Departamento de Química-Física, Universidade de Santiago de Compostela, 15782-Santiago de Compostela, Spain.
[b] Departamento de Física Aplicada, Universidade de Santiago de Compostela, E-15782 Campus Sur s/n, Santiago de Compostela, Spain.

PhD student contribution: Contributing author in the theoretical calculations

Journal information
Journal Name: APL Materials **Publisher:** American Institute of Physics
ISSN: 2166-532X **DOI:** https://doi.org/10.1063/1.4966220
Impact factor in 2016-2017: 4.623 **Quartile in Material Science:** Q1
This article has NOT been reproduced in this thesis, it was only cited **Chapter:** 4

[III] Understanding the lattice thermal conductivity of $SrTiO_3$ from an *ab initio* perspective, *Physical Review Materials* 4, 033606 (2020)

Authors
Adolfo O. Fumega,[*abc] ,Yuhao Fu,[c] Victor Pardo,[ab] and David Singh[*c]

[a] Departamento de Física Aplicada, Universidade de Santiago de Compostela, E-15782 Campus Sur s/n, Santiago de Compostela, Spain.
[b] Instituto de Investigacións Tecnolóxicas, Universidade de Santiago de Compostela, E-15782 Campus Sur s/n, Santiago de Compostela, Spain.
[c] Department of Physics and Astronomy, University of Missouri, Columbia, Missouri 65211-7010, USA

PhD student contribution: First and Corresponding author

Journal information
Journal Name: Physical Review Materials **Publisher:** American Physical Society
ISSN: 2475-9953 **DOI:** https://doi.org/10.1103/PhysRevMaterials.4.033606
Impact factor in 2019-2020: 3.337 **Quartile in Material Science:** Q1 (SJR) or Q2 (JCR)
Reproduced in this thesis with standard author permissions from the American Physical Society **Chapter:** 4

[IV] Ferromagnetic and insulating behavior of $LaCoO_3$ films grown on a (001) $SrTiO_3$ substrate: A simple ionic picture explained *ab initio*, *Physical Review Materials* 1, 054403 (2017)

Authors
Adolfo O. Fumega[*ab] and Victor Pardo[*ab]

[a] Departamento de Física Aplicada, Universidade de Santiago de Compostela, E-15782 Campus Sur s/n, Santiago de Compostela, Spain.
[b] Instituto de Investigacións Tecnolóxicas, Universidade de Santiago de Compostela, E-15782 Campus Sur s/n, Santiago de Compostela, Spain.

PhD student contribution: First and corresponding author

Journal information
Journal Name: Physical Review Materials **Publisher:** American Physical Society
ISSN: 2475-9953 **DOI:** https://doi.org/10.1103/PhysRevMaterials.1.054403
Impact factor in 2017-2018: -, now 3.337 **Quartile in Material Science:** -, now Q1 (SJR) or Q2 (JCR)
Reproduced in this thesis with standard author permissions from the American Physical Society **Chapter:** 5

[V] Effects of Sr doping on the electronic and spin-state properties of infinite-layer nickelates: Nature of holes, *Physical Review B* 102, 224506 (2020)

Authors
Jyoti Krishna,[a] Harrison LaBollita,[a] Adolfo O. Fumega,[bc] Victor Pardo[bc] and Antia S. Botana[*a]

[a] Department of Physics, Arizona State University, Tempe, Arizona 85287, USA.
[b] Departamento de Física Aplicada, Universidade de Santiago de Compostela, E-15782 Campus Sur s/n, Santiago de Compostela, Spain.
[c] Instituto de Investigacións Tecnolóxicas, Universidade de Santiago de Compostela, E-15782 Campus Sur s/n, Santiago de Compostela, Spain.

PhD student contribution: contributing author in the calculations

Journal information
Journal Name: Physical Review B **Publisher:** American Physical Society
ISSN: 2469-9950 **DOI:** https://doi.org/10.1103/PhysRevB.102.224506
Impact factor in 2019-2020: 3.576 **Quartile in Material Science:** Q1 (SJR) or Q2 (JCR)
Reproduced in this thesis with standard author permissions from the American Physical Society **Chapter:** 6

[VI] Electronic structure and magnetic exchange interactions of Cr-based van der Waals ferromagnets. A comparative study between $CrBr_3$ and $Cr_2Ge_2Te_6$, *Journal of Materials Chemistry C* 8 13582-13589 (2020)

Authors
Adolfo O. Fumega,[*ab] S. Blanco-Canosa,[*cd] H. Babu-Vasili,[e] P. Gargiani,[e] Hongze Li,[f] Jian-Shi Zhou,[f] F. Rivadulla[g] and Victor Pardo[*ab]

[a] Departamento de Física Aplicada, Universidade de Santiago de Compostela, E-15782 Campus Sur s/n, Santiago de Compostela, Spain.
[b] Instituto de Investigacións Tecnolóxicas, Universidade de Santiago de Compostela, E-15782 Campus Sur s/n, Santiago de Compostela, Spain.
[c] Donostia International Physics Center, DIPC, 20018 Donostia-San Sebastian, Basque Country, Spain.
[d] IKERBASQUE, Basque Foundation for Science, 48013 Bilbao, Basque Country, Spain.
[e] ALBA Synchrotron Light Source, Cerdanyola del Vallès, 08290 Barcelona, Catalonia, Spain.
[f] Texas Materials Institute, ETC 9.102, The University of Texas at Austin, Austin, Texas, USA.
[g] CIQUS, Centro de Investigación en Química Biolóxica e Materiais Moleculares, and Departamento de Química-Física, Universidade de Santiago de Compostela, 15782-Santiago de Compostela, Spain.

PhD student contribution: First and corresponding author

Journal information
Journal Name: Journal of Materials Chemistry C **Publisher:** Royal Society of Chemistry
ISSN: 2050-7526 **DOI:** https://doi.org/10.1039/D0TC02003F
Impact factor in 2019-2020: 7.194 **Quartile in Material Science:** Q1
Reproduced in this thesis with standard author permissions from the Royal Society of Chemistry **Chapter:** 8

[VII] Controlled Two-Dimensional Ferromagnetism in 1T–$CrTe_2$: The Role of Charge Density Wave and Strain, *Journal of Physical Chemistry C* 124, 38, 21047-21053 (2020)

Authors
Adolfo O. Fumega[*ab] Jan Phillips[ab] and Victor Pardo[*ab]

[a] Departamento de Física Aplicada, Universidade de Santiago de Compostela, E-15782 Campus Sur s/n, Santiago de Compostela, Spain.
[b] Instituto de Investigacións Tecnolóxicas, Universidade de Santiago de Compostela, E-15782 Campus Sur s/n, Santiago de Compostela, Spain.

PhD student contribution: First and corresponding author

Journal information
Journal Name: Journal of Physical Chemistry **Publisher:** American Chemical Society
ISSN: 1932-7447 **DOI:** https://doi.org/10.1021/acs.jpcc.0c04913
Impact factor in 2019-2020: 4.189 **Quartile in Material Science:** Q1
Reproduced in this thesis with standard author permissions from the American Chemical Society **Chapter:** 9

[VIII] Absence of Ferromagnetism in VSe_2 Caused by Its Charge Density Wave Phase, *Journal of Physical Chemistry C* 123, 45, 27802-27810 (2019)

Authors
Adolfo O. Fumega,[*ab] M. Gobbi,[c] P. Dreher,[c] W. Wan,[c] C. González-Orellana,[c] M. Peña-Díaz,[c] C. Rogero,[c] J. Herrero-Martín,[d] P. Gargiani,[d] M. Ilyn,[c] M. M. Ugeda,[c] Victor Pardo[*ab] and S. Blanco-Canosa[*ef]

[a] Departamento de Física Aplicada, Universidade de Santiago de Compostela, E-15782 Campus Sur s/n, Santiago de Compostela, Spain.
[b] Instituto de Investigacións Tecnolóxicas, Universidade de Santiago de Compostela, E-15782 Campus Sur s/n, Santiago de Compostela, Spain.
[c] Centro de Físicade Materiales (CSIC UPV/EHU), Paseo Manuel de Lardizábal, 5, E-20018 Donostia San Sebastián, Gipzukoa, Spain.
[d] ALBA Synchrotron Light Source, Cerdanyola del Vallès, 08290 Barcelona, Catalonia, Spain.
[e] Donostia International Physics Center, DIPC, 20018 Donostia-San Sebastian, Basque Country, Spain.
[f] IKERBASQUE, Basque Foundation for Science, 48013 Bilbao, Basque Country, Spain.

PhD student contribution: First and corresponding author, theoretical part

Journal information
Journal Name: Journal of Physical Chemistry **Publisher:** American Chemical Society
ISSN: 1932-7447 **DOI:** https://doi.org/10.1021/acs.jpcc.9b08868
Impact factor in 2018-2019: 4.309 **Quartile in Material Science:** Q1
Reproduced in this thesis with standard author permissions from the American Chemical Society **Chapter:** 9

[IX] Increasing the number of topological nodal lines in semimetals via uniaxial pressure, *Scientific Reports* 11, 10574 (2021)

Authors
Adolfo O. Fumega,[*ab] Victor Pardo[ab] and Alberto Cortijo[*c]

[a] Departamento de Física Aplicada, Universidade de Santiago de Compostela, E-15782 Campus Sur s/n, Santiago de Compostela, Spain.
[b] Instituto de Investigacións Tecnolóxicas, Universidade de Santiago de Compostela, E-15782 Campus Sur s/n, Santiago de Compostela, Spain.
[c] Departamento de Física de la Materia Condensada, Universidad Autónoma de Madrid, Madrid E-28049, Spain

PhD student contribution: First and corresponding author

Journal information
Journal Name: Scientific Reports **Publisher:** Nature Publishing Group
ISSN: 2045-2322 **DOI:** https://doi.org/10.1038/s41598-021-90165-y
Impact factor in 2019-2020: 3.998 **Quartile in Multidisciplinar:** Q1
Reproduced in this thesis with standard author permissions from the Nature Publishing Group **Chapter:** 10

USC
UNIVERSIDADE
DE SANTIAGO
DE COMPOSTELA

Bibliography

[1] R. M. Martin, *Electronic Structure: Basic Theory and Practical Methods*, Cambridge University Press, **2004**.

[2] T. Lancaster, S. J. Blundell, *Quantum field theory for the gifted amateur*, Oxford University Press, Oxford, **2014**.

[3] M. Dresselhaus, G. Dresselhaus, A. Jorio, *Group Theory: Application to the Physics of Condensed Matter*, Springer Berlin Heidelberg, **2007**.

[4] J. Ziman, *Electrons and Phonons: The Theory of Transport Phenomena in Solids*, Clarendon Press, **1960**.

[5] D. I. Khomskii, *Transition Metal Compounds*, Cambridge University Press, **2014**.

[6] T. Tritt, *Thermal Conductivity: Theory, Properties, and Applications*, Springer US, **2005**.

[7] E. Schrödinger, *Phys. Rev.* **1926**, *28*, 1049–1070.

[8] P. A. M. Dirac, R. H. Fowler, *Proceedings of the Royal Society of London. Series A Containing Papers of a Mathematical and Physical Character* **1928**, *117*, 610–624.

[9] M. Born, R. Oppenheimer, *Annalen der Physik* **1927**, *389*, 457–484.

[10] R. P. Feynman, *Phys. Rev.* **1939**, *56*, 340–343.

[11] J. Harris, *Phys. Rev. A* **1984**, *29*, 1648–1659.

[12] V. Fock, *Zeitschrift für Physik* **1930**, *61*, 126–148.

[13] J. C. Slater, *Phys. Rev.* **1929**, *34*, 1293–1322.

[14] L. H. Thomas, *Mathematical Proceedings of the Cambridge Philosophical Society* **1927**, *23*, 542–548.

[15] E. Fermi, *Endiconti: Accademia Nazionale dei Lincei* **1927**, *6*, 602–607.

[16] P. A. M. Dirac, *Mathematical Proceedings of the Cambridge Philosophical Society* **1930**, *26*, 376–385.

[17] P. Hohenberg, W. Kohn, *Phys. Rev.* **1964**, *136*, B864–B871.

[18] W. Kohn, L. J. Sham, *Phys. Rev.* **1965**, *140*, A1133–A1138.

[19] J. P. Perdew, K. Burke, M. Ernzerhof, *Phys. Rev. Lett.* **1996**, *77*, 3865–3868.

[20] V. I. Anisimov, F. Aryasetiawan, A. Lichtenstein, *Journal of Physics: Condensed Matter* **1997**, *9*, 767.

[21] A. D. Becke, E. R. Johnson, *The Journal of Chemical Physics* **2006**, *124*, 221101.

[22] F. Tran, P. Blaha, *Phys. Rev. Lett.* **2009**, *102*, 226401.

[23] A. H. MacDonald, W. E. Picket, D. D. Koelling, *Journal of Physics C: Solid State Physics* **1980**, *13*, 2675–2683.

[24] K. Lejaeghere, G. Bihlmayer, T. Björkman, P. Blaha, S. Blügel, V. Blum, D. Caliste, I. E. Castelli, S. J. Clark, A. Dal Corso, S. de Gironcoli, T. Deutsch, J. K. Dewhurst, I. Di Marco, C. Draxl, M. Dułak, O. Eriksson, J. A. Flores-Livas, K. F. Garrity, L. Genovese, P. Giannozzi, M. Giantomassi, S. Goedecker, X. Gonze, O. Grånäs, E. K. U. Gross, A. Gulans, F. Gygi, D. R. Hamann, P. J. Hasnip, N. A. W. Holzwarth, D. Iuşan, D. B. Jochym, F. Jollet, D. Jones, G. Kresse, K. Koepernik, E. Küçükbenli, Y. O. Kvashnin, I. L. M. Locht, S. Lubeck, M. Marsman, N. Marzari, U. Nitzsche, L. Nordström, T. Ozaki, L. Paulatto, C. J. Pickard, W. Poelmans, M. I. J. Probert, K. Refson, M. Richter, G.-M. Rignanese, S. Saha, M. Scheffler, M. Schlipf, K. Schwarz, S. Sharma, F. Tavazza, P. Thunström, A. Tkatchenko, M. Torrent, D. Vanderbilt, M. J. van Setten, V. Van Speybroeck, J. M. Wills, J. R. Yates, G.-X. Zhang, S. Cottenier, *Science* **2016**, *351*.

[25] E. Sjöstedt, L. Nordström, D. Singh, *Solid State Communications* **2000**, *114*, 15–20.

[26] G. K. H. Madsen, P. Blaha, K. Schwarz, E. Sjöstedt, L. Nordström, *Phys. Rev. B* **2001**, *64*, 195134.

[27] J. C. Slater, *Phys. Rev.* **1937**, *51*, 846–851.

[28] O. K. Andersen, *Phys. Rev. B* **1975**, *12*, 3060–3083.

[29] D. D. Koelling, G. O. Arbman, *Journal of Physics F: Metal Physics* **1975**, *5*, 2041–2054.

[30] K. Schwarz, P. Blaha, *Comp. Mater. Sci.* **2003**, *28*, 259–273.

[31] H. Hellmann, *The Journal of Chemical Physics* **1935**, *3*, 61–61.

[32] D. R. Hamann, M. Schlüter, C. Chiang, *Phys. Rev. Lett.* **1979**, *43*, 1494–1497.

[33] D. Vanderbilt, *Phys. Rev. B* **1990**, *41*, 7892–7895.

[34] P. E. Blöchl, *Phys. Rev. B* **1994**, *50*, 17953–17979.

[35] P. Giannozzi, S. Baroni, N. Bonini, M. Calandra, R. Car, C. Cavazzoni, D. Ceresoli, G. L. Chiarotti, M. Cococcioni, I. Dabo, A. D. Corso, S. de Gironcoli, S. Fabris, G. Fratesi, R. Gebauer, U. Gerstmann, C. Gougoussis, A. Kokalj, M. Lazzeri, L. Martin-Samos, N. Marzari, F. Mauri, R. Mazzarello, S. Paolini, A. Pasquarello, L. Paulatto, C. Sbraccia, S. Scandolo, G. Sclauzero, A. P. Seitsonen, A. Smogunov, P. Umari, R. M. Wentzcovitch, *Journal of Physics: Condensed Matter* **2009**, *21*, 395502.

[36] G. Kresse, J. Furthmüller, *Phys. Rev. B* **1996**, *54*, 11169–11186.

[37] F. Bloch, *Zeitschrift für Physik* **1929**, *52*, 555–600.

[38] H. Jones, N. F. Mott, H. W. B. Skinner, *Phys. Rev.* **1934**, *45*, 379–384.

[39] J. C. Slater, G. F. Koster, *Phys. Rev.* **1954**, *94*, 1498–1524.

[40] D. Vanderbilt in *Berry Phases in Electronic Structure Theory: Electric Polarization, Orbital Magnetization and Topological Insulators*, Cambridge University Press, **2018**, pp. 327–362.

[41] D. Moldovan, M. Anđelković, F. Peeters, *pybinding v0.9.4: a Python package for tight- binding calculations*, **2017**.

[42] J. B. Goodenough, *Magnetism and the chemical bond*, IEEE Press, New York, **2001**.

[43] N. Metropolis, A. W. Rosenbluth, M. N. Rosenbluth, A. H. Teller, E. Teller, *The Journal of Chemical Physics* **1953**, *21*, 1087–1092.

[44] S. Baroni, S. de Gironcoli, A. Dal Corso, P. Giannozzi, *Rev. Mod. Phys.* **2001**, *73*, 515–562.

[45] P. D. DeCicco, F. A. Johnson, R. A. Smith, *Proceedings of the Royal Society of London. A. Mathematical and Physical Sciences* **1969**, *310*, 111–119.

[46] S. Baroni, P. Giannozzi, A. Testa, *Phys. Rev. Lett.* **1987**, *58*, 1861–1864.

[47] M. T. Yin, M. L. Cohen, *Phys. Rev. B* **1982**, *26*, 5668–5687.

[48] K. Parlinski, Z. Q. Li, Y. Kawazoe, *Phys. Rev. Lett.* **1997**, *78*, 4063–4066.

[49] A. Togo, I. Tanaka, *Scr. Mater.* **2015**, *108*, 1–5.

[50] K. Mizokami, A. Togo, I. Tanaka, *Phys. Rev. B* **2018**, *97*, 224306.

[51] O. Hellman, P. Steneteg, I. A. Abrikosov, S. I. Simak, *Phys. Rev. B* **2013**, *87*, 104111.

[52] E. Noether, *Nachrichten von der Gesellschaft der Wissenschaften zu Göttingen Mathematisch-Physikalische Klasse* **1918**, *1918*, 235–257.

[53] L. D. Landau, *Phys. Z. Sowjet.* **1937**, *11*, 26.

[54] H. A. Kramers, *Proceedings Koninklijke Akademie van Wetenschappen* **1930**, *33*, 959–972.

[55] E. C. Stoner, *Proceedings of the Royal Society of London A: Mathematical Physical and Engineering Sciences* **1938**, *165*, 372–414.

[56] H. A. Jahn, E. Teller, F. G. Donnan, *Proceedings of the Royal Society of London. Series A - Mathematical and Physical Sciences* **1937**, *161*, 220–235.

[57] R. E. Peierls, *Quantum theory of solids*, Clarendon Press, Oxford, **1955**.

[58] N. F. Mott, *Proceedings of the Physical Society A* **1949**, *62*, 416–422.

[59] G. K. Madsen, J. Carrete, M. J. Verstraete, *Computer Physics Communications* **2018**, *231*, 140–145.

[60] W. Li, J. Carrete, N. A. Katcho, N. Mingo, *Comp. Phys. Commun.* **2014**, *185*, 1747–1758.

[61] T. J. Seebeck, *Annalen der Physik* **1826**, *82*, 253–286.

[62] A. Ohtomo, H. Hwang, *Nature* **2004**, *427*, 423–426.

[63] M. A. López-Quintela, L. E. Hueso, J. Rivas, F. Rivadulla, *Nanotechnology* **2003**, *14*, 212.

[64] J. Maeng, T.-W. Kim, G. Jo, T. Lee, *Mat. Res. Bull.* **2008**, *43*, 1649.

[65] J. Mannhart, D. G. Schlom, *Science* **2010**, *327*, 1607–1611.

[66] G. J. Snyder, E. S. Toberer, *Nat. Mater.* **2008**, *7*, 105–114.

[67] Z. Lu, H. Zhang, W. Lei, D. C. Sinclair, I. M. Reaney, *Chemistry of Materials* **2016**, *28*, 925–935.

[68] G. H. Zheng, Z. H. Yuan, Z. X. Dai, H. Q. Wang, H. B. Li, Y. Q. Ma, G. Li, *Journal of Low Temperature Physics* **2013**, *173*, 80–87.

[69] V. Pardo, A. S. Botana, D. Baldomir, *Phys. Rev. B* **2013**, *87*, 125148.

[70] J. Chen, S. Z. Deng, N. S. Xu, W. Zhang, X. Wen, S. Yang, *Applied Physics Letters* **2003**, *83*, 746–748.

[71] P. Limelette, V. Hardy, P. Auban-Senzier, D. Jérome, D. Flahaut, S. Hébert, R. Frésard, C. Simon, J. Noudem, A. Maignan, *Phys. Rev. B* **2005**, *71*, 233108.

[72] I. Terasaki, Y. Sasago, K. Uchinokura, *Phys. Rev. B* **1997**, *56*, R12685–R12687.

[73] R. Moos, A. Gnudi, K. H. Härdtl, *Journal of Applied Physics* **1995**, *78*, 5042–5047.

[74] H. Ohta, S. Kim, Y. Mune, T. Mizoguchi, K. Nomura, S. Ohta, T. Nomura, Y. Nakanishi, Y. Ikuhara, M. Hirano, et al., *Nat. Mat.* **2007**, *6*, 129–134.

[75] H. Unoki, T. Sakudo, *Journal of the Physical Society of Japan* **1967**, *23*, 546–552.

[76] J. Schooley, W. Hosler, M. L. Cohen, *Physical Review Letters* **1964**, *12*, 474.

[77] A. Brinkman, M. Huijben, M. Van Zalk, J. Huijben, U. Zeitler, J. Maan, W. G. van der Wiel, G. Rijnders, D. H. Blank, H. Hilgenkamp, *Nature materials* **2007**, *6*, 493.

[78] N. Reyren, S. Thiel, A. Caviglia, L. F. Kourkoutis, G. Hammerl, C. Richter, C. Schneider, T. Kopp, A.-S. Rüetschi, D. Jaccard, et al., *Science* **2007**, *317*, 1196–1199.

[79] A. Caviglia, M. Gabay, S. Gariglio, N. Reyren, C. Cancellieri, J.-M. Triscone, *Physical review letters* **2010**, *104*, 126803.

[80] J. H. Haeni, P. Irvin, W. Chang, R. Uecker, P. Reiche, Y. L. Li, S. Choudhury, W. Tian, M. E. Hawley, B. Craigo, A. K. Tagantsev, X. Q. Pan, S. K. Streiffer, L. Q. Chen, S. W. Kirchoefer, J. Levy, D. G. Schlom, *Nature* **2004**, *430*, 758–761.

[81] N. Pertsev, A. Tagantsev, N. Setter, *Physical Review B* **2000**, *61*, R825.

[82] V. Martelli, J. L. Jiménez, M. Continentino, E. Baggio-Saitovitch, K. Behnia, *Phys. Rev. Lett.* **2018**, *120*, 125901.

[83] A. Sarantopoulos, E. Ferreiro-Vila, V. Pardo, C. Magén, M. H. Aguirre, F. Rivadulla, *Phys. Rev. Lett.* **2015**, *115*, 166801.

[84] X. Li, K. Maute, M. L. Dunn, R. Yang, *Phys. Rev. B* **2010**, *81*, 245318.

[85] C. Yu, M. L. Scullin, M. Huijben, R. Ramesh, A. Majumdar, *Applied Physics Letters* **2008**, *92*, 191911.

[86] M. S. Dresselhaus, G. Chen, M. Tang, R. G. Yang, H. Lee, D. Wang, Z. Ren, J.-P. Fleurial, P. Gogna, *Advanced Materials* **2007**, *19*, 1043–1053.

[87] D.-W. Oh, J. Ravichandran, C.-W. Liang, W. Siemons, B. Jalan, C. M. Brooks, M. Huijben, D. G. Schlom, S. Stemmer, L. W. Martin, A. Majumdar, R. Ramesh, D. G. Cahill, *Applied Physics Letters* **2011**, *98*, 221904.

[88] S. R. Popuri, A. J. M. Scott, R. A. Downie, M. A. Hall, E. Suard, R. Decourt, M. Pollet, J.-W. G. Bos, *RSC Adv.* **2014**, *4*, 33720–33723.

[89] L. Lindsay, C. Hua, X. Ruan, S. Lee, *Materials Today Physics* **2018**, *7*, 106–120.

[90] Q. Qiao, A. Gulec, T. Paulauskas, S. Kolesnik, B. Dabrowski, M. Ozdemir, C. Boyraz, D. Mazumdar, A. Gupta, R. F. Klie, *Journal of Physics: Condensed Matter* **2011**, *23*, 305005.

[91] Z. Wu, R. E. Cohen, *Phys. Rev. B* **2006**, *73*, 235116.

[92] D. Koller, F. Tran, P. Blaha, *Phys. Rev. B* **2011**, *83*, 195134.

[93] H. Dixit, R. Saniz, S. Cottenier, D. Lamoen, B. Partoens, *J. Phys.: Condens. Matter* **2012**, *24*, 205503.

[94] S. A. Hayward, F. D. Morrison, S. A. T. Redfern, E. K. H. Salje, J. F. Scott, K. S. Knight, S. Tarantino, A. M. Glazer, V. Shuvaeva, P. Daniel, M. Zhang, M. A. Carpenter, *Phys. Rev. B* **2005**, *72*, 054110.

[95] F. J. Wong, S.-H. Baek, R. V. Chopdekar, V. V. Mehta, H.-W. Jang, C.-B. Eom, Y. Suzuki, *Phys. Rev. B* **2010**, *81*, 161101.

[96] R. Kubo, M. Yokota, S. Nakajima, *Journal of the Physical Society of Japan* **1957**, *12*, 1203–1211.

[97] P. M. Chaikin, G. Beni, *Phys. Rev. B* **1976**, *13*, 647–651.

[98] A. Janotti, D. Steiauf, C. G. Van de Walle, *Physical Review B* **2011**, *84*, 201304.

[99] H. Fritzsche, *Solid State Communications* **1971**, *9*, 1813–1815.

[100] C. Kittel, *Introduction to Solid State Physics*, 8th ed., Wiley, **2004**.

[101] T. Okuda, K. Nakanishi, S. Miyasaka, Y. Tokura, *Physical Review B* **2001**, *63*, 113104.

[102] J. R. Petrie, C. Mitra, H. Jeen, W. S. Choi, T. L. Meyer, F. A. Reboredo, J. W. Freeland, G. Eres, H. N. Lee, *Advanced Functional Materials* **2016**, *26*, 1564–1570.

[103] L. Iglesias and F. Rivadulla, private communication.

[104] P. Delugas, A. Filippetti, M. J. Verstraete, I. Pallecchi, D. Marré, V. Fiorentini, *Phys. Rev. B* **2013**, *88*, 045310.

[105] W. Wunderlich, H. Ohta, K. Koumoto, *Physica B: Condensed Matter* **2009**, *404*, 2202–2212.

[106] S. Ohta, T. Nomura, H. Ohta, M. Hirano, H. Hosono, K. Koumoto, *Applied Physics Letters* **2005**, *87*, 092108.

[107] D. Zou, Y. Liu, S. Xie, J. Lin, J. Li, *Chemical Physics Letters* **2013**, *586*, 159–163.

[108] H. Ohta, K. Sugiura, K. Koumoto, *Inorganic Chemistry* **2008**, *47*, 8429–8436.

[109] M. T. Buscaglia, F. Maglia, U. Anselmi-Tamburini, D. Marré, I. Pallecchi, A. Ianculescu, G. Canu, M. Viviani, M. Fabrizio, V. Buscaglia, *Journal of the European Ceramic Society* **2014**, *34*, 307–316.

[110] W. Li, X. Chen, Z. Zheng, Y. Chen, *Computational Materials Science* **2016**, *112*, 107–112.

[111] P. Torres, J. A. Seijas-Bellido, C. Escorihuela-Sayalero, J. Íñiguez, R. Rurali, *Phys. Rev. Materials* **2019**, *3*, 044404.

[112] N. Wang, H. Chen, H. He, W. Norimatsu, M. Kusunoki, K. Koumoto, *Scientific Reports* **2013**, *3*, 3449.

[113] S. R. Popuri, A. J. M. Scott, R. A. Downie, M. A. Hall, E. Suard, R. Decourt, M. Pollet, J.-W. G. Bos, *RSC Adv.* **2014**, *4*, 33720–33723.

[114] C. M. Brooks, R. B. Wilson, A. Schäfer, J. A. Mundy, M. E. Holtz, D. A. Muller, J. Schubert, D. G. Cahill, D. G. Schlom, *Applied Physics Letters* **2015**, *107*, 051902.

[115] A. A. Yaremchenko, S. Populoh, S. G. Patrício, J. Macías, P. Thiel, D. P. Fagg, A. Weidenkaff, J. R. Frade, A. V. Kovalevsky, *Chemistry of Materials* **2015**, *27*, 4995–5006.

[116] C. Chen, M. Bousnina, F. Giovannelli, F. Delorme, *Journal of Materiomics* **2019**, *5*, 88–93.

[117] J. A. Dawson, I. Tanaka, *The Journal of Physical Chemistry C* **2014**, *118*, 25765–25778.

[118] L. Zhang, N. Li, H.-Q. Wang, Y. Zhang, F. Ren, X.-X. Liao, Y.-P. Li, X.-D. Wang, Z. Huang, Y. Dai, H. Yan, J.-C. Zheng, *Chinese Physics B* **2017**, *26*, 016602.

[119] A. M. Dehkordi, S. Bhattacharya, T. Darroudi, M. Karakaya, C. Kucera, J. Ballato, R. Adebisi, J. R. Gladden, R. Podila, A. M. Rao, et al., *MRS Communications* **2018**, *8*, 1470–1476.

[120] C. Yu, M. L. Scullin, M. Huijben, R. Ramesh, A. Majumdar, *Applied physics letters* **2008**, *92*, 191911.

[121] L. Feng, T. Shiga, J. Shiomi, *Applied Physics Express* **2015**, *8*, 071501.

[122] J. P. Perdew, A. Ruzsinszky, G. I. Csonka, O. A. Vydrov, G. E. Scuseria, L. A. Constantin, X. Zhou, K. Burke, *Phys. Rev. Lett.* **2008**, *100*, 136406.

[123] X. Gonze, C. Lee, *Phys. Rev. B* **1997**, *55*, 10355–10368.

[124] R. A. Evarestov, E. Blokhin, D. Gryaznov, E. A. Kotomin, J. Maier, *Phys. Rev. B* **2011**, *83*, 134108.

[125] A. A. Maradudin, A. E. Fein, *Phys. Rev.* **1962**, *128*, 2589–2608.

[126] R. A. Cowley, *Reports on Progress in Physics* **1968**, *31*, 123–166.

[127] D. Wallace, *Thermodynamics of Crystals*, Dover Publications, **1998**.

[128] W. Li, N. Mingo, *Phys. Rev. B* **2014**, *90*, 094302.

[129] J.-J. Zhou, O. Hellman, M. Bernardi, *Phys. Rev. Lett.* **2018**, *121*, 226603.

[130] A. Hasegawa, K. Ohta, T. Yagi, K. Hirose, Y. Okuda, T. Kondo, *Comptes Rendus Geoscience* **2019**, *351*, High-Pressure Mineral Physics Seminar(HPMPS-9, Saint-Malo, France, 24–28 September 2017), 229–235.

[131] J. F. Scott, *Rev. Mod. Phys.* **1974**, *46*, 83–128.

[132] W. Jauch, A. Palmer, *Phys. Rev. B* **1999**, *60*, 2961–2963.

[133] N. Sai, D. Vanderbilt, *Phys. Rev. B* **2000**, *62*, 13942–13950.

[134] Y. Yao, H. Fu, *Phys. Rev. B* **2010**, *82*, 174119.

[135] N. A. Benedek, C. J. Fennie, *The Journal of Physical Chemistry C* **2013**, *117*, 13339–13349.

[136] L. Iglesias, A. Sarantopoulos, C. Magén, F. Rivadulla, *Phys. Rev. B* **2017**, *95*, 165138.

[137] U. Lüders, A. Barthélémy, M. Bibes, K. Bouzehouane, S. Fusil, E. Jacquet, J.-P. Contour, J.-F. Bobo, J. Fontcuberta, A. Fert, *Advanced Materials* **2006**, *18*, 1733–1736.

[138] D. Zhang, X. Xu, W. Wang, X. Zhang, H. Yang, Y. Wu, C. Ma, Y. Jiang, *Rare Metals* **2012**, *31*, 112–116.

[139] M. Cesaria, A. P. Caricato, G. Maruccio, M. Martino, *Journal of Physics: Conference Series* **2011**, *292*, 012003.

[140] M. Zhu, Y. Lin, E. W. C. Lo, Q. Wang, Z. Zhao, W. Xie, *Applied Physics Letters* **2012**, *100*, 062406.

[141] A. Fert, *Angewandte Chemie International Edition* **2008**, *47*, 5956–5967.

[142] M. Götte, M. Joppe, T. Dahm, *Scientific Reports* **2016**, *6*, 36070.

[143] P. Michetti, P. Recher, *Phys. Rev. B* **2011**, *84*, 125438.

[144] F. Katmis, V. Lauter, F. S. Nogueira, B. A. Assaf, M. E. Jamer, P. Wei, B. Satpati, J. W. Freeland, I. Eremin, D. Heiman, P. Jarillo-Herrero, J. S. Moodera, *Nature* **2016**, *533*, 513–516.

[145] M. Señarís-Rodríguez, J. Goodenough, *Journal of Solid State Chemistry* **1995**, *116*, 224–231.

[146] M. W. Haverkort, Z. Hu, J. C. Cezar, T. Burnus, H. Hartmann, M. Reuther, C. Zobel, T. Lorenz, A. Tanaka, N. B. Brookes, H. H. Hsieh, H.-J. Lin, C. T. Chen, L. H. Tjeng, *Phys. Rev. Lett.* **2006**, *97*, 176405.

[147] K. Asai, A. Yoneda, O. Yokokura, J. M. Tranquada, G. Shirane, K. Kohn, *Journal of the Physical Society of Japan* **1998**, *67*, 290–296.

[148] M. Abbate, J. C. Fuggle, A. Fujimori, L. H. Tjeng, C. T. Chen, R. Potze, G. A. Sawatzky, H. Eisaki, S. Uchida, *Phys. Rev. B* **1993**, *47*, 16124–16130.

[149] G. Maris, Y. Ren, V. Volotchaev, C. Zobel, T. Lorenz, T. T. M. Palstra, *Phys. Rev. B* **2003**, *67*, 224423.

[150] A. M. Durand, D. P. Belanger, C. H. Booth, F. Ye, S. Chi, J. A. Fernandez-Baca, M. Bhat, *Journal of Physics: Condensed Matter* **2013**, *25*, 382203.

[151] J. F. Afonso, J. Kune š, *Phys. Rev. B* **2017**, *95*, 115131.

[152] J. Baier, S. Jodlauk, M. Kriener, A. Reichl, C. Zobel, H. Kierspel, A. Freimuth, T. Lorenz, *Phys. Rev. B* **2005**, *71*, 014443.

[153] J. W. Freeland, J. X. Ma, J. Shi, *Applied Physics Letters* **2008**, *93*, 212501.

[154] D. Fuchs, E. Arac, C. Pinta, S. Schuppler, R. Schneider, H. v. Löhneysen, *Phys. Rev. B* **2008**, *77*, 014434.

[155] V. V. Mehta, M. Liberati, F. J. Wong, R. V. Chopdekar, E. Arenholz, Y. Suzuki, *Journal of Applied Physics* **2008**, *105*.

[156] V. V. Mehta, N. Biskup, C. Jenkins, E. Arenholz, M. Varela, Y. Suzuki, *Phys. Rev. B* **2015**, *91*, 144418.

[157] F. Rivadulla, Z. Bi, E. Bauer, B. Rivas-Murias, J. M. Vila-Fungueiriño, Q. Jia, *Chemistry of Materials* **2013**, *25*, 55–58.

[158] A. Posadas, M. Berg, H. Seo, A. de Lozanne, A. A. Demkov, D. J. Smith, A. P. Kirk, D. Zhernokletov, R. M. Wallace, *Applied Physics Letters* **2011**, *98*, 053104.

[159] H. Hsu, P. Blaha, R. M. Wentzcovitch, C. Leighton, *Phys. Rev. B* **2010**, *82*, 100406.

[160] N. Biškup, J. Salafranca, V. Mehta, M. P. Oxley, Y. Suzuki, S. J. Pennycook, S. T. Pantelides, M. Varela, *Phys. Rev. Lett.* **2014**, *112*, 087202.

[161] J. Gazquez, W. Luo, M. P. Oxley, M. Prange, M. A. Torija, M. Sharma, C. Leighton, S. T. Pantelides, S. J. Pennycook, M. Varela, *Nano Letters* **2011**, *11*, 973–976.

[162] J. Gazquez, S. Bose, M. Sharma, M. A. Torija, S. J. Pennycook, C. Leighton, M. Varela, *APL Materials* **2013**, *1*, 012105.

[163] W. S. Choi, J.-H. Kwon, H. Jeen, J. E. Hamann-Borrero, A. Radi, S. Macke, R. Sutarto, F. He, G. A. Sawatzky, V. Hinkov, M. Kim, H. N. Lee, *Nano Letters* **2012**, *12*, 4966–4970.

[164] P. J. Linstrom, W. G. Mallard, *Journal of Chemical & Engineering Data* **2001**, *46*, 1059–1063.

[165] C. Freysoldt, B. Grabowski, T. Hickel, J. Neugebauer, G. Kresse, A. Janotti, C. G. Van de Walle, *Rev. Mod. Phys.* **2014**, *86*, 253–305.

[166] A. Janotti, J. B. Varley, P. Rinke, N. Umezawa, G. Kresse, C. G. Van de Walle, *Phys. Rev. B* **2010**, *81*, 085212.

[167] S. B. Zhang, J. E. Northrup, *Phys. Rev. Lett.* **1991**, *67*, 2339–2342.

[168] M. Topsakal, C. Leighton, R. M. Wentzcovitch, *Journal of Applied Physics* **2016**, *119*, 244310.

[169] S. L. Dudarev, G. A. Botton, S. Y. Savrasov, C. J. Humphreys, A. P. Sutton, *Phys. Rev. B* **1998**, *57*, 1505–1509.

[170] J. G. Bednorz, K. A. Müller, *Zeitschrift für Physik B Condensed Matter* **1986**, *64*, 189–193.

[171] M. R. Norman, *Reports on Progress in Physics* **2016**, *79*, 074502.

[172] V. I. Anisimov, D. Bukhvalov, T. M. Rice, *Phys. Rev. B* **1999**, *59*, 7901–7906.

[173] A. Ikeda, T. Manabe, M. Naito, *Physica C: Superconductivity* **2013**, *495*, 134–140.

[174] A. Ikeda, Y. Krockenberger, H. Irie, M. Naito, H. Yamamoto, *Applied Physics Express* **2016**, *9*, 061101.

[175] M. Crespin, P. Levitz, L. Gatineau, *J. Chem. Soc.* **1983**, *79*, 1181–1194.

[176] M. A. Hayward, M. A. Green, M. J. Rosseinsky, J. Sloan, *Journal of the American Chemical Society* **1999**, *121*, 8843–8854.

[177] M. Hayward, M. Rosseinsky, *Solid State Sciences* **2003**, *5*, 839–850.

[178] D. Li, K. Lee, B. Y. Wang, M. Osada, S. Crossley, H. R. Lee, Y. Cui, Y. Hikita, H. Y. Hwang, *Nature* **2019**, *572*, 624–627.

[179] D. Li, B. Y. Wang, K. Lee, S. P. Harvey, M. Osada, B. H. Goodge, L. F. Kourkoutis, H. Y. Hwang, *Phys. Rev. Lett.* **2020**, *125*, 027001.

[180] X. Wu, D. Di Sante, T. Schwemmer, W. Hanke, H. Y. Hwang, S. Raghu, R. Thomale, *Phys. Rev. B* **2020**, *101*, 060504.

[181] A. S. Botana, M. R. Norman, *Phys. Rev. X* **2020**, *10*, 011024.

[182] K.-W. Lee, W. E. Pickett, *Phys. Rev. B* **2004**, *70*, 165109.

[183] M.-Y. Choi, K.-W. Lee, W. E. Pickett, *Phys. Rev. B* **2020**, *101*, 020503.

[184] M. Hepting, D. Li, C. J. Jia, H. Lu, E. Paris, Y. Tseng, X. Feng, M. Osada, E. Been, Y. Hikita, Y.-D. Chuang, Z. Hussain, K. J. Zhou, A. Nag, M. Garcia-Fernandez, M. Rossi, H. Y. Huang, D. J. Huang, Z. X. Shen, T. Schmitt, H. Y. Hwang, B. Moritz, J. Zaanen, T. P. Devereaux, W. S. Lee, *Nat. Mater.* **2020**, *19*, 381.

[185] F. Zhang, T. Rice, *Phys. Rev. B* **1988**, *37*, 3759.

[186] J. Zhang, A. S. Botana, J. W. Freeland, D. Phelan, H. Zheng, V. Pardo, M. R. Norman, J. F. Mitchell, *Nature Physics* **2017**, *13*, 864–869.

[187] H. Zhang, L. Jin, S. Wang, B. Xi, X. Shi, F. Ye, J.-W. Mei, *Phys. Rev. Research* **2020**, *2*, 013214.

[188] F. Lechermann, *Phys. Rev. B* **2020**, *101*, 081110.

[189] F. Lechermann, *Phys. Rev. X* **2020**, *10*, 041002.

[190] F. Petocchi, V. Christiansson, F. Nilsson, F. Aryasetiawan, P. Werner, *Phys. Rev. X* **2020**, *10*, 041047.

[191] V. Pardo, W. E. Pickett, *Phys. Rev. B* **2012**, *85*, 045111.

[192] J. Zhang, Y.-S. Chen, D. Phelan, H. Zheng, M. Norman, J. Mitchell, *Proceedings of the National Academy of Sciences* **2016**, *113*, 8945–8950.

[193] V. Pardo, W. E. Pickett, *Phys. Rev. Lett.* **2010**, *105*, 266402.

[194] A. S. Botana, V. Pardo, W. E. Pickett, M. R. Norman, *Phys. Rev. B* **2016**, *94*, 081105.

[195] V. I. Anisimov, I. V. Solovyev, M. A. Korotin, M. T. Czy żyk, G. A. Sawatzky, *Phys. Rev. B* **1993**, *48*, 16929–16934.

[196] M. T. Czy żyk, G. A. Sawatzky, *Phys. Rev. B* **1994**, *49*, 14211–14228.

[197] M.-Y. Choi, W. E. Pickett, K.-W. Lee, *Phys. Rev. Research* **2020**, *2*, 033445.

[198] E. R. Ylvisaker, W. E. Pickett, K. Koepernik, *Phys. Rev. B* **2009**, *79*, 035103.

[199] J. Rodriguez-Carvajal, M. Fernandez-Diaz, J. Martinez, *Journal of Physics: Condensed Matter* **1991**, *3*, 3215.

[200] D. Buttrey, J. Honig, C. Rao, *Journal of Solid State Chemistry* **1986**, *64*, 287–295.

[201] P. Mandal, R. K. Patel, D. Rout, R. Banerjee, R. Bag, K. Karmakar, A. Narayan, J. W. Freeland, S. Singh, S. Middey, *Phys. Rev. B* **2021**, *103*, L060504.

[202] P. Anderson, *Materials Research Bulletin* **1973**, *8*, 153–160.

[203] T. Imai, Y. S. Lee, *Physics Today* **2016**, *69*, 30–36.

[204] L. Savary, L. Balents, *Reports on Progress in Physics* **2016**, *80*, 016502.

[205] Y. Tokiwa, T. Radu, R. Coldea, H. Wilhelm, Z. Tylczynski, F. Steglich, *Phys. Rev. B* **2006**, *73*, 134414.

[206] S. A. Zvyagin, D. Kamenskyi, M. Ozerov, J. Wosnitza, M. Ikeda, T. Fujita, M. Hagiwara, A. I. Smirnov, T. A. Soldatov, A. Y. Shapiro, J. Krzystek, R. Hu, H. Ryu, C. Petrovic, M. E. Zhitomirsky, *Phys. Rev. Lett.* **2014**, *112*, 077206.

[207] R. Coldea, D. A. Tennant, A. M. Tsvelik, Z. Tylczynski, *Phys. Rev. Lett.* **2001**, *86*, 1335–1338.

[208] R. Coldea, D. A. Tennant, Z. Tylczynski, *Phys. Rev. B* **2003**, *68*, 134424.

[209] O. A. Starykh, H. Katsura, L. Balents, *Phys. Rev. B* **2010**, *82*, 014421.

[210] M. Abbate, G. Zampieri, J. Okamoto, A. Fujimori, S. Kawasaki, M. Takano, *Phys. Rev. B* **2002**, *65*, 165120.

[211] E. Dagotto, *Nanoscale Phase Separation and Colossal Magnetoresistance*, **2003**.

[212] H.-J. Lin, Y. Y. Chin, Z. Hu, G. J. Shu, F. C. Chou, H. Ohta, K. Yoshimura, S. Hébert, A. Maignan, A. Tanaka, L. H. Tjeng, C. T. Chen, *Phys. Rev. B* **2010**, *81*, 115138.

[213] Y. Xiao, M. Zbiri, R. A. Downie, J.-W. G. Bos, T. Brückel, T. Chatterji, *Phys. Rev. B* **2013**, *88*, 214419.

[214] P. Babkevich, A. Finco, M. Jeong, B. Dalla Piazza, I. Kovacevic, G. Klughertz, K. W. Krämer, C. Kraemer, D. T. Adroja, E. Goremychkin, T. Unruh, T. Strässle, A. Di Lieto, J. Jensen, H. M. Rønnow, *Phys. Rev. B* **2015**, *92*, 144422.

[215] S. M. Butorin, K. O. Kvashnina, J. R. Vegelius, D. Meyer, D. K. Shuh, **2016**, *113*, 8093–8097.

[216] K. Foyevtsova, I. Opahle, Y.-Z. Zhang, H. O. Jeschke, R. Valentı, *Phys. Rev. B* **2011**, *83*, 125126.

[217] E. Jara, J. A. Barreda-Argueso, J. Gonzalez, F. Rodriguez, R. Valiente, *Phys. Rev. B* **2019**, *99*, 134106.

[218] O. Lamba, S. Sinha, *Solid State Communications* **1986**, *57*, 365–371.

[219] W. Zheng, R. R. P. Singh, R. H. McKenzie, R. Coldea, *Phys. Rev. B* **2005**, *71*, 134422.

[220] G. A. Sawatzky, J. W. Allen, *Phys. Rev. Lett.* **1984**, *53*, 2339–2342.

[221] M. M. Sala, V. Bisogni, C. Aruta, G. Balestrino, H. Berger, N. B. Brookes, G. M. de Luca, D. D. Castro, M. Grioni, M. Guarise, P. G. Medaglia, F. M. Granozio, M. Minola, P. Perna, M. Radovic, M. Salluzzo, T. Schmitt, K. J. Zhou, L. Braicovich, G. Ghiringhelli, *New Journal of Physics* **2011**, *13*, 043026.

[222] L. J. P. Ament, M. van Veenendaal, T. P. Devereaux, J. P. Hill, J. van den Brink, *Rev. Mod. Phys.* **2011**, *83*, 705–767.

[223] R. Valiente, F. Rodrıguez, *Journal of Physics: Condensed Matter* **1998**, *10*, 9525–9534.

[224] N. Marzari, A. A. Mostofi, J. R. Yates, I. Souza, D. Vanderbilt, *Rev. Mod. Phys.* **2012**, *84*, 1419–1475.

[225] C. J. Ballhausen, *Introduction to Ligand Field Theory*, **1962**.

[226] M. W. Haverkort, M. Zwierzycki, O. K. Andersen, *Phys. Rev. B* **2012**, *85*, 165113.

[227] Y. Lu, M. Höppner, O. Gunnarsson, M. W. Haverkort, *Phys. Rev. B* **2014**, *90*, 085102.

[228] J. Schlappa, K. Wohlfeld, K. J. Zhou, M. Mourigal, M. W. Haverkort, V. N. Strocov, L. Hozoi, C. Monney, S. Nishimoto, S. Singh, A. Revcolevschi, J.-S. Caux, L. Patthey, H. M. Rønnow, J. van den Brink, T. Schmitt, *Nature* **2012**, *485*, 82–85.

[229] V. Bisogni, K. Wohlfeld, S. Nishimoto, C. Monney, J. Trinckauf, K. Zhou, R. Kraus, K. Koepernik, C. Sekar, V. Strocov, B. Büchner, T. Schmitt, J. van den Brink, J. Geck, *Phys. Rev. Lett.* **2015**, *114*, 096402.

[230] K. S. Novoselov, A. K. Geim, S. V. Morozov, D. Jiang, Y. Zhang, S. V. Dubonos, I. V. Grigorieva, A. A. Firsov, *Science* **2004**, *306*, 666–669.

[231] K. F. Mak, C. Lee, J. Hone, J. Shan, T. F. Heinz, *Phys. Rev. Lett.* **2010**, *105*, 136805.

[232] C. R. Dean, A. F. Young, I. Meric, C. Lee, L. Wang, S. Sorgenfrei, K. Watanabe, T. Taniguchi, P. Kim, K. L. Shepard, J. Hone, *Nature Nanotechnology* **2010**, *5*, 722.

[233] H. Liu, A. T. Neal, Z. Zhu, Z. Luo, X. Xu, D. Tománek, P. D. Ye, *ACS Nano* **2014**, *8*, 4033–4041.

[234] Y. Cao, V. Fatemi, A. Demir, S. Fang, S. L. Tomarken, J. Y. Luo, J. D. Sanchez-Yamagishi, K. Watanabe, T. Taniguchi, E. Kaxiras, R. C. Ashoori, P. Jarillo-Herrero, *Nature* **2018**.

[235] J. M. Park, Y. Cao, K. Watanabe, T. Taniguchi, P. Jarillo-Herrero, *Nature* **2021**, *590*, 249–255.

[236] J.-U. Lee, S. Lee, J. H. Ryoo, S. Kang, T. Y. Kim, P. Kim, C.-H. Park, J.-G. Park, H. Cheong, *Nano Letters* **2016**, *16*, 7433–7438.

[237] W.-B. Zhang, Q. Qu, P. Zhu, C.-H. Lam, *J. Mater. Chem. C* **2015**, *3*, 12457–12468.

[238] Z. Fei, B. Huang, P. Malinowski, W. Wang, T. Song, J. Sanchez, W. Yao, D. Xiao, X. Zhu, A. F. May, W. Wu, D. H. Cobden, J.-H. Chu, X. Xu, *Nature Materials* **2018**, *17*, 778–782.

[239] D. Ghazaryan, M. T. Greenaway, Z. Wang, V. H. Guarochico-Moreira, I. J. Vera-Marun, J. Yin, Y. Liao, S. V. Morozov, O. Kristanovski, A. I. Lichtenstein, M. I. Katsnelson, F. Withers, A. Mishchenko, L. Eaves, A. K. Geim, K. S. Novoselov, A. Misra, *Nature Electronics* **2018**, *1*, 344–349.

[240] D. R. Klein, D. MacNeill, J. L. Lado, D. Soriano, E. Navarro-Moratalla, K. Watanabe, T. Taniguchi, S. Manni, P. Canfield, J. Fernández-Rossier, P. Jarillo-Herrero, *Science* **2018**, *360*, 1218–1222.

[241] B. Huang, G. Clark, D. R. Klein, D. MacNeill, E. Navarro-Moratalla, K. L. Seyler, N. Wilson, M. A. McGuire, D. H. Cobden, D. Xiao, W. Yao, P. Jarillo-Herrero, X. Xu, *Nature Nanotechnology* **2018**, *13*, 544–548.

[242] M. A. McGuire, H. Dixit, V. R. Cooper, B. C. Sales, *Chemistry of Materials* **2015**, *27*, 612–620.

[243] Y. Gao, J. Wang, Z. Li, J. Yang, M. Xia, X. Hao, Y. Xu, F. Gao, *physica status solidi (RRL) – Rapid Research Letters* **2019**, *13*, 1800410.

[244] Y. Zhao, L. Lin, Q. Zhou, Y. Li, S. Yuan, Q. Chen, S. Dong, J. Wang, *Nano Letters* **2018**, *18*, 2943–2949.

[245] Y. Gao, J. Wang, Y. Li, M. Xia, Z. Li, F. Gao, *Physica Status Solidi (RRL) – Rapid Research Letters* **2018**, *12*, 1800105.

[246] V. Carteaux, D. Brunet, G. Ouvrard, G. Andre, *Journal of Physics: Condensed Matter* **1995**, *7*, 69.

[247] I. Tsubokawa, *Journal of the Physical Society of Japan* **1960**, *15*, 1664–1668.

[248] W. Xing, Y. Chen, P. M. Odenthal, X. Zhang, W. Yuan, T. Su, Q. Song, T. Wang, J. Zhong, S. Jia, X. C. Xie, Y. Li, W. Han, *2D Materials* **2017**, *4*, 024009.

[249] Z. Zhang, J. Shang, C. Jiang, A. Rasmita, W. Gao, T. Yu, *Nano Letters* **2019**, *19*, 3138–3142.

[250] N. D. Mermin, H. Wagner, *Phys. Rev. Lett.* **1966**, *17*, 1133–1136.

[251] F. Tran, J. Stelzl, D. Koller, T. Ruh, P. Blaha, *Phys. Rev. B* **2017**, *96*, 054103.

[252] M. D. Kuz'min, *Phys. Rev. Lett.* **2005**, *94*, 107204.

[253] A. Barla, J. Nicolás, D. Cocco, S. M. Valvidares, J. Herrero-Martın, P. Gargiani, J. Moldes, C. Ruget, E. Pellegrin, S. Ferrer, *Journal of Synchrotron Radiation* **2016**, *23*, 1507–1517.

[254] F. Birch, *Phys. Rev.* **1947**, *71*, 809–824.

[255] D. J. Singh, *Phys. Rev. B* **2007**, *76*, 085110.

[256] Z. Yu, W. Xia, K. Xu, M. Xu, H. Wang, X. Wang, N. Yu, Z. Zou, J. Zhao, L. Wang, et al., *The Journal of Physical Chemistry C* **2019**, *123*, 13885–13891.

[257] Y. Uwatoko, "Abstract-L19.00001: Pressure induced insulator to metal crossover in van der Waals ferromagnet CrGeTe3", American Physical Society March Meeting, **2021**.

[258] H. Yoshida, J. Chiba, T. Kaneko, Y. Fujimori, S. Abe, *Physica B: Condensed Matter* **1997**, *237-238*, 525–526.

[259] Y. Sun, R. C. Xiao, G. T. Lin, R. R. Zhang, L. S. Ling, Z. W. Ma, X. Luo, W. J. Lu, Y. P. Sun, Z. G. Sheng, *Applied Physics Letters* **2018**, *112*, 072409.

[260] W. A. Harrison, *Electronic Structures and the Properties of Solids: The Physics of the Chemical Bond*, Dover Publications Inc., New York, **1988**.

[261] C. Gong, L. Li, Z. Li, H. Ji, A. Stern, Y. Xia, T. Cao, W. Bao, C. Wang, Y. Wang, Z. Q. Qiu, R. J. Cava, S. G. Louie, J. Xia, X. Zhang, *Nature* **2017**, *546*, 265–269.

[262] Z. Lin, M. Lohmann, Z. A. Ali, C. Tang, J. Li, W. Xing, J. Zhong, S. Jia, W. Han, S. Coh, W. Beyermann, J. Shi, *Phys. Rev. Materials* **2018**, *2*, 051004.

[263] K. Chang, J. Liu, H. Lin, N. Wang, K. Zhao, A. Zhang, F. Jin, Y. Zhong, X. Hu, W. Duan, et al., *Science* **2016**, *353*, 274–278.

[264] P. Huang, P. Zhang, S. Xu, H. Wang, X. Zhang, H. Zhang, *Nanoscale* **2020**, *12*, 2309–2327.

[265] S. Manzeli, D. Ovchinnikov, D. Pasquier, O. V. Yazyev, A. Kis, *Nature Reviews Materials* **2017**, *2*, 17033.

[266] W. Choi, N. Choudhary, G. H. Han, J. Park, D. Akinwande, Y. H. Lee, *Materials Today* **2017**, *20*, 116–130.

[267] K. Xu, P. Chen, X. Li, C. Wu, Y. Guo, J. Zhao, X. Wu, Y. Xie, *Angewandte Chemie International Edition* **2013**, *52*.

[268] J. Feng, D. Biswas, A. Rajan, M. D. Watson, F. Mazzola, O. J. Clark, K. Underwood, I. Marković, M. McLaren, A. Hunter, D. M. Burn, L. B. Duffy, S. Barua, G. Balakrishnan, F. Bertran, P. Le Fèvre, T. K. Kim, G. van der Laan, T. Hesjedal, P. Wahl, P. D. C. King, *Nano Letters* **2018**, *18*, 4493–4499.

[269] Y. Umemoto, K. Sugawara, Y. Nakata, T. Takahashi, T. Sato, *Nano Research* **2019**, *12*, 165–169.

[270] P. Chen, W. W. Pai, Y.-H. Chan, V. Madhavan, M. Y. Chou, S.-K. Mo, A.-V. Fedorov, T.-C. Chiang, *Phys. Rev. Lett.* **2018**, *121*, 196402.

[271] M. M. Ugeda, A. J. Bradley, Y. Zhang, S. Onishi, Y. Chen, W. Ruan, C. Ojeda-Aristizabal, H. Ryu, M. T. Edmonds, H.-Z. Tsai, A. Riss, S.-K. Mo, D. Lee, A. Zettl, Z. Hussain, Z.-X. Shen, M. F. Crommie, *Nature Physics* **2015**, *12*, 92.

[272] W. Kohn, *Phys. Rev. Lett.* **1959**, *2*, 393–394.

[273] M. D. Johannes, I. I. Mazin, *Phys. Rev. B* **2008**, *77*, 165135.

[274] A. Bussmann-Holder, H. Büttner, *Journal of Physics: Condensed Matter* **2002**, *14*, 7973.

[275] J. Wilson, F. D. Salvo, S. Mahajan, *Advances in Physics* **1975**, *24*, 117–201.

[276] D. J. Eaglesham, R. L. Withers, D. M. Bird, *Journal of Physics C: Solid State Physics* **1986**, *19*, 359.

[277] R. Bianco, I. Errea, L. Monacelli, M. Calandra, F. Mauri, *Nano Letters* **2019**, *19*, 3098–3103.

[278] Y. Wang, J. Ren, J. Li, Y. Wang, H. Peng, P. Yu, W. Duan, S. Zhou, *Phys. Rev. B* **2019**, *100*, 241404.

[279] P. Chen, W. W. Pai, Y.-H. Chan, A. Takayama, C.-Z. Xu, A. Karn, S. Hasegawa, M. Y. Chou, S.-K. Mo, A.-V. Fedorov, et al., *Nature Communications* **2017**, *8*, 516.

[280] M. Bonilla, S. Kolekar, Y. Ma, H. C. Diaz, V. Kalappattil, R. Das, T. Eggers, H. R. Gutierrez, M.-H. Phan, M. Batzill, *Nature Nanotechnology* **2018**.

[281] A. Kokalj, *Journal of Molecular Graphics and Modelling* **1999**, *17*, 176–179.

[282] D. C. Freitas, R. Weht, A. Sulpice, G. Remenyi, P. Strobel, F. Gay, J. Marcus, M. Núñez-Regueiro, *Journal of Physics: Condensed Matter* **2015**, *27*, 176002.

[283] P. M. Williams, C. B. Scruby, W. B. Clark, G. S. Parry, *Le Journal de Physique Colloques* **1976**, *37*, C4–139.

[284] A.-Y. Lu, H. Zhu, J. Xiao, C.-P. Chuu, Y. Han, M.-H. Chiu, C.-C. Cheng, C.-W. Yang, K.-H. Wei, Y. Yang, et al., *Nature Nanotechnology* **2017**, *12*, 744–749.

[285] A. B. Maghirang, Z.-Q. Huang, R. A. B. Villaos, C.-H. Hsu, L.-Y. Feng, E. Florido, H. Lin, A. Bansil, F.-C. Chuang, *npj 2D Materials and Applications* **2019**, *3*, 35.

[286] K. Terashima, T. Sato, H. Komatsu, T. Takahashi, N. Maeda, K. Hayashi, *Physical Review B* **2003**, *68*.

[287] S. V. Borisenko, A. A. Kordyuk, A. N. Yaresko, V. B. Zabolotnyy, D. S. Inosov, R. Schuster, B. Büchner, R. Weber, R. Follath, L. Patthey, et al., *Phys. Rev. Lett.* **2008**, *100*, 196402.

[288] H. Wang, V. Eyert, U. Schwingenschlögl, *Journal of Physics: Condensed Matter* **2011**, *23*, 116003.

[289] T. F. Nova, A. S. Disa, M. Fechner, A. Cavalleri, *Science* **2019**, *364*, 1075–1079.

[290] C. F. Van Bruggen, C. Haas, *Solid State Communications* **1976**, *20*, 251–254.

[291] C. Yadav, A. Rastogi, *Solid State Communications* **2010**, *150*, 648–651.

[292] A. M. Woolley, G. Wexler, *Journal of Physics C: Solid State Physics* **1977**, *10*, 2601.

[293] V. N. Strocov, M. Shi, M. Kobayashi, C. Monney, X. Wang, J. Krempasky, T. Schmitt, L. Patthey, H. Berger, P. Blaha, *Phys. Rev. Lett.* **2012**, *109*, 086401.

[294] J. Diego, A. H. Said, S. K. Mahatha, R. Bianco, L. Monacelli, M. Calandra, F. Mauri, K. Rossnagel, I. Errea, S. Blanco-Canosa, *Nature Communications* **2021**, *12*, 598.

[295] M. Bayard, M. Sienko, *Journal of Solid State Chemistry* **1976**, *19*, 325–329.

[296] S. Barua, M. C. Hatnean, M. R. Lees, G. Balakrishnan, *Scientific Reports* **2017**, *7*.

[297] Q. Cao, F. F. Yun, L. Sang, F. Xiang, G. Liu, X. Wang, *Nanotechnology* **2017**, *28*, 475703.

[298] F. Li, K. Tu, Z. Chen, *The Journal of Physical Chemistry C* **2014**, *118*, 21264–21274.

[299] Y. Ma, Y. Dai, M. Guo, C. Niu, Y. Zhu, B. Huang, *ACS Nano* **2012**, *6*, 1695–1701.

[300] M. Esters, R. G. Hennig, D. C. Johnson, *Phys. Rev. B* **2017**, *96*, 235147.

[301] H.-R. Fuh, B. Yan, S.-C. Wu, C. Felser, C.-R. Chang, *New Journal of Physics* **2016**, *18*, 113038.

[302] J. Yang, W. Wang, Y. Liu, H. Du, W. Ning, G. Zheng, C. Jin, Y. Han, N. Wang, Z. Yang, M. Tian, Y. Zhang, *Applied Physics Letters* **2014**, *105*, 063109.

[303] Á. Pásztor, A. Scarfato, C. Barreteau, E. Giannini, C. Renner, *2D Materials* **2017**, *4*, 041005.

[304] P. M. Coelho, K. Nguyen Cong, M. Bonilla, S. Kolekar, M.-H. Phan, J. Avila, M. C. Asensio, I. I. Oleynik, M. Batzill, *The Journal of Physical Chemistry C* **2019**, *123*, 14089–14096.

[305] D. Biswas, A. J. H. Jones, P. Majchrzak, B. K. Choi, T.-H. Lee, K. Volckaert, J. Feng, I. Marković, F. Andreatta, C.-J. Kang, H. J. Kim, I. H. Lee, C. Jozwiak, E. Rotenberg, A. Bostwick, C. E. Sanders, Y. Zhang, G. Karras, R. T. Chapman, A. S. Wyatt, E. Springate, J. A. Miwa, P. Hofmann, P. D. C. King, Y. J. Chang, N. Lanatà, S. Ulstrup, *Nano Letters* **2021**, *21*, 1968–1975.

[306] M. Liu, C. Wu, Z. Liu, Z. Wang, D.-X. Yao, D. Zhong, *Nano Research* **2020**, *13*, 1733–1738.

[307] Y. Wang, J. Ren, J. Li, Y. Wang, H. Peng, P. Yu, W. Duan, S. Zhou, *Phys. Rev. B* **2019**, *100*, 241404.

[308] G. Duvjir, B. K. Choi, I. Jang, S. Ulstrup, S. Kang, T. Thi Ly, S. Kim, Y. H. Choi, C. Jozwiak, A. Bostwick, E. Rotenberg, J.-G. Park, R. Sankar, K.-S. Kim, J. Kim, Y. J. Chang, *Nano Letters* **2018**, *18*, 5432–5438.

[309] D. Zhang, J. Ha, H. Baek, Y.-H. Chan, F. D. Natterer, A. F. Myers, J. D. Schumacher, W. G. Cullen, A. V. Davydov, Y. Kuk, M. Y. Chou, N. B. Zhitenev, J. A. Stroscio, *Phys. Rev. Materials* **2017**, *1*, 024005.

[310] T. Moriya, *Spin fluctuations in itinerant electron magnetism*, **1985**.

[311] L. Fritsche, B. Weimert, *Physica Status Solidi (b)*, *208*, 287–337.

[312] S. Barua, M. C. Hatnean, M. R. Lees, G. Balakrishnan, *Scientific Reports* **2017**, *7*, 10964.

[313] G. Grüner, *Charge Density Waves in Solids*, Addison-Wesley, **1994**.

[314] W. Zhang, L. Zhang, P. K. J. Wong, J. Yuan, G. Vinai, P. Torelli, G. van der Laan, Y. P. Feng, A. T. S. Wee, *ACS Nano* **2019**, *13*, 8997–9004.

[315] M. Z. Hasan, C. L. Kane, *Rev. Mod. Phys.* **2010**, *82*, 3045–3067.

[316] N. P. Armitage, E. J. Mele, A. Vishwanath, *Rev. Mod. Phys.* **2018**, *90*, 015001.

[317] V. Pardo, W. E. Pickett, *Physical Review B* **2010**, *81*, 245117.

[318] A. A. Burkov, M. D. Hook, L. Balents, *Phys. Rev. B* **2011**, *84*, 235126.

[319] N. B. Kopnin, T. T. Heikkilä, G. E. Volovik, *Phys. Rev. B* **2011**, *83*, 220503.

[320] W. Chen, J. L. Lado, *Phys. Rev. Lett.* **2019**, *122*, 016803.

[321] Y. Shao, A. N. Rudenko, J. Hu, Z. Sun, Y. Zhu, S. Moon, A. J. Millis, S. Yuan, A. I. Lichtenstein, D. Smirnov, Z. Q. Mao, M. I. Katsnelson, D. N. Basov, *Nature Physics* **2020**.

[322] L. M. Schoop, M. N. Ali, C. Straßer, A. Topp, A. Varykhalov, D. Marchenko, V. Duppel, S. S. P. Parkin, B. V. Lotsch, C. R. Ast, *Nature Communications* **2016**, *7*, 11696.

[323] J. Hu, Z. Tang, J. Liu, X. Liu, Y. Zhu, D. Graf, K. Myhro, S. Tran, C. N. Lau, J. Wei, Z. Mao, *Phys. Rev. Lett.* **2016**, *117*, 016602.

[324] M. Neupane, I. Belopolski, M. M. Hosen, D. S. Sanchez, R. Sankar, M. Szlawska, S.-Y. Xu, K. Dimitri, N. Dhakal, P. Maldonado, P. M. Oppeneer, D. Kaczorowski, F. Chou, M. Z. Hasan, T. Durakiewicz, *Phys. Rev. B* **2016**, *93*, 201104.

[325] D. VanGennep, T. A. Paul, C. W. Yerger, S. T. Weir, Y. K. Vohra, J. J. Hamlin, *Phys. Rev. B* **2019**, *99*, 085204.

[326] C. C. Gu, J. Hu, X. L. Chen, Z. P. Guo, B. T. Fu, Y. H. Zhou, C. An, Y. Zhou, R. R. Zhang, C. Y. Xi, Q. Y. Gu, C. Park, H. Y. Shu, W. G. Yang, L. Pi, Y. H. Zhang, Y. G. Yao, Z. R. Yang, J. H. Zhou, J. Sun, Z. Q. Mao, M. L. Tian, *Phys. Rev. B* **2019**, *100*, 205124.

[327] J. Ebad-Allah, M. Krottenmüller, J. Hu, Y. L. Zhu, Z. Q. Mao, C. A. Kuntscher, *Phys. Rev. B* **2019**, *99*, 245133.

[328] M. Krottenmüller, M. Vöst, N. Unglert, J. Ebad-Allah, G. Eickerling, D. Volkmer, J. Hu, Y. L. Zhu, Z. Q. Mao, W. Scherer, C. A. Kuntscher, *Phys. Rev. B* **2020**, *101*, 081108.

[329] S. M. Young, S. Manni, J. Shao, P. C. Canfield, A. N. Kolmogorov, *Phys. Rev. B* **2017**, *95*, 085116.

[330] H. Huang, J. Liu, D. Vanderbilt, W. Duan, *Phys. Rev. B* **2016**, *93*, 201114.

[331] S.-J. Kim, T. F. Fässler, *Zeitschrift für Kristallographie - New Crystal Structures* **2008**, *223*, 325–376.

[332] A. Weiße, G. Wellein, A. Alvermann, H. Fehske, *Rev. Mod. Phys.* **2006**, *78*, 275–306.

[333] G. H. Wannier, *Phys. Rev.* **1937**, *52*, 191–197.

[334] R. Yu, X. L. Qi, A. Bernevig, Z. Fang, X. Dai, *Phys. Rev. B* **2011**, *84*, 075119.

[335] M. Taherinejad, K. F. Garrity, D. Vanderbilt, *Phys. Rev. B* **2014**, *89*, 115102.

[336] C. Li, C. M. Wang, B. Wan, X. Wan, H.-Z. Lu, X. C. Xie, *Phys. Rev. Lett.* **2018**, *120*, 146602.

[337] L. Oroszlány, B. Dóra, J. Cserti, A. Cortijo, *Phys. Rev. B* **2018**, *97*, 205107.

[338] H. Yang, R. Moessner, L.-K. Lim, *Phys. Rev. B* **2018**, *97*, 165118.

[339] J.-W. Rhim, Y. B. Kim, *Phys. Rev. B* **2015**, *92*, 045126.

[340] S. Ram, V. Kanchana, G. Vaitheeswaran, A. Svane, S. B. Dugdale, N. E. Christensen, *Phys. Rev. B* **2012**, *85*, 174531.

[341] J. Zhang, C. Liu, X. Zhang, F. Ke, Y. Han, G. Peng, Y. Ma, C. Gao, *Applied Physics Letters* **2013**, *103*, 052102.

[342] Y. Zhang, X. Shao, Y. Zheng, L. Yan, P. Zhu, Y. Li, H. Xu, *Journal of Alloys and Compounds* **2018**, *732*, 280–285.

[343] Y. Zhang, Y. Li, Y. Ma, Y. Li, G. Li, X. Shao, H. Wang, T. Cui, X. Wang, P. Zhu, *Scientific Reports* **2015**, *5*, 14681.

[344] W. Li, X.-Y. Wei, J.-X. Zhu, C. S. Ting, Y. Chen, *Phys. Rev. B* **2014**, *89*, 035101.

[345] W. Liu, X. Peng, C. Tang, L. Sun, K. Zhang, J. Zhong, *Phys. Rev. B* **2011**, *84*, 245105.

[346] J. Zhou, S. Zhang, J. Li, *NPG Asia Materials* **2020**, *12*, 2.

[347] V. Rajaji, R. Arora, S. C. Sarma, B. Joseph, S. C. Peter, U. V. Waghmare, C. Narayana, *Phys. Rev. B* **2019**, *99*, 184109.

[348] P.-J. Guo, H.-C. Yang, K. Liu, Z.-Y. Lu, *Phys. Rev. B* **2017**, *96*, 081112.

[349] T. Teshome, A. Datta, *ACS Omega* **2019**, *4*, 8701–8706.

[350] Y. Xia, G. Li, *Phys. Rev. B* **2017**, *96*, 241204.

[351] C. Zhang, J. Sun, F. Liu, A. Narayan, N. Li, X. Yuan, Y. Liu, J. Dai, Y. Long, Y. Uwatoko, J. Shen, S. Sanvito, W. Yang, J. Cheng, F. Xiu, *Phys. Rev. B* **2017**, *96*, 155205.

USC UNIVERSIDADE DE SANTIAGO DE COMPOSTELA